SYNTHESIS OF CARBON NITRIDE THIN FILM BY MAGNETRON SPUTTERING TECHNIQUE: ITS STRUCTURAL CHARACTERIZATION AND APPLICATION

A Thesis
Submitted to the Faculty of Engineering & Design
of Dublin City University
for the degree of
Doctor of Philosophy

by

A K M Shaestagir Chowdhury, B.Sc. Eng., M.Sc. Eng.

Materials Processing Research Centre
Dublin City University

Research Supervisor: Dr. David Campbell Cameron

Co-Supervisor: Professor M.S.J Hashmi

September 1998

It is difficult to say what is impossible, for the dream of yesterday is the hope of today and the reality of tomorrow

Robert H. Goddard

DECLARATION

I hereby certify that this material, which I now submit for assessment on the programme of study leading to the award of Ph.D. is entirely my own work and has not been taken from the work of others save and to the extent that such work has been cited and acknowledged within the text of my work.

Signed: _____ ID No.: 94971633

Date: 25 September, 1998

ACKNOWLEDGEMENTS

I would like to thank my academic supervisor Dr. David Cameron for his unceasing enthusiasm, interest, constructive criticism, practical hands-on assistance with the vacuum system and for putting up with me over the years. His expertise, availability to discuss ideas and willingness to give of his knowledge were instrumental in the completion of this thesis. I owe him much gratitude. I also thank him sincerely for facilitating my entrance to the field of Thin Film Technology.

I will be forever indebted to Professor M.S.J. Hashmi who not only funded my project but also supported me unstintingly. Without his support and encouragement this research would not have been done.

Thanks are very much owing to my colleague, Dr. Michael Murphy, Materials Ireland, Trinity College Dublin, for constructing the Penning Source and his continual guidance during these years. Michael has been a constant source of encouragement to me and I wish to extend my sincere thanks to him for always making himself available to offer advice and to discuss the ideas presented in this work.

Thanks are very much owing to Dr. Marty Gregg, Materials Science Div., Department of Pure and Applied Physics, The Queens University Belfast, Northern Ireland, for his technical guidance in Transmission Electron Microscopy (TEM). His criticism and valuable comments on the TEM work presented in this thesis were instrumental in showing unique evidence of the presence of crystalline carbon nitride solids. He is a pleasure to work with.

I would like to thank Professor John R. Abelson, Department of Materials Science and Engineering, University of Illinois at Urbana Champaign, USA, for his valuable comments on IR absorption coefficient measurements. The assistance of Miguel Monclus who did all the nanoindentation works on the carbon nitride films is gratefully acknowledged. The RBS was performed by Dr. Nuno Pessoa Barradas of the University of Surrey, UK. Thanks to Dr. Mike Hopkins of the Department of Physical Sciences, Dublin City University, for his assistance in carrying out the Langmuir Probe measurements. Thanks to Dr. Enda McGlynn, School of Physical Sciences, Dublin City University, for his assistance in carrying out the Raman Spectroscopic analysis. Thanks to Martin Johnson and Liam Domican for their regular support.

Thanks to Professor Ian P. Jones, School of Metallurgy and Materials, The University of Birmingham, UK, Dr. ir Bart Blanpain, Departement Metaalkunde en Toegepaste Materiaalkunde (Chemical division), Katholieke Universiteit Leuven, Belgium, Dr. Dougal G McCulloch and Dr. Alex Merchant, Key Centre

for Microscopy and Microanalysis and Department of Applied Physics, University of Sydney, Australia, for showing their interests in this research.

Many other friends and colleagues at this time in no particular order include Dr. Lisa Looney, Dr. Masrur Chowdhury, Dr. Mahiuddin Ahmed, Dr. Suraiya Akhter, Barbara Buccelli, Enca Perez, Giovanni Pepe, Gareth O'Donnell, Niall Moran, Brian Cohil, Hai Wang, Yousuf Ismail, John Gilvarry, Emmet Caulfield, Michelle Considine and a few Bangladeshi students.

Special thanks are due to the "Hanley" family who looked after me here in Ireland as if they were my own family. I will be forever indebted to Patrick Hanley for his Irish generosity. I owe this family a lot.

I would like to convey my sincere thanks to my family, especially my mom and dad, without whose support and encouragement this thesis would not have been written. Thanks are due to my brothers, sisters, nieces, nephews, who continually inspired me from the family. Special thanks are due to Dr. Mahabub Hossain, who always supported me in every respect. I take Dr. Hossain as a model in my research life. I owe him a lot.

There are many, many individuals who have contributed in major and minor ways to this work. Thanks are due to them, whose names I forgot to mention.

DEDICATION

This thesis is dedicated to my beloved father who always wished me to be a good scientist. He is not with us but I am carrying his spirit all the way to make his dream come true.

SYNTHESIS OF CARBON NITRIDE THIN FILM BY MAGNETRON SPUTTERING TECHNIQUE: ITS STRUCTURAL CHARACTERIZATION AND APPLICATION

ABSTRACT

AKM Shaestagir Chowdhury, B.Sc. Eng., M.Sc. Eng.

The purpose of this investigation was to establish a technique to deposit crystalline carbon nitride material and study its structural properties with the view to its use as hard coating. For the first time, carbon nitride thin films have been deposited, using a Penning-type opposed-target DC reactive sputtering source, that contain large continuous nanocrystalline areas ($>10\mu m^2$) of crystallography consistent with the β-C_3N_4 structure. In addition the creation of these β-C_3N_4 regions has been achieved with low substrate temperatures ($<270^0C$) and high deposition rates (2.5 - 3 $\mu m.hr^{-1}$).

The IR absorption due to carbon-nitrogen bonding was observed to be independent of actual nitrogen content above ~25 at.% N. It has been shown that over the range of 25-44% N/(N+C) there is no systematic variation of absorption coefficient. It was predicted and shown that films with >25 at.% nitrogen content, the nitrogen is mostly bonded to carbon either as C=N or C≡N bonds and a significant amount of nitrogen bonded with itself in IR-invisible structures. It was also seen that the C≡N bond (absorbance at 2200 cm^{-1}) concentration which controls the hardness of the film, can be eliminated at 600^0C. The physical explanation of the weakness of the polymeric CN network is probably due to the formation of this C≡N bonding which terminates the carbon backbone leading to less tightly bound C atoms. This feature was indicated by AES in the C KLL Auger spectrum and defined as a defect related π state in the structure. It was also seen that nitrogen incorporation in the film not only increases the nitrogen-nitrogen bonding but also stabilizes the C-C sp^3 type bonding. The breaking of C-C sp^3 bonds results from the input thermal energy as annealing progresses and leads to graphitisation of the film.

It is also seen that between the Raman D and G peaks there exists a third peak at ~1455 cm^{-1}, designated the "N" peak, which has been assigned to the N=N stretching vibration. As nitrogen incorporation in the film increases, the N=N, C≡N and C–C bonding intensities increase.

The presence of different bonding structures in CN network was also determined by XPS. The core level XPS peaks were assigned to different types of bond by correlating their behaviour as annealing takes place at different temperatures with changes in the bond structure as detected by vibrational

spectroscopy. The valence band XPS spectra show the interlinked carbon backbone nature of the carbon nitride solid and thus identify the structural nature of this solid which is significantly different from diamond-like and graphitic features.

It was seen that the hardness decreases as the C≡N bond concentration increases in the film. The intrinsic film stress was found to be lower for the nitrogenated films than for the pure carbon films. Unlike the film hardness it was found to be independent of the nitrogen content for films with >25 at. % N. It was also found to be independent of the film thickness indicating that the stress was introduced at the film-substrate interface during the initial growth process rather than in the bulk of the film.

This is the first time that structural modification of carbon nitride solid with negative bias was observed by valence band XPS spectra. Valence band XPS spectra show a significant change in structure, i.e., sp^2 to sp^3, in carbon nitride solid when the substrate negative bias was increased from -75 to -150V.

Carbon nitride in thin film form is a good candidate for hard coating but it has poor adhesion on tool steel due to diffusion of nitrogen or carbon atoms into the substrate at the deposition temperature (typically ~325^{0}C). Carbon nitride thin film has been deposited successfully for the first time directly on tool steel. Case hardened surfaces act as a diffusion barrier for nitrogen or carbon atoms from the film. The adhesion properties of the film was considerably improved on the nitrided samples compared to untreated substrates on which the films do not adhere.

The technique discussed here opens a new era in the production of crystalline carbon nitride solids. Successful fabrication of this C-N solid enlightens a new possibility in the field of super hard material.

Declaration
Acknowledgments
Dedication
List of Abbreviations

CONTENTS

ABSTRACT i

Chapter 1 Introduction 1-1

Chapter 2 **Carbon Nitride Compound: A review**

2.1 Carbon Nitride: A new low compressibility compound 2-1
2.2 Theoretical β-C_3N_4 2-3
2.3 Strategy for synthesis of stoichiometric β-C_3N_4 2-8
2.4 Thin film deposition technologies: An overview 2-9

2.4.1 Physical Vapour Deposition (PVD) 2-13
2.4.2 Chemical Vapour Deposition (CVD) 2-15

2.5 Deposition Techniques used for Carbon Nitride thin film 2-16
2.6 Characterisation of Carbon Nitride Thin Films 2-44

2.6.1 Composition of CN compound: A review 2-45
2.6.2 Structure and chemical bonding in CN Solid: A Review 2-47
2.6.3 Mechanical Properties of CN Solid 2-52

2.7 Application of CN Thin Film as Hard Coating: A Review 2-53

Chapter 3 **Sputter deposition and properties of sputtered films**

3.1 Sputtering 3-1
3.2 Mechanism of sputtering 3-3
3.3 Sputtering Technology 3-8

3.3.1 Diode Sputtering 3-9
3.3.2 Planar Magnetron Sputtering 3-10
3.3.3 Mechanism of magnetron sputtering 3-13

3.4 Thin Film Growth Mechanism 3-16

3.4 Thin Film Growth Mechanism 3-16
3.5 Zone Models for thin film growth 3-22
3.6 Film adhesion 3-32
3.7 Film Stress 3-36

Chapter 4 Penning Source: A New approach for Carbon Nitride Thin Film Deposition

4.1 Historical Background of Penning Source 4-1
4.2 Description of the Penning Source used for Carbon NitrideThin Film Deposition 4-5
4.3 The sputtering chamber and accessories 4-9
4.4 Carbon Nitride Thin Film Deposition 4-11
4.5 Magnetic fields in the Opposed Target Penning Source 4-13
4.6 General Operating Characteristics of the Source 4-23
4.7 Plasma species monitoring by Emission Spectroscopy 4-25
4.8 Bias Current Characteristics 4-31
4.9 Langmuir Probe Diagnostics: Basics 4-38
4.10 Plasma Characterisation of the Penning Source by Langmuir Probe 4-42

Chapter 5 Structural Determination: Techniques

5.1 Rutherford Backscattering Spectroscopy (RBS) 5-3

5.1.1 Fundamentals 5-4
5.1.2 Experimental details 5-7
5.1.3 Data Analysis 5-8

5.2 Fourier Transform Infrared (FTIR) and Raman Spectroscopy 5-9

5.2.1 Fundamentals 5-9
5.2.2 Absorption Coefficient of thin film 5-15
5.2.3 Instrumentation of FTIR and Raman Spectroscopy 5-18

5.3 Electron Spectroscopy 5-18

5.3.1 Principles of X-ray Photo Electron Spectroscopy (XPS) 5-19

5.3.1.1 Core Level Spectra and Chemical Shift 5-20

5.3.2 X-ray Photoelectron Valence band spectra 5-21

5.3.3 Principles of Auger Electron Spectroscopy (AES) 5-22

5.3.4.1 Chemical Shift 5-23

5.3.4 Instrumentation of XPS and AES 5-23

5.4 Principles of X-ray diffraction (XRD) 5-24

5.4.1 Intensity of Diffracted X-ray Beams 5-25
5.4.2 Scattering by electron 5-26
5.4.3 Scattering by atom 5-26
5.4.4 Scattering by unit cell 5-27
5.4.5 Instrumentation 5-29

5.5 Transmission Electron Microscopy (TEM) 5-29

5.5.1 Electron diffraction principles 5-30
5.5.2 Selected Area Diffraction (SAD) 5-32
5.5.3 TEM Imaging 5-34

5.5.3.1 Bright Field Image 5-34
5.5.3.2 Dark Field Image 5-34

5.5.4 Sample Preparation 5-35

5.5.4.1 Grinding 5-36
5.5.4.2 Ion Milling 5-36

5.5.5 Instrumentation 5-36

5.6 Nanoindentation Technique 5-36

5.6.1 Measurements of Hardness and Elastic Modulus 5-38
5.6.2 The Oliver and Pharr method 5-38

5.6.2.1 Substrate effects 5-43

5.6.3 Experimental Details 5-44

5.7 Stress Measurements 5-47

5.7.1 Intrinsic stress measurements by Bending Beam Method 5-47

5.8 Adhesion and Frictional Properties Measurements 5-49

5.8.1 Pin-on-disk tester 5-49
5.8.2 Rockwell indenter 5-51

5.8.2.1 Indentation and Adhesion Tests 5-52

Chapter 6 Structural Properties of Carbon Nitride Solid

Part I 6.1 Amorphous Carbon Nitride Films 6.3

6.1.1 Elemental Analysis of CN Solid by RBS 6-3
6.1.2 Bonding structure and absorption coefficient of CN Thin Film by FTIR 6-7
6.1.3 Vibrational properties of CN thin film by Raman Spectroscopy 6-10
6.14 Core level XPS spectra of Carbon Nitride compound 6-23
6.15 Valence Band XPS spectra of Carbon Nitride Solid 6-37
6.1.6 AES Spectra of Carbon Nitride Solid 6-42

Part II 6.2 Continuous crystalline β-C_3N_4 films 6-49

6.2.1 Structural analysis of Carbon Nitride material by X-ray diffraction technique 6-48
6.2.2 TEM analysis of Carbon Nitride Solid 6-61

Part III6.3 Effect of Process Parameters 6-73

6.3.1 Effect of experimental parameters on carbon nitride thin film 6-73
6.3.2 Effect of Hydrogen on CN film 6-86

Part IV 6.4 Mechanical Properties of CN Solid 6-95

6.4.1 Mechanical characterisation by Nanoindentation Technique 6-95

6.4.1.1 Hardness and bonding structure 6-98

6.4.2 Stress measurements 6-101

6.4.2.1 Intrinsic stress in carbon nitride film 6-101

Chapter 7 Carbon Nitride Thin Film as Hard Coating on Tool Steel

7.1 Sample Preparation prior to deposition 7-2

7.1.1 Heat Treatment Furnace 7-3
7.1.2 Nitriding 7-4
7.1.3 Carburising 7-5
7.1.4 Surface Polishing 7-7

7.2 Carbon Nitride thin film coating on case hardened steel 7-8

7.2.1 Mattox's comments on "Surface effects on the growth, adhesion and properties of reactively deposited hard coatings" 7-9

7.3 Structural properties of the films deposited on steel surfaces 7-11

7.3.1 Surface analysis by XPS and RBS 7-11
7.3.2 Vibrational properties by Raman spectroscopy 7-13

7.4 Adhesion and frictional properties of the films 7-15

Chapter 8 Conclusions and Recommendations

8.1 Deposition Technique 8-1
8.2 Characterisation Techniques 8-2
8.3 Film Structure: Amorphous 8-2
8.4 Film Structure: Crystalline 8-5
8.5 Effect of Process Parameters 8-6
8.6 Mechanical Properties of the film 8-7
8.7 Carbon Nitride Thin Film as Hard Coating 8-7
8.8 Strategy for Carbon Nitride thin film deposition 8-8
8.9 Future work 8-10

Publications i

Appendix A Nomenclature in emission spectroscopy A-i

Appendix B XPS Peak Fitting Programme B-i

Appendix C Bending Beam Method C-i

LIST OF ABBREVIATION

AES	Auger Electron Spectroscopy
CN	Carbon Nitride
CVD	Chemical Vapour Deposition
DPBD	Direct Plasma Beam Deposition
ECR	Electron Cyclotron Resonance
FNS	First Negative System
FTIR	Fourier Transform Infrared
IAAD	Ion Assisted Arc Deposition
IBD	Ion Beam Deposition
IBAD	Ion Beam Assisted Deposition
HFCVD	Hot Filament CVD
MIR	Multiple Internal Reflection
OES	Optical Emission Spectroscopy
PVD	Physical Vapour Deposition
PECVD	Plasma Enhanced CVD
PECT	Plasma Enhanced Chemical Transport
RBS	Rutherford Backscattering Spectroscopy
SAD	Selected Area Diffraction
SAIP	Shielded Arc Ion Plating
TED	Transmission Electron Diffraction
TEM	Transmission Electron Microscopy
UHV	Ultra High Vacuum
XPS	X-ray Photoelectron Spectroscopy
XRD	X-ray Diffraction

Chapter 1

Introduction

It is a challenge for materials scientists to design and synthesise new materials possessing exceptional properties, e.g., electrical or mechanical. Although first-principle modeling makes the design part increasingly achievable, production of the predicted material in reality could be an utmost challenge for the experimentalists. Covalent bonded material usually shows the highest bulk modulus (100 to 443 GPa) among all the engineering materials, e.g., rare gas solids (1 to 2 GPa), ionic solids (10 to 60 GPa), simple metals (100 to 300 GPa) [1]. Because of the large bulk modulus values for the covalent bonded materials group, the current focus has been on them and systems similar to diamond.

In 1985, M. L. Cohen [2] postulated a semi-imperical approach to calculate the bulk modulus of materials. He first applied this approach to group IV, III-V and II-VI tetrahedrally bonded materials. For bond lengths d expressed in angstroms, B is given in gigapascals by [1]

$$B = \frac{N_C}{4}\frac{(1972 - 220I)}{d^{3.5}} \qquad (1)$$

where N_C is the coordination number. An empirical ionicity parameter I = 0, 1, and 2 for groups IV, III-V and II-VI solids, respectively, accounts for the reduction in B arising from increased charge transfer. For tetrahedral systems, $N_C = 4$, otherwise N_C is the average coordination number. Charge transfer occurs due to repulsive Pauli

potential that keeps the valence electrons away from the core region [1]. For example, in β-Si_3N_4 structure, the p electrons in the Si cores repel the valence p electrons, whereas the N cores, which are only s-like, do not contribute a strong p repulsion. The result is considerable charge transfer from Si to N and the structure is more ionic bonded. In case of β-C_3N_4, charge transfer is not significant, as because both C and N have the same core structure. The resulting C–N covalent bond is strong and somewhat similar to the C–C bond in diamond [1].

After successful application of this semi-imperical solution to well known system, e.g., β-Si_3N_4, to see its validity, it was found that the model is in close agreement with experimentally observed data [3]. This approach was then used to predict new materials which may have higher B values. To obtain high B values, only minimised d and I were considered. Because small atomic radii imply small d, the first-row atoms of the periodic table are good candidates for this purpose. For example, the radii of C and N are 0.77Å and 0.70 Å respectively. These radii yield d = 1.47Å for C–N bonds and I < 1, Eq. 1 suggests [1] that carbon nitride compounds have high bulk modulii. A prototype crystal structure for β-C_3N_4 was chosen with knowledge of the known structure of β-Si_3N_4. The average coordination number for this structure is $N_C = 3.43$ [1]. Using estimates of I and d, the Eq.1 gives B for β-C_3N_4 ~410 to 440 GPa which is very close or even higher than B ~ 443 GPa for diamond, the hardest material known ever.

Hundreds of experimental efforts to synthesize and characterize new materials have begun based upon the assumption that hardness is determined primarily by the bulk modulus (a measure of its resistance to volume change upon reversible hydrostatic compression) which is given by [1]

$$B = -V\frac{\partial P}{\partial V} \qquad (2)$$

where V and P are volume and pressure, measured in the pressure unit gigapascal (1GPa = 10,000 bar). Super hard materials can be defined as having a micro-hardness exceeding 40 Gpa [1]. Veprek et al [4] suggested that high strength materials should be composed of a high value of the bulk modulus and an appropriate microstructure. They defined bulk modulus B related to the force constant of the inter-atomic bond, i.e. to the second derivative of the bond energy [4]

$$B = \frac{d^2E}{da^2} \tag{3}$$

where a is the bond distance. Thus, a high bond energy and short bond distance are necessary for a high value of B. A high bond energy means a high electron density between the neighboring atoms i.e. a covalent, non-polar bond.

In addition to high hardness, the high strength materials usually possess other unique properties such as high thermal conductivity and compressional strength. This combination of properties makes these materials highly desirable for a number of industrial applications such as super-abrasives, wear resisting coatings, heat-sinks, radiation windows, and even surgical knives [5]. As a selection criterion for a new super hard material, the definition of the term "hardness" should be discussed. This property can suggest the bonding structure of a compound. For example, it is expected to have higher hardness values from the solid composed of shorter bond length. Bond length is another parameter by which the local density of states can be understood.

Boron-Carbon-Nitrogen Ternary system

It can be seen from Table 1 that the hardest materials (top 6) are based on elemental carbon or are ceramic compounds such as the carbides and nitrides of boron as well as carbon nitrides. It is necessary to present their isothermal ternary system. Since

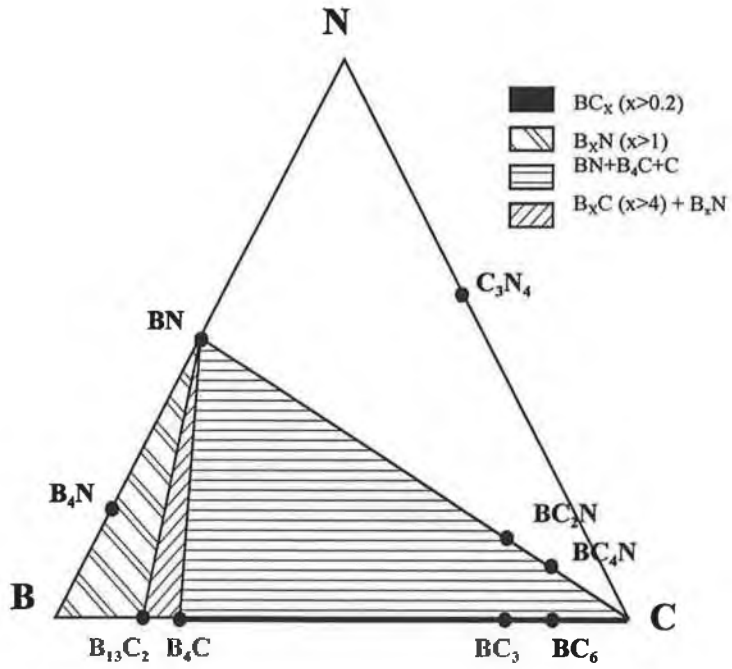

Figure 1: Schematic of the isothermal ternary B/C/N phase diagram at temperatures below the decomposition of the stoichiometric compounds and the regimes of composition of some solid solutions [6].

diamond, cubic boron nitride (c-BN) and boron carbides ($B_{13}C_2$-$B_{12}C_3$) are the hardest materials known, it can be expected that novel superhard compounds will be found in the isothermal ternary phase diagram B/C/N shown schematically in figure 1. This ternary phase diagram can also be a good input for the prediction of C_3N_4 compound as a superhard material.

Definition of Hardness

H. O'Neill [7] mentioned "*Hardness, like the storminess of the sea, is easily appreciated but not readily measured.*" Hardness is not only difficult to measure, it is difficult to define. In a general sense, hardness is a complex property related to the extent to which solids resist both elastic and plastic deformation. For materials with defects, hardness can be limited by many factors including point defects, dislocations, and macroscopic defects [8]. On the microscopic level, for ideal systems, hardness is determined by the bulk modulus, which in turn depends on the nature of the chemical bonding. It is the strength and compressibility of the bond that plays the primary role in a solid's ability to resist deformation.

If the hardness of a material is thought at the atomic level, the definition becomes more clear. For example, a rigid crystal should be more resistant to deformation than a compliant one. Goldschmidt attempted an atomic definition of hardness considering the atomic valences and bond distances. Physical properties of materials, such as, the "volumetric lattice energy" [9,10], bond ionicity [11], melting point [12], and band gap [13,14], can also help to predict hardness with varying degree of success. An alternative approach considers the elastic properties of a material as mentioned by D.M. Teeter [15]. He mentioned that shear modulus (the resistance to reversible deformation upon shear) might well be a predictor of hardness more securely rooted in the nature of the actual deformation processes [15].

Table 1: A subset of Vickers Hardness Values (VHN), Bulk Moduli K_o, and Shear Moduli G_o (Theoritical) [15].

Materials	VHN (GPa)	K_o (GPa)	G_o (GPa)
Diamond C	96±5	443	535
BC_2N	-	408	445
Cubic BN	63±5	400±3	409±6
Defect zincblende C_3N_4	-	448	390
Cubic C_3N_4	-	496	332
β-C_3N_4	-	437	320
B_6O	35±5	228	204
TiB_2	33±2	244	263
SiO_2 (stishovite)	33±2	305±11	220
BP	33±3	169±4	174
B_4C	30±2	247	171±11
WC	30±3	421	-
TiC	29±3	241±1	188±6
SiC	28±3	226±9	196±13
ZrC	27±2	223	166±2
NbC	23±3	229±2	197±15
Al_2O_3	22±2	246±11	162±2
Si_3N_4	21±3	249±3	123±2
$MgSiO_3$ (perovskite)	18±2	256±7	177
HfN	17±2	422	141
VN	15±1	268	159
NbN	14±1	315±28	156
AlN	12±1	203±5	128±2
GaN	12±2	210	120
$ZrSiO_4$	12±1	227	109

Let us consider the current status of the superhard materials in order of different hardness definitions (Table 1). For consistency we have chosen the Vickers hardness test for all, and compare it to the bulk modulus (K_o) and the shear modulus (G_o).

Considering the bulk modulus as the deciding factor for superhard materials, it is clear that Carbon Nitride shows the highest values among the most important engineering materials. The compound β-C_3N_4 is considered to have the β-Si_3N_4 structure and is only a partially tetrahedrally coordinated structure. The unit cell of β-C_3N_4 is hexagonal and contains two formula units. The carbon atoms are sp^3 hybridized and tetrahedrally surrounded by N atoms, whereas nitrogen has a planar trigonal coordination (sp^2 hybridization). The overall structure can be described by a network of CN_4 tetrahedra and NC_3 sites [6].

Although all the phases of C_3N_4 compound discussed above are theoretically predicted, synthesis of these phases in reality, is really a challenge for experimentalists. However, the energetic stability of β-C_3N_4 has been checked upon both chemical [16-19] and thermodynamical [19,20] grounds. The primary chemical concerns are the presence of trigonal planar NC_3 groups and close nitrogen-nitrogen distances. Synthesis of carbon nitrides has been attempted for example by the pyrolysis of organic nitrogen-containing compounds such as melamine-formaldehyde resin and subsequent shock compression of the residues [21]. However, no tetrahedral carbon nitride could be detected in the reaction products. In a similar approach, L. Maya et al. [22] obtained a carbon nitride with trigonally coordinated carbon by the pyrolysis of organic compounds at 700°C and 225 Mpa pressure. Plasma decomposition of CH_4 and N_2 resulted in amorphous solids containing C, N and H, exclusively [23]. High pressure pyrolysis of tetracyanoethylene gave $C_{4.66}N$ with a graphitic structure [24]. Similarly, the gas-phase decomposition of pyridyne in the presence of chlorine at 800°C provided the carbon nitride C_5N with hexagonal sheet structure [25]. Nevertheless, according to theoritical calculations, the synthesis of C_3N_4 should be possible. Therefore, Liu and Cohen suggested the synthesis of amorphous carbon

nitride followed by the application of high pressures and temperatures to induce the formation of crystalline carbon nitride materials [8].

It is now clear that the production of crystalline β-C_3N_4 has been the goal of much research. There have been many reports of amorphous carbon nitride films of uncertain composition but there have only been a few observations of crystalline β-C_3N_4 produced by diode sputtering, laser ablation and hot filament CVD [26-29]. The films reported have been discontinuous with isolated crystals [29] or showing only a few isolated grains in an amorphous matrix [26,28] and in most cases high substrate temperatures (600-950°C) were required.

Subject of thesis

Broadly speaking this thesis is concerned with carbon nitride thin film deposition by magnetron sputtering technique and their physical and mechanical characterisation. The focus is on the process parameters for successful deposition of crystalline β-C_3N_4 films. The thesis is also concerned with the application of this material as hard coating on different substrates.

Aim of this thesis

- To produce crystalline β-C_3N_4 film by sputtering technique.
- To diagnose the plasma of a Penning type oposed-target DC sputtering system to understand the role of energetic species in carbon nitride thin film growth process.
- To establish successful deposition parameter for continuous β-C_3N_4 thin film deposition.
- To characterise the bonding structure of the films and correlate their bonding nature with physical properties.

- To measure the mechanical properties, i.e., hardness, intrinsic stress, of the film and relate these properties with bonding structure, film composition.

- To measure the thermal stability of the film and analyse the structural modification of the film with temperature.

- To evaluate carbon nitride thin film as hard coating on tool steel.

References

1. M.L. Cohen, Science, 261, 307 (1993).

2. M.L. Cohen, Phys. Rev. B, 32(12), 7988 (1985).

3. A.Y. Liu, M.L. Cohen, Phys. Rev. B, 41(15), 10727 (1990).

4. S. Veprek, Surf. Coat. Technol., 97, 15 (1997).

5. Status and Application of Diamond and Diamond-like Materials: An Emerging Technology, MDA 903-89-K-0078, National Research Council, Washington, 1990.

6. R. Riedel, Adv. Mater., 6(7/8), 549 (1994).

7. H.O'Neill, The Hardness of Materials and Its Measurements, Chapman & Hall, London, 1934.

8. A.Y. Liu and M.L. Cohen, Science, 245, 841 (1989).

9. J.N. Plendl and P.J. Gielisse, Phys. Rev., 125, 828 (1961).

10. G. Grimvall and M. Thiessen, in Inst. Phys. Conf. Ser. No. 75, Adam Hilger Ltd., Boston, pp.61, 1986.

11. A. Julg, Phys. Chem. Min., 3, 45 (1987).

12. P.S. Kisly, in Inst. Phys. Conf. Ser. No. 75, Adam Hilger Ltd., Boston, pp.107, 1986.

13. J.J. Gilman, Science, 261, 1436 (1993).

14. J.J. Gilman, Mater. Sci. Eng. A, 209, 74 (1996).

15. D.M. Teter, MRS Bulletin, 23(1), 22 (1998).

16. Y. Guo and W.A. Goddard, Chem. Phys. Lett., 237, 72 (1995).

17. T. Hughbanks and Y. Tian, Solid State Commun., 96, 321 (1995).

18. M.M. Julian and G.V. Gibbs, J. Phys. Chem., 92, 1444 (1988).

19. J.V. Badding and D.C. Nesting, Chem. Mater., 8, 535 (1996).

20. T.H. Hall, Science, 148, 1331 (1965).

21. M.R. Wixom, J. Am. Ceram. Soc., 73, 1973 (1990).

22. L. Maya, D.R. Cole, E.W. Hagaman, J. Am. Ceram. Soc., 74, 1686 (1991).

23. H.X. Han, B.J. Feldman, Solid State Commun., 65, 921 (1988).

24. T. Sekine, H. Kanda, Y. Bando, M. Yokoyama, K. Hojou, J. Mater. Sci. Lett., 9, 1376 (1990).

25. J. Kouvetakis, R.B. Kaner, M.L. Sattler, N. Bartlett, J. Chem. Soc. Commun., 1758 (1986).

26. K. M. Yu, M. L. Cohen, E. E. Haller, W. L Hansen, A. Y. Liu and I. C. Wu, Phys. Rev. B, 49, 5034 (1994).

27. Z. Ze-Bo, L. Yin-An, X. Sie-Shen and Y Guo-Zhen, J. Mater. Sci. Letts., 14, 1742 (1995).

28. C. Niu, Y. Z. Lu and C. M. Lieber, Science, 261, 334 (1993).

29. E. G. Wang, Y. Chen and L. Guo, Physica Scripta, T69, 108 (1997).

Chapter 2

Carbon Nitride Compound: A review

This chapter introduces carbon nitride material and presents a review of studies done by Liu and Cohen [1]. The chapter also presents some pertinent studies conducted by others. An overview of different deposition techniques which were claimed to be successful for carbon nitride thin film deposition is discussed. Success in deposition of crystalline β-C_3N_4 phase is achieved by some of the experimental techniques. The chapter will emphasize on the discussion of the successful deposition techniques. Different characterisation techniques were employed to determine the bonding structure and film morphology. Characterisation techniques which are presented in the literature are discussed. Finally, the current status of the material in view of the presence of β-C_3N_4 is presented.

2.1 Carbon Nitride: A new low compressibility compound

In 1984, C.M. Sung [2] predicted the possible existence of Carbon Nitride, i.e. C_3N_4 material in his unpublished patent disclosure letter at Diamond Technology Centre of Norton Company. Because of their short interatomic distances, these hypothetical materials were suspected to be very hard. This speculation initiated Cohen in 1985 [3] to develop an empirical model and *ab initio* calculation of the bulk modulii for covalent solids formed between carbon and nitrogen. On the basis of this model, properties like bond strength of hypothetical β-C_3N_4 compound were assessed. He suggested theoretically that these materials could have bulk modulii comparable to or greater than

diamond. In 1989 Liu and Cohen [4] suggested that due to the expected short bond length and low ionicity of this compound, its bulk modulus, and hence its hardness, may be comparable to that of diamond. In 1990 they [1] presented a first-principles pseudopotential study of the structural and electronic properties of well known β-Si_3N_4 material and the hypothetical compound β-C_3N_4. The calculated lattice constant, bulk modulus and electronic band structure of β-Si_3N_4 are in good agreement with experimental results which gives support to the findings of this study concerning the properties of unknown carbon-nitrogen compound. Continuous research to synthesise β-C_3N_4 can not only yield a potentially very important material for advanced technology but also enrich the theoretical background to develop new materials. Moreover, If the compound could not be synthesised, other CN_x compounds may exist with similar interest. This chapter will briefly review the theoretical predictions of Liu and Cohen and experimental success to synthesise the predicted compound.

In 1995, P.H. Fang [5] pointed out non-crystalline materials with the empirical formula C_3N_4 were synthesised by E.C. Franklin [6] as long as 70 years ago. But those materials have little similarity in structural properties with β-C_3N_4. A number of possibilities can occur during carbon nitride deposition. Although there have been no unambiguous reports of the formation of crystalline stoichiometric β-C_3N_4 solids so far, however, amorphous CN_x films have been produced. When carbon atoms bond with nitrogen atoms, a number of hybridizations could be possible, such as sp, sp^2 and even sp^3. Kaufman et al. [7] proposed a model for the nitrogen doped carbon solid where nitrogen atoms replace one of the carbon atoms in the carbon-carbon homocyclic ring structure. This is how the carbon nitride solid can have the C=N sp^2 type matrix. Marton et al. [8] and Sjostrom et al. [9] proposed models regarding the bonding nature of this solid. They suggest that a nano crystalline structure which is predicted as β–C_3N_4 could be formed within the sp^2 type C=N matrix. This bonding nature explains the probable mechanical properties which grades this material in the hardness range of diamond. Since many properties, including hardness, depend more on local bonding than on long

range order, amorphous materials that contain a large percentage of nano crystallites may be very important. These nano crystallites act as strengthening particles in the amorphous matrix and thus can explain the higher hardness properties of this type of material.

2.2 Theoretical β-C_3N_4

Liu and Cohen [1] studied well known β-Si_3N_4 structure and predicted the properties of β-C_3N_4. They used the structure where C substitutes Si in the β-Si_3N_4 as a prototype for investigating the properties of possible covalent carbon-nitrogen solids. Diamond, which has the largest bulk modulus (443 GPa), is also the hardest known solid. This was the motivation to propose a theory of the bulk moduli of covalent solids to suggest schemes to increase hardness. This section will be discussed as a review based entirely on Liu and Cohen's empirical work.

Cohen [3] developed an empirical model for the bulk moduli of covalent solids. To achieve a large bulk modulus, two properties are needed: low ionicity and short bond length. Liu and Cohen [4] investigated the structural and electronic properties of a solid of this type using first principles pseudopotential calculations.

In Fig. 1, the structure is shown to consist of buckled layers stacked in an AAA.... Sequence [10]. The unit cell is hexagonal and contains two formula units (14 atoms) with local order such that C atoms occupy slightly distorted tetrahedral sites while N atoms sit in nearly planar triply coordinated sites. This structure can be thought of as a complex network of CN_4 tetrahedra that are linked at the corners. The atomic coordination suggests sp^3 hybrids on the C atoms and sp^2 hybrids on the N atoms. The hexagonal unit cell and the planer coordination of the N sites raise the possibility that this structure may exhibit anisotropic elastic properties. Figure 2 shows the structure in the direction 90^0 to the a-b plane. Small hexagonal walls are observed in this direction, although the structure can be easily demonstrated in the a-b plane (figure 1). However,

on a local scale, the CN_4 tetrahedra are linked in such a way that the in-plane and out-of-plane bonding are similar. The network is three dimensional and is not obviously weak in any direction. This is supported by measurements [11] of the elastic constants of β-Si_3N_4 which show nearly equal in-plane and out-of-plane linear compressibilities. Hence the β-Si_3N_4 structure is a good prototype for studying C_3N_4 solids.

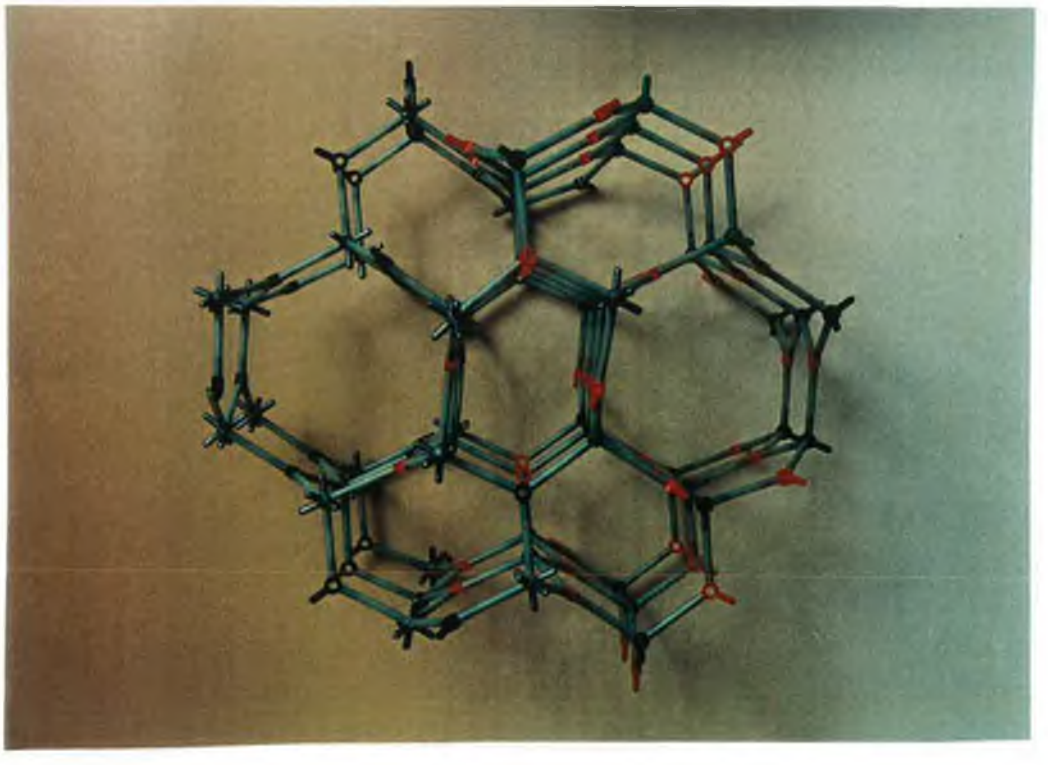

Fig. 1 Structure of β-C_3N_4 in the a-b plane. The c-axis is normal to the page. Half the atoms shown are located in the z=-c/4 plane, the other half are in the z=c/4 plane. The structure consists of these buckled planes stacked in AAA...sequence. All the planes are arranged parallel to the z axis forming walls of large equilateral and smaller elongated hexagonal cylinders (as shown in the centre). The parallelogram shows the unit cell [4].

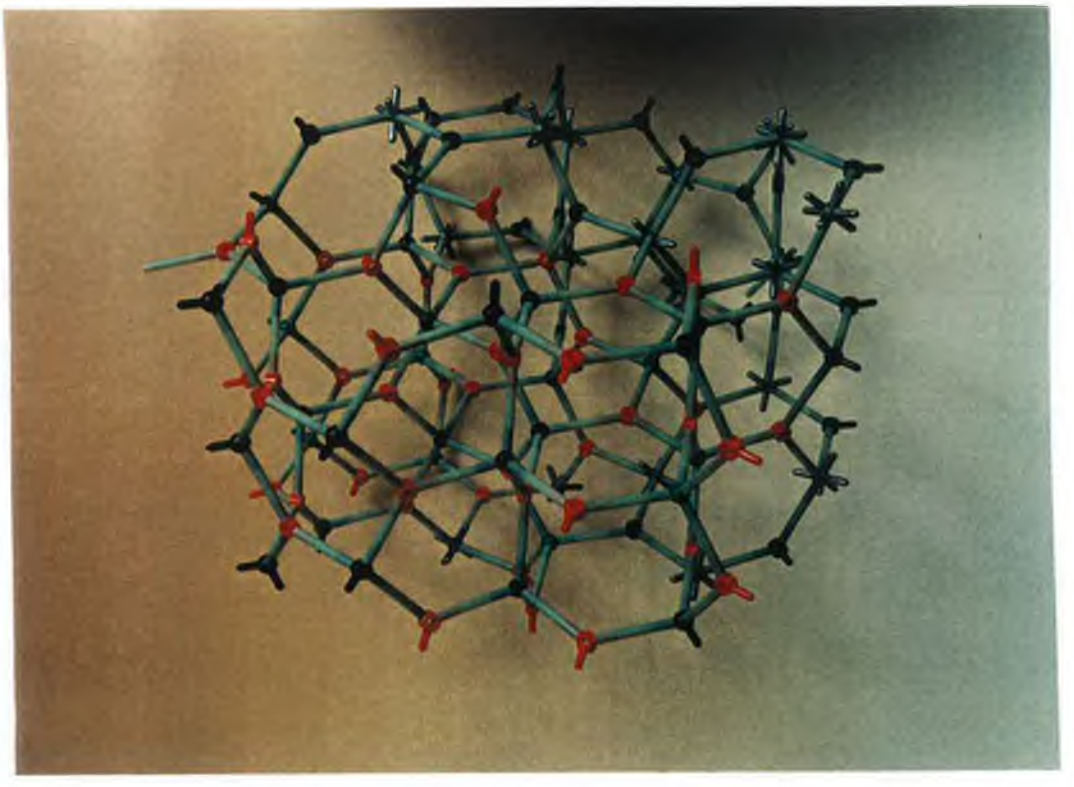

Figure 2: Illustration of the structure in the direction 90° to the a-b plane (parallel to x-axis).

They calculated the structural and electronic properties of the hypothetical compound β-C_3N_4 (C_3N_4 in the β-Si_3N_4 structure) by means of the first principles pseudopotential total energy approach [1]. They determined the structural properties of β-C_3N_4 by calculating the total crystal energy as a function of volume. At the equilibrium volume, the cohesive energy of β-C_3N_4 is calculated to be 81 eV per cell or an average value of 5.8 eV per atom [4]. This moderately large cohesive energy suggests that there is a good chance that β-C_3N_4 is at least a metastable structure. At the calculated equilibrium volume, the average C-N bond length is found to be 1.47 Å [4]. This is in good agreement with the sum of the tetrahedral covalent radii [12] of C and N. The bulk modulus of β-C_3N_4 is determined by fitting the total energy as a function of volume to Murnaghan's equation of state [13] which yields a value of 427 ($\pm$0.15) GPa. For the calculated bond length and an estimated ionicity factor of $\lambda = ½$, the scaling law (eq.1, chapter 1) overestimates the bulk modulus of β-C_3N_4 by about 10%. A similar overestimate is found for the bulk modulus of β-Si_3N_4 which has a measured [11] value of 250 GPa. These overestimates are most likely caused by the structural difference between these materials and the zinc-blende systems on which Eq. 1 was based (chapter 1). In particular, the trigonal coordination of N in β-C_3N_4 and β-Si_3N_4 allows only three electrons per N site to participate in the bonding. The remaining N electrons occupy nonbonding p orbitals perpendicular to the bonding plane. This reduction in the number of bonds compared to a tetrahedral system results in elastic constants that are slightly lower than those predicted by Eq. 1 (chapter 1).

They also compared three different materials: diamond, β-C_3N_4 and BN, to find a relationship of degree of ionicity. It was interesting to see that for β-C_3N_4 the heteropolarity of C-N bond lies in the intermediate stage. The degree of ionicity in β-C_3N_4 can be seen in plots of the charge density. Fig. 3 shows the total valence charge density in the [0001] plane of β-C_3N_4 [4]. This plane contains a central N atom surrounded by its three C neighbors.

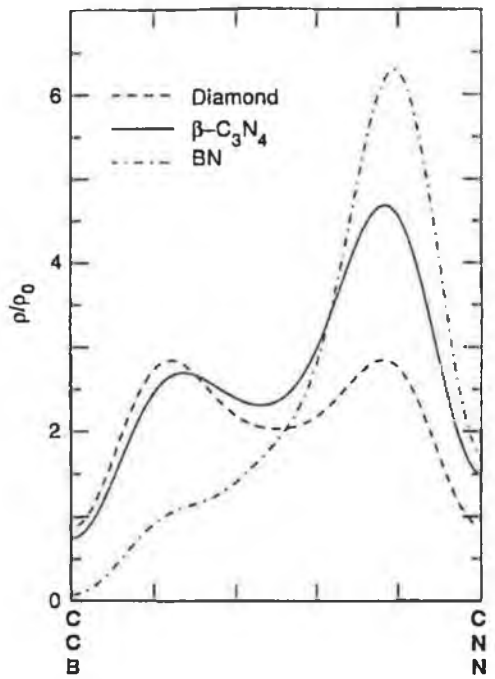

Fig. 3. Normalised valence charge density along the bond in diamond, β-C_3N_4 and BN. The normalization factor, ρ_o, is the number of valence electrons per cell [4].

The bonds are highly directional, as expected for a covalent system [4]. For comparison, linear plots of the charge density along a bond in diamond and BN, as well as β-C_3N_4, are given in Fig. 3. To facilitate comparison between the different structures, the charge densities have been normalized by the total number of electrons per cell. In diamond, there are two local maxima along the bond [4]. The presence of the double hump rather than a single maximum near the centre of the bond is a result of strongly attractive C 2p potential. The two maxima reach a normalized height of 2.9 [4]. With increasing ionicity, the local maximum near the anion grows at the expense of the one near the cation. In β-C_3N_4, the two local maxima remain, but the charge is weighted towards the N site. The height of the peaks are 2.7 and 4.6. In BN, the charge is strongly localized near the N site and the bond exhibits only a single peak of height 6.3 [4]. Thus the

heteropolarity of C-N bond in β-C_3N_4 lies intermediate between purely covalent diamond and partially ionic BN.

They suggested [4] that it may be possible to synthesize a covalent C-N solid such as β-C_3N_4 with compressibility comparable to diamond. A possible starting material is amorphous carbon nitride, which has a polymeric structure [14]. The application of high pressure and temperatures to α-C:N may induce a phase transition to a structure with more tetrahedral bonding. This transition would be similar to the transition of graphite to diamond.

Only the prediction of hardness could show the possibility to consider this material as engineering material. But there are other properties, such as chemical reactivity, thermal stability, fracture toughness should be considered. Above all, the successful fabrication of this low compressibility C-N solid would open a new possibility in the field of super hard material.

2.3 Strategy for synthesis of stoichiometric β-C_3N_4

A strategy can be formulated as a precondition for the synthesis of stoichiometric C_3N_4 solid. These are in good agreement with Veprek's [15] strategy which will be discussed in detail in later chapters. It is thus necessary to discuss the strategy briefly:

1. An intense low pressure nitrogen discharge which provides a high concentration of atomic nitrogen in order to drive the stoichiometry above that of paracyanogen $(CN)_n$.

2. As carbon is three-fold (sp^2) coordinated in $(CN)_n$ but four-fold (the metastable sp^3 hybridization) in C_3N_4 the substrate should be biased during the deposition to provide bombarding with ions at energies of 100-150 eV which stimulates the

formation of sp^3 and decreases that of sp^2 hybrids. A detailed description of sp^3 hybrid formation mechanism is given by Robertson [16].

3. The processes just discussed cannot fully avoid the simultaneous formation of three-fold (sp^2) coordinated CN structure, a temperature ≥800°C should be used to facilitate the evaporation of paracyanogen nuclei whenever formed.

4. Considering the well established crystal chemistry of the iso-structural Si_3N_4 one can expect the formation of amorphous C_3N_4 under the conditions discussed above, because the formation of crystalline β-Si_3N_4 requires temperatures in excess of 1350°C as mentioned by Wells [17]. Thus amorphous Si_3N_4 can be expected when deposited below 1000°C. This point can be ignored when energetic species are formed with suitable C/N ion ratio.

5. Although (strategy 4) very high substrate temperature, i.e., 1000-1200°C may be thermodynamically necessary to obtain crystalline β-C_3N_4 phase, at this high temperature one can expect (if Si is used as substrates) (1) Si diffusion during growth; (2) evaporation and re-deposition of Si; (3) catalytic action of Si in crystal growth. Based on several observations on the growth of this material, the effects (1) and (2) can be ruled out, incorporation of Si together with high substrate temperature has catalytic action for C-N-Si crystal formation Chen et al. [18].

2.4 Thin film deposition technologies: An overview

It is worthwhile to classify the important deposition techniques, although the next section will discuss only a few important techniques which are used to deposit carbon nitride thin film successfully. Table 1 gives a classification of deposition technologies. Detail discussions of all these deposition techniques can be found in most of the Thin Film related text books. Thermal forming processes and liquid phase chemical techniques are the most common type of surface engineering techniques. The liquid-

phase chemical techniques are becoming obsolete because of the dumping problem of toxic chemicals. Thermal Forming processes are still in use because of their flexibility, but these processes are only used for surface modification. However, emphasis are given on vapour deposition techniques due to their process versatility and thus becoming increasingly important for device fabrication, coatings for biomedical implants or even mechanical coating, i.e, decorative or hard coatings. Thin film deposition technologies are either purely physical, such as sputtering or purely chemical, such as gas-phase chemical processes. A number of processes that are based on glow discharges and reactive sputtering combine both physical and chemical reactions; these processes are known as physical-chemical methods. Detail description of all these vapour deposition techniques are not the scope of this thesis, but an attempt is taken to clarify the successful process technologies that are used for carbon nitride thin film deposition. However, It is necessary to discuss briefly the main points on physical and chemical vapour deposition techniques. Table 2 shows the classification of vapour phase deposition techniques.

Table 1: Classification of thin-film deposition technologies

EVAPORATIVE METHOD

Vacuum Evaporation

- Conventinal Vacuum evaporation
- Electron beam evaporation
- Molecular Beam Epitaxy
- Reactive Evaporation

GLOW-DISCHARGE PROCESSES

Sputtering

- Diode sputtering
- Reactive sputtering
- Bias sputtering (ion plating)
- Magnetron sputtering
- Ion beam deposition
- Ion beam sputter deposition
- Reactive ion plating
- Cluster beam deposition (CBD)

Plasma Processes

- Plasma enhanced CVD
- Plasma oxidation
- Plasma polymerization
- Plasma nitridation
- Plasma reduction
- Microwave ECR plasma CVD
- Cathodic arc deposition
- Plasma anodization

GAS-PHASE CHEMICAL PROCESSES

Chemical Vapour Deposition (CVD)

- CVD epitaxy
- Atmospheric-pressure CVD (APCVD)
- Low pressure CVD (LPCVD)
- Metalorganic CVD (MOCVD)
- Photo-enhanced CVD (PHCVD)
- Laser-induced CVD (PCVD)
- Electron-enhanced CVD

Thermal Forming processes

- Thermal Oxidation
- Thermal Nitridation
- Thermal polymerization

- Ion implantation

LIQUID-PHASE CHEMICAL TECHNIQUE

Electro Processes

- Electroplating
- Electroless plating
- Electrolytic anodization
- Chemical reduction plating
- Chemical displacement plating
- Electrophoretic deposition

Mechanical Techniques

- Spray pyrolysis
- Spray-on techniques
- Spin-on techniques

- Liquid phase epitaxy

Table 2: Classification of vapour phase deposition techniques

VAPOUR DEPOSITION TECHNIQUES

I. Physical vapour deposition (PVD)

(a) Evaporation

- Direct
- Reactive
- Activated reactive
- Ion-Beam assisted

(b) Ion Plating

1. Glow Discharge

- DC/RF Diode
- Alternating
- Triode
- Hollow Cathode Discharge
- Cathodic Arc
- Sputter Ion Plating

2. Ion Beam

- Direct Ion Beam
- Ion Beam
- Cluster Ion Beams

(c) Sputtering

1. Glow Discharge

- DC/RF Diode
- Triode
- Magnetron

2. Ion Beam

- Single Ion Beam
- Dual Ion Beam

II Chemical Vapour Deposition (CVD)

- Conventional CVD
- Low-Pressure CVD
- Laser-Induced CVD
- Electron Assisted CVD

III Physical Chemical Vapour Deposition (P-CVD)

- Plasma Enhanced CVD
- Reactive Pulsed Plasma
- Chemical Vapour Polymerization

2.4.1 Physical vapour deposition (PVD)

The basic PVD processes are given in the table 2. All PVD processes consist of three steps. These are [19]

Step 1: Creation of Vapour Phase Species - evaporation, sputtering.

Step 2: Transport from Source to Substrate - The transport of the vapour species from the source to the substrate can occur under line-of-sight or molecular flow-conditions (i.e., without collisions between atoms and molecules); alternately, if the partial pressure of the metal vapour and/or gas species in the vapour state is high enough or some of these species are ionized (by creating a plasma), there are many collisions in the vapour phase during transport to the substrate.

Step 3: Film Growth on the Substrate - This involves the deposition of the film by nucleation and growth processes. The microstructure and composition of the film can be modified by bombardment of the growing film by ions from the vapour phase resulting in sputtering and recondensation of the film atoms and enhanced surface mobility of the atoms in the near-surface and surface of the film.

The following points are to be noted for PVD processes:

1. PVD is a low temperature technology ($< 550^{0}C$); that is an important factor when dealing with materials that are structurally modified with temperature.

2. In glow discharge processes the ion bombardment causes dense novel materials.

3. PVD deposition technique has two main disadvantages: (a) Tubes or blind holes with $depth/\ width > 1$, cannot be coated; (b) complex shaped samples should be faced against the vapour sources to get a good coverage.

4. Virtually any material can be deposited. Magnetron sputtering technique is unique in this regard.

5. PVD process is an environmentally friendly technology and may eventually replace electroplating.

6. The process allows sharp edge condition to be retained.

7. Although these techniques induce high internal compressive stress that limits the thickness of the films this stress delays the fatigue crack within the film.

8. Prior to deposition, substrate cleaning is a precondition for PVD process.

9. This technique results in fine grained structure that reduces the risk of cracking and leaves a smooth surface finish.

2.4.2 Chemical vapour deposition (CVD)

The basic CVD processes are given in the table 2 The CVD process is defined as the deposition of a thin solid film from a chemical reaction involving gas species at heated substrate [20]. For all CVD processes, the determinant factors in film formation are [21]

(a) the rate of delivery of the process gases to the substrate;

(b) the chemical reaction rates for film formation at the substrate surface; and

(c) the rate of removal of reaction by-products [20]

In general, the transport of the gases is determined by the process pressure and the gas flow rates. Diffusion of source gases to, and by-product gases away from the deposition surface is enhanced at low pressures. CVD processes are usually high temperature techniques. The basic or elementary CVD process is one in which all the additional energy is supplied at the heated substrate, and where the rate of reaction is then determined by the temperature of the substrate. There are no inherent restrictions on the nature of the heterogeneous chemical reactions that are used in CVD processes; they can be oxidation, pyrolysis etc. Many authors designate this type of process as thermal CVD. This definition is used to differentiate the thermal CVD processes from other CVD processes in which different sources of energy, such as rf or microwave plasmas, are employed to activate the chemical reaction pathways leading to film deposition. However, in basic CVD processes the temperature of the gas, is the same as that of the substrate which is essential for film growth.

The following points to be noted for CVD processes:

1. CVD is a high temperature deposition, in some cases more than 1000°C is required. Thus substrates should selected accordingly.

2. The most striking advantage of this process is, the gaseous atmosphere envelops the complex geometries, thus tubes or blind holes can be coated.

3. This process solely depends on gas phase chemical reactions, thus not all materials can be deposition by this technique.

4. The process tends to round an edge thus making them less sharp.

5. The process uses and exhausts toxic gases which must be neutralised.

6. It develops tensile stresses in the film due to thermal mismatch between substrate and film.

7. Substrate pre-cleaning is not a precondition for this technique, although low surface roughness is required for optimum tool performance.

8. Films deposited by this process have larger grains.

9. As this is a high temperature process, migration of the lighter elements from the film to the substrate site occur, resulting in a deficiency of that element at that particular layer. This results in non uniformity within the film and causes poor bonding.

2.5 Deposition Techniques used for Carbon Nitride thin film

A number of techniques were applied to deposit Carbon Nitride film so far. Although there are a few claims in depositing crystalline β-C_3N_4 film, most of the films are amorphous in nature. The aim of these techniques was to achieve energetic species of carbon and nitrogen. Some of the techniques are direct, i.e., produced energetic carbon and nitrogen species and then combined them in different chamber to produce C-N film. The magnetron sputtering techniques will be discussed in detail in the following

chapter. The following techniques are used so far for successful deposition of carbon nitride film.

1. Ion Beam Deposition (IBD)

2. Plasma enhanced Chemical Vapor Deposition (PECVD)

3. Hot Filament assisted CVD (HFCVD)

4. Shielded Arc Ion Plating (SAIP)

5. Plasma Enhanced Chemical Transport (PECT)

6. Ion Beam Assisted Deposition (IBAD)

7. Electron Cyclotron Resonance (ECR) Plasma source

8. Direct Plasma Beam Deposition (DPBD)

9. Ion Assisted Arc Deposition (IAAD)

10. Laser Ablation

11. Pyrolysis

Ion Beam Deposition (IBD)

Ion Beam Deposition (IBD) is an unique technique for thin film deposition. Although detail discussion of this technique is not possible here, the basic principle will be discussed in brief and then a modified technique by which ions can be separated to deposit in pure form will be highlighted.

Ion beams are used in thin film deposition in two basic configurations. In primary ion beam deposition (Fig. 4a) the ion beam consists of the desired film material and is deposited at low energy (~ 100 eV) directly onto the substrate.

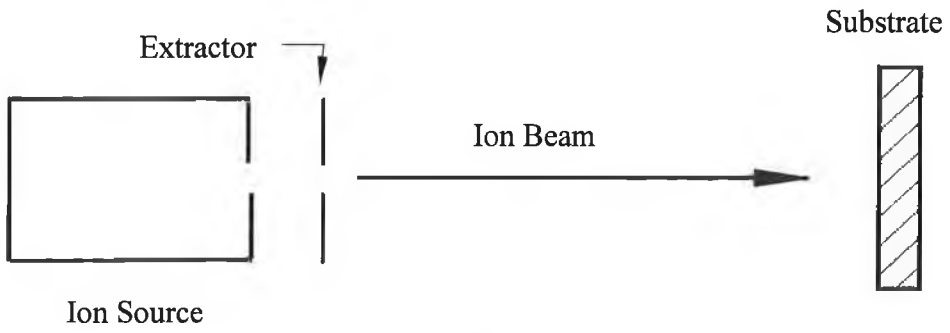

(a)

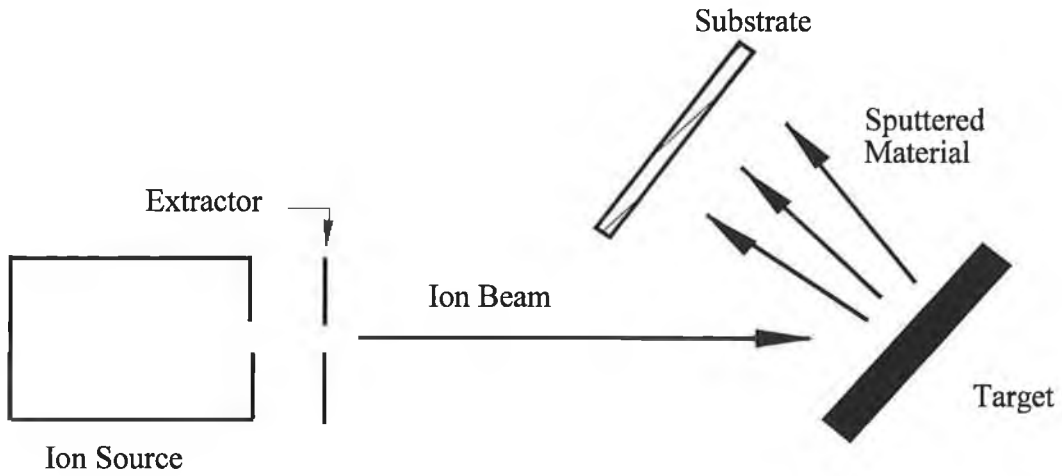

(b)

Figure. 4 Schematic of Ion Beam Deposition configurations. (a) Primary ion beam deposition, with ion beam deposited directly onto substrate, (b) secondary ion beam deposition, with inert or reactive beam sputtering target material onto substrate.

In secondary ion beam deposition (Fig. 4b) which is generally known as ion beam sputter deposition, the ion beam is usually an inert or reactive gas at higher energy (hundreds to thousands of electron volts). The beam is directed at a target of the desired material, which is sputtered and collected on a nearby substrate.

Ion beam deposition allows greater isolation of the substrate from the ion generation process than is found in any other conventional techniques. This enables control over the substrate temperature, gas pressure, angle of deposition, and the type of particle bombardment of the growing film, as well as independent control over the ion beam current and energy. This flexibility characterizes ion beam deposition as a useful technique in the study of thin film growth processes. Although the process looks straightforward production of ions is a challenge. Conventional IBD technique uses (1) Penning ion source [22] (2) Kaufman Ion Source [23,24] or Duoplasmatron [25]. The ionisation mechanism used in most ion sources is electron impact ionization in a low voltage gas discharge. The cross section for electron impact ionization has a maximum at low electron energy, about 70 eV for argon as described by Lotz [26], therefore high electron energies are not needed for efficient ionization. Another important point is the electron supply rate and gas pressure ratio, since the mean free path for ionization is inversely proportional to gas pressure as described by Kaufman [24].

Figure 5 shows the schematic view of IBD set up used by Miyazawa et al. [27]. Here a typical technique will be discussed to demonstrate the process. Then comments will be made on the use of this technique for C-N film deposition. Their source consisted of a duopigatron ion source, a mass separator, a detector, deflectors and a deposition chamber. For Carbon film deposition the C^+ ions are generated in the duopigatron ion source using CO or CO_2 gas, extracted with a voltage between 6 and 20 kV, and mass separated by a sector magnet. C^+ ions are separated by the mass separator thus pure and highly energetic C^+ ions can be produced to deposit carbon based thin film. The ion beam is focused and decelerated by a concave-shaped decelerator and deflected in the

deposition chamber by electrostatic field to eliminate high-energy neutral atoms and electrons generated in a drift tube.

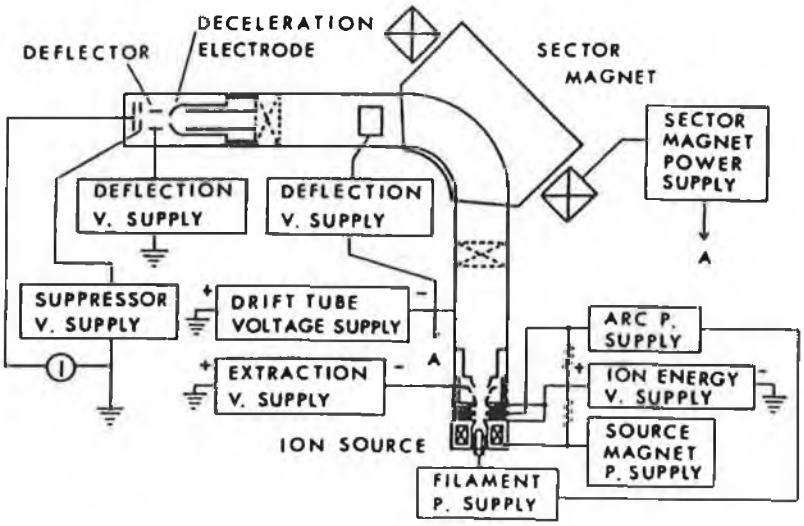

Figure 5. Schematic diagram of the ion beam deposition system [27].

The substrate is grounded so that C^+ ions impinging onto the substrate have the kinetic energy corresponding to the potential of the ion source. The ion current is function of ion energy and drift tube voltage with which the ions are extracted into the drift tube. The ion current is monitored using a Faraday cup with suppresser having an aperture of 1 cm in diameter. Ion current usually depends on the gas pressure. The diameter of the ion beam varies with the ion energy and drift tube voltage. A low-energy ion beam seriously spreads because of space-charge repulsion. The ion beam is focused by using a concave-shaped decelerator. The focal length of the decelerator varies with the ion energy and the drift tube voltage.

This deposition technique is a potential source for carbon nitride thin film. Using a parallel duopigatron ion source N^+ ions can be produced from N_2 gas. Thus C^+ and N^+ ion beams are focused and decelerated in the deposition chamber by the process discussed earlier. The substrate is grounded so that ions impinging onto the substrate have the kinetic energy corresponding to the potential of the ion source. Currently this technique is used to deposit C-N, amorphous Carbon and Diamond like carbon (DLC) thin films.

Plasma Enhanced Chemical Vapor Deposition (PECVD)

Figure. 6. shows a schematic representation of the PECVD reactor used by Kim et al [28]. They slightly modified the conventional system by using a helical resonator plasma source. Although the basic principle for PECVD system is more or less the same. This reactor was used to deposit hydrogenated carbon nitride thin film. The operational principle will be discussed in the following paragraph.

The plasma source consists of a 30 cm long, 7.5 cm diameter Pyrex tube attached to the feedthrough port at the top of the vacuum chamber and copper coil surrounded by a grounded metal cylinder. Plasma is maintained in this source using a radio frequency powered copper coil designed to operate as helical resonator at 13.56 MHz. In a conventional helical resonator, one end of the coil is grounded and the other end is left floating. The rf power is applied at a particular position along the coil between the two ends. The location of the coil loop to be powered is determined by trial and error until the reflected power is minimized. The helical antenna becomes resonant when an integral number of quarter waves of the rf field fit between the two ends.

Resonance occurs when $L = \lambda/4$ or $Lf = c/4$, where L is the unwound length of coil, f is the frequency, λ is the wavelength and c is the speed of light. When this condition is satisfied, the intense electromagnetic fields can sustain a high efficiency plasma at low pressure ($\leq 1.33\text{x}10^{-2}$ mbar). In order to control the impacting ion energy, the rf power

at a frequency of 13.56 MHz is capacitively coupled to the substrate electrode with a diameter of 10 cm and the counter electrode is the grounded wall of the deposition chamber. This gives a large difference between the electrode sizes. Ions are almost immobile, whereas the electrons can follow the temporal variations in the applied potential at the typical rf frequency used (13.56 MHz).

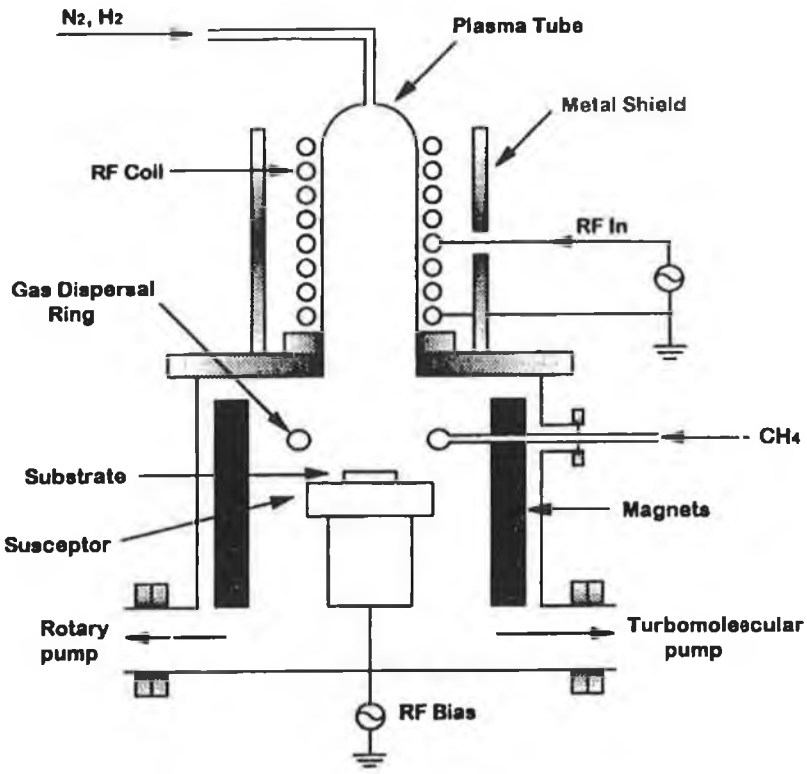

Figure. 6. Schematic diagram of the plasma-enhanced chemical vapor deposition reactor with a helical resonator discharge source [28].

The large differences in electrode size, and also in the electron and ion mobility, produce a negative direct current (dc) self bias V_b on the powered electrode, making it the cathode. Consequently, it is possible to control independently the production rate of reactive species through the plasma source power, and the energy of ion bombardment on the substrate surface through the substrate electrode power. A

permanent magnet system is placed in the reactor to enhance plasma confinement near the substrate.

High purity N_2 gas is supplied to the chamber from the top of the Pyrex tube and flowed through the plasma where it is dissociated. The pure CH_4 gas is introduced through a gas dispersal ring where it is sprayed toward the substrate. The deposition pressure is maintained at 1.33×10^{-3} mbar. All the gases are controlled by gas flow controller. Films are deposited using rf bias at the temperature of ~ 250°C.

This technique is claimed to be well controlled and low temperature PECVD process comparing to other PECVD method. The technique can be successfully used for other hard thin films deposition i.e., diamond, diamond like carbon, cubical boron nitride etc.

Hot Filament CVD (HFCVD)

Wang et al. [29] used hot filament CVD technique to deposit crystalline carbon nitride thin film. The basic principle is more or less same for all HFCVD processes. Figure 7 shows the HFCVD process used by Leyendecker et al [30] for diamond deposition.

For diamond deposition the key parameter is to provide a hydrogen to methane gas flow ratio of about 100 to 1. This is necessary because the hydrogen preferentially etches the graphite sp^2 bonds in favour of the sp^3 tetrahedral diamond bonding. Thermionic electrons from the tungsten filaments used are also thought to assist in this process. Figure 7 shows the deposition chamber. The system is evacuated by suitable vacuum pumps to maintain low pressure deposition.

The mode of operation for carbon nitride deposition is to some extent different. Negative bias is applied to the substrates to enhance the ion bombardment which is essential for carbon nitride deposition. In this case high pure nitrogen (99.999%) and methane (99.9%) were mixed as the reactive gas source and carbonized tungsten filament

is heated to dissociate methane. A DC power supply is used to generate a plasma discharge between the filament and the substrate, which increases the activation of nitrogenous precursors. The deposition pressure is maintained at 1.33×10^{-3} mbar. Although Wang et al. [29] claimed deposition of crystalline β-C_3N_4 by this technique, formation of C-Si-N ternary system can not be ruled out at this high deposition temperature as discussed by Chen et al. [18].

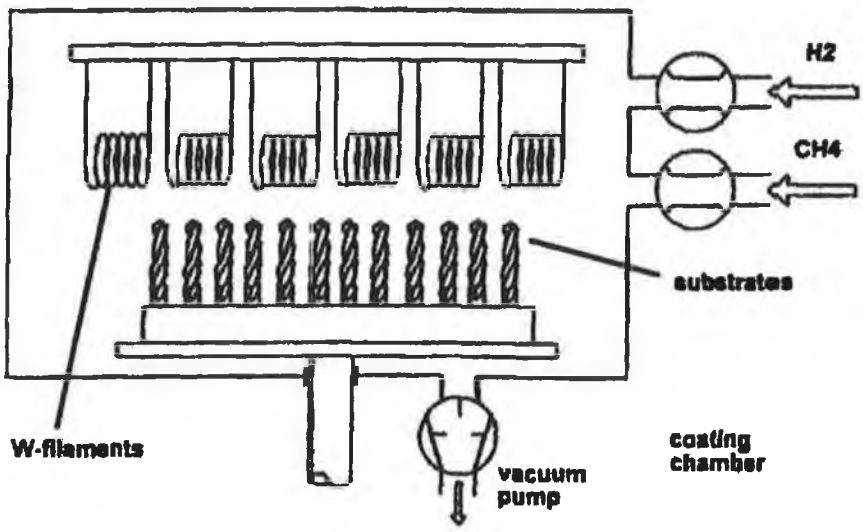

Figure 7: An apparatus for HFCVD of diamond film [30].

The deposition parameter used by Wang et al. [29]

(a) Growth on silicon substrate: Filament temperature 2100°C; Substrate temperature 750-950°C; Substrate bias -300 eV; Filament-substrate distance 5-8 mm; Working pressure 1 to 20 mbar.

(b) Growth on nickel substrate: Filament temperature 2100°C; substrate temperature 850°C; Substrate bias -380 eV; Filament-substrate distance 8 mm; Working pressure 1 mbar.

Shielded Arc Ion Plating (SAIP)

Figure. 8. shows a Nissan Electric MAV 15.2N shielded arc ion plating reactor. The reactor was used by Taki et al. [31] for carbon nitride film deposition. The system consits of a stainless steel chamber. Gases are supplied to the chamber through mass flow controller (M.F.C). The substrate itself acts as an anode.

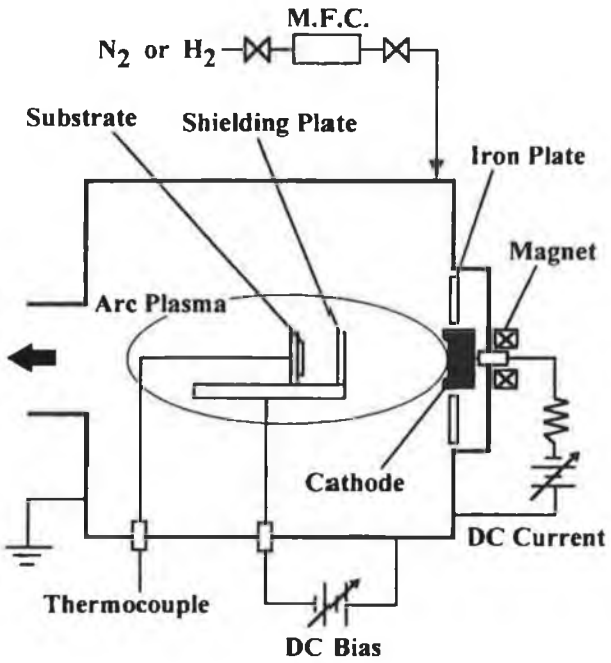

Figure. 8. Schematic diagram of Shielded Arc Plating System [31]

The material to be deposited is mounted on the cathode. A high current typically ~80 to 100 A is supplied to the cathode thus produces the arc plasma. Gases inserted inside the chamber are ionised. Ionised gases come in contact with the solid particles from the

cathode while they pass through the plasma to the substrate. Iron plates are used as ground shields to prevent the sputtering of the target assembly. A magnetic field is also used to reduce the random motion of the electrons. These electrons act as further ionising source. To enhance the deposition rate substrate bias can be applied. The chamber is pumped down to $5x10^{-5}$ mbar during deposition.

For carbon nitride deposition, a high purity graphite target is usually used as a cathode. Usually high purity nitrogen gas is used through the M.F.C. Typical working pressure is 10^{-5} mbar . The substrate is usually heated up to 60 to 380°C and biased up to -1kV (dc). In film preparation the plasma is generated at 60 to 80 A (dc). This reactor can also be used to deposit diamond, DLC or amorphous carbon.

Plasma Enhanced Chemical Transport (PECT)

Chemical transport of evaporated species of solid by gas is an unique application for C-N, diamond or other carbon based thin films. Although detailed description of this process is not the scope of this thesis, a brief discussion will be presented to highlight its uniqueness over conventional CVD process. Veprek [32] discussed transport phenomena of evaporated species of carbon by different gases based on type of films required. His theory will be discussed here in brief and then its application for Carbon nitride deposition.

A chemical transport process in the vapor phase consists of the following three steps:

(a) chemical evaporation of a solid

(b) transport of gaseous reaction products in the gas phase from the charge to the deposition zone

(c) reverse reaction leading to the deposition of a solid

The knowledge of the equilibrium composition of the system of interest at given conditions (temperature, pressure) is of principal importance for any theoretical prediction of the transport. However, in a number of systems the kinetics may play the most important role as described by Schafer [33] and Kaldis [34]. The non-isothermal plasma should be used in such cases, when one or more of the steps (a), (b) and (c) cannot occur without a plasma, as pointed out by Hauptman [35] and Veprek [36]. The reaction of carbon with molecular nitrogen is strongly endothermic and step (a), the chemical evaporation, does not occur at a temperature of about 1000°C. However, in a low pressure plasma having a high energy content this reaction proceeds at this temperature and carbon may be transported in a plasma gradient (decreasing plasma energy, $E_2 \rightarrow E_1$). On the other hand, the reactions of carbon with molecular oxygen and hydrogen are strongly exothermic and the transport then occurs in the direction of increasing energy of plasma ($E_1 \rightarrow E_2$) as mentioned by Veprek [32].

Chemical evaporation of solids, transport of carbon with nitrogen

If the chemical equilibrium of a heterogeneous reaction [32]

$$A\,(s) + b\,B\,(g) \rightleftharpoons C\,(g) \qquad (1)$$

is shifted extremely to the left without a plasma, no transport of solids *A* may occur in such a system. The step (a), the chemical evaporation, is hindered thermodynamically. An energy equal or higher than the reaction enthalpy of the reaction (1) is necessary for chemical transport to be possible in a plasma. This energy may be available as the energy of a metastable molecule or the dissociation energy of the gaseous transporting agent *B*. Two conditions have to be satisfied:

(a) The dissociation energy of the transporting agent B must be equal to or higher than the enthalpy of the reaction (1)

(b) The reaction has to proceed fast. Particularly, the reactions of atoms of the transporting agent B with the solids A must be faster than their recombination on the surface of A. The latter will be expected to be faster than the reaction of atoms with the surface at a low temperature, because of very low activation energies for the heterogeneous recombination of atoms as described by Wright et al. [37] and King et al. [38]. At high temperature this reaction can be enhanced.

The transport of carbon in a nitrogen plasma is an example of this process. The reaction of carbon with molecular nitrogen is strongly endothermic and at a temperature of about 1400°K the chemical equilibrium lies extremely on the left. This reaction can be shown as:

$$C(s) + \tfrac{1}{2} N_2(g) \rightleftharpoons CN(g) \qquad (2)$$

This reaction is weakly exothermic and the condition (a) is satisfied. The reaction will also be fast at a temperature of about 1000°C as pointed out by Veprek [32]. The transport of carbon is then expected to proceed from a zone of a high energy E_2 to a zone of a lower energy E_1 of the plasma.

Chemical deposition of solids

The deposition of solids from the gas phase in a system occurs where the chemical equilibrium of the transport reaction

$$A(s) + b\,B(g) \rightleftharpoons C(g) \qquad (3)$$

is shifted extremely to the right under thermodynamical equilibrium conditions (at given temperature and pressure). The electrical discharge is started in the gaseous compound C. When the inner energy of the discharge plasma grows (e.g. by increasing the discharge current), the compound C will increasingly be decomposed, until isolated

atoms of the substance A appear in the gas phase. If the partial equilibrium pressure of the solid A (s) at the translational temperature of the plasma is lower than the partial pressure of the atoms A occurring in the gas phase by dissociation of the compound C, the solid A (s) will be deposited.

This technique was carried out by Veprek [39] for C-N film deposition. Figure. 9 shows this experimental apparatus. The reactor consists of a discharge tube (1) made of silica glass with an inner diameter of 7.5 cm and length of 50 cm with pumping port (2) and gas inlet (3). On the left hand side (fig. 9) a flange made of aluminum (4) with a substrate holder (5), which could be inserted at a given position into the discharge tube, is mounted. The temperature of the substrate holder is controlled by an electric heater (6) and controller (7). All values of the temperature reported hereafter refer to that indicated by the thermocouple (TC) which is inserted into the substrate holder head. A high frequency (hf) glow discharge is excited by a generator (8) operating at a frequency of 27 MHz and delivering a power up to 4 kW. The external electrodes (9) and (10) are made of copper and cooled by water. The left electrode is grounded, while the right one is at the hf potential. High purity nitrogen gas is used and controlled manually or mass flow controller. The tube is evacuated by using a rotary pump and 10^{-2} mbar pressure is maintained during deposition. The high hf discharge current density within the high purity graphite insert (11) provides a high degree of dissociation of nitrogen and a temperature of about 610-980°C at hf powers of 1 and 3 kW, respectively. Under these conditions CN radicals are formed and transported by the gas flow into the deposition zone on the left (fig.9) where the temperature of the gas, of the walls, and of the substrate varies between about 300 and 600°C for powers of 1 and 3 kW, respectively.

Under these conditions paracyanogen CN films are deposited on the walls of the tube and at the substrate. Using the same technique other carbon based films can be deposited.

Based on the same principle Jou et al. [40] designed a PECT apparatus to deposit diamond film. The plasma-enhanced chemical transport process seems to be very useful technique for carbon based film due to the process simplicity. Figure. 10 shows another PECT apparatus used by Jou et al. [40] at University of California, Los Angeles. The electrode are installed inside a Pyrex chamber. Two graphite rods, 2.5 cm and 1 cm in diameter, are used as cathode and anode respectively. The graphite cathode is the only carbon source available for diamond synthesis.

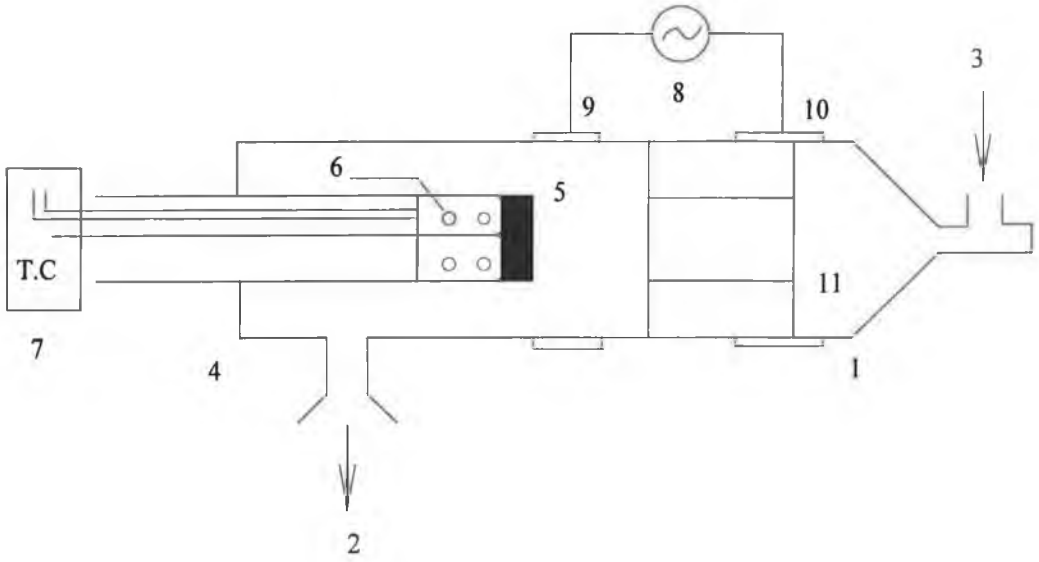

Figure. 9. Schematics of the apparatus used for the deposition of carbon nitride film by means of PECT technique [39].

The substrate is attached to the top of the anode with colloidal silver or colloidal graphite paste. The cathode and the substrate surfaces are separated by 0.6 cm. An electrically isolated vacuum feedthrough is used to connect the cathode to a d.c. power supply. The plate on top of the Pyrex bell-jar is electrically floating. The bottom plate is grounded. Water is flowed through the feedthrough on the bottom plate to prevent overheating. The feedthrough on the top plate is cooled by blowing air through it. A mechanical pump is connected to the system which pumped the apparatus down to $\sim 2.5 \times 10^{-2}$ mbar.

The system is back filled with high purity hydrogen 133.3 mbar and pumped down to 0.133 mbar three times before starting the deposition process. Required amount of hydrogen gas pressure is maintained and the chamber is closed. This is called a static or no-flow system. A hydrogen plasma is initiated by high voltage circuitry in the power supply. The hydrogen plasma heats up the cathode, and carbon is transported from the hot carbon cathode surface to a lower temperature substrate surface. Typical conditions for diamond deposition are a hydrogen pressure of 133.3 mbar and d.c power of 1.0 A and 450 V. The surface temperature of the cathode, measured with an optical pyrometer, is about 950°C, assuming that the emittance of graphite is 1.0. The substrate temperature varies from 700 to 850°C. It is measured by placing a thermocouple just below the back side of the specimen.

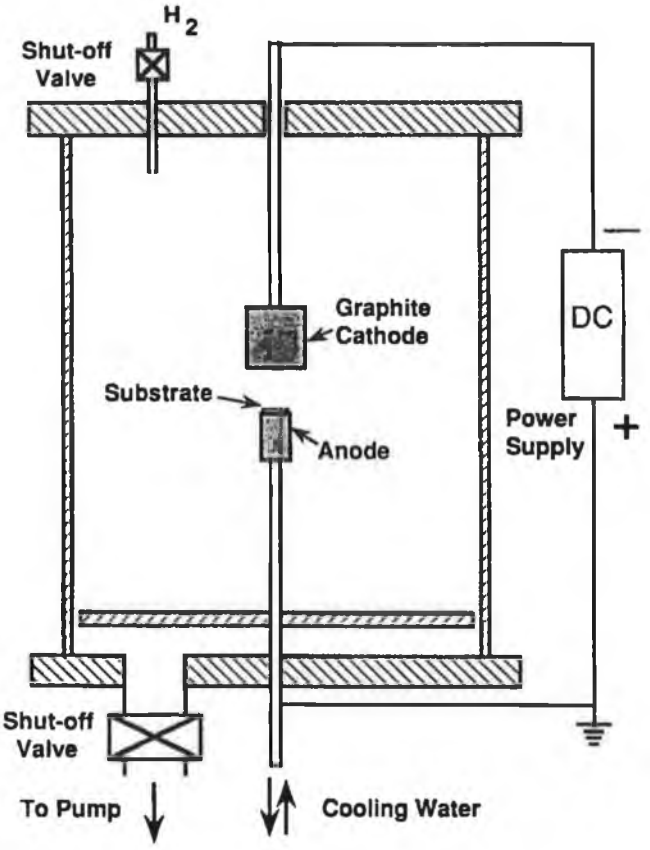

Figure. 10. Schematic diagram of a PECT system [40].

Ion Beam Assisted Deposition (IBAD)

Ion Beam Assisted Deposition (IBAD) employs an ion source (could be reactive, for carbon nitride deposition usually nitrogen ions) to direct a beam of ions at the substrate during deposition. The source of other species of the required film could be an evaporation source or a sputter arrangements. An obvious advantage for ion assisted deposition is that both processes can be easily incorporated in an existing vacuum deposition system. In most cases various broad beam ion sources are utilised for this dual purpose. This dual technique has many advantages. The principle advantage is that the operator has control over the relative arrival rates of each species at the sample surface, as well as control over the ion energy. This is quite unlike a plasma-based reactive deposition, where the flux and energy of the energetic species are strongly coupled, and the arrival rate of the reactive species is affected by the deposition rate and gettering effects on the walls.

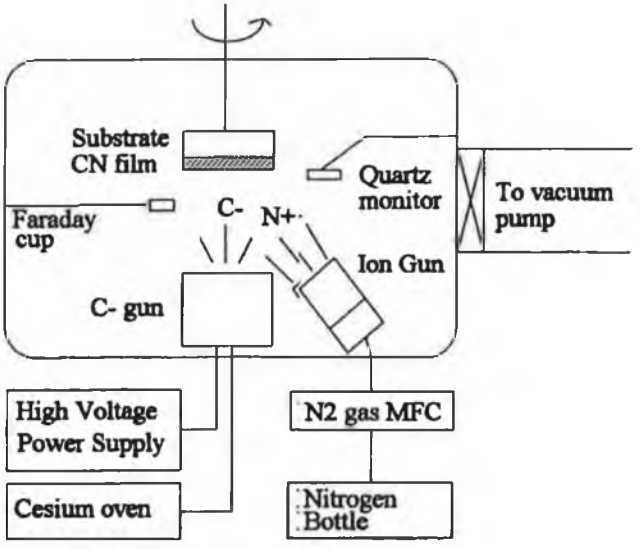

Figure. 11. The schematic drawing of the Ion Beam Assisted deposition system [41].

Figure. 11 shows an IBAD system used by Murzin et al. [41] for carbon nitride film deposition. Their system consists of a Kaufman ion source and a negative carbon ion source based on sputtering technique.

They deposited carbon nitride films in a vacuum chamber equipped with a sample transferring load lock. The working background pressure prior to deposition is 1.33×10^{-6} to 10^{-7} mbar. To maintain the uniform deposition, the substrates are rotated during deposition using an electrically isolated feedthrough at a constant speed of 1-5 rpm. A deposition monitor is used to monitor the deposition rate of carbon. A digital multimeter monitores the absorbed ion current during deposition. The temperature of the substrates as determined by a thermocouple pressed to the back side of the substrates shows substrate temperature $\sim 80^{\circ}C$ during deposition.

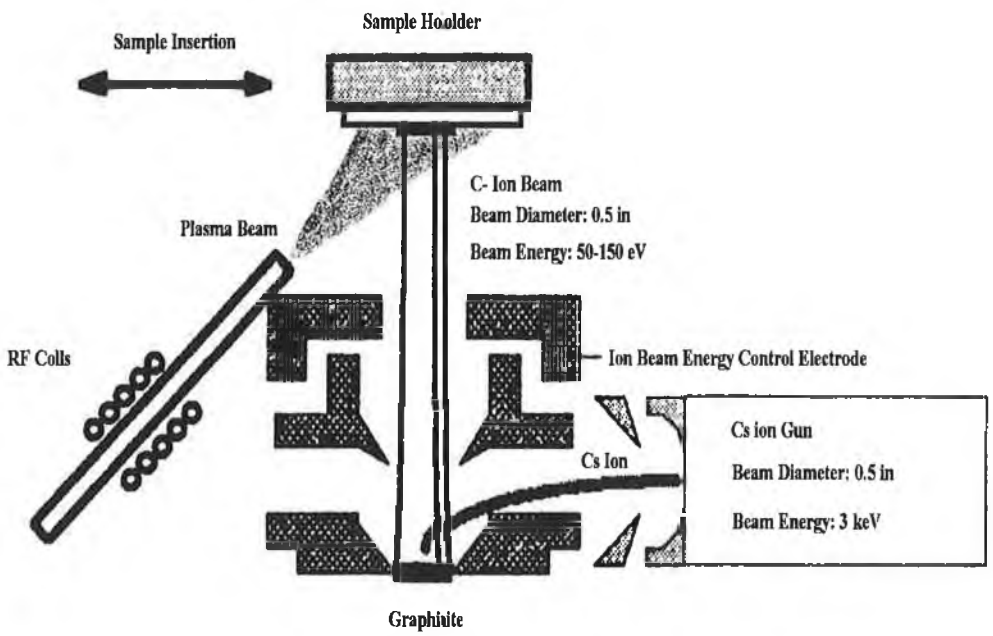

Figure. 12. The schematic drawing of a cylinder geometry negative carbon ion source [41].

A Kaufman ion gun produces a 3 cm diameter beam of nitrogen ions, which is shown to consist of mostly N_2^+ ions. The nitrogen ion energy is 50-500 eV and is mixed up with negatively charged carbon ions to form C-N film on a suitable substrate. The current of nitrogen ions setup by a DC power supply is in the range from 5 to 25 mA. Single-grid ion source geometry is used and the screen grid is removed from the ion source, but since the acceleration grid is made of graphite, the sputtered species do not contaminate the carbon nitride films. The single-grid geometry provides ion-beam currents as high as 95 mA. It can be noted here that the 2-gridded Kaufman source is more suitable for higher energy (hundreds of eV) and high flux. These sources operates best with inert gases. However, such sources are routinely used in oxygen for the deposition and modification of dielectric films. The single-gridded Kaufman source has high output current densities at low energy (20-150 eV). In a reactive environment with O_2 and N_2, the single grid can last 3-4 times longer than with Ar. This increased durability is due to the formation of lower sputter yield compounds (oxides or nitrides) on the grid surface. These compounds are not present when operating the source with inert gases. The gridless, in general, is quite useful for high current, large area, low energy bombardment. This is most appropriate for reactive deposition or bombardment during deposition cases. This source has only a single filament, which is easily accessible on the front of the source, and is thus more compatible with reactive species than the conventional Kaufman-type sources.

Figure. 12. shows schematic drawing of the negative carbon ion gun. A beam of cesium ions generated by a small solid-state cesium source impinges upon a graphite target and sputters carbon species away. Cesium coverage on a surface is known to lower the work function of materials, thereby enhancing electron transfer to outgoing sputtered particles; forming a negatively charged carbon ion beam. The beam is then accelerated to a desired energy and directed to the substrate. The energy of carbon ions was varied between 50 to 750 eV. The carbon ion current as measured by the current meter is 1-5 μA. This apparatus can be used successfully for diamond deposition also.

Electron Cyclotron Resonance (ECR) Plasma source

Microwave discharges have experienced intense interest and use in recent years. Their electrodeless nature together with their ability to create high densities of excited and charged species have made both high pressure and low pressure microwave discharges an attractive technology for many plasma processing applications. By using the appropriate microwave applicators, microwave discharges can be efficiently created and maintained from pressures above several atmospheres (1-3) to sub-mbar pressures (4-14) resulting in high pressure discharges with high temperature ($\geq$ 1000K) for thermal processing applications, and low temperature and low pressure discharges for applications such as thin film deposition and etching.

An important development in low pressure and low temperature microwave plasma processing is the electron cyclotron resonance (ECR) discharge. From the name ECR, microwave energy is coupled to the natural resonant frequency of the electron gas in the presence of a static magnetic field. This resonant frequency occurs when the electron cyclotron frequency equals the excitation frequency. The cyclotron frequency is found as [42]

$$\omega_{ce} = \frac{eB}{m_e} \qquad (4)$$

where e is charge on an electron, B is the strength of the static magnetic field, and m_e is the electron mass. In an actual discharge, this condition can be satisfied in a volume or surface layer within the discharge where the static magnetic field strength is adjusted to resonance, i.e. $\omega = \omega_{ce}$ and a component of electric field is perpendicular to the static magnetic field. The electrons are accelerated in this ECR volume and inturn ionize and excite the neutral gas. The result is low pressure, almost collisionless, plasma which can be varied from a weakly to a highly ionized state by changing discharge pressure, gas flow rates and input microwave power. The electrodeless and noncollisional heating

nature of the discharge together with the availability of well established, low cost microwave power supplies make ECR plasma sources attractive for plasma processing applications.

A typical ECR plasma experiment will be discussed here for carbon nitride deposition. Figure. 13. shows an experimental set up of the ECR plasma source used by Nowak et al. [43]. A high vacuum stainless steel chamber pumped by a Balzers two-stage 180 *l/s* turbo molecular pump was used for the experiment. This system allows low base pressure (< $5X10^{-8}$ mbar) as well as fairly high operating pressure (10^{-1} to 10^{-2} mbar) at full pumping speed to be achieved.

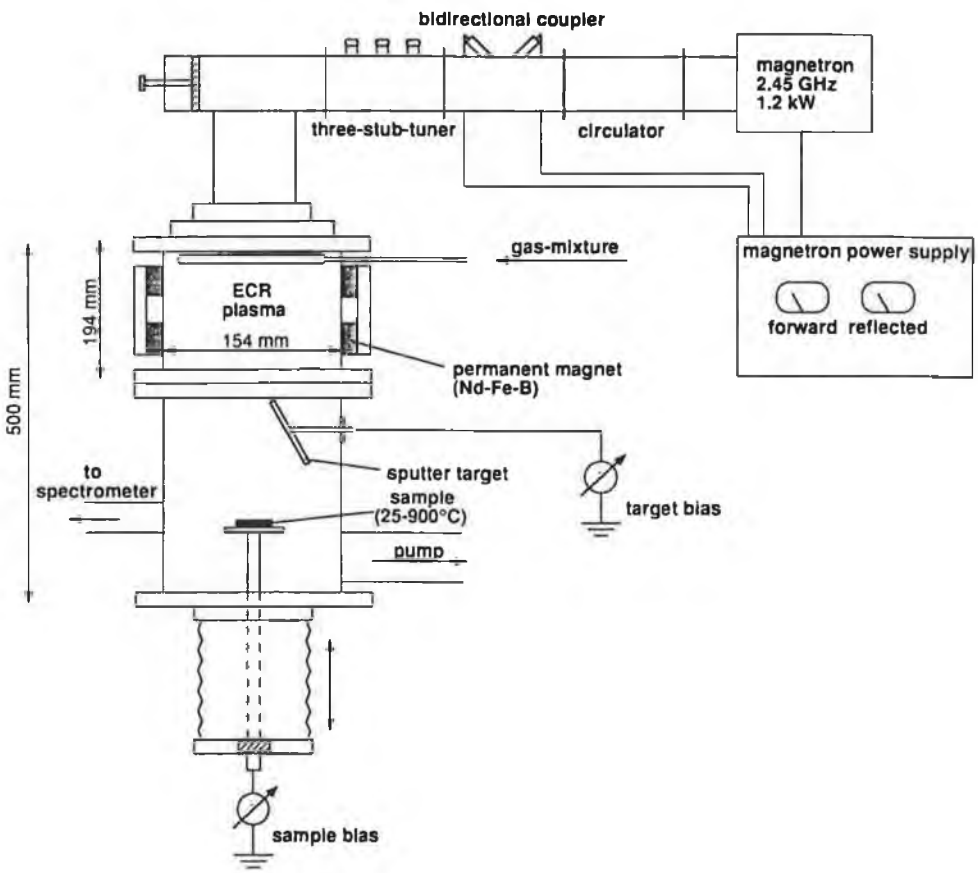

Figure. 13. Experimental setup of the ECR plasma source [43].

The gases were introduced inside the chamber by mass flow controller. The camber is divided into two parts. The upper part contains the ECR zone where the plasma is ignited. The lower part contains the transfer mechanism to the spectrometer as well as the parts for pumping and pressure measurement. The microwave system uses a 2.45 GHz, 1.2 kW magnetron which can be controlled in power from 10 to 100% and which allows a modulation up to 10 kHz. The waveguide system includes a circulator with water load, a dual directional coupler for measurement of forward and reflected power, a three-stub tuner, and a coupling piece to a circular waveguide. The static magnetic field for the ECR condition is obtained by permanent rare-earth $Nd_2Fe_{14}B$ magnets.

Direct Plasma Beam Deposition (DPBD) Technique

The direct plasma beam deposition technique is a new addition to the PVD technology. Weber et al. [44] used this process for carbon nitride deposition. This section will discuss about their set up and technique.

In this type of deposition technique usually a r.f. plasma beam is employed. For carbon nitride deposition C atoms are sputtered from a graphite target and injected into the nitrogen-argon mixtures or pure nitrogen plasma. By utilizing the self-biasing effect between a low pressure plasma carrying an r.f potential and a grounded extraction electrode, a beam of monoenergetic ions with an equal number of co-travelling electrons (Plasma beam) is produced. This technique was first discussed by Oechsner et al. [45].

The same biasing effect is also utilized for the ion bombardment of the C target. The homogeneous electrically neutral plasma beam being provided by this source makes any deposition process independent of the actual conductivity conditions at the substrate or the growing film. Thus, the DPBD process is appropriate for growing insulating layers. The technique is unique, as any hydrogen incorporation into the deposited C-N films is avoided in contrast to plasma-assisted methods using hydrocarbon gases to deliver the C component.

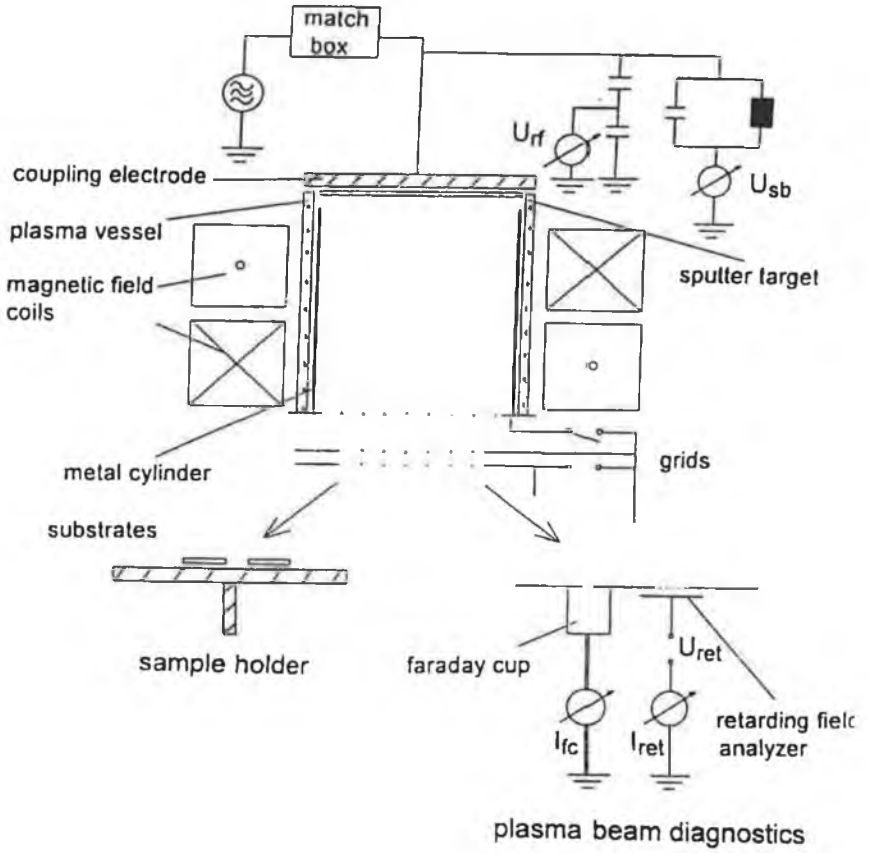

Figure. 14. Schematic of the plasma beam source for the DPBD process [45].

A schematic of the DPBD apparatus is shown in the figure. 14 used by Weber et al. [46]. The mixed C^+, N_2^+, N^+, Ar^+ plasma beam is directed perpendicularly on to the suitable substrate. A high purity graphite target was mounted on the coupling electrode by which the r.f. potential was applied to the source plasma. The sputter-injected carbon atoms are particularly post ionized by plasma electrons and co-extracted with the plasma gas ions into the deposition chamber. The ion energy and current density in the plasma beam were measured with a retarding field analyser and a Faraday cup respectively, mounted together with the substrates on a manipulator in the deposition

chamber. The plasma beam was maintained to produce ion energy of 100eV. The beam current density can be controlled by magnetic field applied onto the plasma, and can be maintained the order of 0.4 mA cm^{-2} (for either beam component). N_2^+:N^+ ratio was found to be 5 in the plasma beam by using separate mass spectrometer.

Ion Assisted Arc Deposition (IAAD)

Among the ion assisted deposition techniques ion assisted arc deposition technique permits the synthesis of hard materials onto ambient temperature substrates. The properties of thin films may be enhanced greatly when the depositing atoms are subjected to low energy ion bombardment.

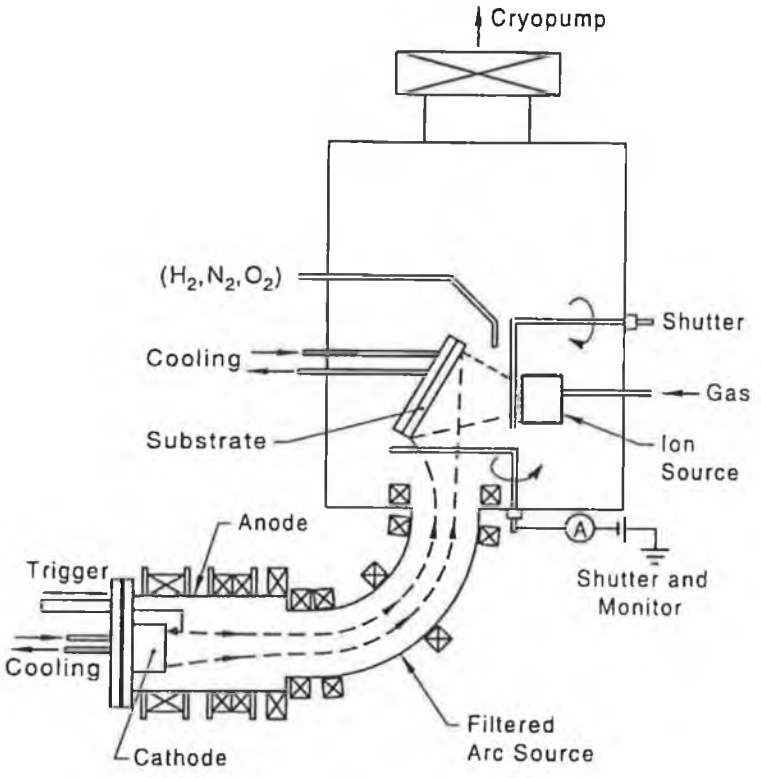

Figure. 15. Schematic of the ion assisted arc deposition system [49].

The arc evaporation process offers the possibility of intrinsic self bombardment due to the high percentage of low energy ionized material present in the evaporant. The main restriction of microdroplets of cathode material also present in the arc evaporation may be overcome by means of magnetic filtering enabling the deposition of high quality carbon, carbon nitride and TiN films. In general all ion assisted deposition process permits control over the rate of evaporation, the ion flux, ion energy and background gas composition as well as the relative arrival rate of the neutral to ion species at the substrate. Hard carbon films and other wear resistant coatings such as TiN have been deposited by IAD but in general the process has been restricted to low deposition rates due to the high evaporation temperatures of some materials such as C, and to line-of-sight coating as a result of the geometry and low throwing-power at the relatively high vacuum used in IAD system as described by Ullmann et al [47] and Fujimoto et al [48].

The deposition of thin films by vacuum arc evaporation offers a number of advantages over conventional ion based technology but suffers a major drawback in that micron sized droplets of cathode materials are deposited onto the substrate. This has restricted the application of arc evaporation to metallurgical and tool coatings. However, the development of filtered arc technology has permitted the deposition of particle free films of high optical quality and good electrical properties as mentioned by Martin et al [49]. The filtered arc produces a plasma beam which contains highly ionised cathode material which may be condensed onto a substrate as a thin film.

Martin et al [50] deposited carbon nitride film using Ion Assisted Arc Deposition technique. In their work they examined the technique of IAAD in which materials deposited by a filtered arc system were subjected to ion bombardment from a separate ion source with the objective of modifying film properties and lowering the process temperatures.

The experimental arrangement is shown in figure. 15. The vacuum chamber was cryopumped to a base pressure of 10^{-6} mbar. A filtered arc source was used to produce

positive ion fluxes of carbon. In this case the carbon arc was operated at 60 A DC. High purity cathodes were used. The beam diameter was approximately 40 mm and the positive ion current could be varied from 200 mA to 600 mA. The depositing films were bombarded with N_2 or N_2/Ar ions produced by a 25 mm Kaufmann ion source which was operated over the energy range of 300-1200 eV.

Laser Ablation

Recently laser ablation technique became popular for thin film deposition. Detail description of this technique is not prime objective of the present work but a general idea will be given to understand the technique for carbon nitride thin film deposition. Film deposition by laser ablation is carried out by irradiation of the target by a focused laser beam. The basic principle of this deposition process is the laser beam ablates target materials from the target and materials are transferred to the substrates. As a result, a film is grown on the substrate. The mechanism that leads to material ablation depends on laser characteristics, as well as the optical, topographical and thermodynamical properties of the target. Various kinds of pulsed laser are often employed for film deposition by laser ablation. Laser ablation has following characteristics over the conventional deposition techniques:

(a) Materials with high melting-points can also be deposited if the materials absorb the laser light.

(b) Almost no contamination is present, unlike the situation often observed in films prepared using an evaporation heater or filament.

(c) It is possible to prepare films in an oxidation environment with relatively high pressure because of the absence of a heater or filament in the deposition chamber.

(d) The target composition is transferred to the film, leading to stoichiometric deposition.

(e) A large number of droplets of submicron size are often seen on the surface of the deposited film.

When the laser radiation is absorbed by solid surface, electromagnetic energy is converted first into electronic excitation and then into thermal, chemical and even mechanical energy to cause evaporation, ablation, excitation, plasma formation and exfoliation. Evaporants form a 'plume' consisting of a mixture of energetic species including atoms, molecules, electrons, ions, clusters, micron-sized solid particulates and molten globules.

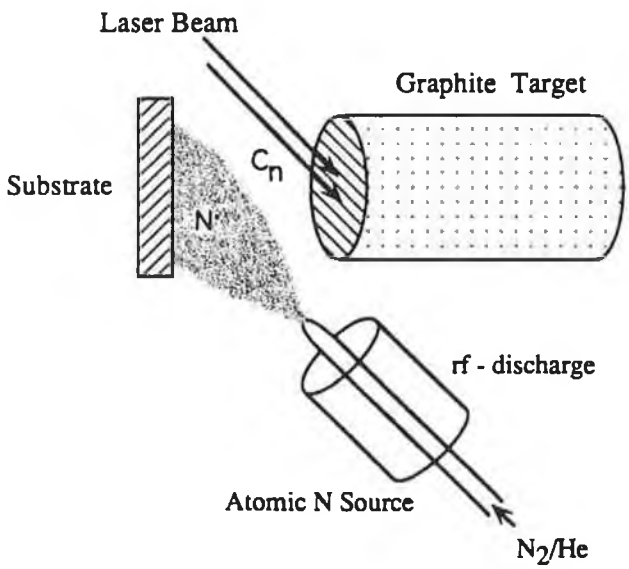

Figure. 16. Schematic diagram of the experimental set-up for carbon nitride growth. The apparatus is contained within a vacuum chamber [52].

The collisional mean free path inside the dense plume is very short. As a result, immediately after the laser irradiation, the plume rapidly expands into the vacuum from the target surface to form a nozzle jet with hydrodynamic flow characteristics. The only

disadvantage is the presence of micron sized particulates, and the narrow forward angular distribution that makes large-area scale-up a very difficult task. The large area scale-up has many engineering solutions by restoring the laser or the substrate using rotation and translation. Formation of micron-sized particulates, sometimes called splashing is an intrinsic problem. However, splashing can eliminate using mechanical velocity selector. A velocity selector that acted as a high-velocity pass filter are placed between the target and the substrate to remove the slow-moving particulates. Again, using target/laser beam interaction geometry the particulates can be removed completely. A detailed description of this technique and related phenomena are discussed by Chrisey et al. [51].

Figure. 16 is an experimental set-up for carbon nitride deposition used by Zhang et. [52]. Carbon fragments were produced by ablation of high-purity pyrolytic graphite in a vacuum chamber using a KrF excimer laser (248 nm). A N_2-seeded He flow was passed through a radio frequency (rf) discharge source to generate a reactive nitrogen beam consisting primarily of atomic nitrogen. This reactive nitrogen atom beam intersects the carbon ablation plume at the substrate surface. The film was grown on suitable substrate at $\sim 200^0$C.

Pyrolysis

The method employed involves high temperature decomposition of various organic or metal-organic precursors. Maya et al [53] successfully used this technique for carbon nitride deposition. They used organic precursors with relatively high nitrogen content, i.e. Tetracyanoethylene, Diaminomaleonitrile, etc. and heated them in quartz ampules at 800^0C for 3 hours. The ampules are cooled and then opened into a vacuum line to measure the volatile products. Condensable volatiles are trapped at -196^0C and examined by FTIR while non condensable products are identified by means of a mass analyzer. High pressure pyrolyses are conducted in a platinum capsules containing the above mentioned precursors. The capsules are subjected to 225 MPa hydrostatic pressure at

700°C for periods of about 70 h in a cold seal autoclave system. The capsules were subjected to a rapid isobaric quench to room temperature and opened into the vacuum line to measure the volatiles.

Although the technique is very simple, hydrogen contamination could be possible during CN film deposition. The technique is sometimes very useful for diamond or DLC deposition.

2.6 Characterization of Carbon Nitride Thin Films

This section reviews the structural and mechanical characterisation of carbon nitride thin films. Before going to the reviews of structural and mechanical properties of the solid, it will be worthwhile to classify the principal characterisation techniques. The techniques are discussed briefly in chapter 5. Table 3 lists the principal characterisation techniques and their uses.

Table 3: Chracterisation techniques used for structural and mechanical properties analysis of thin film

(a) Structure

1. Crystal Strcture

TEM (Transmission Electron Microscopy)
XRD (X-ray diffraction)

2. Molecular Structure

FTIR (Fourier Transform Infra-Red)
Raman Spectroscopy

(b) Phase distribution/Morphology

SEM (Scanning Electron Microscopy)
TEM (Transmission Electron Microscopy)

(c) Surface Analysis

1. Elemental

AES (Auger Electron Spectroscopy)
XPS (X-ray Photo Electron Spectroscopy)
RBS (Rutherford Backscattering Spectroscopy)

2. Molecular/Compound

FTIR
Raman Spectroscopy
XPS

(d) Mechanical Characterisation

Nanoindentation (Hardness/Bulk Modulus)

The following sections will discuss the works so far done by different researchers on structural and mechanical properties of carbon nitride thin films using different characterisation techniques and will highlight the need for further study.

2.6.1 Composition of CN compound: A Review

The [N]/[C] ratio appears to be one of the most important considerations for the production of crystalline carbon nitride films. Mechanical properties may improve with increasing N content as observed by Yeh et al. [54] and Li et al. [55]. On the other hand for a-CN:H films, a decrease in hardness compared to pure a-C:H could be observed as mentioned by Schwan et al. [56]. Sjostrom et al. [57] reported decreasing [N]/[C] ratios with increasing substrate temperature, while Kumar et al [58] reported decreasing hardness with increasing substrate temperature. Thus the relationship between nitrogen content and mechanical properties is yet to be understood.

Haller et al [59], Niu et al. [60], Sjostrom et al [57] Xiong et al [61] used Rutherford Backscattering Spectroscopy (RBS) to determine the overall composition of C-N films. The determination of average film composition is most reliable from RBS. It may be,

however, difficult to use RBS in the case of relatively thin films because of the signal from the heavier substrate. Not only that, signal from heavier elements, i.e. Fe, if present in the film as impurity, could be very difficult to subtract from carbon and nitrogen signal.

Perhaps partly because of the difficulties in using RBS and partly because of easy access, surface analytical techniques such Auger Electron Spectroscopy (AES) or X-ray Photo Electron Spectroscopy (XPS) have been widely used for the determination of the composition of C-N films. The correct application of these techniques is not straightforward. Since both rely on detection of inelastic electron emission, the limited escape depth of such electrons makes these methodes surface sensitive. Hence they do not provide information relevant to the whole film, only to the surface. This is not a problem if the analysed films are homogeneous. However, Chen et al. [62], Kaufman et al [7], Torng et al [63], Yeh et al [54], Li et al [55] and many others used these techniques to analyse the films.

When films are analysed ex situ, significant hydrocarbon adsorption and some N loss may take place on the surface. Sometimes films surface are precleaned by argon ion bombarment prior to ex situ XPS and AES analyses. Preferential nitrogen sputtering could be possible by this type of precleaning, thus results lower nitrogen content film. Marton et al. [64] observed a dramatic decrease of the N signal after sputtering began. On the otherhand C-C sp^3 phase is a metastable structure as mentioned by Torng et al [63]. This phase can be degraded into graphitelike (sp^2) or even amorphous carbon by this sputtering as mentioned by McFeely et al [65].

2.6.2 Structure and chemical bonding in CN Solid: A Review

X-ray and Transmission electron microscopic studies

Niu et al [60], Haller et al [59] used Transmission Electron Diffraction (TED) to identify the β-C_3N_4 phase. The intensity of the X-ray diffraction peak depends on a number of factors: atomic shape factor is one of them. As carbon and nitrogen are light elements, the diffracted beam coming from crystalline carbon nitride phase is very weak, as confirmed by the low intensity of the XRD peaks from the crystalline phase. Moreover, the (200) diffraction peak of the β-C_3N_4 phase, is very close to the Si (200) peak, thus β-C_3N_4 crystalline phase identification using XRD is very difficult unless the film is extremely thick. In contrast to XRD, electron diffraction is not affected by atomic shape factor, thus very intense diffraction rings or spots can be obtained if the material is crystalline. Xiaoming et [66], Szmidt et al. [67] used Transmission Electron Microscopy (TEM) to observe the film morphology and to calculate crystal size. Chen et al [62], Kumar et al [59], Amir et al [68], Cui et al [69] used scanning electron microscope (SEM), Amir et al [68] used Atomic Force Microscopy (AFM), Chen et al [62], Torng et al [63], Xiong et al [61] used Electron Energy Loss Spectroscopy (EELS) to find the crystalinity of the film.

X-ray photoelectron and Auger electron spectroscopic studies

A number of papers have been published describing the XPS Carbon 1s and Nitrogen 1s core level spectra in carbon nitride solid. The assignments of various peaks should show good agreement between the bond strength (i.e. dissociation energy) of that bond within the film and the relevant peak energy in XPS. These assignments should be supported by vibrational spectroscopic studies. Lopez et al. [70] showed various assignments of C(1s) and N(1s) peak. The main C-N bonding peaks are assigned by analogy with the carbon and nitrogen peak positions in pyridine. These suggest peaks due to sp^2 type bonding at 286.6 and 400.5 eV for the C1(s) and N1(s) respectively and at 287.3 and

399.8 eV due to sp^3 bonding. As their films contained oxygen, the presence of C-O (290 eV) and N-O (404 eV) bonding XPS peak assignments at the higher energy level is reasonable, although the peak position at ~404 eV energy level is usually assigned due to physisorbed N_2 molecules as discussed by Nilson et al [71]. Baker et al. [72] recently showed that C-O containing species lead to erroneous components over a wide range of binding energies. They also tried to assign the peak positions on the basis of vibrational spectroscopic studies. Their assignments for N(1s) peaks were N-sp^3 C bonding at 398.4 eV, N-sp^2 C bonding at 400.25 eV and N-N bonding at 402.8 eV. They described the N-N bonding as trapped N_2 within the film, not as a surface contamination. The presence of C≡N sp type bonding was observed in their FTIR spectra, but the reasons for the absence of this bonding in the XPS peak is not clear. Marton et al. [73] theoretically and experimentally tried to establish a correlation between the assigned peaks. They assigned the C(1s) deconvoluted peaks at 285.9 eV and 287.7 eV as due to sp^2 and sp^3 bonded carbon respectively and a peak at 288.3 eV due to C-O bonding. The N(1s) deconvoluted peaks at 400.0 eV and 398.3 eV were thought to be due to sp^2 and sp^3 bonded nitrogen respectively. They also assigned a peak at 402.5 eV as due to N-O or trapped N_2 within the film. They compared their assigned peaks with the pyridine and hexamethylenetetramine systems. Kohzaki et al. [74] also tried to correlate the FTIR findings with XPS peaks, but their peak assignments due to C≡N bonding is not clear. Hammer et al. [75] recently tried to prove the presence of N-N bonding rather than N-O bonding at 402.8 eV. They carried out depth profile analysis on their films and found that an increase of the small 402.8 eV peak occurs with depth, indicating that this peak corresponds to a bonding configuration within the material and not due to oxidation or surface contamination. They also argued that although Barber et al [76] assigned the peak due to –C≡N (nitrile) at 399.4 eV, the binding energy for –N≡C (isonitrile) would be expected at a lower value, due to their higher electron density at the N atom. Our C≡N peak assignment at 398.8 eV is in good agreement with their argument (see later discussion). Zheng et al. [77] discussed the possible bonding configuration of carbon and nitrogen in C-N film. They assigned the deconvoluted peaks due to sp^3 and sp^2 type C-

N bonding configuration at 400.0 and 398.3 eV respectively. They also consider the N-O peak at 402.0 eV to be due to surface contamination. The assignment of these peaks by Gouzman et al. [78] on nitrogen implanted carbon films is different. They stated that the binding energy positions of the peaks suggest different degrees of electronegativity of the nitrogen atoms present in the implanted layer. They assigned different peaks at 398.1 eV, 399.4 and 401.3 as due to C≡N, C–N and N–N or N=N respectively. They also suggested that >N=N< and –N=N– fragments contribute to the 401.3 eV peak position. Rossi et al. [79] assigned the N(1s) deconvoluted peaks at 398.2 eV and 400.2 eV as due to N≡C (nitrile) and N=C (imine) bonded nitrogen respectively, although the reasons for these peak positions were not clear. It can be seen from this discussion that there is much disagreement about the identification of different C-N peaks. It is clear that the presence of N-N bonding at ~402 eV is expected rather than N-O bonding when nitrogen bonds with itself within the film as mentioned by Hammer et al. [75] and Gouzman et al. [79]. Thus there is still a need to clarify the assignment of the peaks due to C-N bonding and to justify the peak positions, in particular for oxygen-free films; not on the basis of comparison with pyridine, urotropine or other C-N polymeric structures but on the basis of the stability of their bonds by annealing, behaviour which should be reflected in their vibrational properties.

In chapter 6 the behaviour of the bonding structure of as-deposited carbon nitride films will be described as a function of their nitrogen content and the annealing temperature. The various components of XPS peaks due to different bond types will be identified from a comparison of the behaviour of these peaks with the bonding structures identified from Fourier Transform Infra Red Spectroscopy (FTIR) and Raman Spectroscopy. The changes in bonding due to nitrogen content and annealing will be studied.

The nature of the Auger peak is highly sensitive to the bonding structure of the solid. Lurie et al. [80] studied extensively the AES carbon spectra of diamond, graphite and amorphous carbon. Lurie et al [80], Boyd et al [81], Torng et al [63], McFeely et al [65]

studied extensively the bonding nature of C-N film. The Auger signal for carbon is very sensitively dependent on the exact bonding nature and atomic arrangement of the structure. The sp^3 phase can be degraded [65] into graphite like (sp^2) or even amorphous carbon by argon ion bombardment. Thus there is a need to study the as grown structure by AES without any ion bombardment on the film surfaces or even heat treatment of the film. Auger electron spectroscopic study on carbon nitride film will be discussed in chapter 6.

Infrared (IR) and Raman spectroscopic studies

When carbon bonds with nitrogen, a number of bonding hybridisations can be possible: sp, sp^2 and sp^3. Detection of these bonds by FTIR (Fourier Transform Infra Red) or Raman spectroscopy depends on the symmetry of the compound formed by carbon and nitrogen atoms. A number of optic modes are considered as IR and Raman active depending on the selection rules. The total zone-centre optic modes can be given as the following irreducible representation for graphite [82]:

$$\Gamma = A_{2u} + 2B_{2g} + E_{1u} + 2E_{2g} \qquad (5)$$

The A_{2u} and E_{1u} modes are IR active and are observed at 867 and 1588 cm^{-1} respectively [83]. The E_{2g} modes are Raman active and are observed at 42 and 1581 cm^{-1} [84]. The B_{2g} modes are optically inactive and will not be considered further. The E-symmetry modes exhibit in-plane atomic displacements while A and B symmetry modes have out-of-plane displacements. Kaufman et al. [7] studied nitrogen-doped amorphous carbon film containing up to 20 at.% nitrogen and found that carbon-nitrogen bonding breaks the symmetry in sp^2 domains and causes the Raman-active G and D bands to become IR-active. However, carbon nitride with a higher nitrogen content (~44 at.%) needs to be observed in terms of the symmetry mechanism to see the effects of excess nitrogen in the bonding structure. Solin [85] mentioned that for a three dimensional graphite structure the Raman active zone-centre optic modes are E_{2g} and E_{1u}. For amorphous

carbon the E_{2g} mode is the symmetric Raman-active G band (usually 1584 cm^{-1}) and E_{1u} is weakly IR-active (usually 1588 cm^{-1}) [7]. The Raman-active D band (usually 1360 cm^{-1}) appears due to bond-angle disorder in the sp^2 graphite-like microdomains or a lack of coherence between adjacent graphite-like planes [86,87,88]. The E_{2g} and E_{1u} modes are shown schematically in the figure 17.

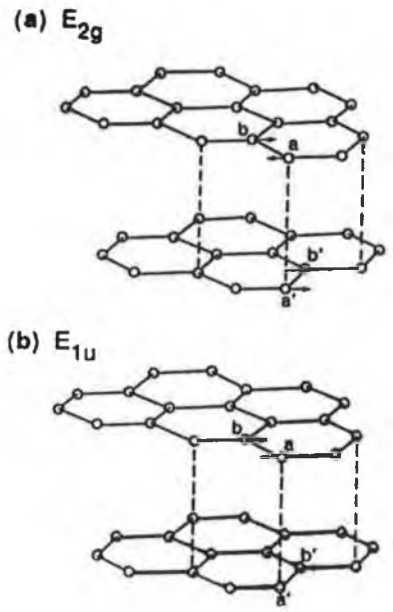

Figure 17: The E_{2g} (a) and E_{1u} (b) modes in graphite [7].

Atoms a and b in the carbon-carbon ring move with an opposing oscillation. Pairs in adjacent sheets (a' and b') oscillate 180° out of phase with respect to a and b. For a single sheet (graphene), this vibration has E_{2g} symmetry and is IR forbidden because there is no change in dipole moment in the plane of the sheet. For graphite, which has a three-dimensional structure, this mode splits into the E_{2g} and E_{1u} modes [7]. The E_{2g} is the symmetric Raman-active G band (1584 cm^{-1}) and the E_{1u} is weakly IR active (1588 cm^{-1}) because the net dipole moment is small [7]. If there is no correlation between layers, the E_{1u} vibration is absent in the infrared spectrum because there is no perpendicular component to break the symmetry of the vibration. As the domain size increases, the intensity of the D band decreases with respect to the G band [7,86]. So far, a few papers

have been published on first and second order Raman scattering for characterisation of graphite-like and CN materials [7,87,89,90,91]. Annealing of the films causes changes in structure which may affect the symmetry and help to produce symmetry sensitive information of the material being treated. Thus, there is still need to study the vibrational properties of carbon nitride solid by FTIR and Raman Spectroscopy.

2.6.3 Mechanical properties of CN Solid

So far the composition and bonding structure of carbon nitride solid, observed by different researchers, are discussed. It will be interesting to see (1) compositional; (2) structural influences on mechanical properties, i.e., hardness and intrinsic stress of the film, at various temperature.

Hardness measurements on thin films can be subject to serious influence from the substrate. But if the film is thick then this problem can be overcome. Due to enormous elestic recovery (~80%), as mentioned by Sjostrom et al [92], microhardness technique for C-N film is not recommended. They used nanoindentation technique for measuring hardness and elastic modulus of the material.

Li et al. [93] also carried out nanoindentation tests on carbon nitride thin films. They pointed out that carbon nitride materials has yield strength exceeding 5 GPa, which is higher than that for most alloys and ceramics. The hardness value of carbon nitride films, obtained using nanoindentation technique, vary from 10 to 40 GPa depending on the deposition techniques. Sjostrom et al [92] mentioned that the average hardness values (7-9 GPa) for carbon nitride films grown at 400 and 500^{0}C are same as that of Si (7.1 GPa) and in between those of amorphous carbon film (6.3 GPa) and sapphire (16 GPa), whereas the elastricity is considerably higher than for these reference materials. They also tried to co-relate these interesting mechanical properties with bonding structure. In 1995 they mentioned that hardness value of ~60 GPa and elastic recovery of 85% can be obtained from carbon nitride material [9]. They proposed that structures

consisting of a three-dimensional network of covalently bonded C and N atoms can exhibit extreme hardness vales. They also proposed that the incorporation of N leads to a structure of buckled planes with fullerenelike features that give rise to very high film elasticities. Thus, it will be interesting to see how C-N bonding with various C/N ratios influences the hardness values of the solid.

2.7 Application of CN Thin Film as Hard Coating: A Review

As a recent interest on new superhard material, carbon nitride solid drew undoubtedly keen interest of the materials scientists. We have seen that a number of papers have been published regarding synthesis of this material using different techniques. Focus was given to understand the bonding structure and stability of this material at the early stage. It is seen that continuous crystalline β-C_3N_4 structure can be synthesized, although the amorphous CN solid exists as a dominating portion of the compound. Probably Yeh et al [94] studied for the first time this material as a hard coating of magnetic storage media, i.e, NiP/AlMg substrate. They mentioned that sp^3 bonded CN film can have good wear resistance, although the existance of sp^3 bonded carbon nitride was not clear. They mentioned that nitrogen stabilises sp^3 bonded carbon. This sp^3 bonded structure is responsible for better wear characteristics. Chen et al [95] studied the tribological properties of carbon nitride thin films using polysrystalline zirconium as substrates. Their study showed that when deposited on zirconium, the material exhibits superior wear resistance and adhesion under lubricated sliding conditions. Under dry sliding conditions, it displays friction performance comparable to diamond. They suggested that this material has potential importance as a new wear-resistant coating for tribological applications. Zou et al [96] studied the wear characteristics of carbon nitride thin films, deposited on CoCrTa magnetic layer. They concluded that carbon overcoats with more nitrogen present shows lower frictional coefficient which is essentially required for hard disk overcoat. Deng et al [97] recently studied the adhesion properties of carbon nitride thin film on Si (111) wafer by nanoscratch techniques. They

compared adhesion properties of CN films with SiC and a:C ultra thin films. They found extremely good adhesion of this material on Si wafer. Liu et al [98] deposited carbon nitride thin film on hard disk as substrates and proposed the material as a possible candidate for hard disk overcoat, although they did not do any durability testing on the films. Zhang et al [99] deposited carbon nitride thin film on actual hard disk and found good scratch resistance properties of this material. They proposed this material as a good candidate as an overcoat film for proximity recording.

It can be seen from the above discussion that carbon nitride thin film can be used as hard coating for magnetic storage media. A similar application of this material can be done on tool steel.

References

1. A.Y. Liu and M.L. Cohen, Phys. Rev. B, 41, 10727 (1990).
2. C.M. Sung and M. Sung, Mater. Chem. Phys., 43, 1 (1996).
3. M.L. Cohen, Phys. Rev. B, 32, 7988 (1985).
4. A.Y. Liu and M.L. Cohen, Science, 245, 841 (1989).
5. P.H. Fang, J. Mater. Sci. Res. Lett., 14, 536 (1995).
6. E.C. Franklin, J. Amer. Chem. Soc., 44, 486 (1922).
7. J.H. Kaufman, S. Metin, D.D. Saperstein, Phys. Rev. B, 39, 13053 (1989).
8. D. Marton, K.J. Boyd, A.H. Al-Bayati, S.S. Todorov, J.W. Rabalais, Phys, Rev. Lett., 73 (1), 118 (1994).

9. H. Sjostrom, S. Stafstrom, M. Boman, J.-E, Sundgren, Phys. Rev. Lett., 75(7), 1336 (1995).

10. O. Borgen and H.M. Seip, Acta Chem. Scand., 15, 1789 (1961).

11. L. Cartz and J.D. Jorgensen, J. Appl. Phys., 52, 236 (1981).

12. J.C. Phillips, Bonds and Bands in Semiconductors, Academic, New York, 1973.

13. F.D. Murnaghan, Proc. Nat. Acad. Sci. USA, 30, 244 (1944).

14. H.-X. Han and B.J. Feldman, Solid State Commun., 65, 921 (1988).

15. S. Veprek, Surf. Coat. Technol., 97, 15 (1997).

16. J. Robertson, Surf. Coat. Technol., 50, 185 (1992).

17. A.P. Wells, Structural Inorganic Chemistry, 5th edn., Clarendon, Oxford, 1984.

18. L.C. Chen, D.M. Bhusari, C.Y. Yang, K.H. Chen, T.J. Chuang, M.C. Lin, C.K. Chen, Y.F. Huang, Thin Solid Films, 303, 66 (1997).

19. R.F. Bunshah, in Deposition Technologies for Films and Coatings, R.F. Bunshah edn, Noyes Publication, New Jersey, 1982.

20. W. Kern and V.S. Ban, Chemical Vapour Deposition of Inorganic Thin Films, in Thin Film Processes, J.L. Vossen and W. Kern edn., Academic Press,New York, pp.258, 1978.

21. G. Lucovsky, D.V. Tsu and R.J. Markunas, Formation of Thin Film by Remote Plasma Enhanced Chemical Vapour Deposition (Remote PECVD), in Handbook of Plasma Processing Technology, S.M. Rossnagel, J.J. Cuomo and W.D. Westwood edn., Noyes Publications, New Jersey, 1990.

22. F.M. Penning, Physica, 4, 71 (1937).

23. H.R. Kaufman and P.D. Reader, Am. Rocket Soc. [Pap.] No. 1374-60 (1960).

24. H.R. Kaufman, Adv. Electron. Electron Phys., 36, 265 (1974).

25. M. von Ardenne, Tabellen der Elektronenphysik, Ionenphysik und Ubermicroskopie, Dtsch. Verlag Wiss., pp. 554, Berlin, 1956.

26. W. Lotz, Astrophys. J. Suppl. Ser. 14 (128), 207 (1967).

27. T. Miyazawa, S. Misawa, S. Yoshidam S.I. Gonda, J. Appl. Phys., 55(1), 188 (1984).

28. J.H. Kim, D.H. Ahn, Y.H. Kim, H.K. Baik, J. Appl. Phys., 82(2), 658 (1997).

29. E.G. Wang, Y. Chen, L. Guo, Physica Scripta, T69, 108 (1997).

30. T. Leyendecker, O. Lemmer, S. Esser, M. Frank, in Third Intl. Conf. On Applications of Diamond Films Related Mater., A. Feldman, Y. Tzeng, W.A. Yarborough, M. Yoshikawa, M. Murakawa edn., 1995.

31. Y. Taki, T. Kitagawa, O. Takai, Thin Solid Films, 304, 183 (1997).

32. S. Veprek, J. Cryst. Growth, 17, 101 (1972).

33. H. Schafer, Chemische Transportreaktionen, Verlag Chemie, Weinheim/Bergstr., Academic Press, New York, 1964.

34. E. Kaldis, J. Cryst. Growth, 5, 376 (1969).

35. Z. Hauptman, unpublished, Prague, 1967.

36. S. Veprek and Z. Hauptman, Z. Anorg. Allgem. Chem., 359, 313 (1968).

37. A.N. Wright and C.A. Winkler, Active Nitrogen, Academic Press, New York, 1968.

38. A.B. King and H. Wise, J. Phys. Chem., 67, 1163 (1963).

39. S. Veprek, J. Weidmann, F. Glatz, J. Vac. Sci. Technol. A, 13(6), 2914 (1995).

40. S. Jou, H.J. Doerr, R.F. Bunshah, Thin Solid Films, 253, 95 (1994).

41. I.H. Murzin, G.S. Tompa, E.W. Forsythe, J. Wei, V. Muratov, T. Fischer, J. Vac. Sci. Technol. A, 15(3), 1179 (1997).

42. J. Asmussen, Electron Cyclotron Resonance Microwave Discharge for Etching and Thin Film Deposition, in Handbook of Plasma Processing Technology, S.M. Rossnagel, J.J. Cuomo, W.D. Westwood edn., Noyes Publications, New Jersey, 1990.

43. S. Nowak, P. Groning, O.M. Kuttel, M. Collaud, G. Dietler, J. Vac. Sci. Technol. A, 10(6), 3419 (1992).

44. F.-R. Weber, H. Oechsner, Surf. Coat. Technol., 74-75, 704 (1995).

45. H. Oechsner, H.J. Fuber, J. Waldorf, A. Fuchs, Proc. 1st Int. Conf. On Plasma Surf. Engg., Garmisch-Partenkirchen, 1988, Vol. II, DGM Informationsgesellschaft, Oberursel, pp.1017, 1989.

46. F.-R. Weber, H. Oechsner, Surf. Coat. Technol., 59, 234 (1993).

47. J. Ullmann, U. Falke, W. Scharff, A. Schroer, G.K. Wolf, Thin Solid Films, 232, 154 (1993).

48. F. Fujimoto and K. Ogata, Jpn. J. Appl. Phys., 32, L420 (1993).

49. P.J. Martin, R.P. Netterfield, A. Bendavid, T.J. Kinder, Surf. Coat. Technol., 54, 136 (1992).

50. P.J. Martin, X. Wang, A. Bendavid, T.J. Kinder, SPIE, 2364, 465 (1994).

51. D. Chrisey and G. Hubler, Pulsed Laser Deposition of Thin Films, Wiley, New York, 1994.

52. Z.J. Zhang, S. Fan, J. Huang, C.M. Lieber, J. Electron. Mater., 25(1), 57 (1996).

53. L. Maya, D.R. Cole, E.W. Hagaman, J. Am. Ceram. Soc., 74(7), 1686 (1991).

54. T.-A. Yeh, C.-L. Lin, J.M. Sivertsen, J.H. Judy, IEEE Trans. Magnetics, 27, 5163 (1991).

55. D. Li, S. Lopez, Y.W. Chung, M.-S. Wong, W.D. Sproul, J.Vac. Sci. Technol. A, 13, 1063 (1995).

56. J. Schwan, W. Dworschak, K. Jung, H. Erhardt, Diamond Rel. Mater., 3, 1034 (1994).

57. H. Sjostrom, I. Ivanov, M. Johansson, L. Hultman, J.-E. Sundgren, S.V. Hainsworth, T.F. Page, L.R. Wallenberg, 9th Internatl. Conf. On Thin Films, Hofburg, Vienna, Austria, 1993.

58. S. Kumar and T.L. Tansley, Sol. Stat. Comm., 88 803 (1993).

59. E.E. Haller, M.L. Cohen, W.L. Hansen, Hard Carbon Nitride and Method for Preparing Same, US Patent No. 5, 110, 679 (1992).

60. C. Niu, Y.Z. Lu, C.M. Lieber, Science, 261, 334 (1993).

61. F. Xiong, R.P.H. Chang, C.W. White, MRS Fall Meeting, 1992.

62. M.Y. Chen, D. Li, X. Lin, V.P. Dravid, Y.-W. Chung, M.-S. Wong, W.D. Sproul, J. Vac. Sci. Technol. A, 11, 521 (1993).

63. C.J. Torng, J.M. Sivertsen, J.H. Judy, C. Chang, J. Mater. Res., 5, 2490 (1990).

64. D. Marton, K.J. Boyd, J.W. Rabalais, Internatl. J. Modern Phys. B, 9(27), 3527 (1995).

65. F.R. McFeely, S.P. Kowalczyk, L. Ley, R.G. Cavell, R.A. Pollak, D.A. Shirley, Phys. Rev. B, 9, 5268 (1974).

66. H.E. Xiaoming, L.I. Wenzhi, L.I. Hengde, Chinese Science Bulletin, 40(20), 1752 (1995).

67. J. Szmidt, A. Werbowy, K. Zdunek, A. Sokowska, J. Konwerska-Hrabowska, S Mitura, Diamond Rel. Mater., 5, 564 (1996).

68. O. Amir and R. Kalish, J. Appl. Phys., 70, 4958 (1991).

69. X.T. Cui, Z.H. Zhang, Q.Chen, K. Paschke, D.W. Pan, J.R. Liu, Z.S. Zheng, J. Kulik, F. Romeo-Borja, L.T. Wood, W.K. Chu, MRS Spring Meeting, 1994.

70. S. Lopez, H.M. Dunlop, M. Benmalek, G. Tourillon, M.-S. Wong and W.D. Sproul, Surface and Interface Anal., 25, 315 (1997).

71. A. Nilson, O. Bjorneholm, H. Tillborg, B. Hernnas, R.J. Guest, A. Sandell, R.E. Palmer and N. Martensson, Surf. Sci., 287-288, 758 (1993).

72. M.A. Baker and P. Hammer, Surf. and Interface Anal., 25, 301 (1997).

73. D. Marton, K.J. Boyd, A.H. Al-Bayati, S.S. Todorov and J.W. Rabalais, Phys. Rev. Lett., 73(1), 118 (1994).

74. M. Kohzaki, A. Matsumuro, T. Hayashi and M. Muramatsu and K. Yamaguchi, Jap. J. Appl. Phys., 36, 2313 (1997).

75. P. Hammer, M.A. Baker, C. Lenardi and W. Gissler, J. Vac. Sci. Technol. A, 15(1), 107 (1997).

76. M. Barber, J.A. Conner, M.F. Guest, I.H. Hillier, M. Schwartz, and M. Stacey, J. Chem. Soc. Faraday Trans. II, 69, 551(1973).

77. W.T Zheng, H. Sjostrom, I Ivanov, K.Z. Xing, E. Broitman, W.R. Salaneck, J.E. Greene and J.-E. Sundgren, J. Vac. Sci. Technol. A, 14(5), 2696 (1996).

78. I. Gouzman, R. Brener and A. Hoffman, Surf. Sci., 331-333, 283 (1995).

79. F. Rossi, B. Andre, A. van Veen, P.E. Mijnarends, H. Schut, F. Labohm, M.P. Delplancke, H. Dunlop and E. Anger, Thin Solid Films, 253, 85 (1994).

80. P.G. Lurie and J.M. Wilson, Surface Science, 65, 476 (1977).

81. K.J. Boyd, D. Marton, S.S. Todorov, A.H. Al-Bayati, J. Kulik, R.A.Zuhr and J.W. Rabalais, J. Vac. Sci. Technol. A, 13(4) (1995), 2110.

82. K.K. Mani and R. Ramini, Phys. Status Solidi B, 61 (1974) 659.

83. R.J. Nemanich, G. Lucovsky and S.A. Solin, Solid State Commun., 23 (1977) 117.

84. R.J. Nemanich, G. Lucovsky and S.A. Solin, in M. Balkanski (ed.), Lattice Dynamics, Flammarion, Paris, 1975, p.619.

85. S.A. Solin, Physica B, 99 (1980) 443.

86. R.O.Dillon, J.A. Woollam and V. Kathanant, Phys. Rev. B, 29 (1994) 3482.

87. Y. Taki, T. Kitagawa, O. Takai, Thin Solid Films, 304 (1997) 183.

88. F. Tuinstra and J.L. Koenig, J. Chem. Phys., 53 (1970) 1126.

89. R.J. Nemanich and S.A. Solin, Phys. Rev. B, 20 (2), (1979) 392.

90. M. Y. Chen, D. Li, X. Lin, V.P. Dravid, Y.P. Chung, M.S. Wong and W.D. Sproul, J. Vac. Sci. Technol A, 11(3), (1993) 521.

91. D. Beeman, J. Silverman, R. Lynds and M.R. Anderson, Phys. Rev. B, 30 (2), (1984) 870.

92. H. Sjostrom, I. Ivanov, M. Johansson, L. Hultman, J.-E. Sundgren, S.V. Hainsworth, T.F. Page, L.R. Wallenberg, Thin Solid Films, 246, 103 (1994).

93. D. Li, Y.W. Chung, M.S. Wong, W.D. Sproul, J. Appl. Phys., 74(1), 219 (1993).

94. T.-A. Yeh, C.-L. Lin, J.M. Sivertsen, J.H. Judy, IEEE Trans. Magnetics, 27(6), 5163 (1991).

95. M.Y. Chen, X. Lin, V.P. Dravid, Y.W. Chung, M.S. Wong, W.D. Sproul, Tribology Trans., 36(3), 491 (1993).

96. P. Zou, M. Scherge, D.N. Lambeth, IEEE Trans. Magnetics, 31(6), 2985 (1995).

97. H. Deng, T.W. Scharf, J.A. Barnard, J. Appl. Phys., 81(8), 5396 (1997).

98. Y. Liu, C. Jiaa, H. Do, A. Eltoukhy, IEEE Trans. Magnetics, 33(5), 3106 (1997).

99. B. Zhang and B. Wei, IEEE Trans. Magnetics, 33(5), 3109 (1997).

Chapter 3

Sputter deposition and properties of sputtered films

This chapter will briefly describe the magnetron sputtering technique, crystal growth process and thin film growth mechanism. Although this research involved deposition of C-N thin film by Penning type opposed target reactive DC sputtering technique, which will be discussed in the next chapter, a clear understanding of the magnetron sputtering technique will help in understanding the Penning type reactor. The chapter also discusses the ions' interactions with surfaces and its effect during thin film growth process.

3.1 Sputtering

Sputtering *is a process operating on an atomic or molecular scale whereby an atom or molecule of a surface is ejected when the surface is struck by a fast incident particle* [1]. The process of sputtering is straightforward. The momentum of the incident atom is transferred to the atoms in the target material and this momentum transfer can often lead to the ejection of a surface atom. In order for the sputtering process to be efficient, the incident particle also has to be of atomic dimensions. A very small particle, such as an electron, does not carry enough momentum to be effective, whereas a large particle, such as an ion is massive enough to interact with individual atoms or molecules in the surface. Figure 1. shows the interactions of ions with surfaces. In the sputtering process the solid is usually called the target and the incident particles are ions. The interactions of ions result:

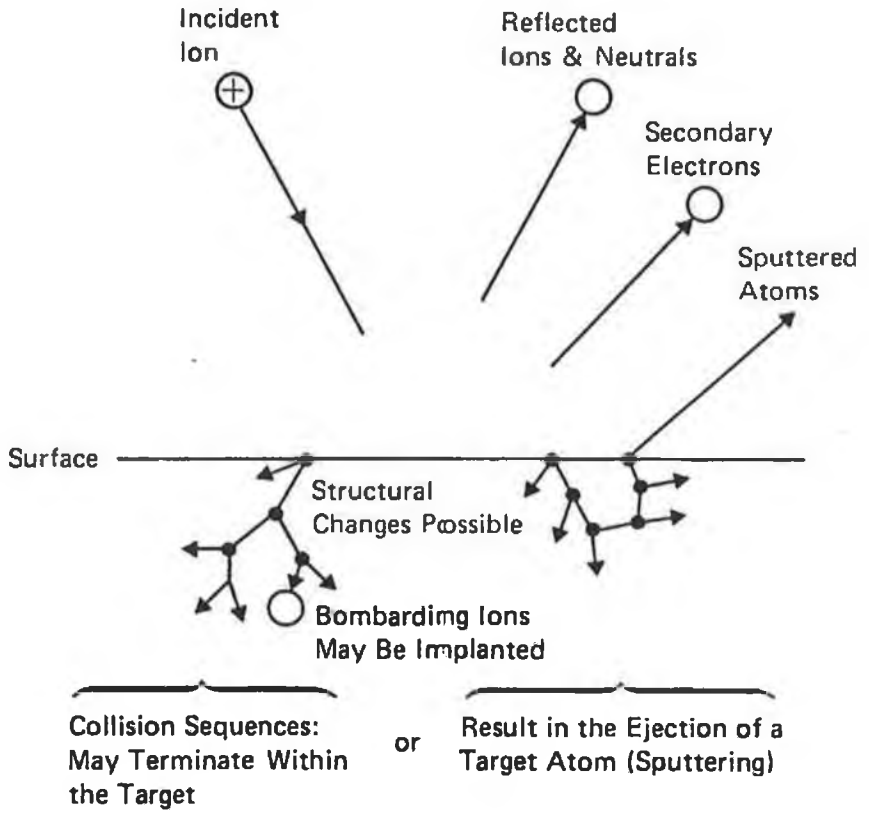

Figure 1: Ion to surface interaction, i.e. the sputtering process [1].

- The ion may be reflected, probably being neutralized in the process.
- The impact of the ions may cause the target to eject an electron, usually referred to as a secondary electron.
- The ions may case implantation into the solid.
- The ion impact may cause lattice defects, changes in electrical charge levels i.e. radiation damage or even change in stoichiometry of the surface layer.

- The ion impact may set up a series of collisions between atoms of the target, possibly leading to the ejection of one of these atoms. This ejection process is known as sputtering.

3.2 Mechanism of sputtering

The incident particle could be either an ion or a neutral atom. Ions are normally used since they can easily be accelerated by an electric field, whereas neutrals cannot be. Furthermore, the ions are likely to be neutralized by the Auger emission of an electron from the target as the ion approaches, so that the impacting species are eventually mostly neutral. The series of collisions in the target, generated by the primary collision at the surface, is known as a collision cascade (Figure 1). It is very uncertain whether this cascade leads to the sputter ejection of an atom from the surface or whether the cascade moves into the interior of the target, gradually dissipating the energy of the primary impact, ultimately to lattice vibrations, i.e. heat. Thus the energy of the sputtered atoms could be a few percentage of the energy incident particle which makes the process very inefficient. The collision phenomena occurring in the target, often referred to as target kinetics.

The Sputtering Yield

The sputtering process is quantified in terms of the sputtering yield. This term can be defined as the number of target atoms ejected per incident particle. The yield depends on the target species, and on the bombarding species and its energy and angle of incidence. It is insensitive to the target temperature [2]. It is also independent of whether the bombarding species is ionized or not, as ions have a high probability of being neutralized by Auger electrons prior to impact [3]. Molecular bombarding species behave as if the atoms of the molecule arrived seperately with the same velocity as the molecule and initialed their sputtering events [2]. The yield tends to be greatest when the mass of the bombarding particle is of the same order of magnitude or larger than

that of the target atoms. The use of inert gas ions avoids chemical reactions at the target and substrate. Accordingly, argon is generally used because of its mass compatibility with materials of engineering interest and its low cost of course. However, krypton, xenon and helium are sometimes used. Sometimes a mixture of these gases can give high sputtering rate for some materials.

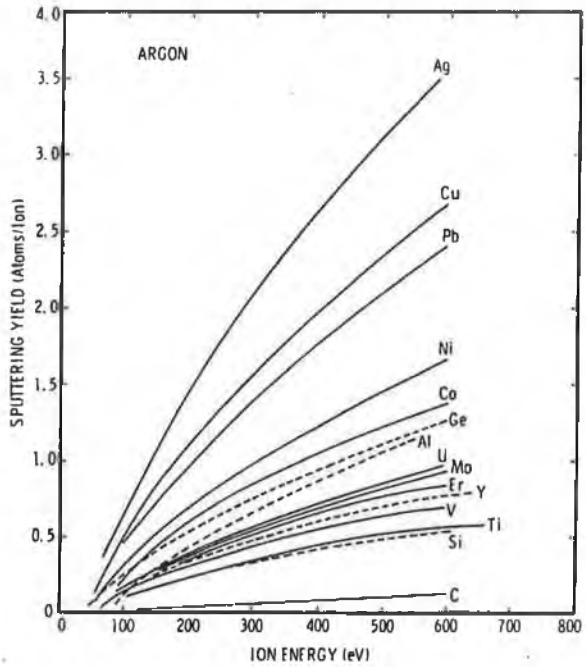

Figure 2: Variation of sputtering yield with ion energy at normal angle of incidence. Data from: Stuart et al. [4], Rosenberg et al. [5] and Behrisch et al. [6].

Sputtering yields are determined experimentally. Figure 2 shows yield versus ion energy data for several materials under normal ion incidence. The yield dependence on the bombarding ion energy is seen to exhibit a threshold of about 10-30 eV, followed by a near-linear range which may extend to several hundred eV. At higher energies the dependence is less than linear. The sputtering process is most efficient from the standpoint of energy consumption when the ion energies are within the linear range.

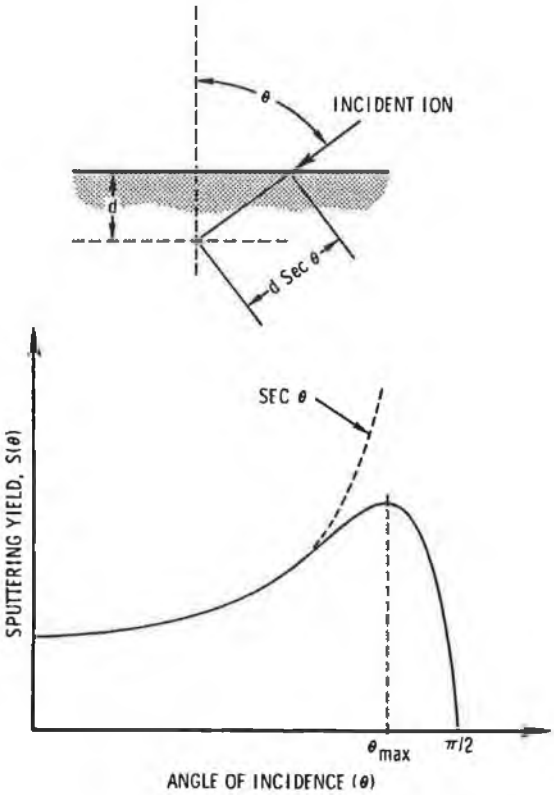

Figure 3: Schematic diagram showing variation of sputtering yield with ion angle of incidence, taking constant ion energy [7].

The general dependence of the yield on the ion angle of incidence is indicated in figure 3 [7]. It is seen that the yields of most metals are about unity and within an order of magnitude of one another. This is in contrast, for example, to evaporation, where the rates for different materials at a given temperature can differ by several orders of magnitude [8].

An expression for the yield which can be written in the form shown in Eq. 1 and 2, has been derived by assuming perpendicular ion incidence onto the target consisting of a random array of atoms (i.e. polycrystalline materials) with a planer surface [9,10,11].

$$S = k\varepsilon \frac{E}{U} \alpha (M_t / M_i) \tag{1}$$

The yield is seen to depend directly on the energy transfer function ε, which is

$$\varepsilon = \frac{4 M_i M_t}{(M_i + M_t)^2} \tag{2}$$

Where, M_t and M_i stand for mass of target material and incident particle. The term $\alpha(M_t/M_i)$ is a near-linear function of M_t/M_i, E is the kinetic energy of the incident ion, U is the heat of sublimation for the target material, and k is a proportionality constant. For engineering materials the mass dependence term of eqn. 1, εα, does not vary greatly from one material to another. The primary material-sensitive factor is the heat of sublimation, and this is only a first power dependence. This is in contrast to chemical and thermal process that depend exponentially on an activation energy.

It is seen that when $M_i < M_t$ it may be reflected backward in a single collision, and that the energy of the reflected ion may be a significant fraction of its initial energy. For a 180^0 reflection this fraction is

$$\left(\frac{M_i - M_t}{M_i + M_t} \right)^2 \tag{3}$$

If $M_i \geq M_t$, the ions can eject atoms from target surface as the net energy transfer function, ε, for ejection process is high. If $M_i > M_t$ the ion can still be reflected backward only as the result of more than one collision prior to impact [12]. In this case, ions lose energy during several collisions and the energy transfer function is not enough to eject target atoms. Since the ions have high probability of being neutralized prior to impact, they are reflected as energetic neutrals which are therefore not influenced by the electric field over the target surface [13]. The momentum flux represented by the

reflected species contributes to substrate heating [14]. In sputtering devices, which operate at low working gas pressures the reflected and neutralized ions may reach the substrates with little loss of kinetic energy due to gas phase collisions [12]. Consequently, the reflected species bombard and can become entrapped in the growing coating [15,16,17,18].

The incident energy of ions E in eqn. 1 is an another factor for considering sputter yield. In practice, it is seen that sputter yield will increase linearly with ion energy up to 1keV, after that yield becomes relatively constant. When the input ion energy becomes higher than 1keV, the excess energy is distributed through a larger volume, thus the energy transmitted to the surface layers remains more or less constant. At very high energies, i.e, >10 keV, yield decreases as ion implantation becomes dominant.

Sputtering of compound targets

Commercially compound targets are also sputtered. In this case the most important thing is to achieve coatings the same composition of the targets. To achieve this the target is maintained sufficiently cool to avoid diffusion of constituents, the target does not decompose, reactive contaminants are not present, the gas phase transport of the components is the same, and the sticking coefficient for the components on the substrate are the same. There is still problem when the homogeneous material composed of species having different individual sputtering yields of masses. The higher sputtering yield materials will be sputtered fast, thus leave an altered layer on the target surface containing predominantly low yield materials. It is essential that there must be an adjustment period during which the compositions of the species in a surface layer adjust until the product of the effective sputtering yield times surface concentration for each species is proportional to its concentration in the target [12]. Thus, it is necessary that diffusion from the bulk not replenish the reduced concentrations of high yield materials in the altered layers.

Sputtering with reactive species

Sputtering by reactive species is very important in compound formation. In this case reduced yields are commonly observed and compound could be formed on the target surface. Such surface interactions are seen to influence significantly the surface topography that develops on the target. 20 keV O_2^+ bombardment of an iron target yielded a considerably smoother surface than 20 keV Ar^+ bombardment [19]. Sometimes the reactive species are chemisorbed on the target surface during direct sputtering. It is seen that such species are sputtered as atoms with yields that are of the same order of magnitude or higher than those of elemental materials [20]. The deposition of carbon nitride thin film is a type of reactive sputtering. In this case, a fraction of N_2^+ ions from the plasma are chemisorbed forming CN species at graphite surface. These CN species are sputtered and can be identified by Optical Emission Spectroscopy. This will be discussed in detail in the chapter 4.

3.3 Sputtering Technology

So far the mechanism of sputtering was discussed. The implementation of sputtering process as a technology depends on the successful production and supply of ions over the surface of the target. In this case low pressure glow discharge is the most cost-effective ion source. A wide range of glow discharge apparatus geometries have been used to increase the ion supply and thus the sputtering rate, increase the target area and thus the available deposition area, reduce the plasma heating of the substrate, permit a lowering of the working gas pressures and facilitate the coating of particular substrate shapes. In this section the commonly used apparatus types will be discussed briefly. In the next chapter a newly developed sputtering device based on Penning geometry will be discussed in detail. This apparatus provides higher degree of ionisation which is one of the most important factors for crystalline carbon nitride film production by sputtering technique.

3.3.1 Diode Sputtering

In this simple arrangement a target is located within a vacuum chamber and biased negatively. The chamber is evacuated to high vacuum and then backfilled with an inert gas. The target is negatively biased and a glow discharge plasma is ignited. In this process the cathode serves a dual capacity. It is the target or source of coating material as well as the cathode electrode for sustaining the glow discharge. It is noted that the nature of the plasma is such that virtually the entire discharge potential is dropped from the plate to a distance several millimetres away. This region is referred to as the cathode sheath [21]. Those parts of the target where a discharge is not desirable are shielded. Positively charged Argon ions in the glow diffuse to the target vicinity and are accelerated to impact on the target causing sputtering. Electrons are also created from the plasma volume and pass over to the anode. Because of the relatively low mobility of the ions compared to the electrons, most of the electrical potential that is applied between the anode and cathode by the power supply is consumed in the sheath region. Thus strong electric fields are formed, and ions passing from the plasma volume to the cathode are accelerated by these fields and on impact at the cathode produce the desired sputtering. These sputtered target atoms may then find their way to the substrates to form a coating. The cathode diameter is typically 10 to 30 cm and the cathode to anode spacing about 5 to 10 cm. Such systems are operated with both dc and rf power supplies. Typical operating parameters are a pressure of 10^{-1} mbar, a potential of 1000-5000 dc volts, a current density of 1 mA cm^{-2} and a deposition rate of 40 mm per minute. Figure 4 illustrates the process. Yu et al. [22] first used a typical diode sputtering system for crystalline β-C_3N_4 film deposition.

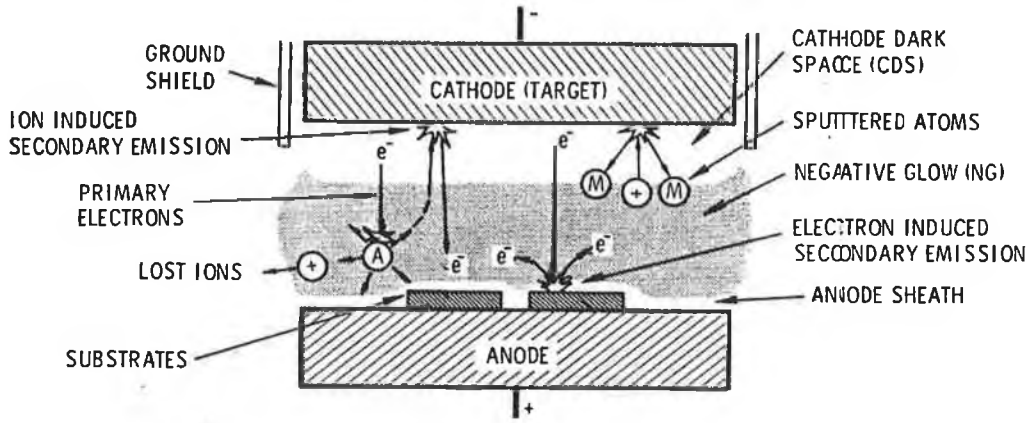

Figure 4: Schematic representation of the sputtering phenomena in a planar diode sputtering source [17].

3.3.2 Planar Magnetron Sputtering

The first planer magnetron sputtering system was described by Chapin in 1974 [23]. The importance of the work lies in the high sputter rates which are achievable with this device as compared with the ordinary diode sputtering. Even today, the fundamentals of the original design are unchanged. The disadvantages of this system are, poor target utilisation and arcing on the target surface. Thornton and Penfold [24] defined magnetrons *as diode sputtering sources in which magnetic fields are used in concert with the cathode surface to form electron traps which are so configured that the E X B electron drift currents close on themselves.*

The standard magnetron geometry is similar to that of the diode arrangement but with a magnetic circuit located behind the target such that magnetic field lines form as shown in figure. 5.

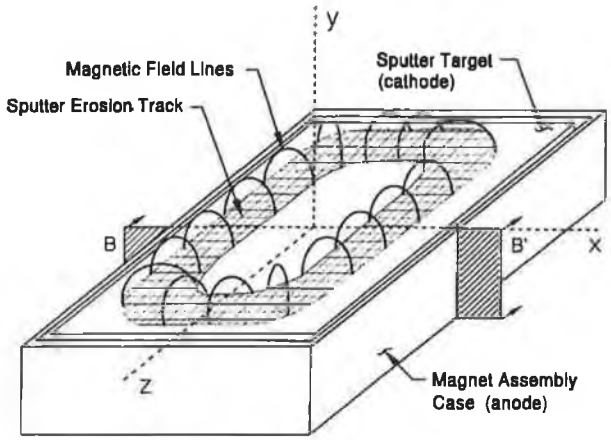

Figure 5: Sketch of a rectangular planar magnetron [25].

The figure shows the sketch of a simple planar magnetron whose sputter erosion track is quasi-rectangular. The magnetic field is produced by an assembly of permanent magnets such that the field lines emerge from, arch over and re-enter the sputter target plate. The case which contains the magnet assembly is connected to ground potential and, in this sketch, functions as the anode of the discharge. An intense glow discharge forms in the tunnel defined by the field line arches. Typical magnetrons have characteristic dimensions which range from a few cm to more than 500 cm. They operate at at voltages in the range 200-900, at pressures in the range $4.5X10^{-3}$ to 0.375 mbar, with field strengths in the range 50-400 Gauss and at power levels ranging from 1 watt to 120 kW. Power densities as high as 200 W/cm^2 have been used [26]. At power densities in excess of 80 W/cm^2 copper has been self-sputtered [26]. In this case enough ions are formed from the sputtered copper atoms so that a stable discharge is maintained without the help of argon gas.

The low operating pressure in magnetron sputtering means that redeposition of sputtered materials back onto target is less likely. This is another way to get increased

deposition rate. The main deposition rate limiting factors in magnetron sputtering are the thermal conductance of the target, the efficiency of the water cooling, the melting point of the target material and the target sputtering yield. Another advantage of the magnetron sputtering is that sputtered atoms are less likely to lose energy in collisions. This implies greater activation of the growing film which leads to denser coatings. Also careful designed magnetron has better control over ion bombardment by comparison with diodes.

Generic rectangular planar magnetron

Figure 6 shows the magnetron of figure 5 in a simplified cross section taken through the plane B-B′. Item 1 is the non magnetic metal case which houses the magnet assembly; item 2 is an insulator which isolates the magnet assembly from the case; item 3 is the magnetizable rear yoke of the magnet assembly which can be made from soft iron or mild steel; item 4 are the permanent magnets which supply the field; and item 5 are magnetizable pole pieces for the magnets. The sputter target rests on the pole pieces. The necessary vacuum seals and cooling water channels are omitted for simplicity.

The contours located above the target surface show the magnetic field lines generated by the magnets. The intense discharge of the electron trap, which are released from the cathode surfaces by ion bombardment, forms in the tunnel which is defined by the accented pair of field lines. It is centered at the positions where the field lines are tangential to the cathode as they emerge and, terminated by the first set of field lines which intersect an anode. The real anode in figure 6 is the magnet casing (item 1).

The dotted line indicates the original cathode surface while the solid contours indicate the profile which develops after an extended period of sputter erosion. The eroded material can be deposited onto substrates which are attached to the indicated substrate carrier. As the erosion track deepens the operating characteristic of the discharge changes as does the profile of sputtered material at the substrate plane. In most cases the

erosion track is more V-shaped than figure 6 indicates because there is considerable cross deposition of sputtered material from one side of the erosion track to the other. Poor utilisation of target material occurs in the simple magnetron depicted by figure 6. However, careful positioning of magnets at the back of the target can improve target utilisation.

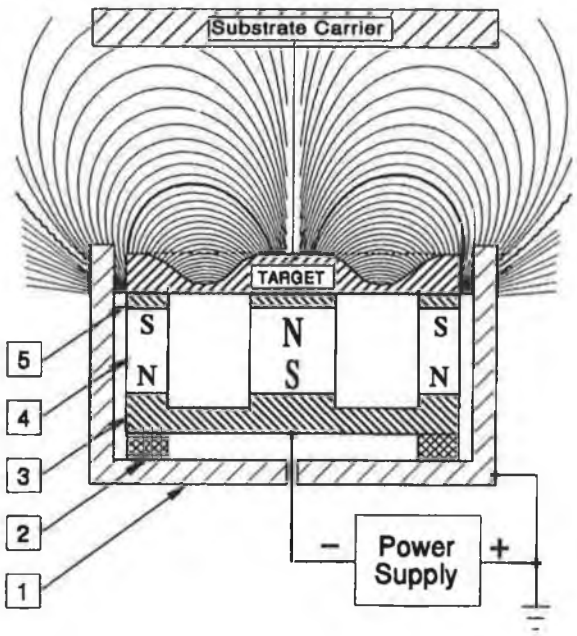

Figure 6: A generic rectangular planar magnetron in cross section showing the magnetic field lines [25].

3.3.3 Mechanism of magnetron sputtering

The basic idea behind magnetron sputtering technique is to trap electrons near the target surface so as to increase their ionising effect. This is achieved with electric and magnetic fields that are generally perpendicular.

In sputtering discharges, the sputtering rate depends directly on the ion flux, and this in turn depends on the density of ions in the plasma. The major limitation on ion density is the recombination of ions with electrons. This commonly happens on the walls of the vacuum vessel.

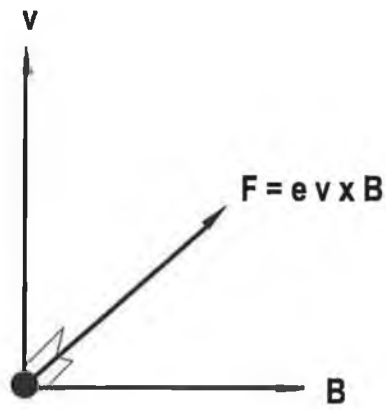

(a)

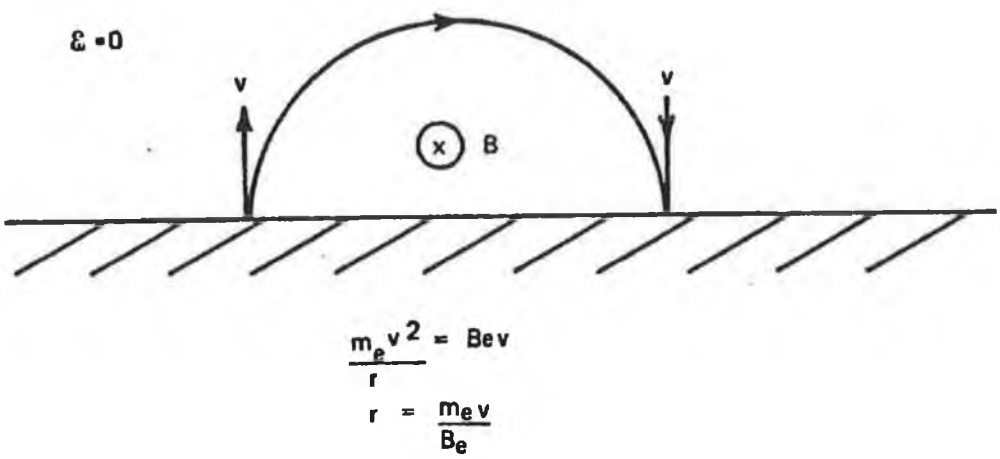

(b)

Figure 7: (a) The electromagnetic force F is perpendicular to both v and B. (b)The influence of a magnetic field on electron motion [1].

The use of a magnetic field is primarily to trap electrons close to the sputtering target, so as both to prevent them from escaping to the walls where they will cause ion loss by recombination, but also to cause them to create ions by electron impact close to the sputtering target where they are most useful.

The interaction between the magnetic field B and an electron with vector velocity v is to create a force F on the electron, where $\mathbf{F = e\ v \times B}$, so that F is in a direction orthogonal to both the magnetic field and electron velocity vectors (figure 7.a). As a result there is a strong tendency for the electron to travel in an epicycloidal motion close to the target surface where both the magnetic field strength and the electron velocity are large. By contrast, the relatively large mass and low velocities of the ions produces much less trapping of the ions, although this can still be significant effect. By this means of magnetic enhancement, ion fluxes can be increased to several tens of $mA.cm^{-2}$, with corresponding increases in deposition rates. Figure 7(b) represents the influence of a magnetic field on electron motion, considering the electron emitted with velocity v from a surface into a region of magnetic field B (into the paper) and zero electric field ($\varepsilon=0$). In a similar way to the axial magnetic field case, the electron will describe a semicircle of radius r given by $\mathbf{m_e v/Be}$ [1] (m_e, the mass of electron) .

Balanced and unbalanced magnetron

Planar magnetrons are generally two types, (a) Balanced and (2) Unbalanced magnetron. A balanced magnetron is one in which the magnetic fluxes of the opposing poles are equal. This is most easily achieved by ensuring that the surface area of both north and south poles are equal. On the other hand, an unbalanced magnetron is one in which the magnetic fluxes of the opposing magnetic poles are not equal. Figure 8 depicts this feature. This imbalance in the magnetic field strength can be achieved by either making the outer ring or inner ring of magnets stronger. Usually, the outer ring is made stronger of the two so that the magnetic field lines emitting from the edges of the magnetron are directed towards the substrate. This magnetic field line configuration

serves to confine the plasma between the target and the substrate, thus provides high density, low energy ion bombardment of the growing film. Thus unbalanced magnetron facilitates the deposition of thin films onto substrates more satisfactorily than balanced magnetrons.

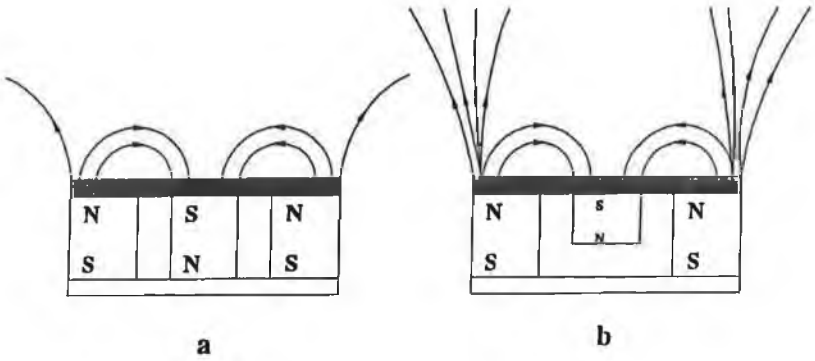

Figure 8: (a) Schematic representation of Balanced Magnetron showing the magnetic field lines; (b) Unbalanced Magnetron representing the same.

3.4 Thin film Growth mechanism

The growth models of thin films are based on different deposition techniques. Here emphasis will be given on growth model of sputtered deposited thin film. The coating atom condensation process can be explained as occurring in three steps. First, incident atoms transfer kinetic energy to the substrate lattice and become loosely bonded 'adatoms'. This energy transfer is efficient, even for energetic sputtered atoms. The theory was derived by K.L. Chopra [27]. Second, the adatoms diffuse over the surface, exchanging energy with the lattice and other adsorbed species, until they either are desorbed, by evaporation or back-sputtering, or become trapped at low energy sites. Once the coating becomes continuous, growth proceeds similarly, by adatoms arriving and diffusing over the coating surface until they are desorbed or become trapped in low energy sites. Finally, in the third step the incorporated atoms readjust their positions within the lattice by bulk diffusion processes. Before going to the detail discussion on

growth mechanism, the effect of ions, electrons and neutral particle bombardment on substrate will be discussed briefly.

Effect of electron bombardment

In the case of planer diode devices the substrates are generally in contact with the plasma. Thus, even if the substrates are electrically isolated, they are subjected to bombardment by energetic primary electrons from the cathode. These energetic electrons are typically 100 to 1000 eV [28]. The effect of these electrons are very important in case of film growth as they are the primary source of substrate heating in such devices. The effect of heating by electron bombardment can be reduced by substrate cooling. This effect is automatically reduced when deposited at high working pressure due to less mean free path of the electrons. These electron energies can be utilised by entrapping them into a magnetically confined plasma. In case of the Penning source which will be discussed in the later chapter, the electrons are entrapped in the magnetically confined plasma. These electrons help in the production of a higher degree of ionisation. As they are confined, the effect of substrate heating by electrons are dramatically reduced.

Effect of ion bombardment

Ion bombardment on the substrate surface may be expected to increase the nucleation density by causing surface damage. The diffusion process can be increased due to excitation of surface phonons by ion bombardment. It is also expected to enhance the mobility of adatoms by transferring kinetic energy to them. M. Marinov [29] described the effect of energetic ion bombardment on surface. He mentioned that due to transferring kinetic energy an acceleration of the nucleation, growth and coalescence of the nuclei result.

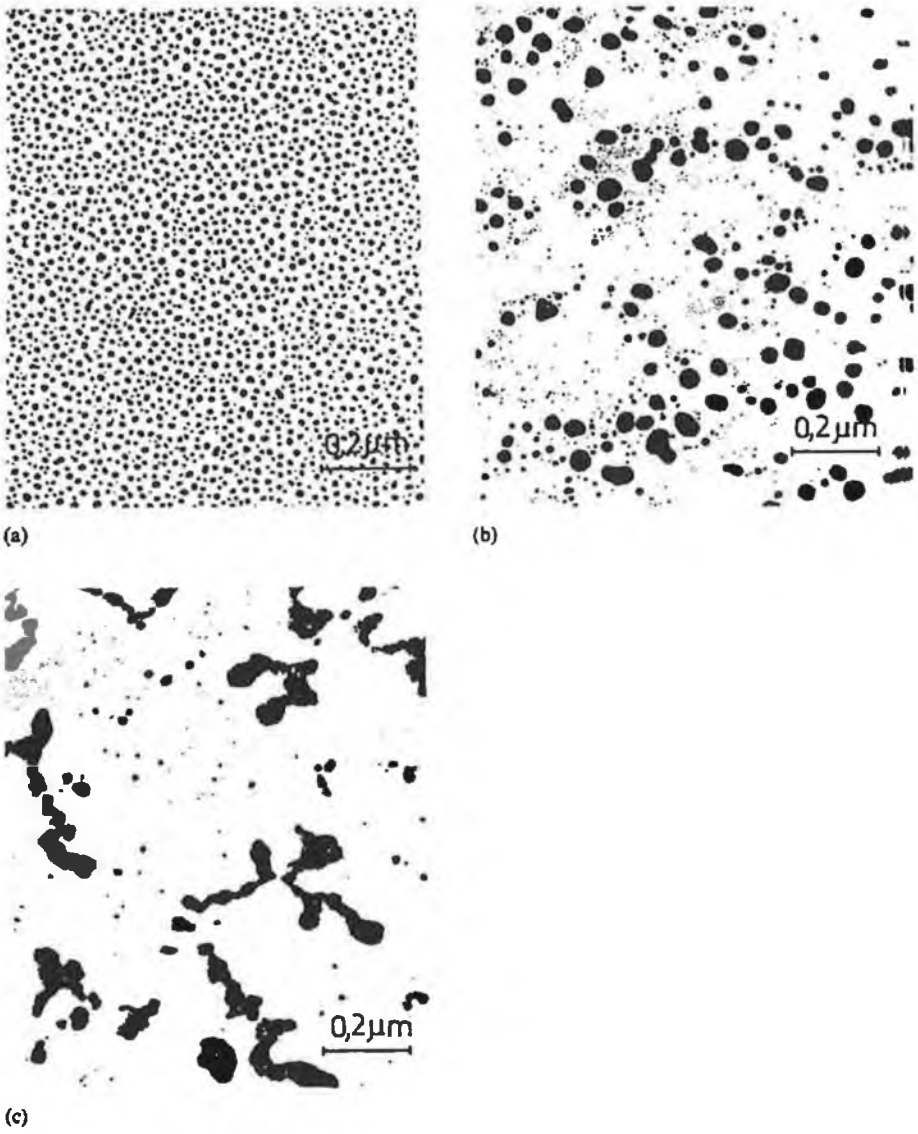

Figure 9: Electron micrographs of silver island films (a) without ion bombardment; (b) with weak ion bombardment; (c) with strong ion bombardment [27].

Eltoukhy et al. [30] reported that ion bombardment makes the surface diffusion coefficients more than five orders of magnitude greater than the thermal values during the sputtering deposition of InSb/GaSb superlattice structure. Low energy ion bombardment during film growth has also been found to increase the growth

temperature range over which stoichiometric films of compound semiconductor such as GaSb and InSb can be grown as reported by Eltoukhy et al. [31]. D.M. Mattox [32,33] reported that ion bombardment has been found to have a large influence on the interface structure and thus on the adhesion of coatings. He mentioned that the mechanism may be an increase in the density of nucleation sites, and therefore a reduction in the amount of agglomeration and void formation that occurs during the initial island growth. The effect of ion bombardment during silver island formation can be depicted in the Figue. 9 [29].

Effect of neutral species bombardment

The effect of neutral bombardment is similar to that of ion bombardment. For magnetron sputtering system all the neutral species may impinge on the surface of a film as it is growing. Neutrals give up momentum and energy as do ions which also give up their charge. The major effect of ions and neutrals are to increase adatom mobility on the growing film.

However, the ion to neutral ratio is an important factor in growth process. The effect of bombardment of these species on the growing film should be considered. For nonreactive bombarding species the effects can be summarized as follows: (1) momentum transfer (knock-on displacement); and (2) direct temperature effects. These processes can in turn cause various effects as the thin film grows, including enhanced surface mobility, enhanced accumulation of nuclei, desorption of surface impurities, redistribution of atoms in the film and also the implantation of bombarding species into the growing film [34]. Theoretical support, based on molecular dynamics calculations, for these experimental results has been given by Muller [35]. He reported that (1) ion bombardment during growth removes overhanging atoms and causes void regions to remain open until filled by new depositing atoms, (2) sputtered atoms are redeposited mainly in voids, (3) ions induce surface diffusion (diffusion distance is a few interatomic

spacing), local heating, collapse of voids and recrystallisation. His theoretical predictions can be depicted by the figure. 10.

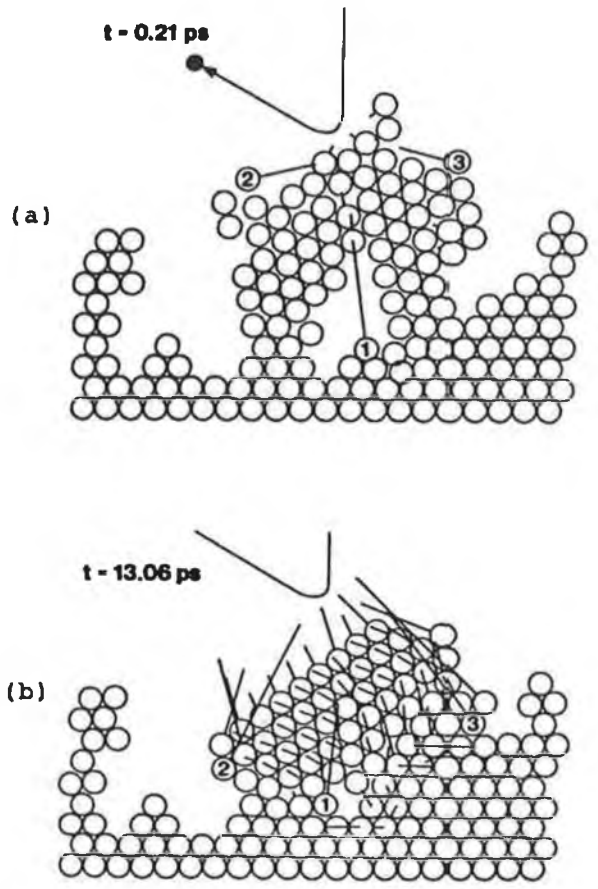

Figure 10: Shows the collapsing of voids due to impact of 100 eV Ar ion during densification of Ni film. Here 't' indicates two different times for the densification. 1, 2, 3 indicate the displacement of the atoms before and after densification [35].

The packing density, defined as the fraction of atoms occupying the first nine layers above the substrate, is shown in the figure. 11. For maximum packing density both ion energy and ion neutral flux ratio are important parameters to consider. Muller [35] performed simulation using two dimensional molecular dynamics approach to see the effect of ion to neutral ratio on the growth process.

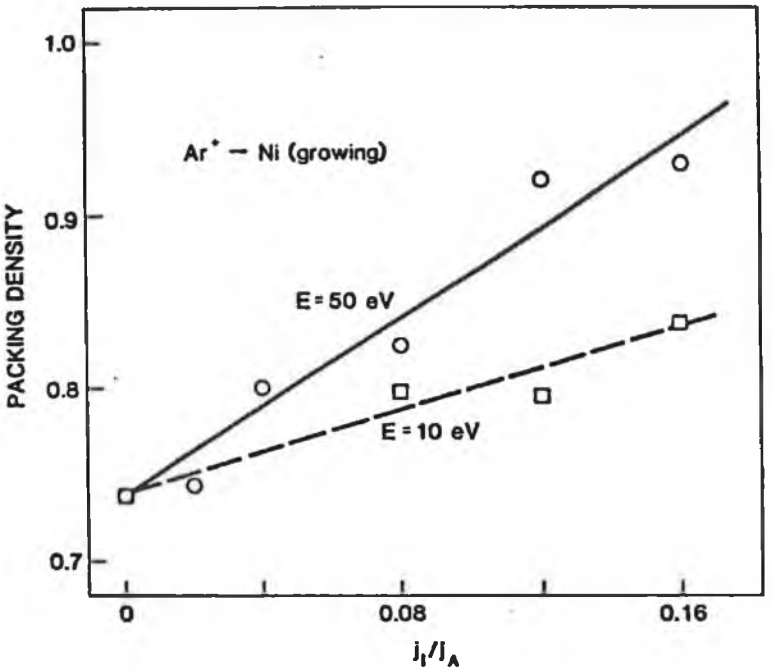

Figure 11: Packing density as a function of the ion-to atom flux ratio, J_I/J_A, for Ar ion energies of E = 10 eV and 50 eV [35].

Figure. 11 shows the effect of ion to neutral ratio on packing density. The density increases linearly with ion to atom flux ratio. For $J_I/J_A > 0.3$ at E=10 eV and $J_I/J_A > 0.2$ at E=50 eV the curves in the figure. 11 are expected to reach the maximum packing density and then stay constant. Here J_I and J_A are ion and atom flux respectively and E denotes energy of ion. Figure 12 displays the density versus ion energy for a fixed value of $J_I/J_A = 0.16$ and shows the trend of increasing density due to increase in ion energy. The curves are rather a trend to understand the process in other materials, although the experiment was done on Ni. Such trend was also observed in growing Ge films by Ar ions [36]. The density increases rapidly at low ion energies because a weakly bonded porous structure is easier to reorder and densify than a more closely packed one. This approach was justified by the experimental work of Yehoda et al [36]. Rohde [37] pointed out that the ion to neutral ratio is nearly constant for a given system geometry,

gas species and cathode material. Simply increasing the discharge current does not increase the ion flux, because neutral production during sputtering will also increase.

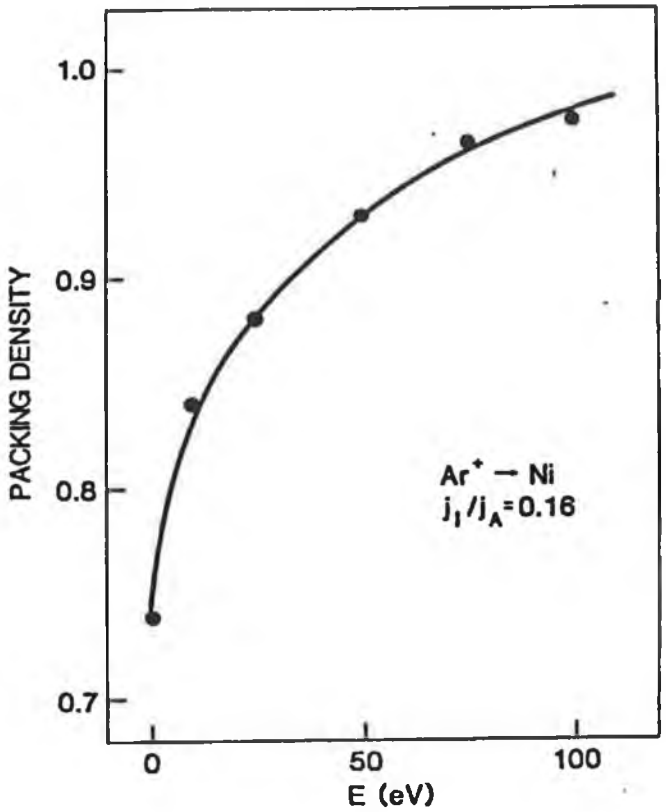

Figure 12: Packing density versus Ar ion energy E, for a fixed ion-to-atom flux ratio of J_I/J_A = 0.16 [35].

3.5 Zone Models for thin film growth

So far, species produced during sputtering and their interaction with surfaces are discussed. This section will discuss the effects of these interactions on thin film growth. The growth process very much depends on electrons, ions and neutral bombardment. These dependencies again are controlled by the system geometry, gas pressure and technique used. During the growth process the atomic movement involves four basic processes: shadowing (a simple geometric interaction between the roughness of the growing surface and the angular directions of the arriving coating atoms), surface

diffusion, bulk diffusion and desorption as mentioned by Thornton [38]. These processes can be explained in terms of surface roughness, the activation energies for surface, bulk diffusion and the sublimation energy. For many materials these energies are related [39,40] and proportional to the melting point [41]. Structure zone models proposed by Movchan and Demchishin [42] predicts three structural forms or zones as a function of T/T_m , where T is the substrate temperature and T_m is the coating-material melting point. They deposited thick coatings (0.3 to 2 mm) of Ti, Ni, W, ZrO_2, Al_2O_3 and later Fe [43] by electron beam evaporation. They pictured their model as a function of T/T_m in terms of the three zones shown in figure. 13 each with its own characteristics structure and physical properties. Although this model was developed primarily to explain the relation between microstructure and preparation conditions in the case of crystalline metallic films, there have been several reports of its application to both amorphous and crystalline ceramic films [44,45] and amorphous semiconductor films [46,47,48].

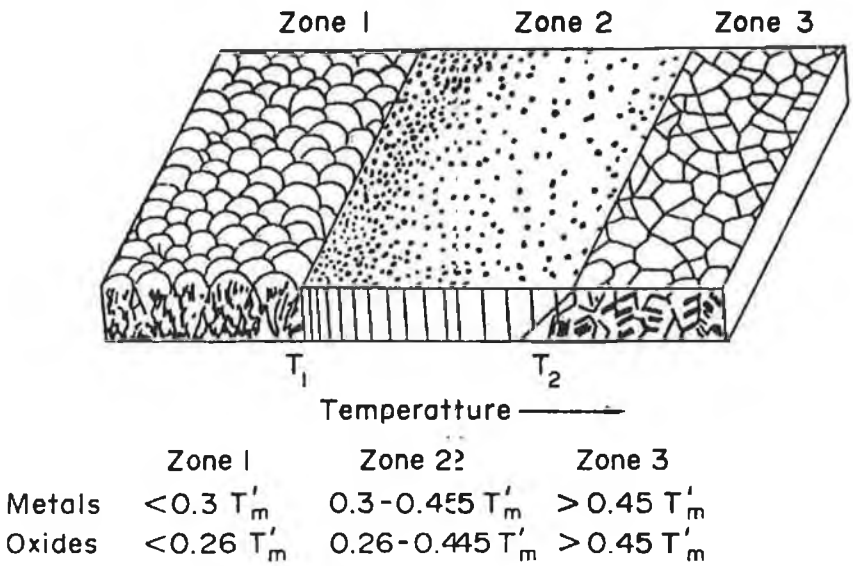

Figure 13: Schematic of Structure Zone Model by Movchan and Demchishin [42].

Zone 1 (T/T_m <0.3) consists of tapered crystals with domed tops which are separated by voided boundaries. The internal structure of the crystals is poorly defined, with a

high dislocation density. The crystal diameter increases with T/T_m, and that dependence indicates a very low activation energy and implies very little surface diffusion. Metallic deposits have good hardness but they have little bond strength.

Zone 2 ($0.3 < T/T_m < 0.5$) consists of columnar grains seperated by distinct, dense, intercrystalline boundaries; the surface has a smooth, mat appearance. Dislocations are concentrated in the grain boundary regions. Grain sizes increase with T/T_m and may extend through the coating thickness at high T/T_m. The grain width dependence on T/T_m yields an activation energy about equal to that for surface diffusion. Metallic deposits have properties similar to cast metals.

Zone 3 ($0.5 < T/T_m < 1$) consists of equiaxed grains with a bright surface. The grain diameters increase with T/T_m and yield an activation energy corresponding to that for bulk self-diffusion. The structure and properties of the coatings correspond to annealed metal.

Thronton's extended Zone model in terms of sputtering process

Thronton [49,50] added an additional axis to account for the sputtering gas (Ar) and proposed the diagram shown in figure. 14. The diagram is based on examination of 25 to 250 μm-thick coatings of Ti, Cr, Fe, Cu, Mo and Al alloy deposited on metal and glass substrates using magnetron sputtering sources.

The pronounced Zone I structure was promoted by substrate roughness, high argon pressure, and an oblique component to the deposition flux (such a flux is usually observed in hollow-cathode discharge). A transition zone (Zone T), consisting of a dense array of poorly defined fibrous grains without voided boundaries (which is specifically Thorton's finding), was identified between Zones I and II in the modified Zone model. In this case columnar grains in Zone II tended to have highly faceted surfaces. At high T/T_m the surfaces were smooth, with grooved grain boundaries. The Zone II columnar

grains increased in width with T/T_m, and wide columnar rather than equiaxed grains were often observed at high T/T_m. The working gas pressure had little influence on the substrate at high T/T_m.

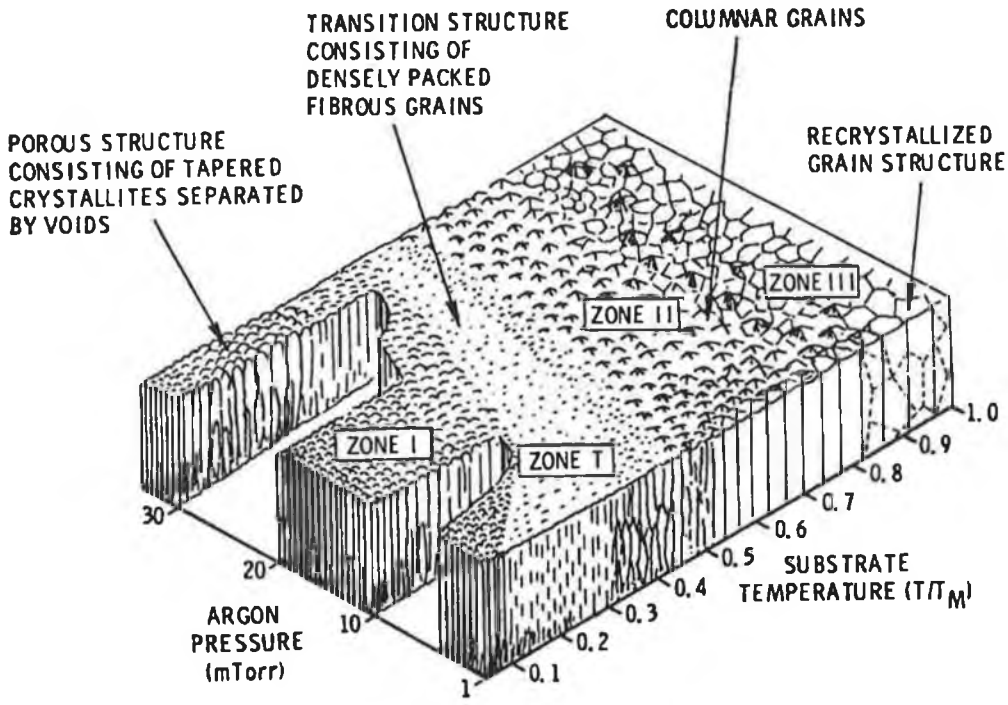

Figure 14: Schematic of modified Structure Zone Model by Thornton [49].

In summary, Zone 1 is associated with coating-flux shadowing that is not overcome by adatom surface diffusion. Shadowing induces open boundaries because high points on the surface receive more coating flux than valleys. It is caused by surface roughness which can result from the shapes of the initial nucleii, from preferential nucleation at substrate inhomogeneities, from substrate roughness and preferential growth as mentioned by Thornton [38]. This effect is pronounced when there is significant oblique component in the coating flux. At higher pressures the oblique component is enhanced by collisions. The presence of this Zone to elevated temperatures depends on the degree of substrate roughness (figure. 15.a). It is promoted, even on smooth substrates, by elevated inert gas pressures at low T/T_m (figure. 15.b). The zone 1

structure is recognised by columnar crystallites defined by open boundaries that are not influenced by heat treatment at hight T/T_m (>0.5). The Zone T structure is defined as the form taken by the Zone 1 structure in the limit of zero T/T_m on any infinitely smooth substrate. The Zone T structure is the internal structure of the Zone 1 crystallites.

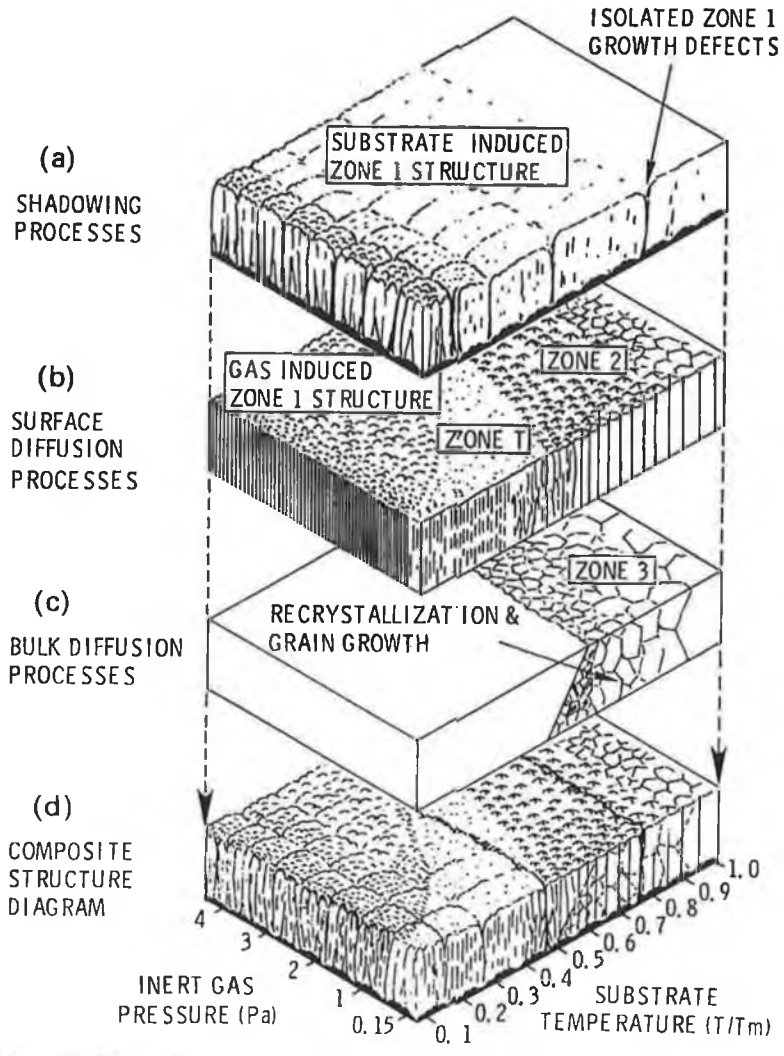

Figure 15: Schematic representation showing the superposition of physical processes that establishes structural zones [38].

It is recognised by its fibrous, poorly defined character. The range of Zone T may be different in evaporated and sputtered deposits because of the high kinetic energy of

sputtered atoms and plasma bombardment. Zone 2 is characterised by the growth due to adatom diffusion. It is generally characterised by columnar shaped crystallites which may approach a near-equiaxed shape, and which are separated by dense intercrystalline boundaries. Sometimes the growth takes the form of plateslets or needles. Zone 3 is characterised by bulk diffusion processes such as recrystallization and grain growth. Grain shape may be equiaxed or columnar, depending on structure and stress distribution formed during initial deposition. Zone 3 is recognised by dense grain and twin boundaries and by grain shapes that do not coincide with the substrate and coating surface topographies.

Comments on Zone model by others

The cause of the porous columnar microstructure of Zone 1 vapour deposited films was first illustrated by Henderson et al [51]. They treated the coating atoms as hard spheres impacting at a 45^0 angle which were allowed to relax only to the nearest "pocket" where they could make contact with previously deposited spheres. Dirks et al [52] performed similar tests for normal and angular incidence. It is interesting to note that when two impacting species of different diameter were used to simulate binary alloy deposition, the number of voids increased. Both sets of theoretical data show a tendency for columns to lean toward the incident flux. They also indicate coating density which is substantially less than that observed experimentally. This led to the suspicion that columns formation might cause low coating density. Kim et al. [53] performed a simulation in which the sticking coefficient was less than unity. The result of this simulation was a dense coating with retention of the columnar orientation, although it was hard to observe the columnar features. Here is the point of considering the transition Zone T. Although the sticking coefficient is less than unity, denser coating is observed. This model presents higher degree of structural anisotropy in these deposits than the lower density deposits.

The formation of directional columns result voided sponge-like inter and antra granular anatomy of Zone 1. This model was supported by Westwood [54]. He reported an inverse relationship between film density and sputter gas pressure in platinum films. Nakahara and colleagues [55,56] and Fabis [57] experimentally found small voids (10-50Å) near the substrate surface in the sputtered, evaporated and electroplated films.

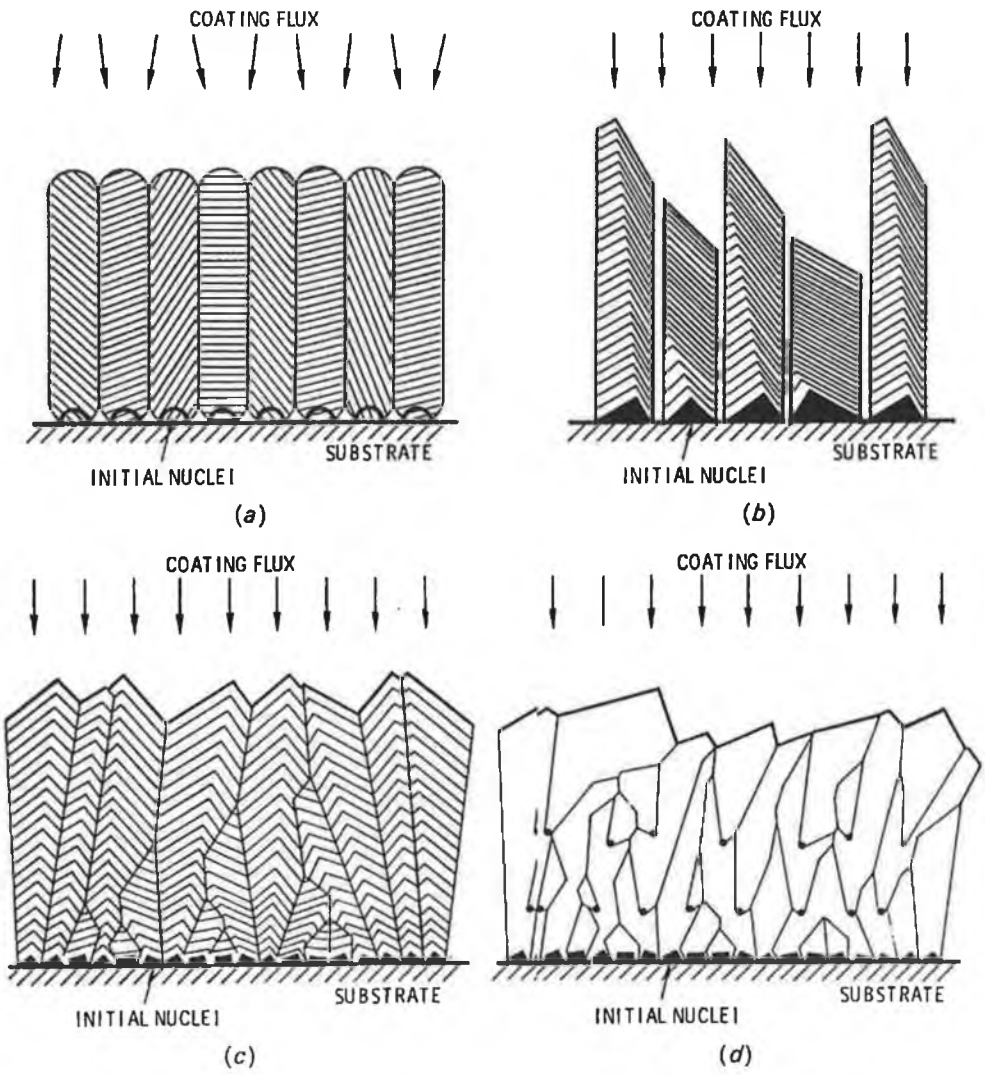

Figure 16: Two-dimensional growth structures constructed for several extreme cases of adatom surface diffusion. (a) Zero surface diffusion, unity condensation coefficient; (b) Zero surface diffusion, condensation coefficient dependent on crystallographic surface; (c) Infinite surface diffusion; (d) Infinite surface diffusion with periodic renucleation [58].

Van der Drift [58] produced a model for surface diffusion related growth process which could be a similar approach to Zone 2 growth model. Figure 16 illustrates some extreme cases in crystal growth process for two dimensional growth structures. Figure 16.a shows the case of zero surface diffusion and unity condensation coefficient. The coating flux is normal, with some side scattering assumed so that crystals are not one-dimensional. The orientation of the initial nucleii is preserved. The structure is of a Zone T form. Figure 16.b shows the case of zero surface diffusion and a condensation which depends on the substrate crystallographic surface. Here the crystal face which receives the most coating flux grows out of existence. The structure is of a Zone 1 form. Figure 16.c shows the case of infinite surface diffusion. Here the surface diffusion redistributes the coating flux, thus the effect of condensation coefficient does not make any difference in the growth process. The growth rate is assumed to be the same on all crystal planes. The direction of fastest growth is from the centre to the farthest point on the crystal. This is a dense columnar Zone 2 structure. Figure 16.d is similar to figure 16.c except that periodic renucleation is allowed. The resulting structure is still columnar.

Zone 3 is defined as the region of zone diagram where bulk diffusion has a dominant influence and thus results equiaxed grain structure. Sometimes open grain boundaries are seen in this zone. This was observed by Thornton [38] and discussed before.

Modified Zone model by Messier et al.

Messier et al [59,60] revised the structure zone model to account for the evolutionary growth stages of structure development as well as the separate effects of thermal and bombardment induced mobility. They also introduced Zone T as a subzone within the Zone 1. In original zone model by Movchan and Demchishin and the revised model by Thornton, the growth process was considered in thick film. But Messier et al. developed his model for thin to untra thin films. Thus he derived the growth process in relation to nanostructure. Their model is based on Ge, a-Ge, a-Si:H, WO_3, SiC, TiB_2, BN materials.

In their model three general structural units are recognised: nano, micro and macrocolunns and associated with nano, micro and macrovoids [46,48].

Messier et al. considered the effect of sputtered species energy on growth process. Figure. 17 shows the contribution of bombardment effect on growth process.

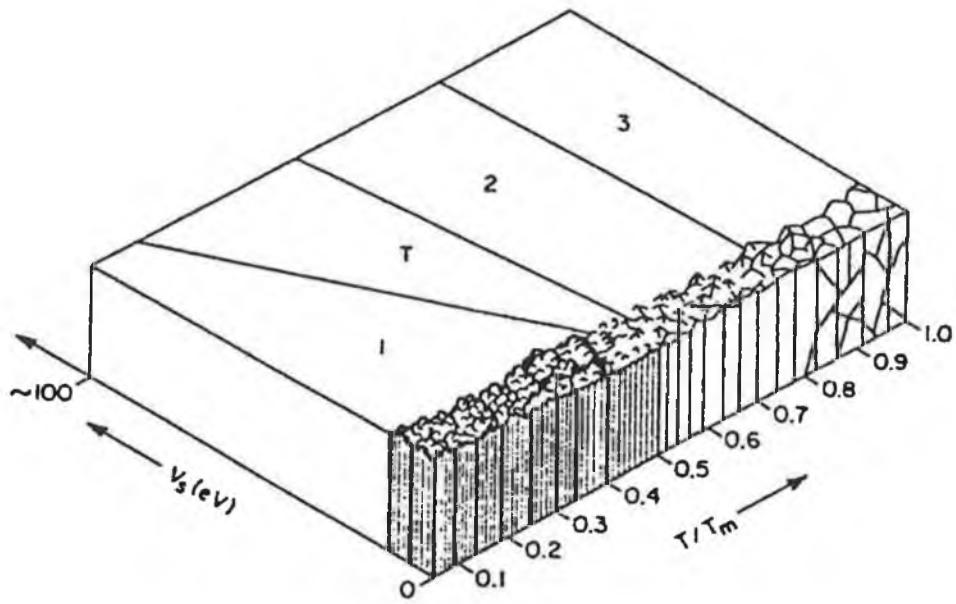

Figure 17: Modified Structure Zone Model showing the effects of both bombardment and thermal induced mobility by Messier et al. [59].

As plasma enhanced sputtering techniques are related to nonequilibrium and energetic bombardment, the original zone model needs revision. On the other hand the nature of vapour species, their adsorption-desorption nature and thus the adatom bond strength can be controlling factor for adatom mobility. These processes are generally called chemically induced mobility which is usually seen in the activated plasma process such as sputtering. Messier et al. just considered the thermal and bombardment effect on the growth process. As seen from the Figure. 17, at no bombardment the zone T is small and may not even exist. By the time sufficient activation energy (kT) can densify the physical structure and the crystal structure has developed to give large columnar grains

(zone 2). As bombardment energy increases the width of the zone T increases, primarily due to zone 1 decreasing in width while zone 2 boundary and its width remain more or less the same. In this case the physical structure can develop faster than the crystal structure since bombardment apparently leads to longer range mobility (1-10 nm) while not leading to any appreciable increase in crystal structure development.

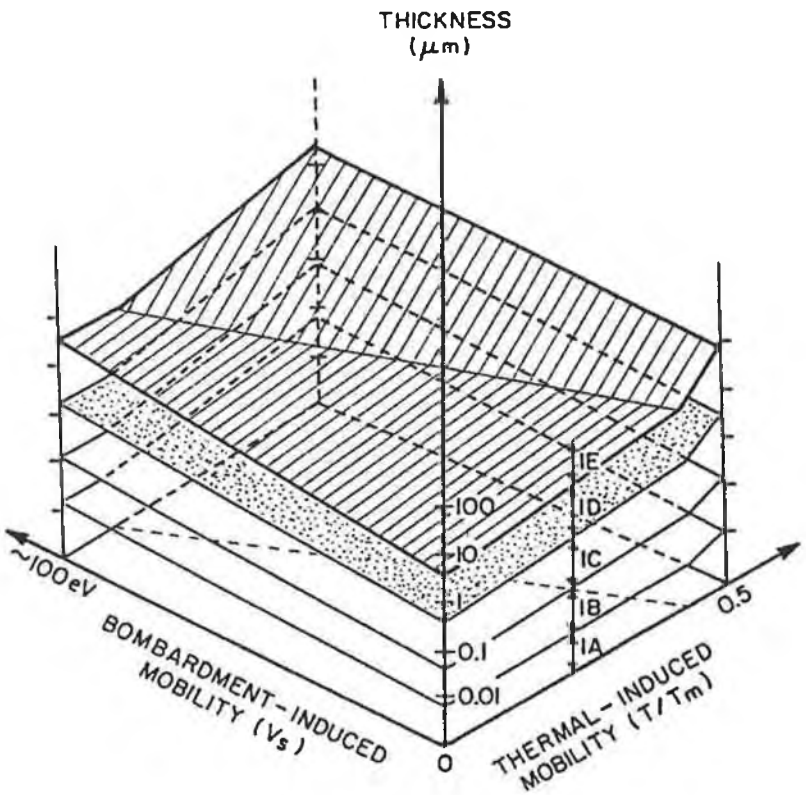

Figure 18: Revised Structure Zone Model for Zone 1 physical structure by Messier et al. [59].

Figure 18 shows their modified zone 1 structure model. In this model all the distinct levels of physical structure, column or void sizes are considered and assigned subzones 1A, 1B, 1C, 1D, 1E which correspond to characteristic column sizes 1-3, 5-20, 20-40, 50-200 and 200-400 nm respectively. Larger size columns are expected (for thicker films) and can be assigned 1F, 1G etc and so on. They pointed several important features as shown in figure 18. First, the thickness is given as a log scale since the evolution appears

to proceed in such a nonlinear fashion. Second, although the boundaries are shown as distinct planes, in fact they are continually changing and the boundaries only represent the more dominant observable changes. Third, the physical structure development is recognised to be a function of both thermal and bombardment induced mobilities and so that if either one is low then structure development is fast. Fourth, the two mobility parameters are not simply additive but act in combined way above a threshold, which is taken to be the zone 1-T boundary from figure 17.

This revised zone model does not replace the previous zone model but it recognises several important additional features, thus idealizes the present sputtered deposited thin film growth.

3.6 Film adhesion

Mattox [61] defined "good adhesion" as that the interfacial region (or nearby material) does not fail under assembly or service conditions nor at unacceptably low stress levels under test condition. Adhesion or adhesive strength of thin film is a macroscopic property and depends on the bonding across the interfacial region, local stresses and the adhesive failure mode. The failure mode depends on the type of stress developed during the growth process and also type of stress to which the interfacial region is subjected. Intrinsic stress in the interfacial region of thin film will be discussed in the later sections of this chapter. The ASTM defines adhesion as the "condition in which two surfaces are held together by either valence forces or mechanical anchoring or by both together".

Types of adhesion

Adhesion is often classified into five distinct types depending on the microstructure of the interface. Various modes of adhesion is pictured in the figure 19. In actual case most interfaces consist of more than one of these at the same time.

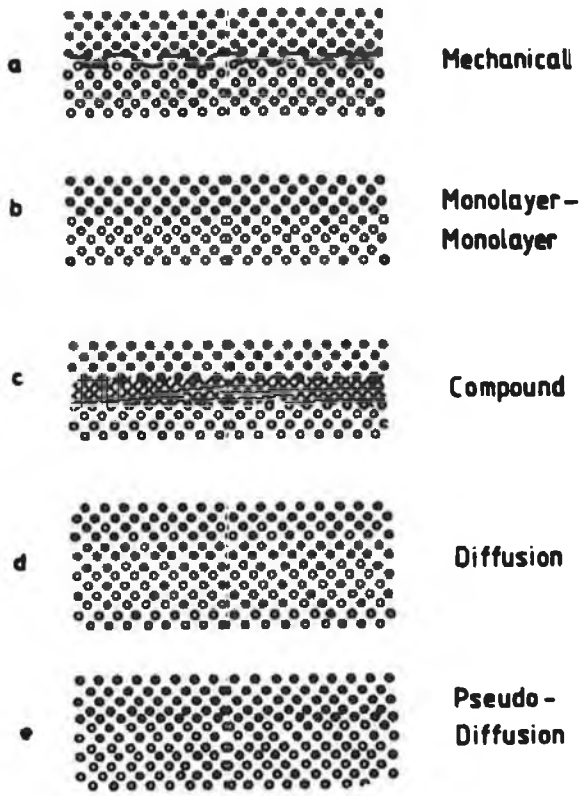

Figure 19: Classification of the various modes of adhesion after Hintermann [62].

(1) Mechanical anchoring: This type is found usually on rough surfaces. The coating materials penetrate onto the substrate and key into it. This type of adhesion is not usually seen in the thin film but is particularly important in thermal and plasma spraying where surface to be coated are precleaned by grit blasting process.

(2) Abrupt: This type is characterised by an irregular transition from the film material to the substrate material. Usually the transition region has a thickness in the range of 2-5Å. Thin gold film on NaCl is a good example of this type. Interfaces of this type form when no diffusion occurs, there is little chemical reaction, and the substrate surface is dense and smooth.

(3) Chemical bonding: These interfaces are characterised by a constant chemical composition across several atomic layers and usually is a diffusion dominated process. They result from chemical reactions between film and substrate atoms.

(4) Diffusion interface layers: these interfaces can be formed when there is at least partial solubility (interdiffusion) between the film and substrate materials. These type of interfaces are usually formed during the high temperature CVD coatings. These interfaces are brittle in nature, have Kirkendall voids and develop stress induced microcracks. Due to different diffusion rate in the film and substrate materials, voids are formed.

(5) Pseudo-diffusion interface layers: These interfaces are formed by ion implantation into the substrate with subsequent film growth. The only difference between these layers and the diffusion interface layers is pseudo-diffusion interfaces can form from materials which do not mutually diffuse. Substrate bombardment can be a controlling factor to enhance the solubility by creating point defects and stress gradients. This type can be seen in the sputtered deposited thin film.

Some major factors affecting the adhesion performance of a thin film coating is illustrated in the figure 20 which is drawn for the case of a film being peeled at the interface due to initiation and propagation of an interface fracture. The interface energy γ_I, which describes the state of electronic bonding of the interface atoms, must always be an important quantity governing interface adhesion. It is related to the thermodynamic energy of adhesion E_{ad} by the expression [63],

$$E_{ad} = \gamma_s + \gamma_f - 2\gamma_I \qquad (4)$$

where γ_s and γ_f are surface free energies for the substrate and film respectively. However, interface chemical bonding is the most important factor to be considered to attain good adhesion.

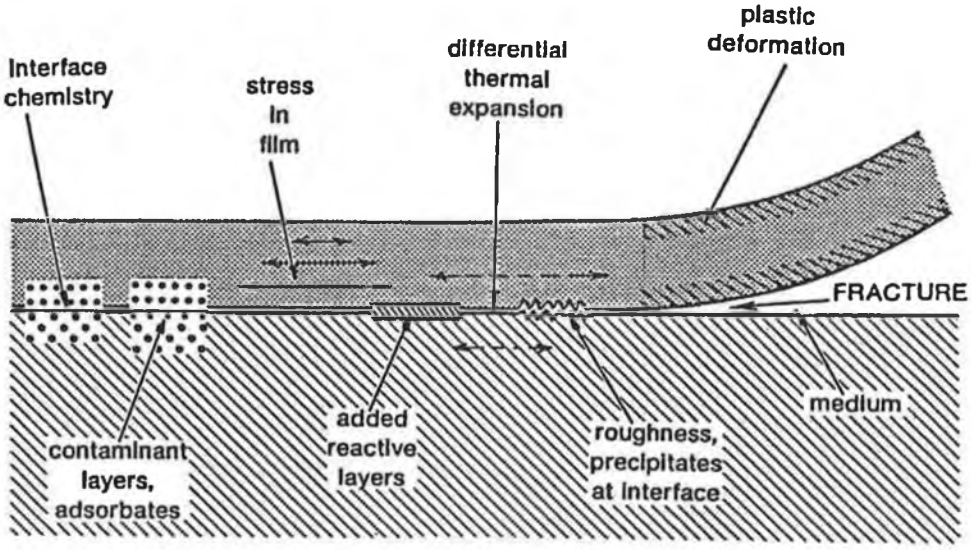

Figure 20: A schematic illustration of some major factors affecting the adhesion performance of a thin film coating on a substrate [63].

Adhesion Enhancement

Ions generally used at an energy where collisional processes dominate at the interface, is an excellent technique. However, adhesion enhancement can be done by the following ways:

(1) Substrate cleaning is essential to achieve good adhesion. To get rid of organic contaminants vapour degrease is sometimes done and an alkaline or acid rinse is necessary to get rid of inorganic contaminants. There would be intermediate water rinses. Ultrasonic baths are commonly used to preclean substrate. For rough surfaces grit blast can be used. Although the vapour degrease process is an effective one, due to environmental unfriendliness this technique is becoming obsolete.

(2) The substrate can be sputter cleaned to reveal a fresh substrate surface. *In situ* RF plasma etching of the substrate is preferable to DC since the former can etch away any remaining insulating contaminants. Sputter cleaning before deposition can alter elemental composition of the surface. Due to sputtering post-annealing of the substrate can improve adhesion. It can also form stable binary/ternary bonding during deposition. Finally it makes the substrate bonding structure disordered and thus enhance the surface to form dangling bonds.

(3) A good strategy for improving adhesion is to use an interlayer. This interlayer should bond well with the substrate and the coating material. Multiple and graded interlayer often used in PVD processes. During low temperature ($\sim 300^0$C) deposition of Titanium Nitride on steel Titanium is usually used as an interlayer. The compatibility of the coating on the substrate is a prime factor to consider for deposition. For Carbon nitride thin film deposition on tool steel a nitrided layer was used which will be discussed in later chapter.

3.7 Film Stress

Virtually all metallic and inorganic compound films are in stress of some description. This behaviour of thin film does not depend on the deposition technique. The total stress in the film is composed of a thermal stress and an intrinsic stress. The thermal stress is due to the difference in the thermal expansion coefficients of the coating and substrate materials. The intrinsic stress is due to the accumulating effect of the crystallographic flaws that are built into the coating during deposition [64].

Internal stress in thin film is an important topic to consider as it can seriously influence the film's performance. The parameter T/T_m which was discussed in the Zone Model section, is particularly important in understanding different stress related behaviour for different materials. In soft, low melting point materials such as aluminium, typical deposition conditions involve a relatively high T/T_m. Under these conditions, bulk

diffusion, which becomes increasingly important with increasing T/T_m, relaxes the intrinsic stresses and prevents their accumulation [64]. Thermal stresses on the other hand resulting from the temperature changes which occur after the deposition completed or in subsequent annealing cycles can drive these diffusion processes in such a way that material transport occurs, and holes and hillocks are produced in the films. In hard, higher melting point materials such as chromium, typical deposition conditions involve a relatively low T/T_m. Under these conditions intrinsic stresses can accumulate and dominate over thermal stresses. The film-to-substrate bond must be capable of withstanding the force produced by the integrated stress throughout the film. In the intrinsic stress case this force increases with film thickness and can be much larger than the forces provided, for example, by a typical tape adhesion test. Thus stress cracking, buckling, and poor adhesion are commonly observed when the film thickness exceeded a critical value which may be as low as several hundred angstroms.

Thermal Stresses

When a coated substrate is at a temperature that is different from its temperature during deposition, a thermal stress will be present as a result of the differences in the film and substrate thermal expansion coefficients. For the thin films used in decorative coatings, the film thickness are generally less than 10^{-4} times the substrates thickness. Under these conditions, plastic flow in the substrate can generally be neglected and the thermal stress induced in the film by the film substrate bonding is given in a one-dimensional approximation (neglecting the Poisson effect) by the following equation [65,66],

$$\sigma_{th} = E_f(\alpha_f - \alpha_s)(T_s - T_a) \qquad (5)$$

where E_f is Young's modulus, α_f and α_s are the average coefficients of thermal expansion for the film and substrate, T_s is the substrate temperature during deposition, and T_a is the temperature during measurement. A positive value of σ_{th} corresponds to a tensile stress. Temperature differences between the conditions of deposition and application, or

temperature associated with post-deposition annealing processes, can result in thermal stresses that exceed the yield strength of the film and are capable of fracturing even relatively strong coating-to-substrate bonds.

Intrinsic Stresses

The intrinsic stresses are similar to the internal stresses that are formed in a bulk material during cold working. In the cold work case, the stresses result from the strain which is associated with the various lattice defects created by the deformation. However, the density of defects that are trapped into a film during deposition can be two orders of magnitude higher than that produced by the several cold-work treatment of a bulk material [66]. At low T/T_m the intrinsic stress develops in the films are sometimes comparable with the yield strength of the material. Thus intrinsic stresses are strongly dependent on the deposition conditions. Thornton [64] tried to correlate intrinsic stresses with deposition condition. He mentioned that the energy which is stored in a film or cold-worked metal by the stresses acts as a thermodynamic driving force which tends to relax the stresses (by vacancy, interstitial, and dislocation movement) if temperature is such that T/T_m is in the range 0.1-0.3. The phenomenon is known as recovery [67,68]. At higher T/T_m (0.3-0.5) the stresses are relaxed by the recrystallization of the strained grains into new strain free grains [67,68]. Thus at substrate temperatures such that T/T_m is greater than 0.2, recovery and recrystallization relax the intrinsic stresses and reduce their accumulation in a growing film. Usually Zone 1 structure is too porous to support stresses and has rough, poorly reflecting surfaces. Recovery limits the intrinsic stresses in Zone 2. In the Zone 3 structure recovery and or recrystallization limits the intrinsic stresses. Figure 21 shows a representation of the total stress generated in a thin film as a function of T/T_m. The substrate temperature T is assumed to be greater than the final measurement temperature (room temperature), and the film thermal expansion coefficient is assumed to be greater than that of the substrate, so that a tensile thermal stress is generated (eqn. 5) when the substrate is cooled. At low T/T_m the intrinsic stress dominates over the

thermal stress. When T/T_m exceeds about 0.25-0.3 (zone 2), the recovery processes are operative so that the intrinsic component of the stress is reduced. At higher T/T_m, the thermal stress dominates. A linear increase in thermal stress with T/T_m is shown.

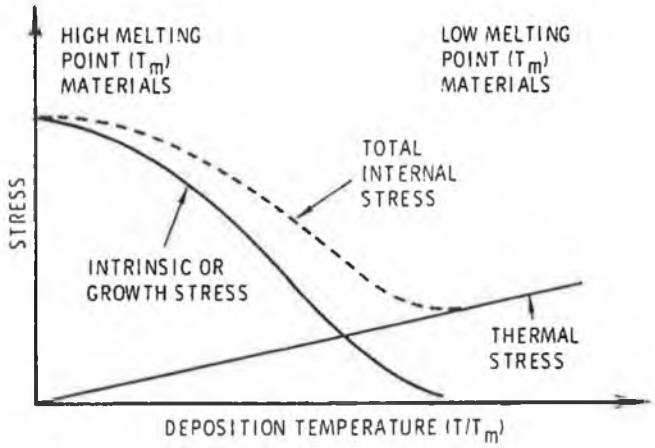

Figure 21: Schematic representation of thermal and intrinsic stress contributions [64].

Stress distribution

Stress generation in the film itself a complex phenomenon. The details of the stress distribution between a coating and substrate can be very difficult. Thronton [64] formulated a model for stress distribution in the film and the substrate. Figure 22 illustrates an idealized representation of the normal stresses across the cross-section of a homogeneous film and free standing substrate at a point far from edge. The stress distribution is determined by requirements that the sum of the normal forces and bending moments over the total cross-section be zero [65]. The first requirement means that stresses of an opposite sign must form in the substrate to balance those in the film. The stresses thus reverse sign at the interface.

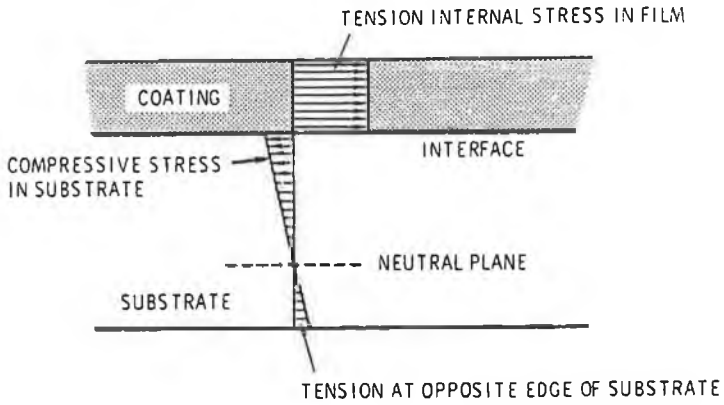

Figure 22: Schematic representation of stress distribution across coating and substrate cross-section [64].

The second requirement means that the substrate must bend to balance the bending moment which is produced by the stressed film on one of its surfaces. Thus the stresses in the substrate must change sign as shown in the figure. 22, so that the substrate stresses on the surface opposite the coating have the same sign as those in the coating. In most decorative coating cases, the film thickness is much less than that of the substrate, so that the stress in the substrate is only a very small fraction of that in the film. Under these conditions the substrate bending is negligible. Accordingly no variation in film stress, due to substrate bending, is shown in figure 23.

The intrinsic stress must become zero at a free edge of the coating, as shown in figure 23. Typically, the intrinsic stresses are relatively constant throughout the coating thickness, as shown in figure 23. Under this condition the interface shear stress is proportional to the coating thickness and to the gradient in the average intrinsic stress along the coating [69]. Thus, the interface shear stress is concentrated at the film edge, as indicated in figure 23. A de-adherence stress, which is normal to the interface and

dependent on the gradient of the shear stress, is also predicted to develop [69]. Consequently, the interface bond must withstand a shear force per unit width of the coating which is proportional to the coating thickness (integrated stress) and an associated normal force. Therefore, for a given intrinsic stress level and coating-to-substrate bonding, there is a maximum coating thickness that can be tolerated before loss of adhesion results. The consideration just described, although discussed with respect to intrinsic stresses, also apply to thermal stresses.

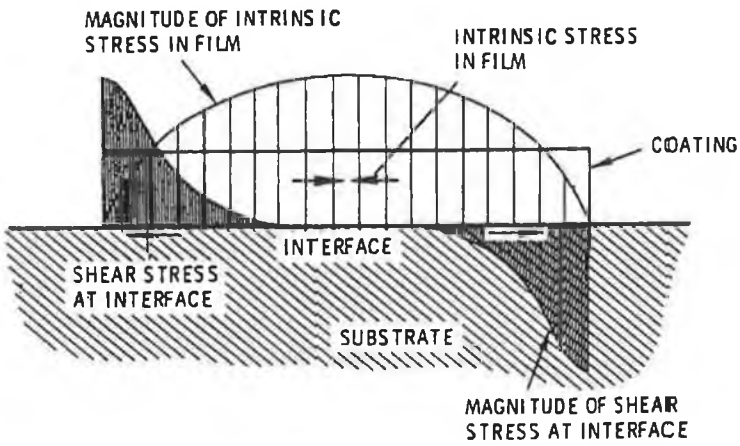

Figure 23: Schematic representation of interface shear stress distribution [64].

Effect of Sputtering on Film Stress

Although film stresses in terms of deposition temperature and microstructure are discussed so far, in sputtering technique the source geometry, angle of incidence of sputtered species, working gas pressure can play an important role in stress generation. When the coating flux is normal to the substrate, the columnar crevices are very narrow and the coating have the dense fibrous structure as discussed in (Zone T) structure zone model. As the Argon working gas pressure is raised, many of the sputtered atoms will undergo collisions with the argon during their migration to the substrate. This

collisional scattering will develop an oblique component in the coating flux, as shown in the figure. 24.

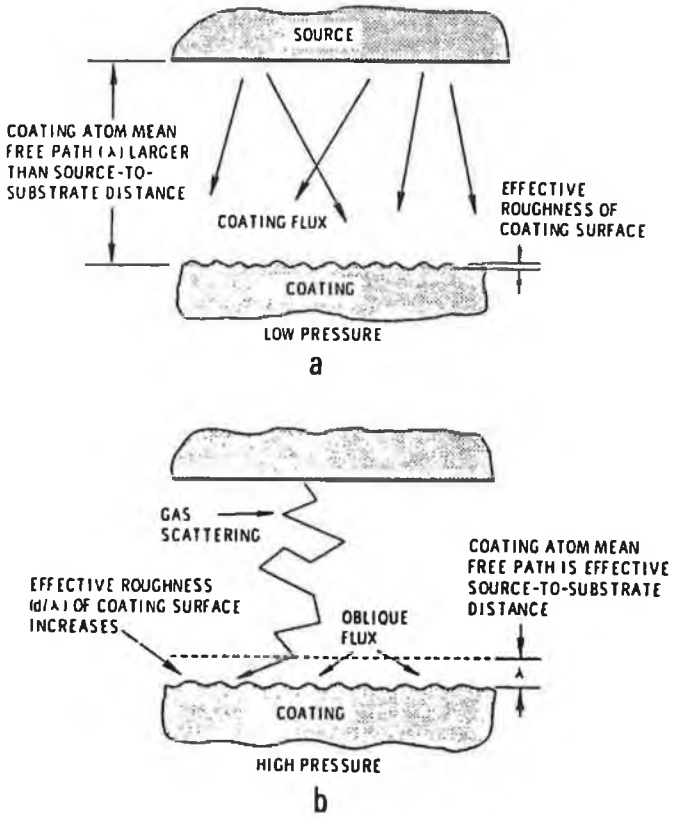

Figure 24: Schematic representation of influence of working pressure in producing oblique component in coating flux [64].

The average distance from the substrate to the point of last collision for the arriving coating atoms will be equal to the coating atom mean free path λ. As the argon pressure is increased, λ becomes smaller, and the oblique component becomes more effective. This can be explained in other way, as λ becomes smaller relative to the characteristic coating roughness d, the effective roughness of the coating surface increases, as far as its influence on the development of an open columnar structure is concerned. Porous structures are promoted at low T/T_m by an oblique component in the deposition flux,

resulting from substrate orientation or from an elevated working pressure as discussed above.

The tendency to develop an open structure is believed to be countered by bombardment of energetic argon atoms reflected at the cathode. A possible atomic peening mechanism is illustrated in figure 25. The magnitude of both the average energy and the flux of these species increases with the atomic mass of the coating material. High working pressure reduce this energy by scattering the reflected argon atoms. Thus the onset of the tensile stresses is extended to higher angles of incidence or higher pressures as the atomic mass of the coating material is increased. It is seen that the argon flux is greatest and most energetic for small scattering angles.

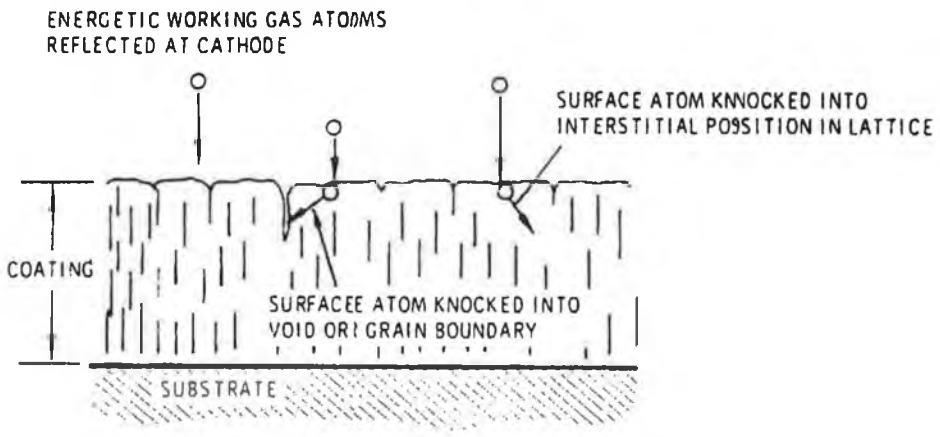

Figure 25: Atomic peening model for production of compressive stresses in sputtered coatings deposited at low working pressure [64].

In summary, this chapter introduced the principles of magnetron sputtering technique. Effect of neutral atoms, ions and electrons bombardment on film growth is also discussed which will be very helpful for understanding the carbon nitride film growth. It is also important to know how the effects of these bombardment can be manipulated to obtain control over crystalline carbon nitride film deposition. Although the structure zone model discusses metallic films growth mechanism, the model can be a good

starting for predicting the growth mechanism the of crystalline and amorphous ceramic films. Thornton and later Messier developed the model that became more suitable in terms of sputtered deposited thin film. Film growth mechanism is related to microstructure and thus dominates its mechanical properties. Even the influence of the angle of incident of sputtered atoms controls the films morphology. The relationship of sputter deposited thin film and their mechanical properties, e.g., stress, adhesion that can be controlled by suitable sputter geometry are discussed. Yu et al. [22] first produced crystalline non continuous β-C_3N_4 films by diode sputtering technique. It is seen that in the case of diode sputtering, substrates are in contact with the plasma and are therefore subjected to bombardment by the plasma electrons and ions as well as by the energetic primary electrons. This electron bombardment effect not only causes higher substrate temperature but also has effect on film growth. A possible reason of their non continuous crystals of β-C_3N_4 by diode sputtering technique can be presumed. The concurrent use of conventional magnetron sputtering technique by Kola et al. [70], Sjostrom et al. [71], Li et al. [72] for carbon nitride film deposition showed that the films prepared by this method are completely amorphous. Thus it is necessary to have a sputtering system where electrons can be completely trapped to rule out the effect of electron bombardment. Penning type opposed target geometry that will be discussed in detail in the next chapter has this control over electrons. These trapped electrons cause a higher degree of ionisation and that can be one of the key factors for crystalline carbon nitride deposition. This chapter has given significant background knowledge to analyse the growth mechanism of crystalline carbon nitride films deposited by a Penning source and its mechanical properties.

References

1. B Chapman, "Glow discharge processes: Sputtering & Plasma Etching", John Wiley & Sons, New York, 1980.

2. G.K. Wehner and G.S. Anderson, in Handbook of Thin Film Technology, L. Maissel and R. Glang edn., McGraw Hill, New York, pp. 3-1, 1970.

3. H.D. Hagstrum, Phys. Rev., 104, 317 (1956).

4. R.V. Stuart and G.K. Wehner, J. Appl. Phys., 33, 2351 (1962).

5. D. Rosenberg, G.K. Wehner, J. Appl. Phys., 33, 1842 (1962).

6. R. Behrisch, Ergeb, Exakt. Naturw., 35, 295 (1964).

7. B. Navinsek, Progress in Surface Sci., 7, 49 (1976).

8. J.A. Thornton, Proceedings 19th SAMPE Symposium, Buena Park, CA (April 1974).

9. P. Sigmund, Phys. Rev., 184, 383 (1969).

10. P. Sigmund, J. Vac. Sci. Technol., 17, 396 (1980).

11. P.D. Townsens, J.C. Kelly, N.E.W. Hartley, Ion Implantation, Sputtering and Their Applications, Academic Press, New York, pp. 111, 1976.

12. J.A. Thornton, in Deposition Technologies for Films and Coatings, R.F. Bunshah edn., Noyers Publications, New Jersey, 1982.

13. J.L. Vossen, J. Vac. Sci. Technol., 8, S12 (1971).

14. J.A. Thornton, Thin Solid Films, 54, 23 (1978).

15. H.F. Winters and E. Kay, J. Appl. Phys., 38, 3928 (1967).

16. I. Brodie, L.T. Lamont, Jr., R.L. Jepson, Phys. Rev. Lett., 21, 1224 (1968).

17. W.W. Lee and D. Oblas, J. Vac. Sci. Technol., 7, 129 (1970).

18. W.W. Lee and D. Oblas, J. Appl. Phys., 46, 1728 (1975).

19. K. Tsunoyama, T. Suzuki, Y. Ohashi, Jpn. J. Appl. Phys., 15, 349 (1976).

20. H.F. Winters and P. Sigmund, J. Appl. Phys., 45 4760 (1974).

21. A. von Engle, Ionized Gasses, Oxford University Press, London, 1965.

22. K.M. Yu, M.L. Cohen, E.E. Haller, W.L. Hansen, A.Y. Liu, I.C. Wu, Phys. Rev., 49 (7), 5034 (1994).

23. J.S. Chapin, U.S. Patent 4, 166, 018 (1974).

24. J.A. Thornton and A.S. Penfold, in Thin Solid Processes, J.L. Vossen and W. Kern edn., Academic Press, New York, pp. 75, 1978.

25. A.S. Penfold, in Handbook of Thin Film Process Technology, D.A. Glocker, S.I. Shah edn, Institute of Physics Publishing, Bristol, pp. A3.2:1, 1995.

26. R. Kulka, T. Krug, R. Ludwig, K. Wilmes, Vacuum, 41, 1958 (1990).

27. K.L. Chopra, Thin Film Processes, McGraw Hill, New York, pp. 138, (1969).

28. D.J. Ball, J. Appl. Phys., 43, 3047 (1972).

29. M. Miranov, Thin Solis Films, 46, 267 (1977).

30. A.H. Eltoukhy and J.W. Greene, Appl. Phys. Lett., 33, 343 (1978).

31. A.H. Eltoukhy, S.A. Barnett, J.E. Greene, J. Vac. Sci. Technol., 16, 321 (1979).

32. D.M. Mattox, Thin Solid Films, 18, 173 (1973).

33. D.M. Mattox, "Thin-Film Adhesion and Adhesive Failure-A Perspective", in Adhesion Measurements of Thin Films, Thick Films and Bulk Coatings, ASTM STP 640, K.L. Mittal edn., American Society for Testing Materials, pp. 54, 1978.

34. T. Takagi, Thin Solid Films, 92, 1 (1982).

35. K.-H. Muller, Phys. Rev. B, 35, 7906 (1987).

36. J.E. Yehoda, B. Yang, K. Vedam, R. Messier, J. Vac. Sci. Technol. A, 6, 1631 (1988).

37. S.L. Rohde, in Plasma Sources for Thin Film Deposition and Etching, M.H. Francombe, J.L. Vossen edn., Academic Press, pp. 235, 1994.

38. J.A. Thornton, Ann. Rev. Mater. Sci., 7, 239 (1977).

39. K.L. Chopra, Thin Film Phenomena, McGraw Hill, New York, pp. 140, 1969.

40. J.W. Geus, in Fast Ion Transport in Solids, Solid State Batteries and Devices, W. Van Gool edn., North Holland, Amsrerdam, pp. 331, 1973.

41. J.H. Brophy, R.M. Rose, J. Wulff, The Structure and Properties of Materials, 2:82, 192, Wiley, New York, pp. 216, 1964.

42. B.A. Movchan, A.V. Demchishin, Phys. Met. Metallogr., 28, 83 (1969).

43. B.A. Movchan, A.V. Demchishin, L.D. Kooluck, J. Vac. Sci. Technol., 11, 869 (1974).

44. K.H. Guenther, Thin Solid Films, 77, 239 (1981).

45. K.H. Guenther, Appl. Opt., 20, 1034 (1981).

46. R. Messier, S.V. Krishnaswamy, L.R. Gilbert, P. Swab, J. Appl. Phys., 51, 1611 (1980).

47. R.C. Ross and R. Messier, J. Appl. Phys., 52, 5329 (1981).

48. P. Swab, S.V. Krishnaswamy, R. Messier, J. Vac. Sci. Technol., 17, 362 (1980).

49. J.A. Thornton, J. Vac. Sci. Technol., 11, 666 (1974).

50. J.A. Thornton, J. Vac. Sci. Technol., 12, 830 (1975).

51. D. J. Henderson, M.B. Brodsky, P. Chaudhari, Appl. Phys. Lett., 25, 641 (1974).

52. A.G. Dirks and H.J. Leamy, Thin Solid Films, 47, 219 (1977).

53. S. Kim, D.J. Henderson, P. Chaudhari, 47, 155 (1977).

54. W.D. Westwood, J. Vac. Sci. Technol., 11, 466 (1974).

55. S. Nakahara, Thin Solid Films, 45, 421 (1977).

56. S. Nakahara, K. Kuwahara, A. Nishimura, Thin Solid Films, 72, 297 (1980).

57. F.M. Fabis, Thin Solid Films, 128, 57 (1985).

58. A. Van Der Drift, Philips Res. Rpt., 22, 267 (1967).

59. R. Messier, A.P. Giri, R.A. Roy, J. Vac. Sci. Technol. A, 2(2), 500 (1984).

60. R. Messier and J.E. Yehoda, J. Appl. Phys., 58(10), 3739 (1985).

61. D.M. Mattox, in Adhesion and Surface Preparation, Deposition Technologies for Films and Coatings, R.F. Bunshah edn, Noyes Publications, New Jersey, pp. 63, 1982.

62. H.E. Hinterman, in Wear and Corrosion Resistant Coatings by CVD and PVD, H.K. Pulker edn., Expert Verlag, pp. 56, 1989.

63. J. Baglin, in Interface Structure and Thin Film Adhesion, Handbook of Ion Beam Processing Technology, J.J. Cuomo, S.M. Rossnagel, H.R. Kaufman edn., Noyes Publications, New Jersey, pp. 279, 1989.

64. J.A. Thornton, Thin Solid Films, 171, 5 (1989).

65. R.W. Hoffman, in The mechanical properties of non-metallic thin films, Physics of Non-metallic Thin Films, NATO Advanced Study Institute Series, B-14, Plenum, New York, 1970.

66. K.L. Chopra, Thin Film Phenomena, McGraw Hill, New York, 1969.

67. A.B. Guy, Elements of Physical Metallurgy, Addison-Wesley, Reading, MA, 1959.

68. P.G. Shewmon, Transformations in metals, McGraw Hill, New York, 1969.

69. R.A. Hunt and B. Gale, J. Phys. D, 5, 359 (1972).

70. P.V. Kola, D.C. Cameron, B.J. Meenan, K.A. Pischow, C.A. Anderson, N.M.D Brown and M.S.J. Hashmi, Surface and Coatings Technology, 74-75, (1995), 696.

71. D. Li, X. Chu, S.C. Cheng, X.W. Lin, V.P. Dravid, Y.P. Chung, M.S. Wong, W.D. Sproul, Appl. Phys. Lett., 67 (2), 203 (1995).

72. H. Sjostrom, L. Hultman, J.-E. Sundgren, S.D. Hainsworth, T.F. Page, G.S.A.M. Theunissen, J. Vac. Sci. Technol. A 14 (1), 56 (1996).

Chapter 4

Penning Source: A New approach for Carbon Nitride Thin Film Deposition

Initially a few groups [1-9] tried to grow carbon nitride films by conventional magnetron sputtering technique, but the nitrogen concentration of the films were very low and the films properties showed to be amorphous in nature. To increase the nitrogen incorporation and its effect on crystalline features in the C-N film was the motivation for using a Penning source. There are quite a few points to be considered for the production of β-C_3N_4. The degree of ionisation of the reactive species, the N_2^+/N_2, C/N_2^+ ratios, elimination of energetic electron bombardment and low deposition temperature are to be considered for successful continuous crystalline β-C_3N_4 films. Considering all these features a Penning-type opposed target DC sputtering technique was used for crystalline carbon nitride thin film deposition. The chapter discusses the plasma characteristics, magnetic field theory, I-V characteristics of this source.

4.1 Historical Background of Penning Source

The Penning source [10] is one in which *two opposing cathodes have a magnetic field perpendicular to the cathode surface* [11]. J. Murphy [11] mentioned that *secondary electrons emitted during sputtering are in the main constrained to reside within the volume between the cathodes*. Thus an intense discharge which is sustainable down to low pressures can be ignited. The motivation for studying this kind of geometry is a belief that higher degree of ionisation in the plasma at low operating pressure ($<5\times10^{-4}$ mbar) represents a way forward for magnetron sputtering technology for Carbon Nitride thin

film deposition. Although this system is new for carbon nitride thin film deposition, Harper [12] and Naoe et al. [13] used sources based on this geometry. Later Window et al. [14] described some useful features of a similar sputtering system based on this geometry.

Naoe et al. [13] described an apparatus shown in the figure. 1. Their motivation

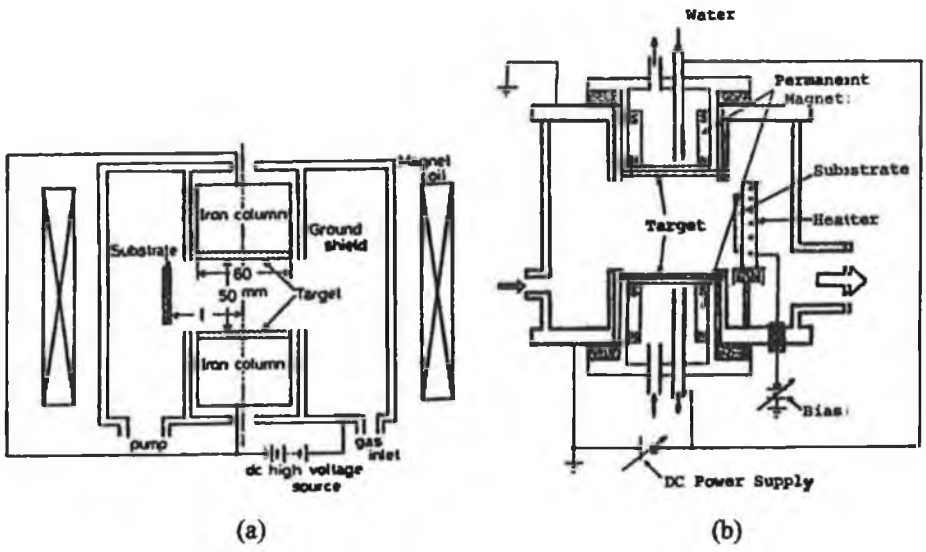

Figure. 1: (a) Schematic of the original Penning source from Naoe et al. [13]. Here a solenoid was used to produce the magnetic field. (b) Schematic of a later version of the Penning source of Naoe et al. In this case a ring of permanent magnets have replaced the solenoid. This arrangement gives better target utilisation.

for using this source was the need to achieve reasonable deposition rates from a ferromagnetic target material.

M.J. Murphy [11] reported that for adequate ferromagnetic deposition rates in conventional magnetrons it is necessary to use very strong magnets to saturate the target thereby reducing its permeability and/or use a very thin target. He also mentioned that these purposes require the establishment of a suitably strong transverse magnetic field component B_x above the target surface. By constructing a Penning type source Naoe et

al overcame this difficulty since the plasma discharge in this device depends solely on the perpendicular B_y component of magnetic field for confinement. Later they [15,16,17] went on to sputter ferromagnetic materials using a permanent magnet design. One variation is shown in figure 1(b). Better target utilisation is one of the advantages of this source. The magnetic field is much weaker mostly because of the greater inter-magnet distance of 14 cm. This was not a serious concern because at 10-15mT it is still sufficient to confine secondary electrons and prevent substrate overheating. This was important to Naoe et al. because their early work [13,15,16] aimed to deposit onto plastic polyimide film substrates with an eye to recording media applications. Maximum deposition rates were an impressive 0.4μm per minute. The lowest working pressure mentioned is $3x10^{-3}$ mbar [13].

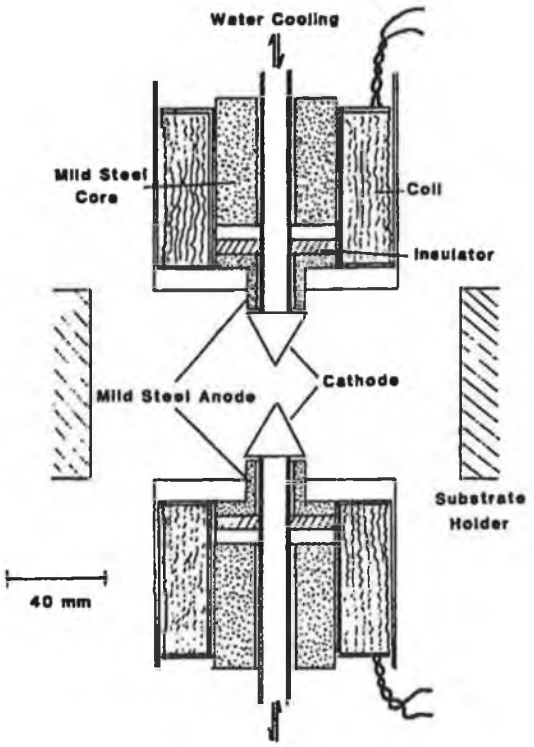

Figure 2: Schematic of the Penning deposition system designed by Window et al. The conical cathodes are used to direct the flux in the direction of the substrate.

Window et al. [14] were interested to enhance ion bombardment at the substrate while maintaining the high deposition rate of the conventional sputter magnetron. In their own words the aim was to produce *"an intense plasma which extends well away from the cathode surface and close to the substrate surface"*. However they managed to create a source which was capable of providing 0.4 ions per deposited atom at substrate distance of 72 mm [14]. Figure 2 shows the source which they used to achieve the order of 0.1 ions per deposited atom higher than can be achieved by using conventional magnetrons.

Although Naoe et al. [13,15,16] were concerned to deposit ferromagnetic materials using the penning source, a diversion was seen when this type of source was used [17,18,19] to achieve high rate deposition of aluminium oxides by AC discharges. After that no application was reported for materials deposition using sources based on Penning geometry. In 1996 M.J. Murphy [11] came up with the idea to build a sputtering source using Nd-Fe-B permanent magnets based on Penning geometry. With this system the lowest operating pressure could be $1x10^{-4}$ mbar which is two orders of magnitude lower than the system built by Window et al. Furthermore the discharge power is at least an order of magnitude higher and the most important feature, magnetic field strengths up to ten time greater than was used in the apparatus of Window et. At. Thus this source works in a different regime to the device described by others [13,14]. Later Murphy and coworkers [20] applied this apparatus for the production of carbon nitride material. It is seen that the use of Nd-Fe-B magnets ensures a very high flux density in the inter-target region. The electrons therefore experience strong magnetic confinement between the two cylindrical targets leading to very intense ionisation in the plasma and a high ion flux at the substrate. The characteristic of this system for Carbon Nitride thin film deposition will be discussed in detail in this chapter.

Although the source has some limitation, such as, the deposition rate from the source will fall away rapidly with distance, this is true for other commercially very successful sputtering source or even electron beam evaporation techniques, i.e Balzers evaporators, as well.

However, the characteristic of this source will be given for Carbon Nitride thin film deposition which is of interest. The chapter will give theoretical background for the operation of this source. Plasma diagnostic for the plasma generated by this source is given. I-V characteristics will also be presented to see the ion current characteristics of this apparatus during the Carbon Nitride thin film deposition.

4.2 Description of the Penning Source used for Carbon Nitride Thin Film deposition

A schematic of the Penning Source is given in Figure 3. Features are the very strong NdFeB magnets positioned behind the 12cm diameter targets, efficient forced water cooling of the target, use of Viton temperature resistant O-rings near the target and use of a Teflon sheet and Nylon bushes to electrically isolate the target from the grounded outer body of the device (Figure 4). Figure 3 also shows the schematic positioning of the source within the vacuum chamber and illustrates the resulting plasma. It can be seen that the Penning Sources can be moved independently of one another so that the inter target distance can be varied. An additional option is to change the magnetic field by either changing the target thickness, moving the magnets within the Penning Source, reducing the number of magnets behind each body, altering the inter magnet spacing or a combination of one or more of these techniques. The substrate holder is mounted to the side of the device and can be electrically biased. A full description of the practical design of the Penning source is given by M.J. Myrphy [11].

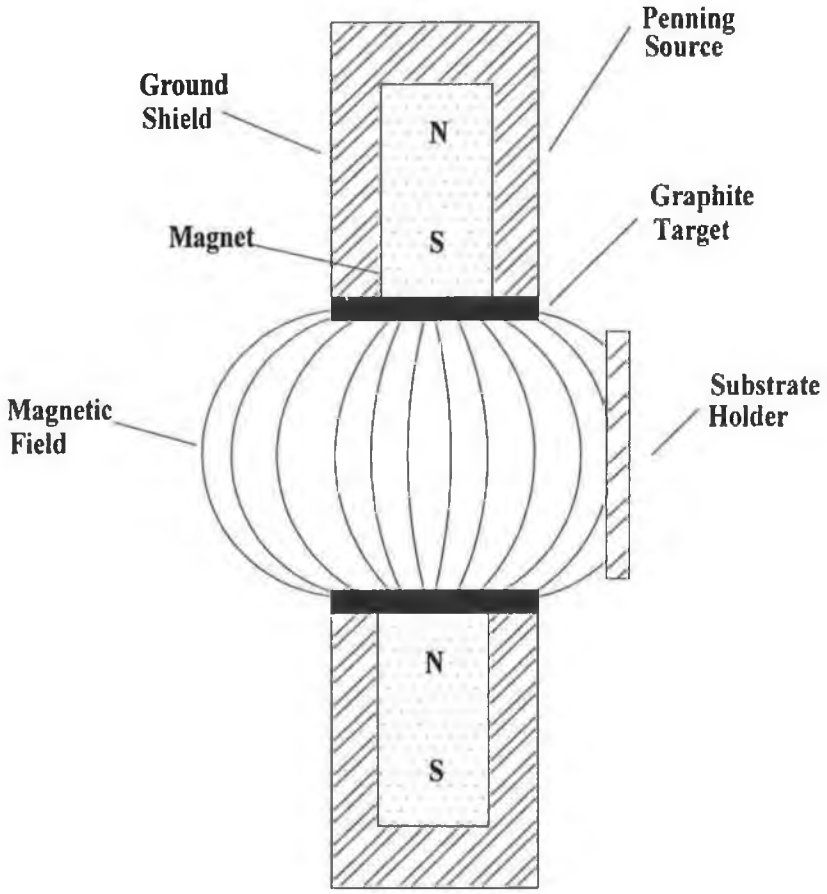

Figure 3: A schematic of the Penning Source within the vacuum chamber.

Figure 4: (a) Different component of the Penning-type source. From the left, (1) steel ground shield, (2) Aluminium magnetron body, (3) Nd-Fe-B magnet placing on an aluminium stage, (4) a Teflon plate for electrical isolation (at the bottom of the magnet stage).

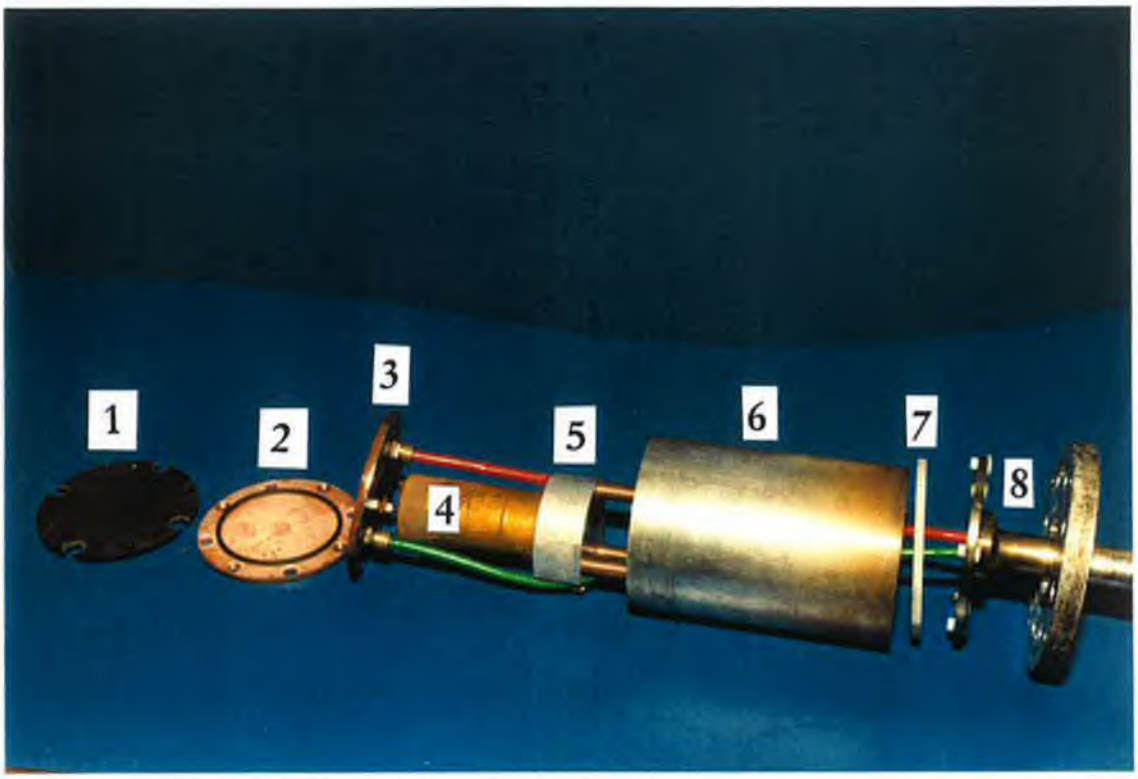

Figure 4: (b) A complete arrangement of different components of a Penning source. From left (1) Graphite target, (2) copper backing plate with O-ring, (3) copper cooling plate with is connected with an electrical cable and water inlet (red nylon tube) outlet (green nylon tube), (4) Nd-Fe-B magnet, (5) magnet stage, (6) magnetron body, (7) Teflon plate, (8) bottom plate of the magnetron and corresponding feedthrough.

4.3 The sputtering chamber and accessories

Vacuum Chamber

The vacuum chamber with accessories is shown schematically in figure 5. The chamber comprises a top plate (750mm diameter x 25mm) and a bottom plate (750mm dia. x 25mm). The effective height and diameter of the chamber is 660mm and 650mm respectively. The chamber was originally designed for running a conventional magnetron sputtering system. Thus the chamber still has 4 magnetron ports (330x184 mm each). The chamber has 8 rotatable shutter ports (50.8 mm dia.), 4 plasma emission spectrometer ports (50.8mm dia.), 1 thermocouple feedthrough flange (KF25), 1 high vacuuum port (200mm dia.), 1 backing line port (KF40). There are 1 KF40 and 1 KF50 viewports, 1 KF25 optical pyrometer port. Two Penning type magnetrons are inserted inside the chamber, one from the top and other from the bottom. The flanges are all O-ring sealed , using either Viton or Nitrile elastomers. KF clamping arrangements with various dimensions were employed to facilitate the sealing for various flanges and apparatus. The chamber was fabricated using non-magnetic AISI 304 stainless steel. It is a double skinned wall to enable the circulation of water (for heating or cooling) when necessary. A detailed drawing of the chamber is given by P.V. Kola [21].

The chamber top plate and walls are usually raised by means of a pulley system in order to load substrates and other maintenance purposes.

Accessories

The chamber is evacuated using a varian VHS-6 diffusion pump (2400 l/s) and backed by a Varian SD-700 rotary backing pump (765 l/min). A VAT control Gate valve (series 64) was used to control the diffusion pumping. The roughing and backing lines are controlled by Varian (NW40, A/O) Block valves. These valves are electro-pneumatically controlled and is actuated by an air compressor (~5 bar). The backing

line is filtered by using a foreline trap (Model BHD, S/N 28N052) in between the rotary and diffusion pumps. Rechargeable Zeolite molecular sieve was used in the foreline trap.

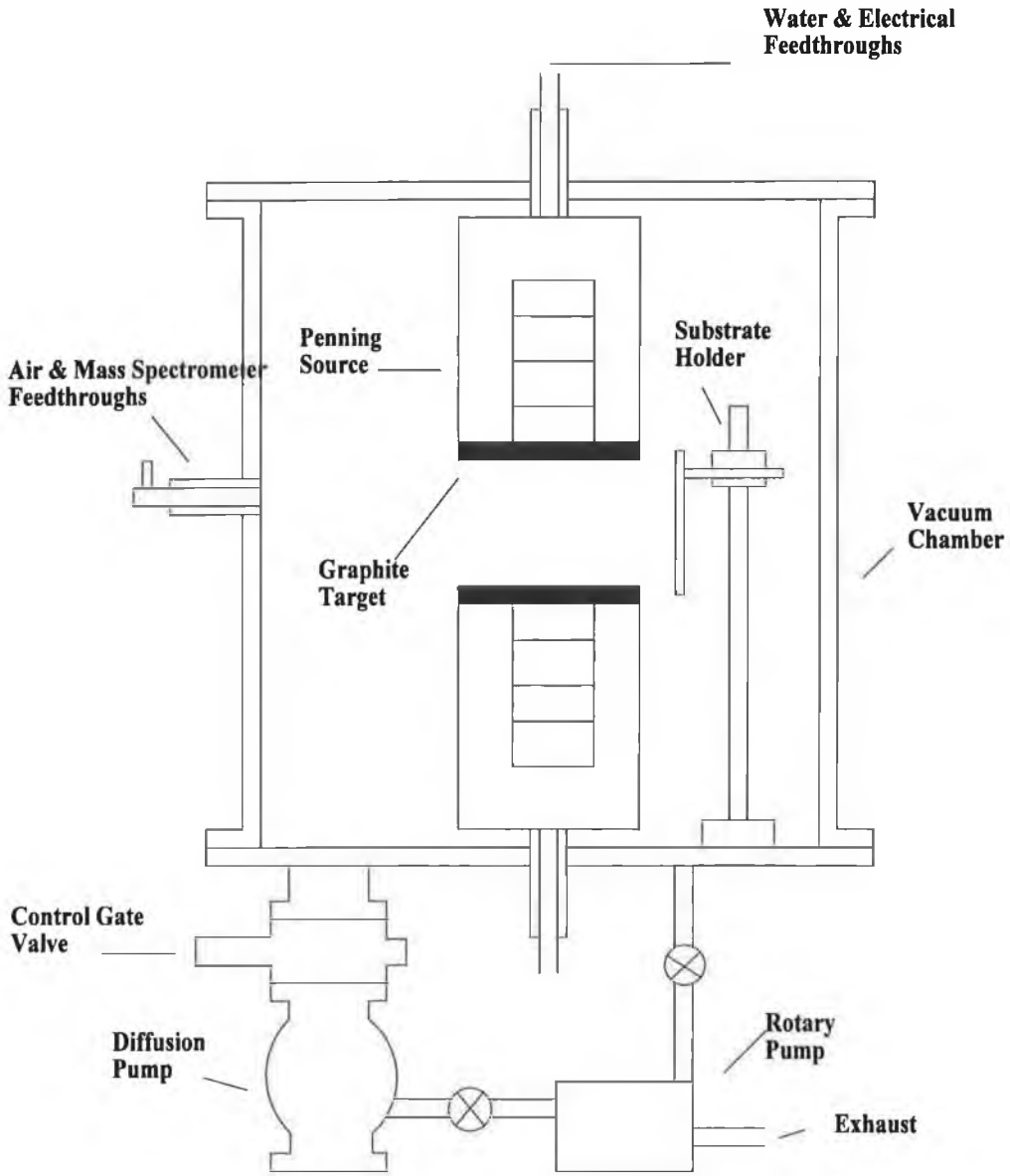

Figure 5: Schematic of the Penning Source within the vacuum chamber and accessories.

A residual gas analyser (Spectra Vacscan, Leda-Mass product, UK) was used for gas analysis and leak detection. A Varian V60 Turbomolecular pump (65 l/s) is sometimes used to evacuate the chamber to maintain the working pressure of the spectrometer. Advanced Energy MDX 5kW Magnetron Drives are used to drive the Penning Source. In addition, an Advanced Energy RFX 1250 RF supply with an automatic matching unit was used for biasing and argon sputter cleaning of substrates. An advanced Energy RFX 600 was also used for this purpose as an alternative.

The flow rates of both working and reactive gas were controlled by a Tylan mass flow controller (type FC280A) and a Tylan mass flow meter (type FC260) respectively. The gas flows were controlled and monitored by a Tylan (RO28) flow control unit. The capacity of both the meter and controller was 100sccm. The total pressure of the chamber was monitored by the use of Edwards Penning (type CP25-K, model D145-37-000) and Pirani (type PRL 10, model D021-58-000) gauges which were controlled by an Edward Pirani-Penning controller (type 1005). Another Pirani gauge (type PRM 10, model D021-66-000) monitored the pressure on the backing line. All valves were electro-pneumatic.

4.4 Carbon Nitride Thin Film Deposition

Carbon Nitride films were grown on polished n-type (100) silicon substrates by the Penning Source as shown schematically in figure 3. For these depositions the inter-target distance was 10cm and the target diameter was 12 cm. The substrates, which were unheated, were placed parallel to the axis on the centre line between the targets and 13.6 cm away from it. The substrates were clamped on a 1.5 mm thickness stainless steel substrate holder. Prior to clamping these substrates were ultrasonically cleaned in acetone and methanol for 30 minutes before loading. Prior to deposition, the substrates were Ar^+ sputter etched *in situ* to remove surface contamination for 10 minutes at a pressure of 1.5×10^{-4} mbar using a 13.56 MHz RF supply which gave a substrate bias of -450 V. The background pressure during deposition was 1×10^{-3} mbar and typical target

power was ~ 13 $W.cm^{-2}$. The temperature varied from 120°C after sputter cleaning to 325°C after deposition. The sputtering targets were graphite of 99.95% purity and the sputter gas was a mixture of argon and nitrogen of variable composition. The gas purity was 99.999% in each case.

Temperature profile during deposition

A "K" type thermocouple was used to measure the growth temperature. The measurements were taken in two ways. The first temperature was recorded after sputter cleaning by Ar at ~-450 V bias for 10 mins. At that time the temperature was recorded 120°C. Then the deposition was started and -50V bias voltage was employed during this time. The temperature effect due to -50V bias was very low as compared to the exposed plasma temperature. As most of the samples were grown for 5 and 30 minutes, two separate temperature readings were taken for those deposition times. For 5 minutes grown samples the temperature was 273°C and for 30 mins grown samples the temperature was 320°C after deposition. However a temperature profile was plotted (Figure 6) during film growth for 30 minutes. This profile was taken without any pre-cleaning treatment.

Post-Annealing treatment

Post-Annealing studies were carried out at temperatures up to 600°C at a pressure of ~10^{-5} mbar with a diffusion pumped system. Above 625°C the film structure became disrupted and they became mechanically altered therefore a limit of 600°C was put on the annealing studies. The post-annealing system is shown in the figure 7. Samples were loaded on a Tungsten bench. The temperature was controlled by a variac with ±10°C accuracy and a "K" type thermocouple was used to monitor the temperatures. These post-annealing experiments were done in an Edwards evaporation system. The system comprises a vacuum bell jar which can be evacuated by a diffusion pump.

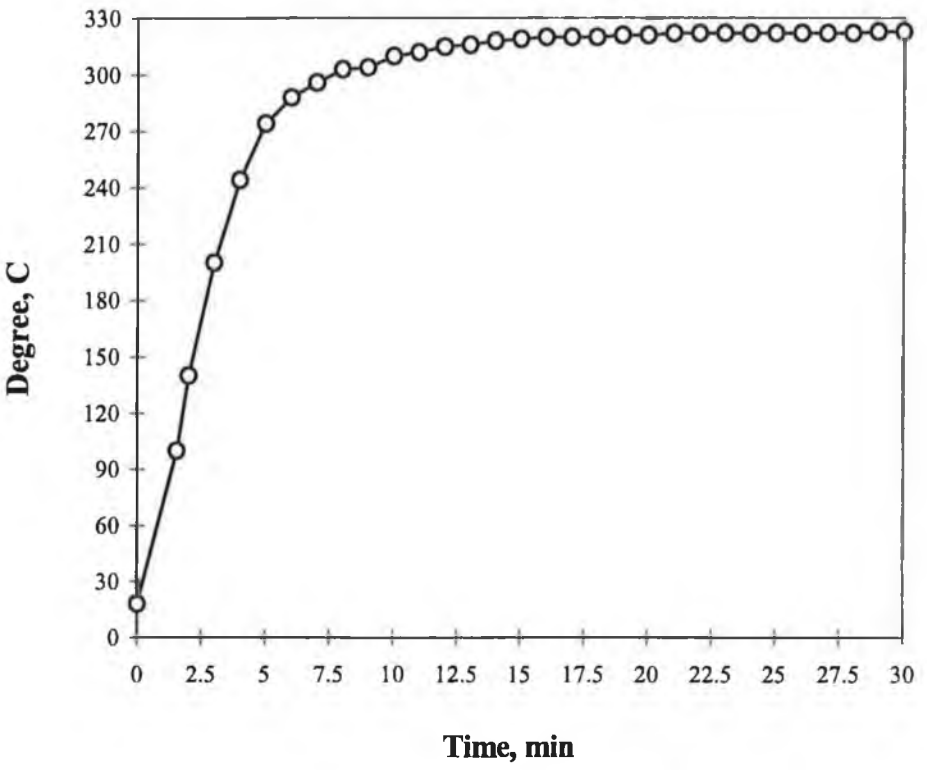

Figure. 6: Temperature profile during the film growth. The deposition parameters are: Current 3.0A, 1050V and -50 bias voltage. Deposition pressure was $1x10^{-3}$ mbar.

4.5 Magnetic fields in the Opposed Target Penning Source

It is important to discuss the magnetic field characteristics before going to detail discussion in carbon nitride thin film deposition. Because the growth mechanism of this film can be explained by the interaction between the species produced by the source and the substrate. A detailed derivation of the equations for magnetic field calculation is given by M.J. Murphy [11], therefore the section will only introduce the equations for ease of understanding of the effect of magnetic field of this system on carbon nitride film deposition. Thus a review of the magnetic field theory for the system is required.

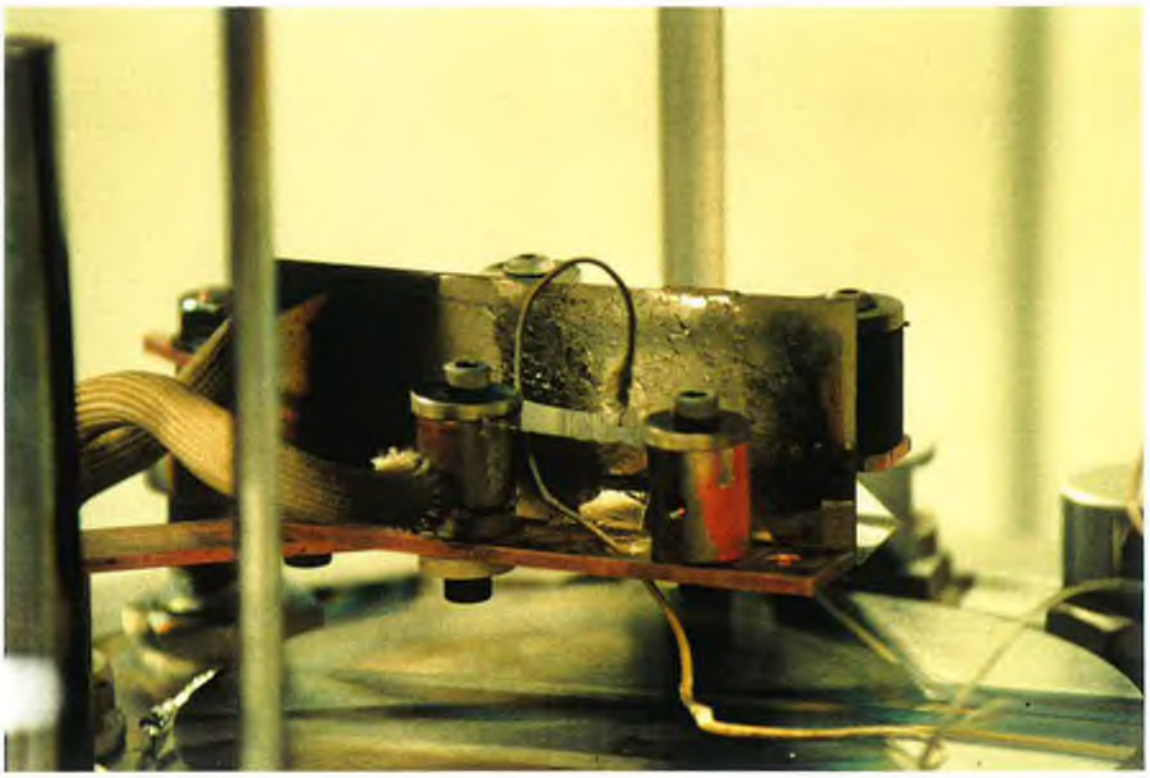

Figure 7: (a) The Tungsten stage where samples are placed. A K-type thermocouple tip is placed on the heating stage. The tip directly contacts the film surface to monitor exact film temperature.

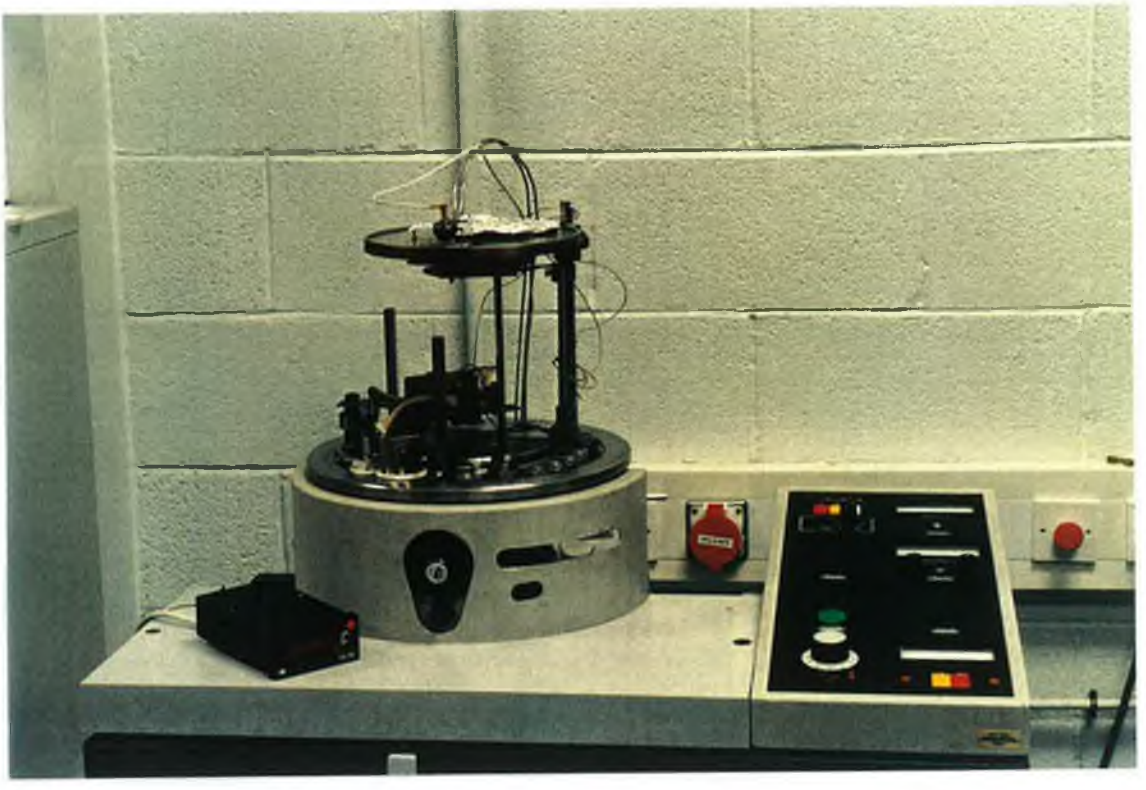

Figure 7: (b) Edwards evaporation system (without cover). The system was used as a post post-annealing chamber.

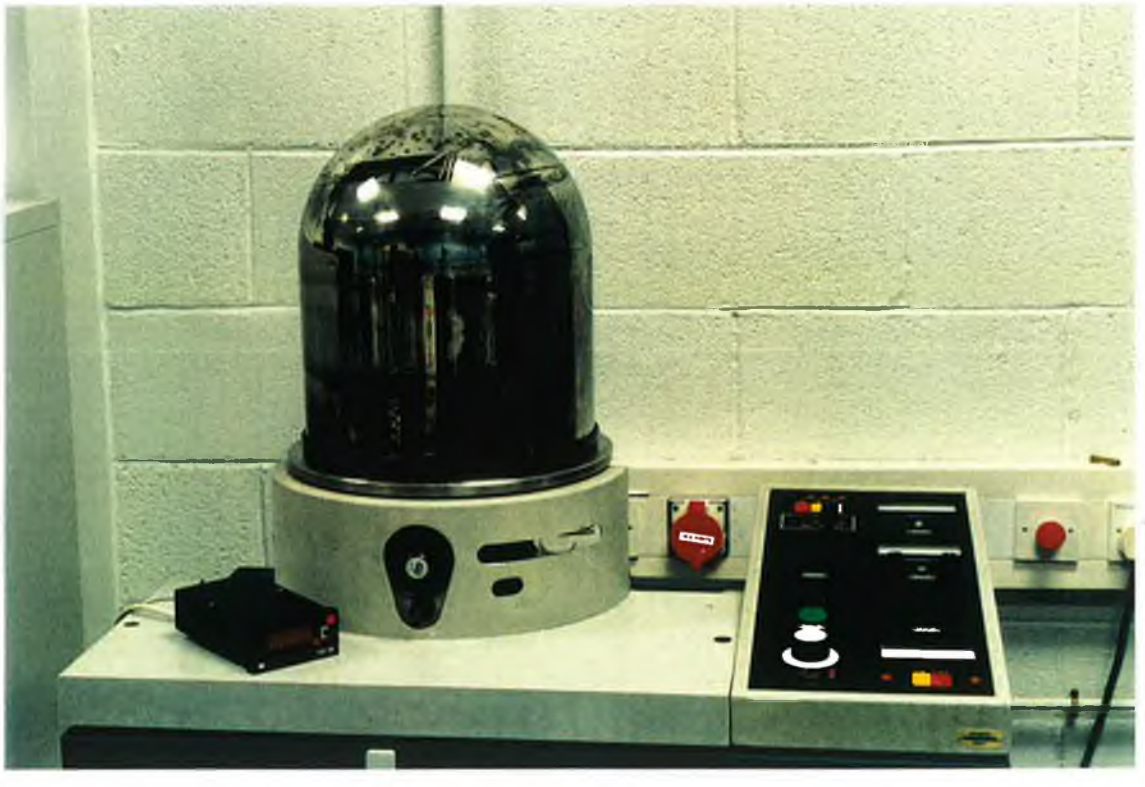

Figure 7: (c) The complete post-annealing system with cover (bell jar).

In order to design the source the magnetic field which exists within the device was calculated by slightly adapting equations given by Durand [22]. The results describe the magnetic flux, the radial component of magnetic field and the axial component of magnetic field for a single pole of a cylindrical magnet. The magnet is assumed to have a permeability equal to that of air and to be unchanged in the presence of external magnetic fields. This holds good for many rare earth and some ferrite magnets. Since the Penning source essentially contains two identical axisymmetric cylindrical magnets the overall expression for the flux and magnetic field is given by superimposing the contributions from each of four poles. Figure 8 shows the component magnetic fields at the surface of the target.

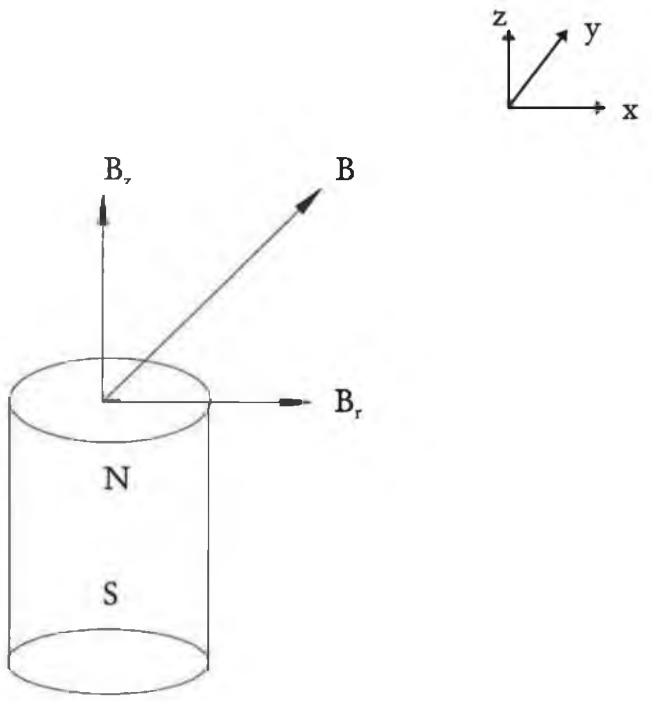

Figure 8: Schematic of the components of the magnetic field at the surface of the target.

For a single pole the flux is given by [11]

$$F(R,z)=\frac{M}{4\pi}\left\{1+\frac{\varepsilon}{2}\left(1-\varepsilon^{*}\right)\left(\frac{R^{2}}{a^{2}}-1\right)\right\}-$$

$$\frac{aB_{rem}}{\pi}\frac{R\cdot\left(z-z_{0}\right)}{r_{1}}\left\{\frac{1}{m}\left(K(m)-E(m)\right)+\left(\frac{1}{n}-1\right)\left(K(m)-Pi(n,m)\right)\right\} \tag{1}$$

The expression for the radial component of magnetic field is given by

$$B_{r}(R,z)=\frac{B_{rem}}{2\pi}\frac{r_{1}}{R}\left\{\left(1-\frac{m}{2}\right)\left(K(m)-E(m)\right)\right\} \tag{2}$$

The expression for the z-component of magnetic field is given by

$$B_{z}(R,z)=\frac{B_{rem}}{4\pi}\left\{\varepsilon\cdot\left(1-\varepsilon^{*}\right)\pi+\frac{2\left(z-z_{0}\right)}{r_{1}}\left[\varepsilon^{*}\cdot\sqrt{1-n}\cdot Pi(n,m)-K(m)\right]\right\} \tag{3}$$

The total magnetic field is given by

$$B=\sqrt{B_{r}^{2}+B_{z}^{2}} \tag{4}$$

where B_{rem} is the remanant magnetic field of the magnets, a is the radius of the cylindrical magnet, (R,z) are the coordinates of the field points in question, M is the magnetic charge at the magnet pole given by $M=2\pi a^{2}B_{rem}$,

$$\varepsilon=\begin{cases}-1 \text{ if } z-z_{0}<0\\ 0 \text{ if } z-z_{0}=0\\ 1 \text{ if } z-z_{0}>0\end{cases} \quad \& \quad \varepsilon^{*}=\begin{cases}-1 \text{ if } R<a\\ 0 \text{ if } R=a\\ 1 \text{ if } R>a\end{cases} \tag{5}$$

the complete elliptic integrals of the first, second and third kinds are defined as

$$K(m) = \int_0^{\frac{\pi}{2}} \left(1 - m \cdot Sin^2\omega\right)^{-\frac{1}{2}} d\omega \tag{6}$$

$$E(m) = \int_0^{\frac{\pi}{2}} \left(1 - m \cdot Sin^2\omega\right)^{\frac{1}{2}} d\omega \tag{7}$$

$$Pi(n,m) = \int_0^{\frac{\pi}{2}} \left(1 - n \cdot Sin^2\omega\right)^{-1} \left(1 - m \cdot Sin^2\omega\right)^{-\frac{1}{2}} d\omega \tag{8}$$

where

$$m = \frac{4a \cdot R}{r_1^2}, n = \frac{4a \cdot R}{(a+R)^2}, r_1 = \sqrt{(a+R)^2 + (z - z_0)^2} \tag{9}$$

The equations assume that the disc is axisymmetric about the z-axis at a particular z-coordinate z_0.

Figure 9 [11] shows the calculated magnetic flux lines for the inter-magnet spacing 15 cm (inter-target spacing ~10 cm). M. J. Murphy [11] mentioned that when the magnets are 5 cm apart the minimum axial magnetic field is about 0.32T while at 20 cm apart the field is still a respectable 0.025T. The use of these strong Neodymium Iron Boron magnets ensures a very high flux density in the inter-target region. The electrons therefore experience strong magnetic confinement between the two cylindrical targets leading to very intense ionisation in the plasma and a high ion flux at the substrate which is considered to be an important factor for crystalline β-C_3N_4 film deposition.

Effective energy well for electrons and ions in the Penning Source plasma

The methodology for calculating the effective potential well for energetic electrons/ions in an azimuthally symmetric conventional sputter magnetron has been described by

Sheridan et al. [24]. Applying this methodology the expression for the effective potential is given by [11]

$$\psi = \frac{e^2\left(A_\theta(r,z) - A_\theta(r_1,z_1)\right)}{2mr^2} \tag{10}$$

where

$$A_\theta = \frac{F(r,z)}{2\pi r} \tag{11}$$

Where (r,z) is the field point, (r_1,z_1) is taken as the birthplace of the particle and A_θ is the only relevant component of the vector potential.

It is noted that the depth of the potential well is directly proportional to the square of the charge and inversely proportional to its mass. Figure 10(a-c) illustrates the confinement of an electron emitted at various radii along the target of the Penning source. It is to be noted that all axes units are in metres. It can be seen that electrons emitted at target radii much greater than the magnet radius are still well confined by the magnetic field trap. There is also electrostatic repulsion at either target. So in the absence of scattering electrons can never escape the plasma. There is also ion confinement and curves for a 10 eV C^{++} ion are indicated in Figure 11(a-d). Clearly the ions are not confined in the same way as electrons since they are attracted to the cathode surfaces. Equation. (10) reveals that a doubly charged ion will see an effective potential well four times deeper than a singly charged ion of the same mass. It can be seen that for example confining a 1 eV C^{++} ion is identical to confining a 4eV C^{+}. It is also to be noted that unlike electrons ions are easily reabsorbed at the cathodes.

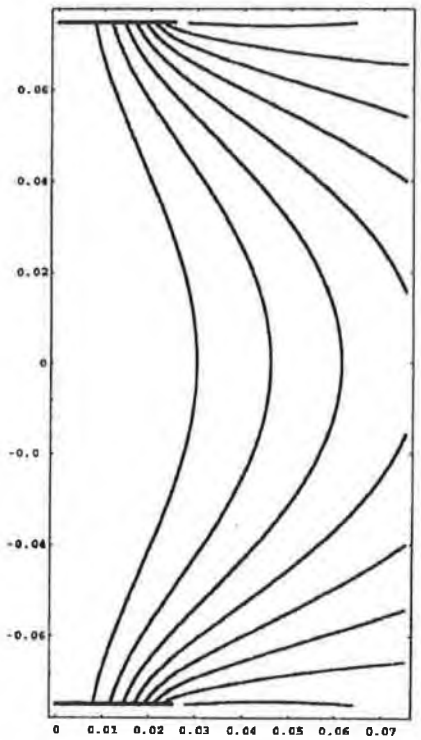

Figure 9: The magnetic flux distribution for an intermagnet spacing of 15 cm [11]. Lines encountered in going clockwise from the point (0, -0.075) are {-0.02, -0.04, ..., -0.20 Wb ($x10^{-3}$)} (Only one half of the distribution is shown from the central axis outward).

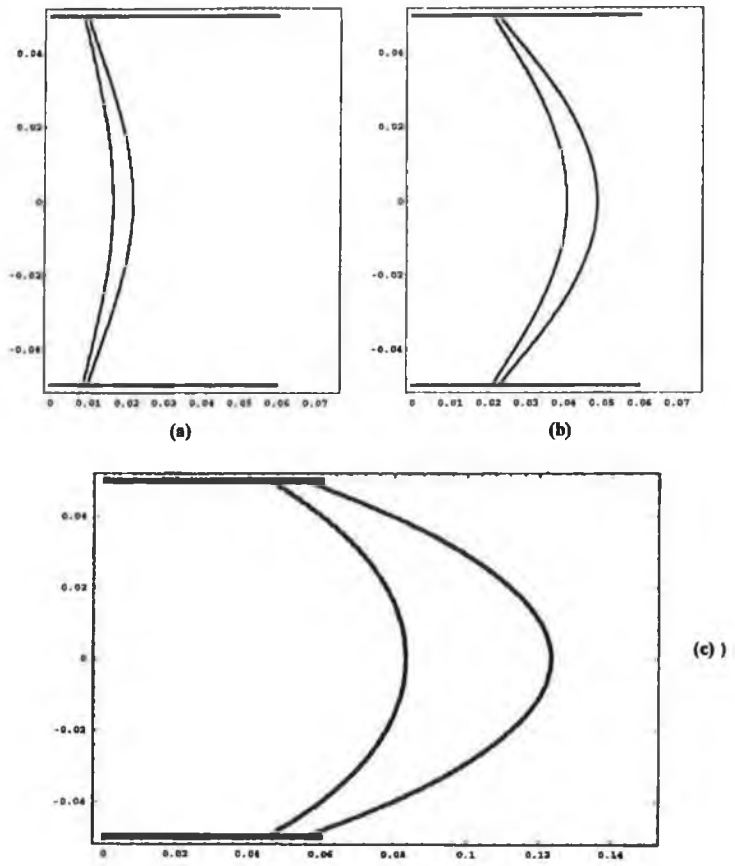

Figure 10(a-c): The effective potential well as seen by a 1500 eV electrons located just infront of the target of the Penning apparatus. The inter-magnet spacing is taken at 14 cm and the inter-target spacing is 10 cm. The diagrams (a-c) correspond with an electron being initially located at 10mm, 22.5mm and 50mm radii respectively. The trap is defined by the region within the crescent shapes and those outside are forbidden [11].

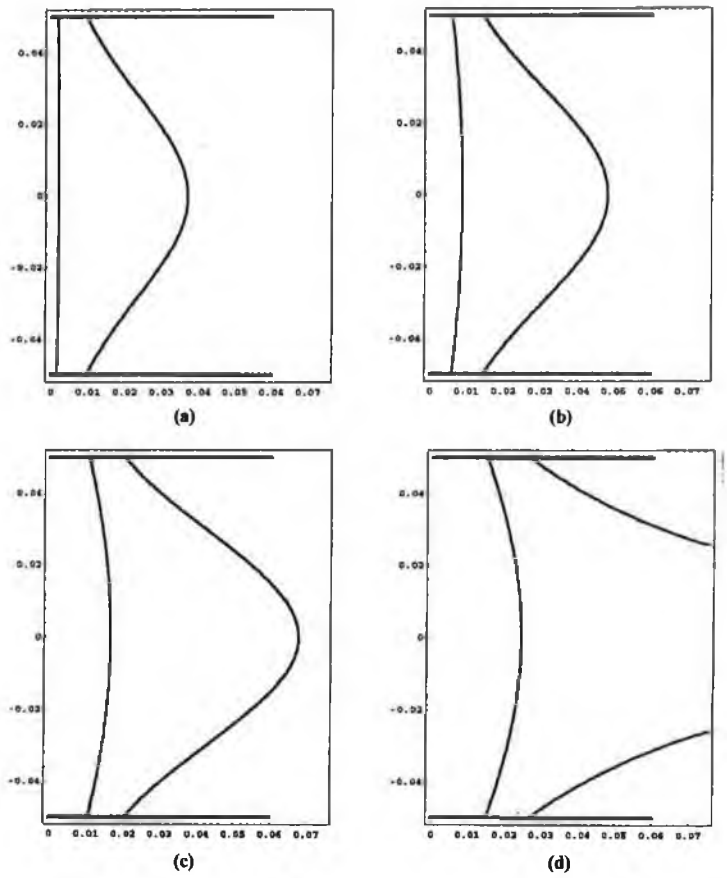

Figure 11(a-d): The effective potential well as seen by a 10 eV C^{++} ion located just in front of the target in the Penning source. The inter-target spacing is taken 10 cm. The diagrams (a-d) correspond to the ion being located at 0.5, 1.0, 1.5 and 2.0cm radial distances respectively. The trap is defined by the region within the crescent shapes and those outside are forbidden [11].

4.6 General Operating Characteristics of the Source

The plasma is sustainable down to $1x10^{-4}$ mbar of nitrogen. This is at least two orders of magnitude lower pressure than for a conventional magnetron. Voltage limitation (1250V max.) of the available 5kW power supply is the only factor preventing high plasma intensity operation at lower pressure; a pressure range of $1x10^{-3}$ mbar to $1.5x10^{-4}$ mbar was maintained for carbon nitride thin film deposition. The usual inter-target distance is 10cm though the device is readily operated at distances up to 20cm with the height of the vacuum chamber determining this limit.

Whenever transportable charge carriers are present in a conductive medium, the conductivity of that medium, σ, is given by [24]

$$\sigma = qn\mu \tag{12}$$

Where, q is the charge, n is the number of charged particles and μ is the proportionality constant, called the mobility of the charge carriers. If there is more than one species of charged particles, the conductivity is the sum of the contributions of all the species, and it can be written as [24]

$$\sigma = \sum_i q_i n_i \mu_i \tag{13}$$

We know, Conductance, G

$$G = \frac{\sigma A}{L} \text{ and } \sigma \propto n \tag{14}$$

$$\therefore G \propto n \tag{15}$$

where A is cross section of the medium, L is the length. As current (I) is proportional to the number of charged particle (n), $G \propto I$. From equation. 14 it can be seen that conductance also depends on geometrical shape of the conducting medium and directly proportional to the conductivity of the medium. Figure 12 shows the relation between conductance of the discharge as a function of discharge current. The relationship of the plot is quasi-linear. The fact that the shape of the plasma volume between the space of the Penning sources is bulged cylinder. This could be a possible reason why the conductance varies not exactly in a linear manner with current.

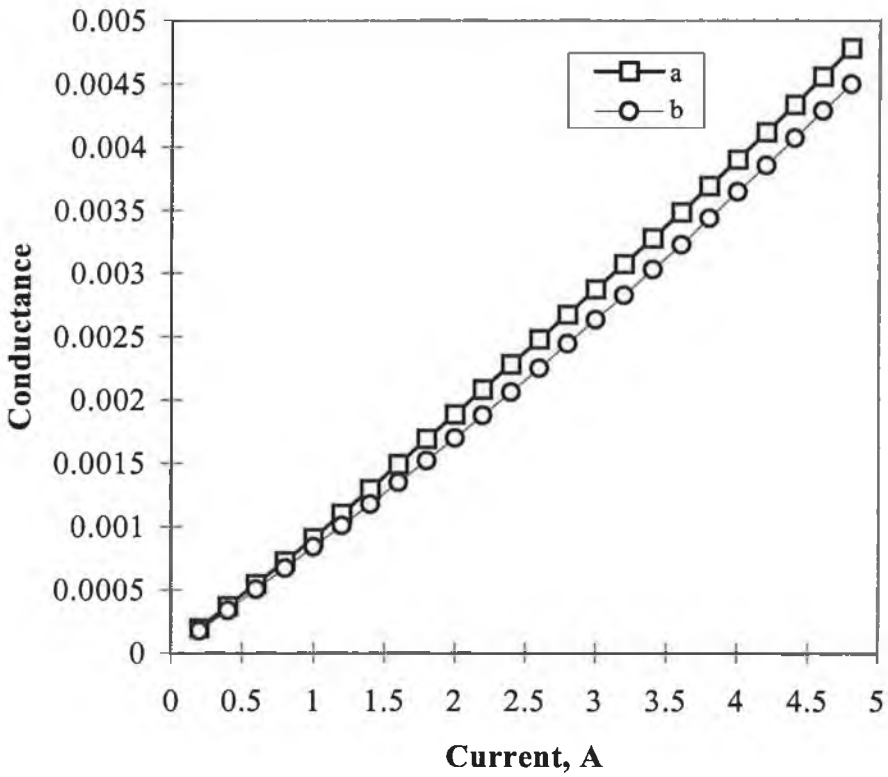

Figure 12: Conductance of the conducting media as a function of discharge current. Here, "a" indicates higher pressure ($1x10^{-3}$ mbar) and "b" indicates lower pressure ($1.5x10^{-4}$ mbar).

4.7 Plasma species monitoring by Emission Spectroscopy

The plasma species, especially N_2^+ ion can be controlled by discharge current or partial pressure of the chamber. These features can be monitored by emission spectroscopy.

Principles of Emission Spectroscopy

Under normal condition the electrons of an atom are stable and reside at their original energy level. If this atom or ion is excited by some external energy, a few electrons become excited and raised to higher energy level. Thus the atom or ion becomes excited and can radiate energy of characteristic wavelength when the excited electrons come back to their ground state. This how the emission spectroscopy works.

When gas or solid is atomised and partially ionised by plasma (or by any other process), the electrons undergo transitions to higher energy levels. This excited particles when comes back to less excited state, the corresponding emission wavelengths can be recorded by measuring the difference in energy between the particular orbital involved in this transition process. The transition of an atom from energy level E_2 to a lower energy level E_1 gives rise to a radiation quantum which can be given by [25]

$$E_2 - E_1 = hc / \lambda \qquad (16)$$

where λ is the wavelength usually expressed in nanometres (nm). These emitted quanta of energy originated from discrete transitions constitute the emission spectrum of the particular atom. As the electron configuration of each element is different from that of other elements, its emission spectrum is also unique. This principle will be used to identify the species in the plasma. The change in their relative intensity will also be monitored due to change in discharge current and working pressure.

Emission spectroscopy of N_2 plasma

The lowest electronic configuration of N_2 molecule can be written as [26]

$$N_2\ (Z = 14) = KK\ (\sigma_g 2s)^2\ (\sigma_u 2s)^2\ (\pi_g 2p)^4\ (\sigma_g 2p)^2$$

In case of molecular nitrogen the 2p orbital is completely filled and notation for the ground state is $^1\Sigma_g^+$. Depending on the excitation energy given to the molecule the outer most electrons of nitrogen molecule takes different electron configuration. Thus electrons are excited to higher orbital giving the signature of different excitation levels.

For N_2^+, the electronic configuration can be given as [26]

$$N_2^+\ (Z = 13) = KK\ (\sigma_g 2s)^2\ (\sigma_u 2s)^2\ (\pi_g 2p)^4\ (\sigma_g 2p)^1$$

In case of N_2^+ species, the outer most shells are deficient of one electron and notation for the ground state is $^2\Sigma_g^+$. Figure 13 shows the energy level diagram of nitrogen molecule. Two ionisation limits corresponding to the two two states $^2\Sigma_g^+$ and $^2\Sigma_u^+$ of N_2^+ (at 125666 and 151232 cm^{-1}) are not shown in this figure for simplicity [27,28]. Notation used for electronic transition is presented in Appendix A.

In a nitrogen plasma, the First Positive System (FPS), attributed to the transition ($B^3\Pi_g$ - $A^3\Sigma_u^+$) and Second Positive System (SPS), attributed to the transition ($C^3\Pi_u$ - $B^3\Pi_g$) can be developed readily. The SPS can be easily detected in 200-600nm range in DC or RF discharge and will be discussed here.

Similarly, for N_2^+, the First Negative System (FNS), attributed to ($B^2\Sigma_u^+$ - $X^2\Sigma_g^+$) occurs readily in a plasma at moderate pressure. The Second Negative System (SNS), due to the transition ($C^2\Sigma_u^+$ - $X^2\Sigma_g^+$) occurs at 191-206 nm range. The intensity of SNS is usually low due to their weak C - X transition and will not be considered in our case.

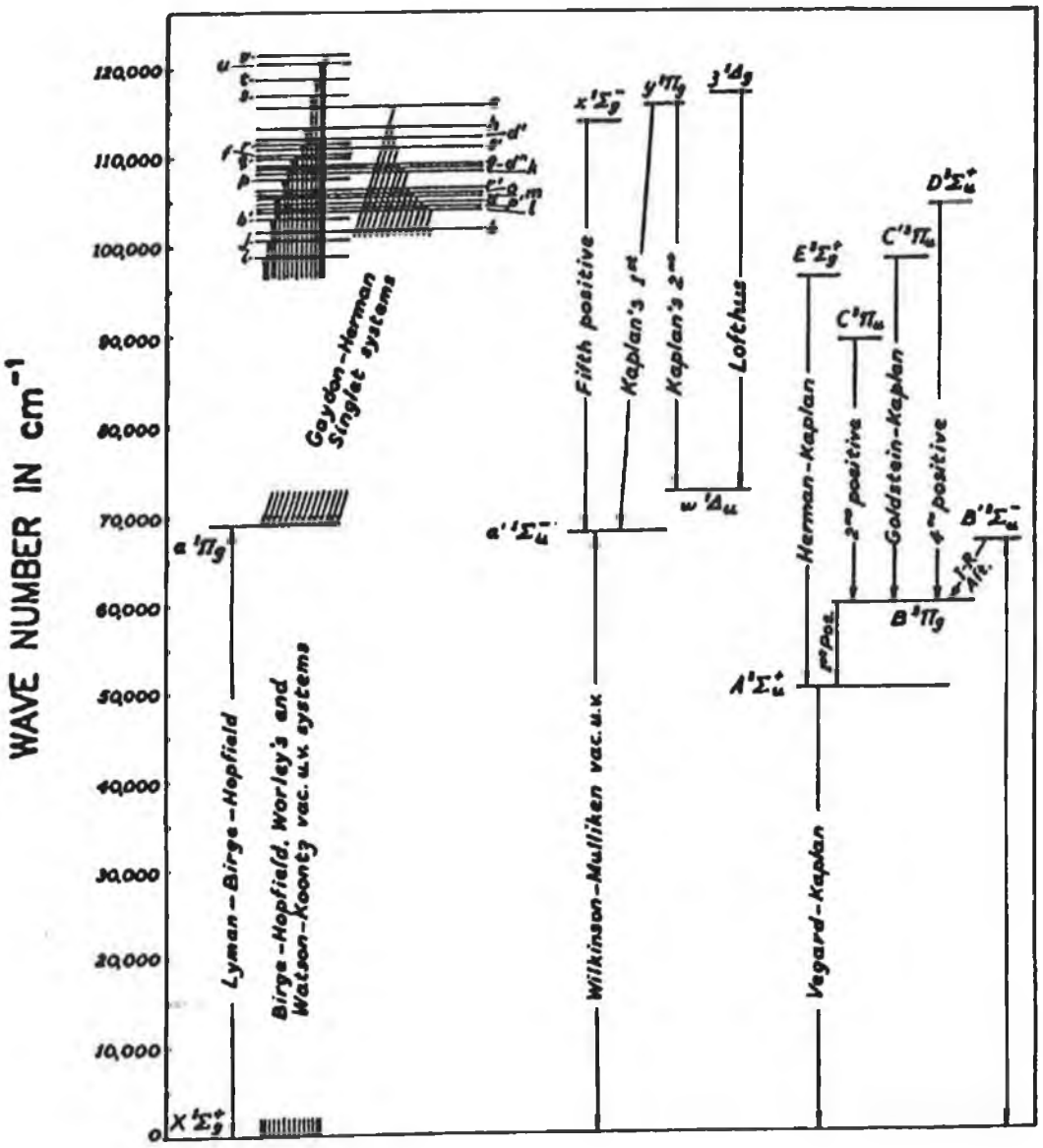

Figure 13: Energy level diagram of the N_2 molecule. Two ionization limits corresponding to the two states $^2\Sigma_g^+$ and $^2\Sigma_u^+$ of N_2^+ (at 125666 and 151232 cm^{-1}) are not shown in this figure [27,28].

Instrumentation

The essential components of an emission spectroscopic analytical system are: a source for excitation, a wavelength-dispersing unit and a detector.

Optical emission spectroscopy (OES) measurements were performed using a Digitwin Sofie instrument. The detector scans emission spectra at 200-900 nm range. The light emitted from the plasma was transmitted to the spectrometer by means of an optical quartz fibre.

The plasma emission intensities are measured directly from the spectrum by converting the height of the peak according to the gain of the system. The observed peak positions are compared with the reference peaks given by the instrumental data library.

In-situ emission spectral diagnostics

Figure 13 shows the optical emission from the plasma during sputtering. Striking features include the high level of N_2^+ ions relative to the neutral nitrogen and also the presence of CN radicals in the plasma. Table 1 and 2 summarises the optical emission spectra from the plasma during sputtering shown in the figure 14.

These CN radicals appear to arise due to nitrogen incorporation in the graphite target rather than by chemical sputtering from the substrate or chamber walls. If argon replaces the nitrogen as the sputtering gas then the emission due to CN does not immediately stop but slowly disappears over several minutes as fresh material is sputtered from the graphite target. This is not due to the time required for the gas composition in the chamber to change since a slow reduction occurs even with a delay between sputtering in nitrogen and argon. The role which the CN radicals carry out in the deposition process is not clear at this stage.

Table 1: Spectral assignments for emission from N_2 plasma

λ_{obs}(nm)	λ_{rref} (nm)	Species	Transition
317	315.93	SPS of N_2	$C^3\Pi_u$ - $B^3\Pi_g$
332	333	SPS of N_2	$C^3\Pi_u$ - $B^3\Pi_g$
353.2	353.67	SPS of N_2	$C^3\Pi_u$ - $B^3\Pi_g$
358	357.69	SPS of N_2	$C^3\Pi_u$ - $B^3\Pi_g$
376	375.54	SPS of N_2	$C^3\Pi_u$ - $B^3\Pi_g$
391.5	391.44	FNS of N_2^+	$B^2\Sigma_u^+$ - $X^2\Sigma_g^+$
428.5	427.81	FNS of N_2^+	$B^2\Sigma_u^+$ - $X^2\Sigma_g^+$

Table 2: Spectral assignments for emission from other species in N_2 plasma

λ_{obs}(nm)	λ_{rref} (nm)	Species
356	356.35	CN
388	388.5	CN
428.5	428.76	C^+

Figure 15 shows the N_2^+ ion (391.5 nm) intensity as a function of discharge current. It is interesting to see that the ionised nitrogen species increases with increasing discharge current and is independent of nitrogen pressure. This is due to the fact that in a confined plasma ionised nitrogen species increase as the discharge current increases. Increase in nitrogen gas pressure in the plasma does not increase the number of ionised species. The validity of this statement can be confirmed by the analyses of the film deposited at different nitrogen pressure (low to high) keeping other deposition parameters constant. Table 3 gives the analyses of such two films.

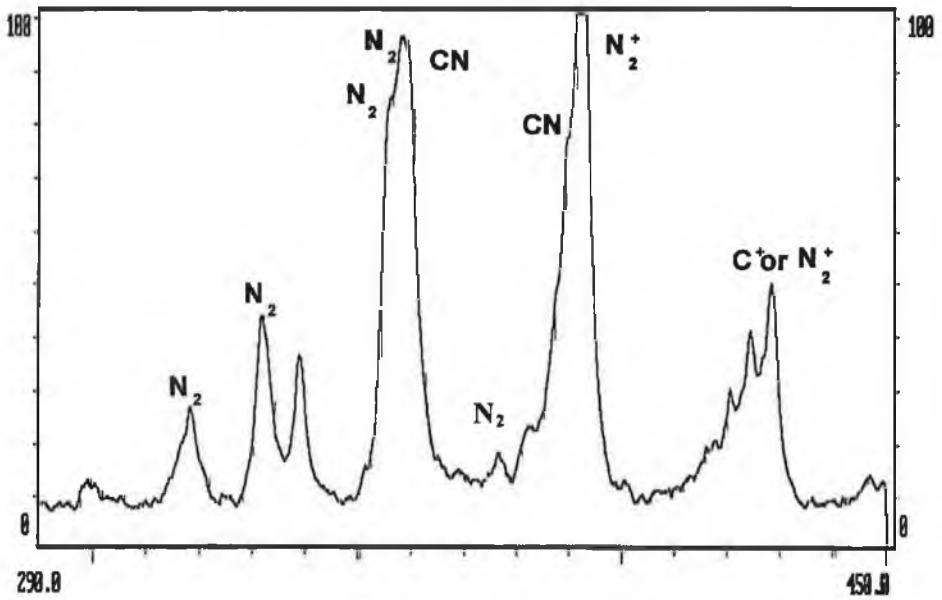

Figure 14: A typical optical emission spectrum for the nitrogen plasma during carbon nitride film deposition. The positions of the peaks are indicated in nm.

Table 3: Elemental analyses of carbon nitride film by RBS

Sample no.	Nitrogen gas pressure (mbar)	C at. %	N at.%	O at.%	Fe at.%
PCN3	1.5×10^{-4}	57	39	0	3.7
PCN5	1×10^{-3}	58	38	0	3.9

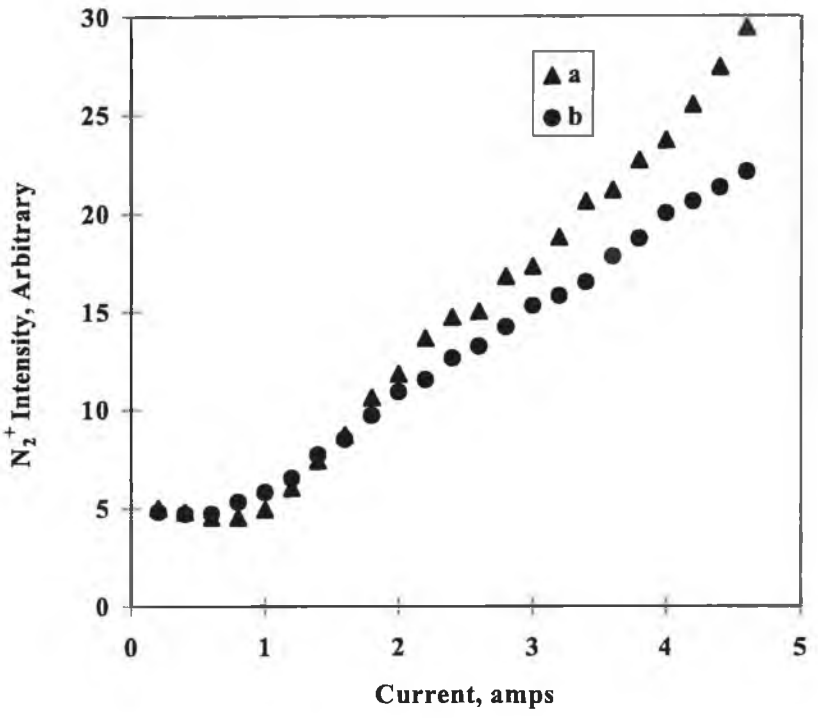

Figure 15: N_2^+ ion intensity as a function of discharge current. Here, "a" indicates higher pressure ($1x10^{-3}$ mbar) and "b" indicates lower pressure ($1.5x10^{-4}$ mbar).

No significant variation of nitrogen incorporation in the films can be seen with variation of nitrogen gas (Table 3).Thus increase in nitrogen gas pressure does not increase the number of ionised nitrogen species.

4.8 Bias Current Characteristics

In order to get the insight of the plasma produced by the Penning source and its influence on deposition, a 2cm diameter steel probe was employed to face the plasma. The bias current to the probe as a function of probe bias voltage was examined at probe

distances of approximately 9cm, 12cm and 14cm from the Source axis and with 10cm and 5cm inter-target distance. This was done at pressure of 1.5×10^{-4} mbar and current of 3 amps. An exception is the 5cm distance where heat generated due to the plasma can melt the viton O-rings and thus damage the source.

Figure 16(a) shows the curve obtained at 10.6cm away from the axis of the source. The target to target distance is 10cm. The self-bias of the probe is -11V for 3 amps current.

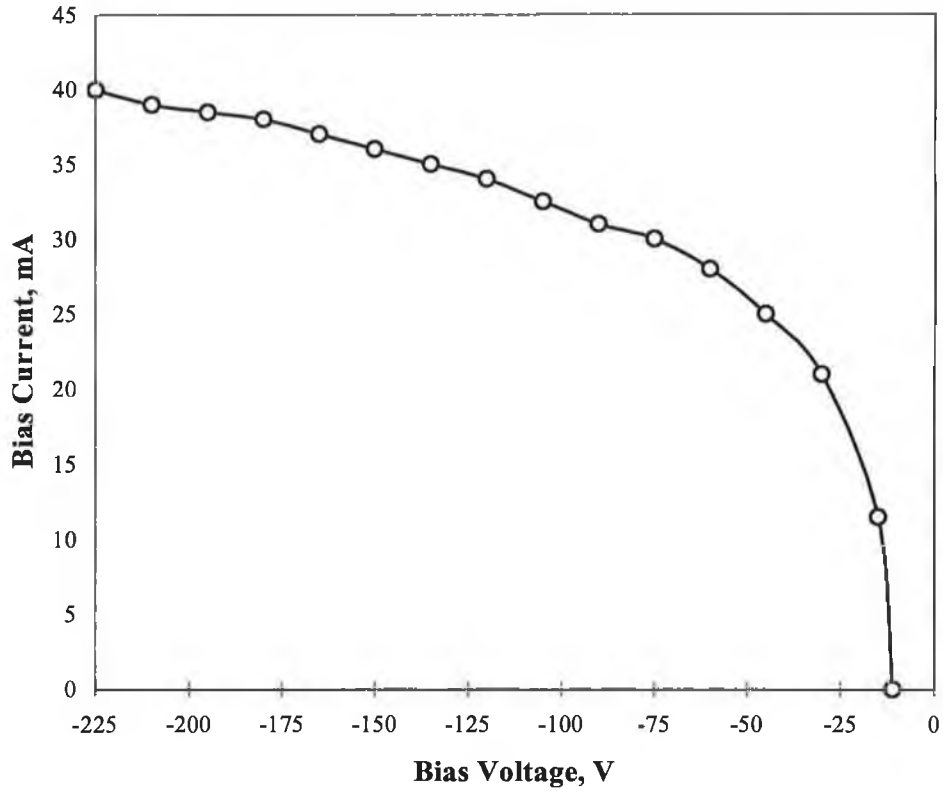

Figure 16(a): The bias current to a 2cm diameter disk as a function of applied negative bias voltage. The measurements were performed at discharge current of 3 Amps at a pressure of 1.5×10^{-4} mbar. The distance of the probe from the source axis is 10.6cm and the inter-target distance is 10cm.

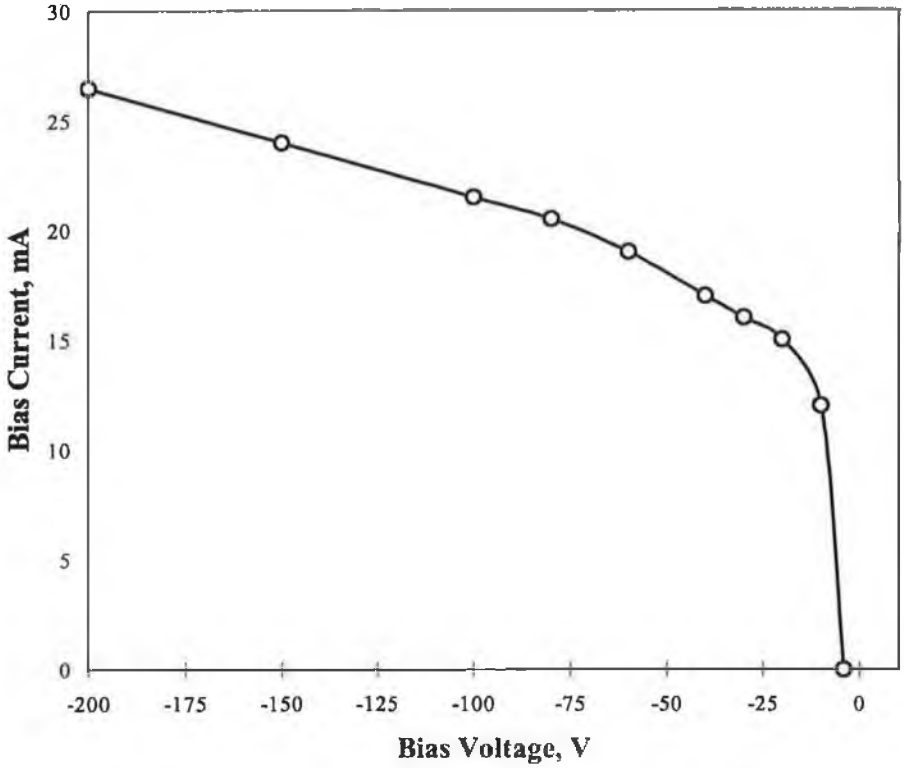

Figure 16(b): The bias current to a 2cm diameter disk as a function of applied negative bias voltage. The measurements were performed at discharge current of 3 Amps at a pressure of 1.5×10^{-4} mbar. The distance of the probe from the source axis is 13.6cm and the inter-target distance is 10cm.

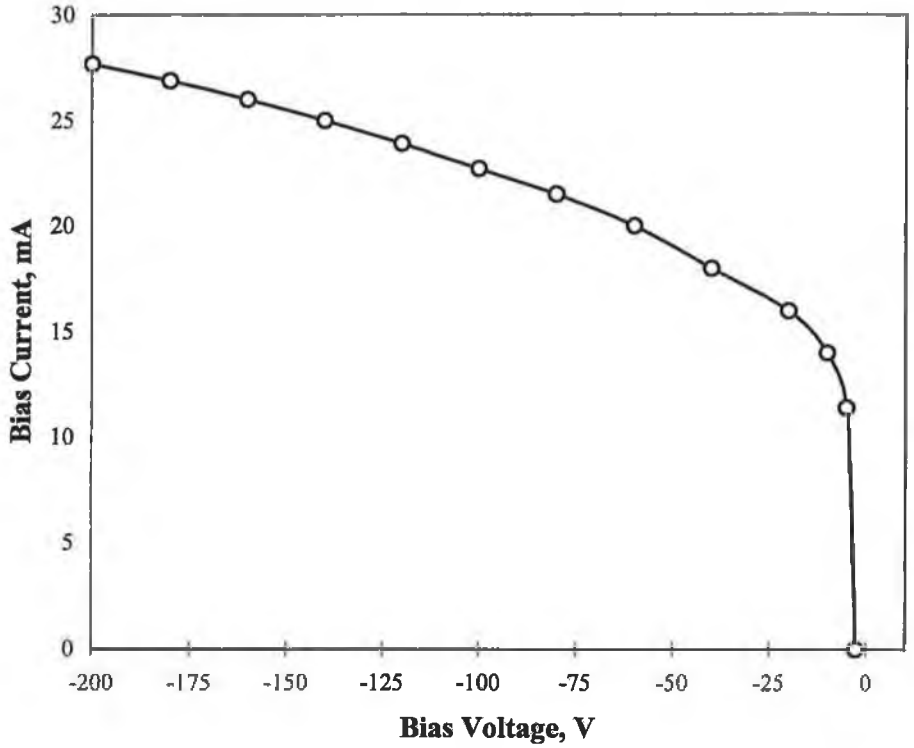

Figure 16(c): The bias current to a 2cm diameter disk as a function of applied negative bias voltage. The measurements were performed at discharge current of 3 Amps at a pressure of 1.5×10^{-4} mbar. The distance of the probe from the source axis is 15.6cm and the inter-target distance is 10cm.

If the probe is taken at 13.6cm away from the source axis, the self bias of the probe becomes -4 volt (figure 16b). The self bias voltage becomes -2.6V when the probe is taken at 15.6cm from the source axis (figure 16c). Thus the probe faces more electron when it is closer to the plasma. Figure 17(a) shows the curve obtained at 10.6cm away from the axis of the source. The target to target distance is 5cm and the self-bias of the probe is +4V for 3 amps current. If the probe is taken at 13.6cm away from the source axis the self-bias becomes +1.9V for the same current (figure 17b). This is due to fact that the electrons are completely trapped when the inter-target distance is 5cm. Thus ion bombardment can be increased by changing the target and sample position. The effect of electron bombardment was reduced by applying negative bias to the samples during deposition.

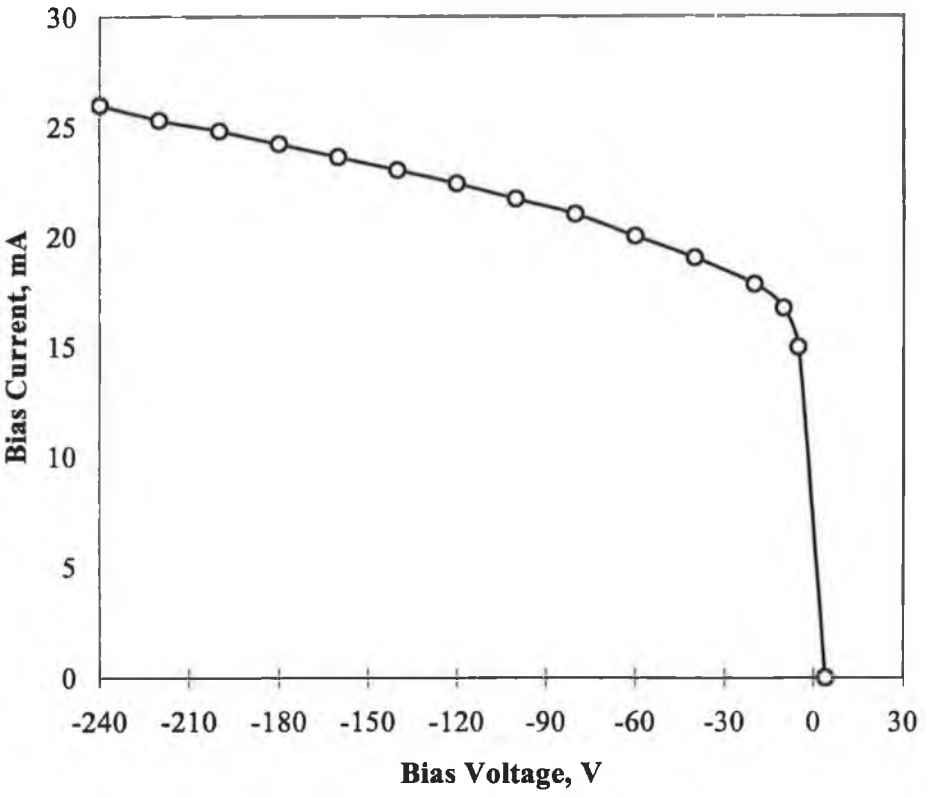

Figure 17(a): The bias current to a 2cm diameter disk as a function of applied negative bias voltage. The measurements were performed at discharge current of 3 Amps at a pressure of 1.5×10^{-4} mbar. The distance of the probe from the source axis is 10.6cm and the inter-target distance is 5cm.

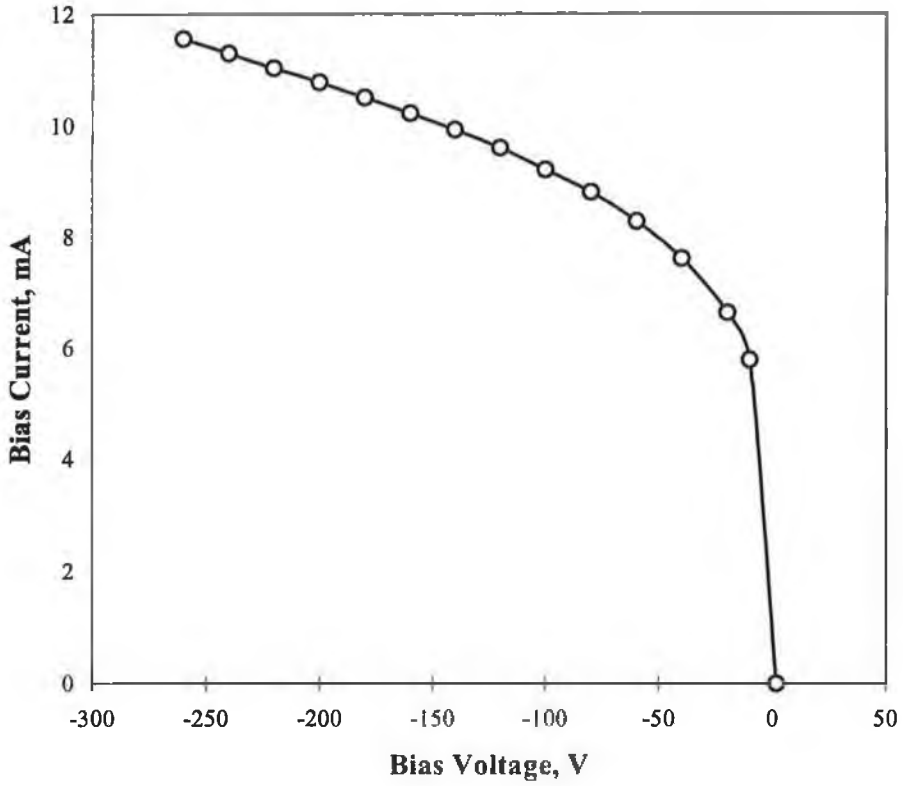

Figure 17(b): The bias current to a 2cm diameter disk as a function of applied negative bias voltage. The measurements were performed at discharge current of 3 Amps at a pressure of 1.5×10^{-4} mbar. The distance of the probe from the source axis is 13.6cm and the inter-target distance is 5cm.

4.9 Langmuir probe diagnostics: Basics

The probe diagnostics are performed from the I-V characteristics which depends on the size and shape of the probe. Probe size is limited by the current drawn in comparison to the effective ionization or source current in the local plasma volume. A typical probe I-V characteristics are given in figure 18.The important features are the "knee" labeled K, the floating potential (where I = 0) labeled F, the ion saturation current labeled I^*_I and the electron saturation current labeled I^*_e. The bias voltage corresponding to the knee at K is usually identified as the plasma potential (V_p).

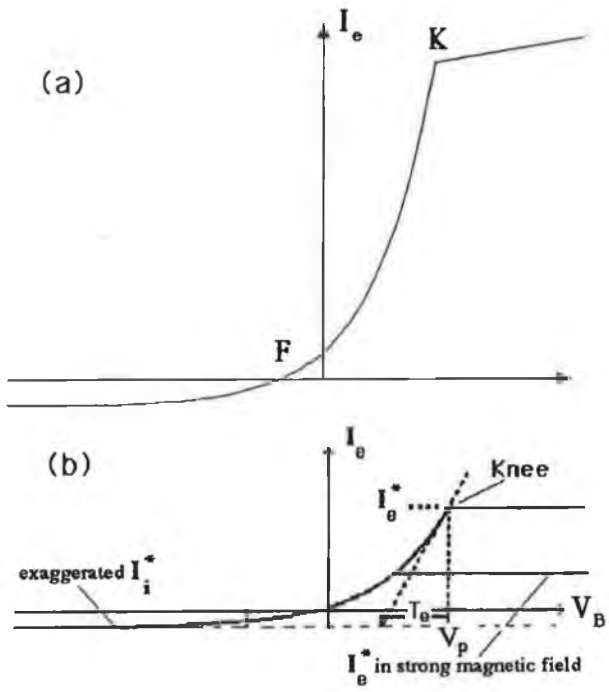

Figure 18: Langmuir probe I-V characteristics. (a) Schematic I-V characteristic with an increase in I^*_e above V_p corresponding to a weakly increasing effective area. (b) Schematic interpretation of I-V characteristic [29].

The ion saturation current can be estimated to be [29]

$$I_i^* \approx 0.6 n_e e \sqrt{\frac{T_e}{m_i}} S \tag{17}$$

where S is the probe area, m_i the ion mass, T_e the electron temperature, e the electron charge and n_e (cm^{-3}) is electron density. It is to be noted here that the result does not depend on the ion temperature T_i and is independent of bias voltage.

The plasma electron density is known once I^*_I is measured and T_e is determined. Assuming Maxwellian electrons, the I-V characteristics curve between K and F in figure can be written [29]

$$I_e = -I_i^* + I_e^* \exp(-\eta) \tag{18}$$

where,

$$\eta \equiv e\left(\frac{V_p - V_B}{T_e}\right) \tag{19}$$

T_e is determined from the slope of the I-V characteristic graphed on semilog paper. Values of T_e are typically a few eV and combined with plasma densities of 10^{10} cm^{-3} give ion saturation current densities of the order of 0.2 mA cm^{-2} [29]. This is the basis of Langmuir probe plasma diagnostics.

Description of the Langmuir Probe System

A tuned Langmuir probe (Scientific Systems Ltd.) was used to measure the plasma characteristics of the Penning source. The probe geometry and parameter extraction have been discussed in detail by M.B. Hopkins [30]. The probe is forced to float at the discharge potential by ensuring that the probe-plasma impedance, Z_p, is much less than the probe-ground impedance, Z_s. The probe circuit is then a potential divider with the

discharge potential appearing across Z_s and the probe floats relative to the plasma potential. In the DCU probe a series of miniature self-resonant coils is used to achieve impedance, $Z_s > 100$ kΩ at 13.56 MHz and $Z_s > 10$ kΩ at the 2nd and 3rd Harmonics. The probe-plasma impedance, Z_p, is calculated to be in the region of a few hundred ohms (at 13.56 MHz if discharge plasma is ignited by RF):

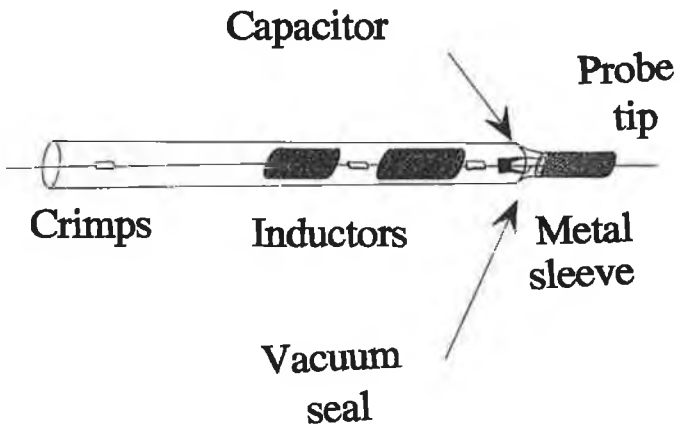

Figure 19(a): The tuned probe [30].

This is achieved by making the probe holder close to the probe tip of conducting material and capacitively coupling it to the probe. This shield has an area of approximately 2 cm^2 and is made of stainless steel. This shunt capacitor, C_2, dominates the plasma-probe impedance but has no effect on the direct current collected to the probe, it is doubtful that the conducting wall of the probe holder will deplete the plasma to much greater extent than an insulating wall as neither draw a direct current. Figure 19(a) shows a simple schematic of the probe used in this research and fig. 19(b) an equivalent circuit of the probe. It is to be noted here that there is a parasitic capacitance C_s between the probe surface and the ground. This is normally shielded by the plasma. However, if the tuned inductors are located outside the plasma then C_s is no longer

negligible. In the case of glass walled chambers it is conceivable that the blocking inductors can be placed outside the plasma region, this is not possible in metal walled chamber. A value of C_s of 0.1 pF (Z_s=117 kΩ) will be sufficient to shunt Z_p and load the probe. For this reason the tuned inductors must always be inside the plasma and as close to the probe tip as possible.

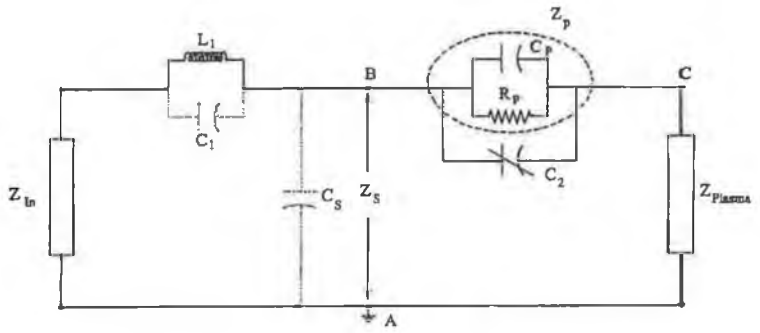

Figure 19(b): Equivalent circuit of the tuned probe [30].

Probe Geometry

The diameter of the probe tip is 0.38 mm, and the probe holder 1.5 mm increasing to 7 mm at the inductors, efforts are currently being made to reduce it to < 5 mm. The probe length is typically 10 mm and is designed to prevent any increase in probe collection area by a sputtered conductive layer: This problem often goes undetected as the conductive layers can have high resistance and are "burned-off" during electron collection, however the layer can contribute to ion current collection. The conductive layer appears on the insulator and when a connection is made to the probe tip, the collection area of the probe increases. The connection is prevented by having a recessed gap between probe tip and insulator. The diameter of the probe is chosen 0.38 mm so that the probe normally operates in a "thin sheath" mode. In practice the probe size

should not be excessive as it will deplete the plasma. In general, as the increasing probe radius approaches the mean free path of the collected species the current to the probe is decreased. In this work the probe was cleaned by electron bombardment heating before each set of measurements. The probe can also significantly alter the charge balance in the plasma greatly perturbing the plasma, two probes are the best way to check for such effects as is discussed below: one probe monitors the plasma floating potential while the second probe is introduced and biased to obtain the current-voltage (I-V) characteristics.

4.10 Plasma Characterisation of the Penning Source by Langmuir Probe

So far, the general characteristics of the cylindrical geometry Penning-type opposed target source were discussed. The motivation for constructing the system is a belief that the degree of ionisation of the gas will be higher due to a magnetic trap resulting higher deposition rates. There is a need to investigate the plasma characteristic during deposition of carbon nitride films. This section will show the basic plasma characteristics, i.e., electron density n_e, electron temperature T_e, electron velocity and energy distribution functions and plasma potential V_p. Langmuir probes, in principle, provide a simple and relatively wider diagnostics for measuring the plasma parameters in low-pressure discharges. In their simplest form, Langmuir probes are bare wires inserted into a plasma (figure 19a) as discussed before. They can indicate the presence of electron or ion beams or indicate the presence and magnitude of fluctuating rf in plasmas. The use of a Langmuir probe to investigate nitrogen plasmas is common. But the study becomes complex when there is a magnetic trap, in this case due to an opposed target Penning-type geometry which acts as a magnetic filter. Several things could happen during the excitation of energetic particles: hot electrons could be generated, cooling of the hot electrons could occur due to the presence of the magnetic filter, a radial electric field could occur due to the out ward migration of electrons. These possibilities make the system more complex. However, the section will illustrate the features which will be helpful to explain the growth mechanism of CN compound.

For the Langmuir probe measurements the deposition pressures were kept at 1.5×10^{4} and 6×10^{4} mbar and the substrate was biased at 0 or -50 V with a 13.56 MHz RF supply. The deposition parameters are shown in the table 4. No significant difference was seen in plasma characteristics when the substrate bias was changed. Therefore later on, only the results for -50 V bias are discussed. Figure 20 shows a diagram of the positioning of the probe within the deposition chamber. It should be noted that the 200 mm position of the probe extension on the graphs shown in the results section equates to the edge of the target and the probe moves further away from the target as the probe distance measurement is reduced.

Table 4: Deposition Parameters

Operating Condition	RF bias Voltage	Current (A)	Target Voltage (V)	Chamber pressure (mbar)
1	-50	3.0	1143	$1.5X10^{4}$
2	-50	4.5	1060	$6.0X10^{4}$
3	0	4.5	1060	$6.0X10^{4}$

As shown in figure 20 the maximum insertion distance of the Langmuir probe (200 mm) corresponds to the outer edge of the cathodes. It was not possible to obtain readings from the probe in the inter cathode space since the insertion of the probe into this region caused the plasma to extinguish. In all Langmuir probe measurements Maxwellian electron energy distribution was considered.

Plasma potential

In a conventional (unmagnetised) plasma, the plasma potential is slightly positive and remains approximately constant throughout the bulk of the plasma outside the electrode sheaths. As can be seen from fig. 21, the plasma potential in this system behaves quite differently. It remains negative for a long distance away from the cathode sheath and only becomes positive near the chamber walls. This occurs because of the

magnetic confinement of the electrons between the opposed cathodes. This negative space charge in the magnetic confinement region gives rise to an electric field and a (somewhat non-linear) increase in potential with distance away from the cathode axis as shown in fig. 21.

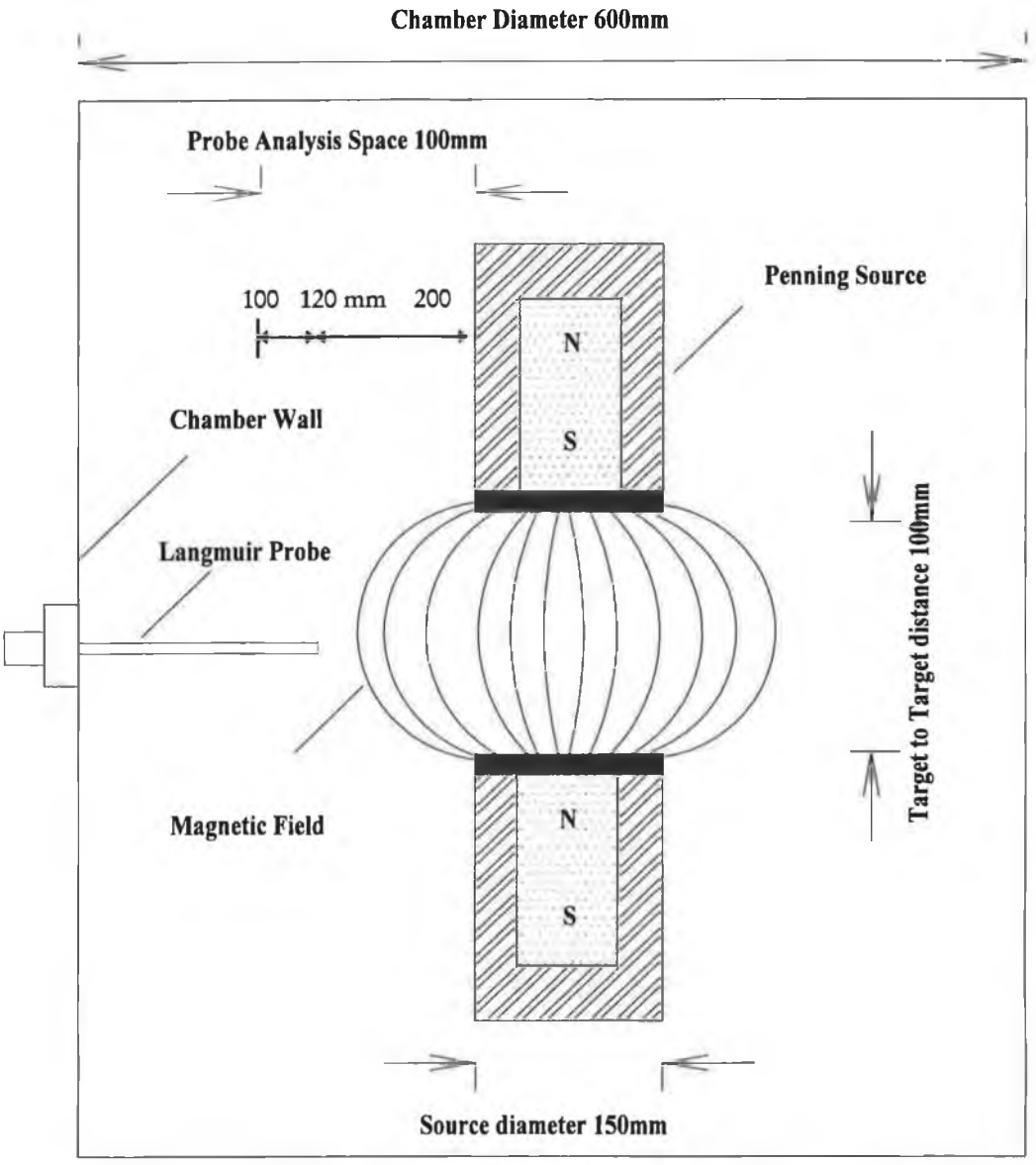

Figure 20: Schematic diagram of the Penning Source and the Langmuir Probe

Floating potential

The floating potential which is the potential taken up by an isolated body in the plasma is related to the plasma potential and the electron temperature according to the equation [29]

$$V_f = V_p - (3.3 + 0.5 \ln \mu) \frac{T_e}{e} \qquad (20)$$

where, V_f is floating potential (V), V_p is Plasma potential (V), T_e is Electron temperature (eV), e is Electron charge, μ is atomic mass (amu).

As shown in fig. 22 the floating potential also shows the effects of magnetic confinement of the electrons. According to the above equation, the electron temperature, T_e, will be minimum when the difference V_p-V_f is minimum, i.e V_f is maximum. By comparing figures 21, 22 it can be seen that this occurs at a probe position of ~150 mm. A plot of the electron temperature vs. probe position, figure 23 bears this out. The figure 20 shows that the electron temperature is high close to the inter-cathode region, reduces as the electrons move away from the most intense region of magnetic confinement and increases again outside this region. This can be explained as follows. There is a high density of hot electrons in the magnetic trap due to the intense plasma and the magnetic confinement. Very low energy electrons are able to drift and diffuse out of the trap thus the average electron energy at the outer regions of the trap will be lower. However, at the edges of the trap these cold electrons will still see an electric field therefore they will start to accelerate again and hence their average energy will rise. Once they leave the region influenced by the electric field then their energy will remain constant.

Electron density

As shown in fig. 24, the electron density at the edge of the inter-cathode space rises to $>1.8\times10^{11}$ at a pressure of 6×10^{-4} mbar and $>8\times10^{10}$ cm^{-3} at 1.5×10^{-4} mbar. It is expected to be considerably higher on the cathode axis. This corresponds to an ionisation ratio of $>1.1\%$ and 2% respectively. Thus on the cathode axis the ionisation level will be very high allowing intense activation of the molecules to occur.

Ion flux

Figure 25 shows the ion flux falling off with distance from the cathode as expected. For the normal deposition conditions for carbon nitride used in this system, the substrate is held at a distance corresponding to the 150 mm point in the figures. At this point, for a pressure of 6×10^{-4} mbar, the current density due to ions at the substrate is ~7 $mA.cm^{-2}$. This corresponds to an ion flux of 4.4×10^{16} cm^{-2} s^{-1}. We can calculate the ion to neutral flux ratio at the substrate by the following argument.

The film growth rate is approximately 2 $\mu m.hr^{-1}$which is equivalent to 5.6×10^{-8} cm s^{-1}. If we assume the film structure is that of β-C_3N_4 (which it is not necessarily but makes a reasonable starting point for the calculations) then the unit cell dimensions are a, b = 6.44Å [31], c = 5.65 Å [32] then the volume of the unit cell is 2c(asin30°.bcos30°) = 203 $Å^3$ which is 2.03×10^{-22} cm^3. In conjunction with the growth rate this gives a C_3N_4 molecular deposition rate of 2.8×10^{14} cm^{-2} s^{-1}. As each C_3N_4 molecule contains 3 carbon atoms the carbon atom arrival rate at the substrate must be 8.4 $\times10^{14}$ cm^{-2} s^{-1} if the sticking coefficient is assumed to be 1. Thus the ratio of incorporated carbon to bombarding ions (which are predominantly nitrogen) is ~0.02. Also the impingement rate of neutral background nitrogen molecules is given approximately by [33]

$$r = 2.7\times10^{22}(MT)^{-0.5}p \quad \text{cm}^{-2}\text{s}^{-1} \tag{21}$$

where, M is the molar mass of the nitrogen molecule (g), T is the temperature (K), p is the pressure (mbar).

For nitrogen molecules at 300 K this corresponds to 1.8×10^{17} cm^{-2} s^{-1}. The ion to neutral arrival ratio at the substrate is then ~ 0.25.

The conclusion of these calculations is that the film deposition process is highly activated because of the high ion to neutral arrival ratio at the substrate.

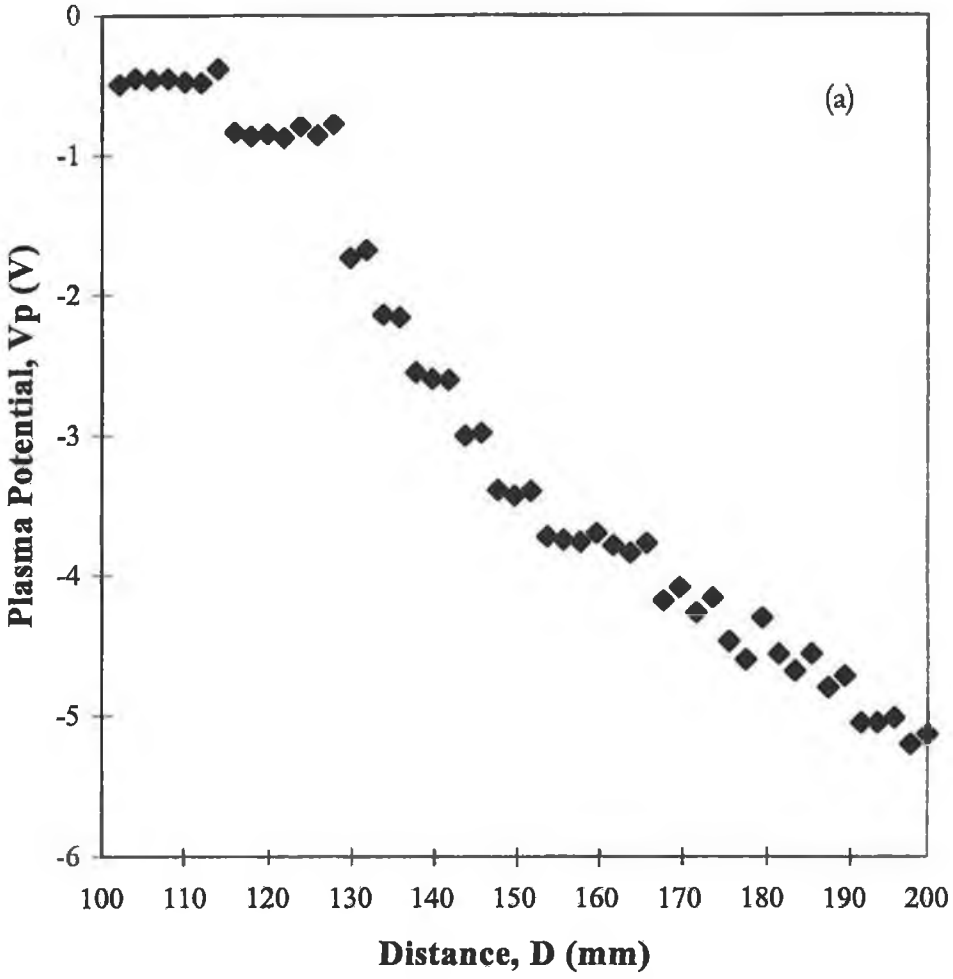

Figure 21: Plasma Potential as a function of distance of the probe (a) Bias -50V, 4.5A, 1060V, 6X10^{-4} mbar.

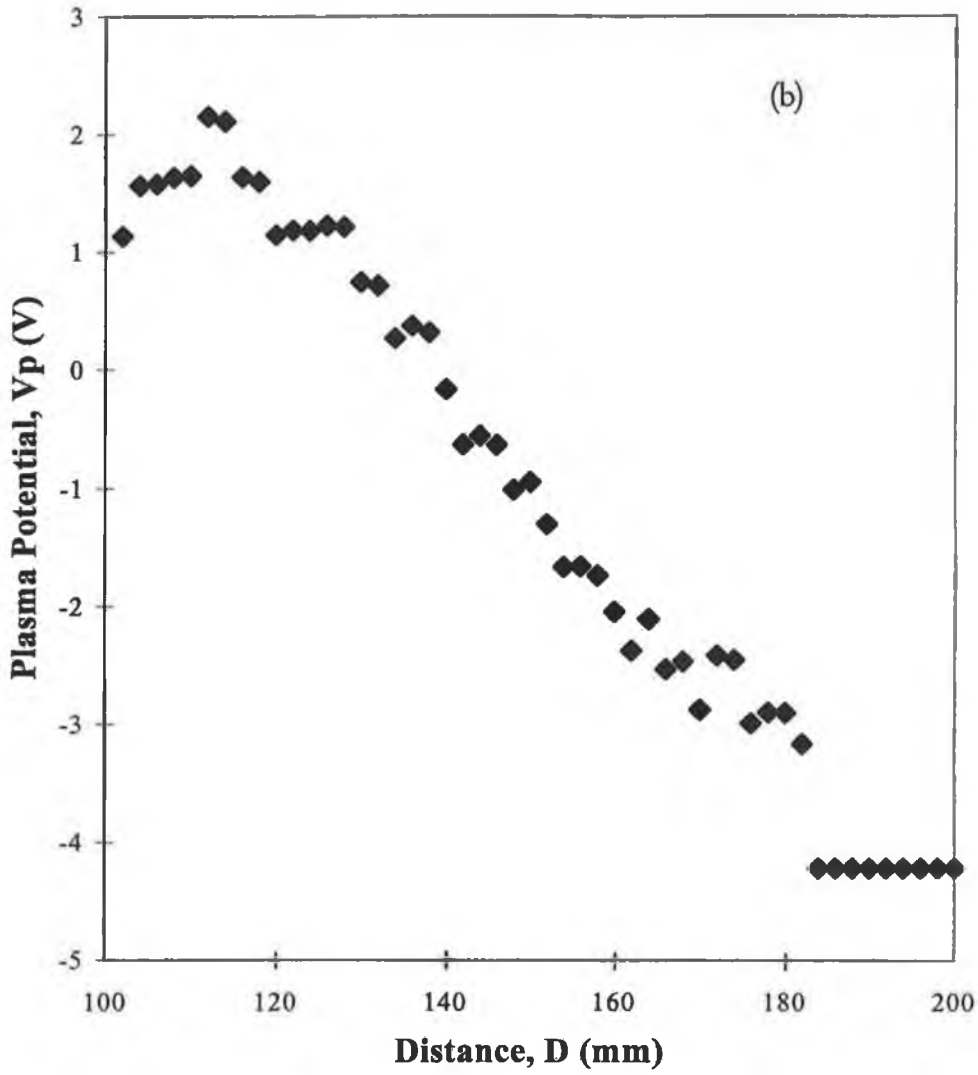

Figure 21: Plasma Potential as a function of distance of the probe (b) Bias -50V, 3.0A, 1143V, 1.5X10^{-4} mbar.

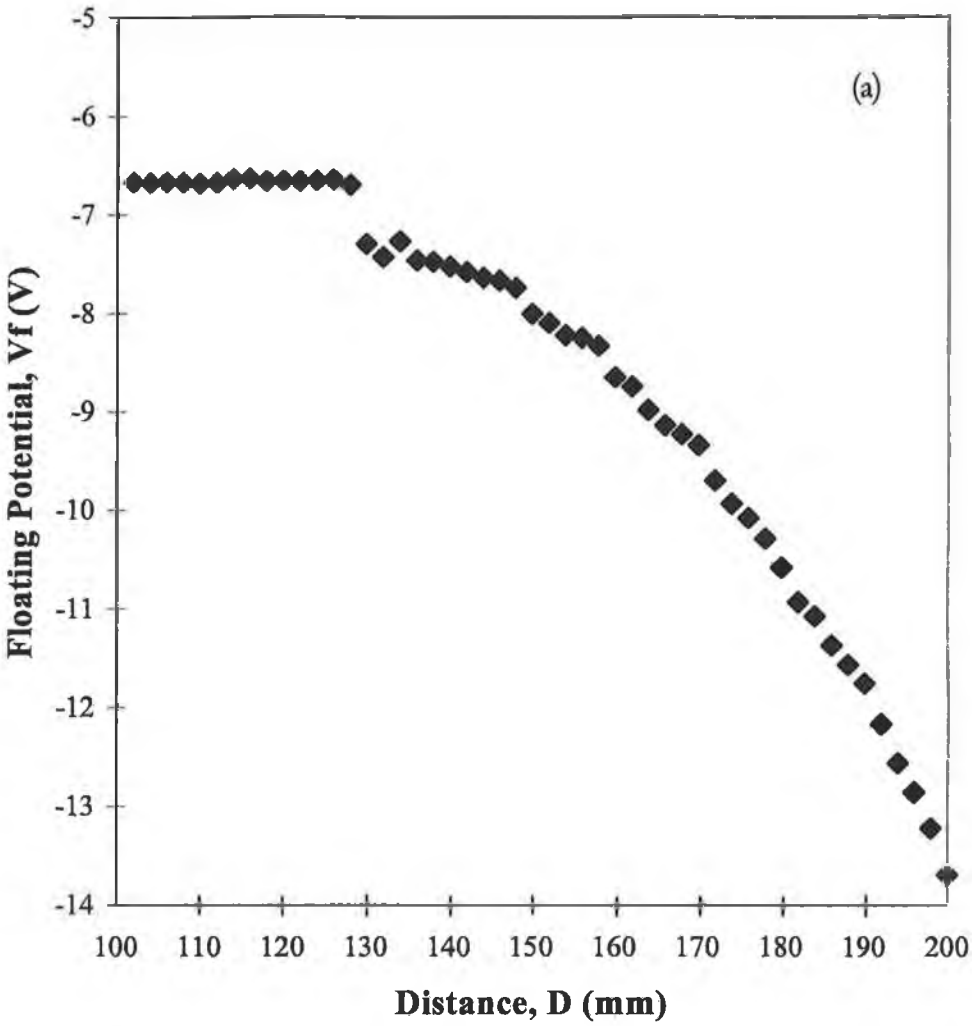

Figure 22: Floating Potential as a function of distance of the probe (a) Bias -50V, 4.5 A, 1060 V, 6X10^{-4} mbar.

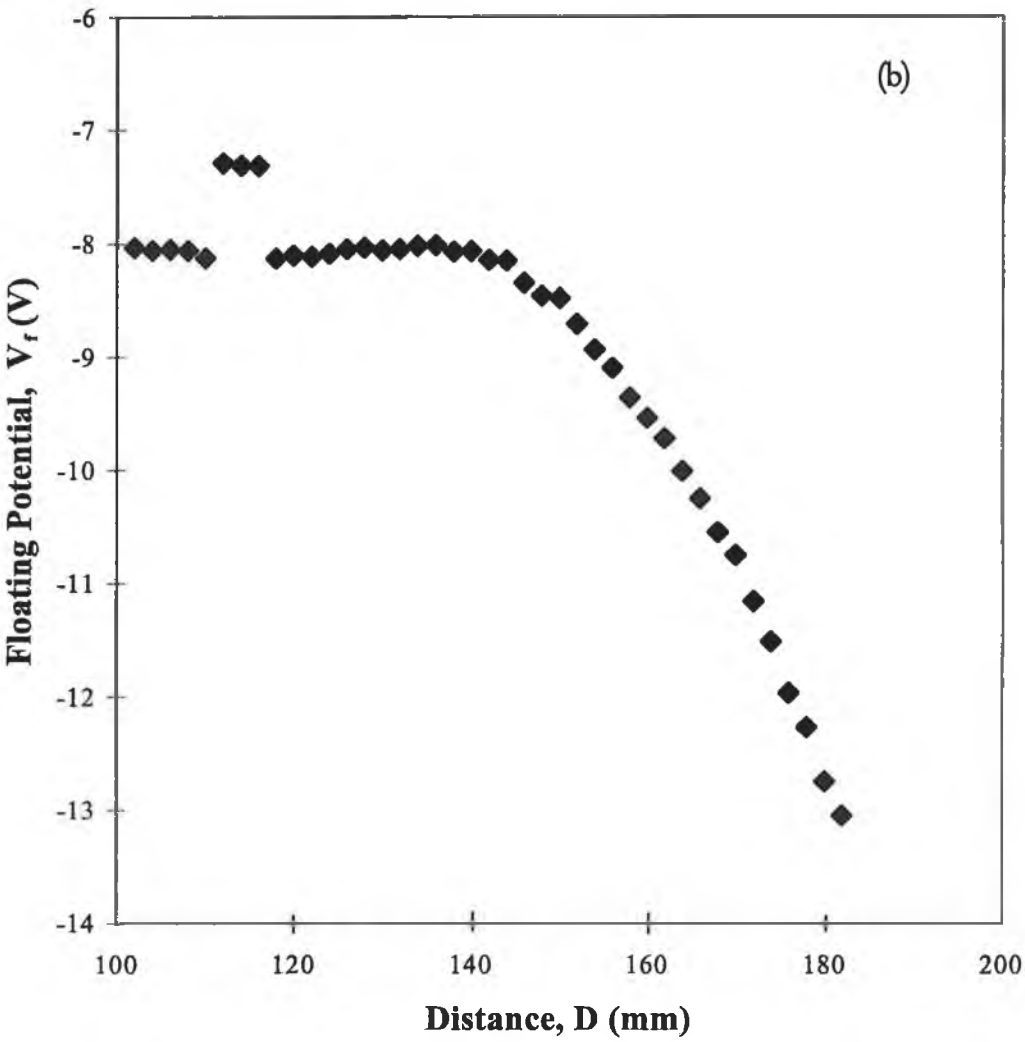

Figure 22: Floating Potential as a function of distance of the probe (b) Bias -50V, 3.0 A, 1143V, 1.5X^{-4}mbar.

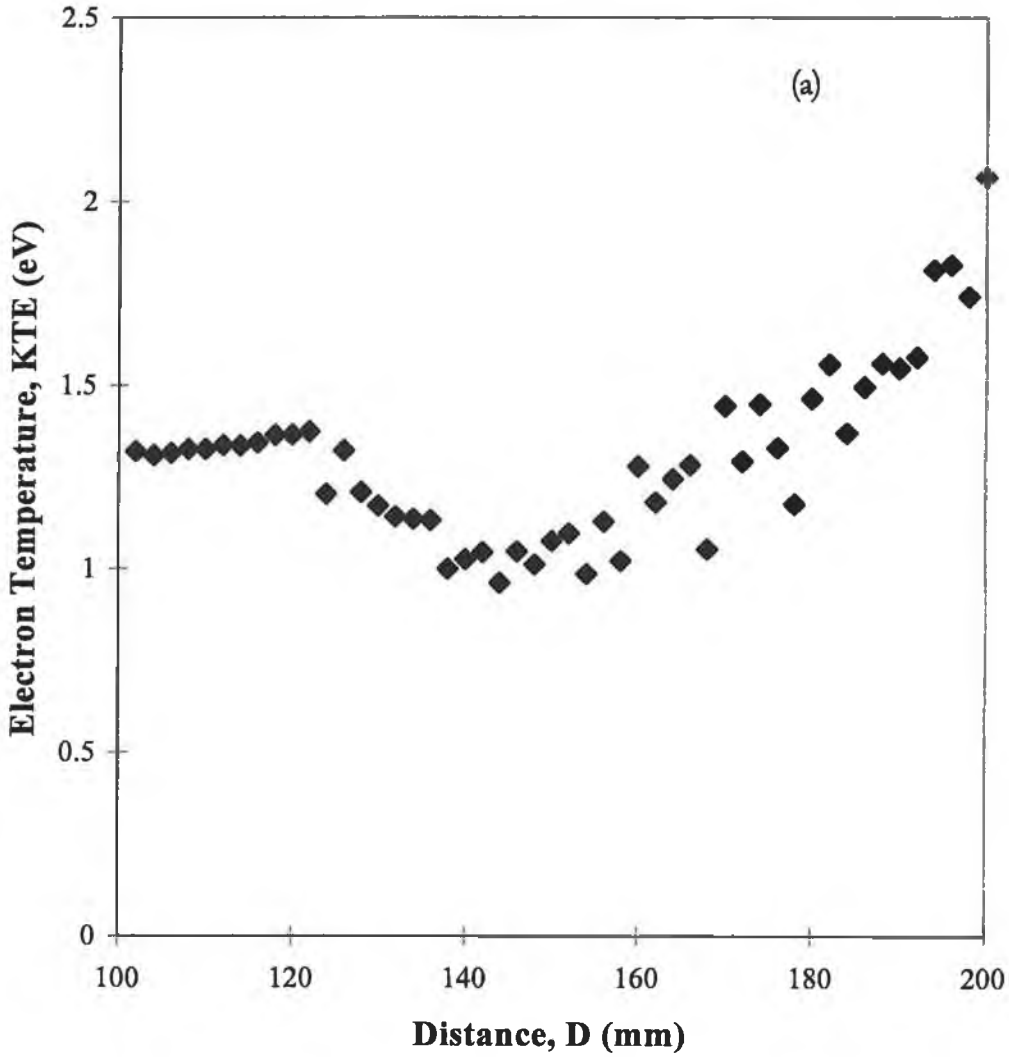

Figure 23: Electron Temperature as a function of distance of the probe (a) Bias-50V, 4.5A, 1060V, 6X10^{-4} mbar.

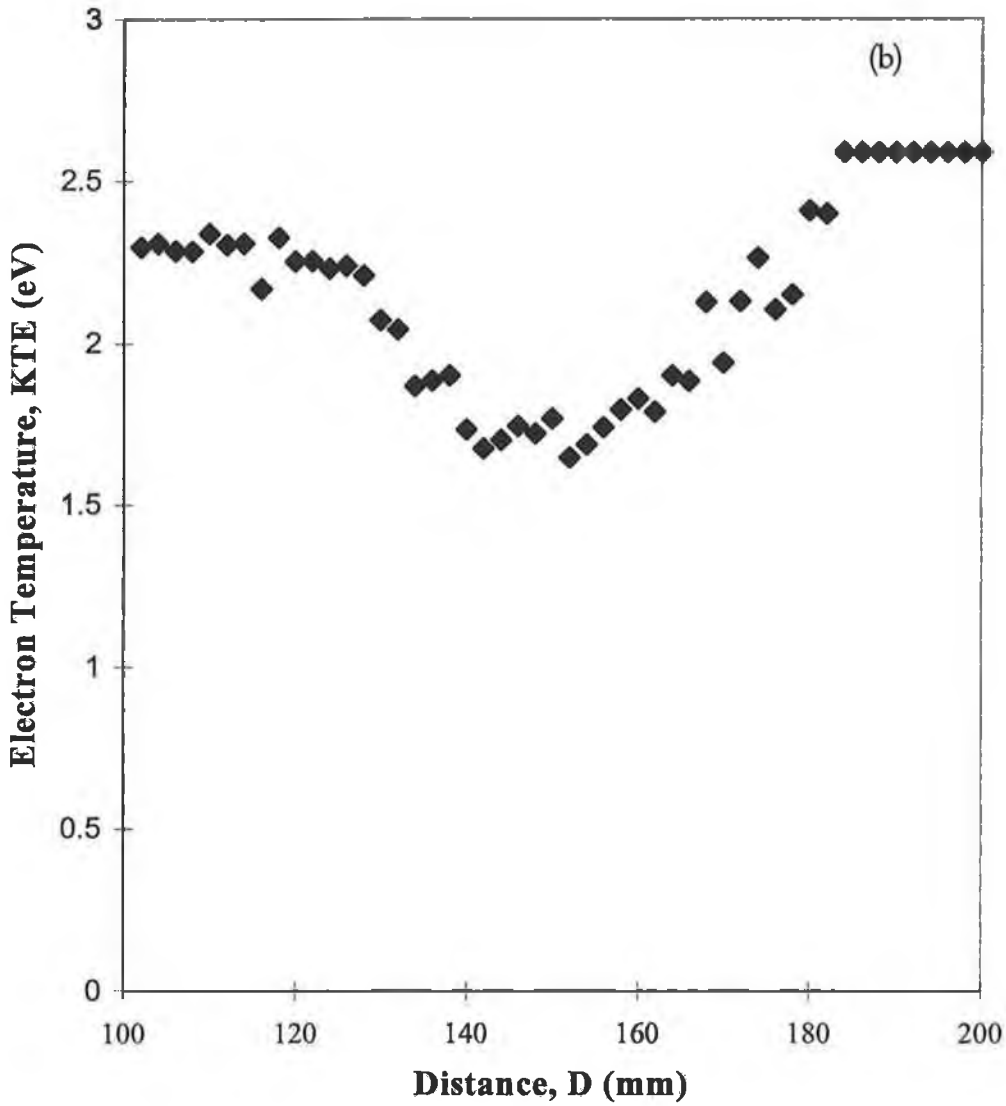

Figure 23: Electron Temperature as a function of distance of the probe (b) Bias -50V, 3.0A, 1143V, 1.5X10^{-4} mbar.

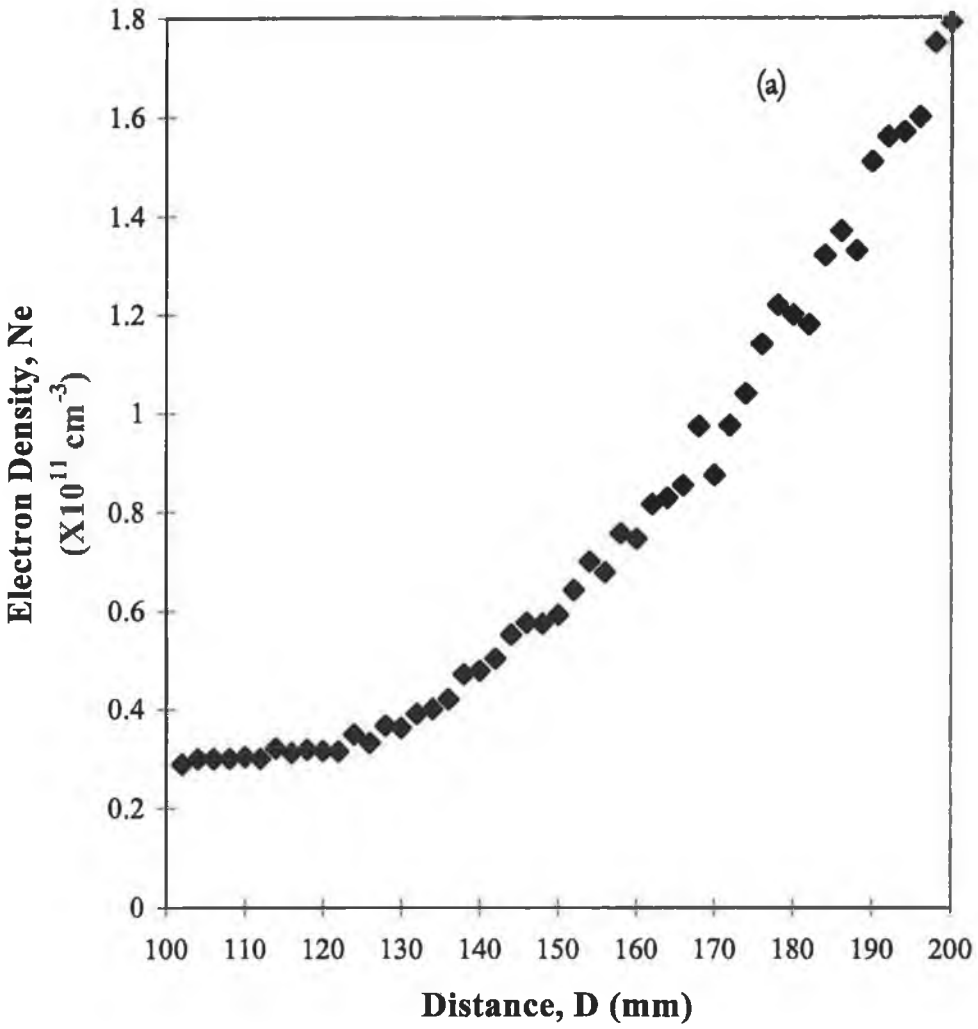

Figure 24: Electron Density as a function of distance of the probe (a) Bias -50V, 4.5A, 1060V, 6X10^{-4}mbar.

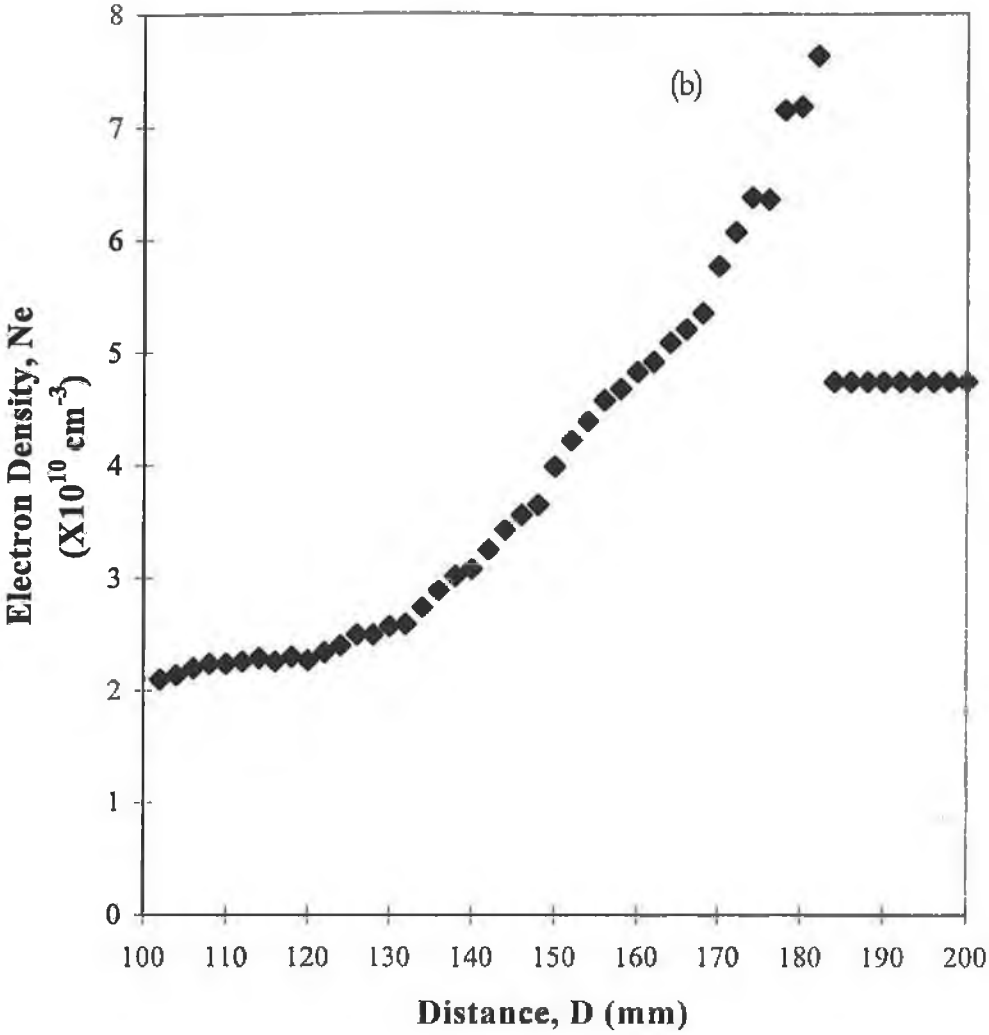

Figure 24: Electron Density as a function of distance of the probe (b) Bias -50V, 3.0A, 1143V, 1.5X10^{-4}mbar.

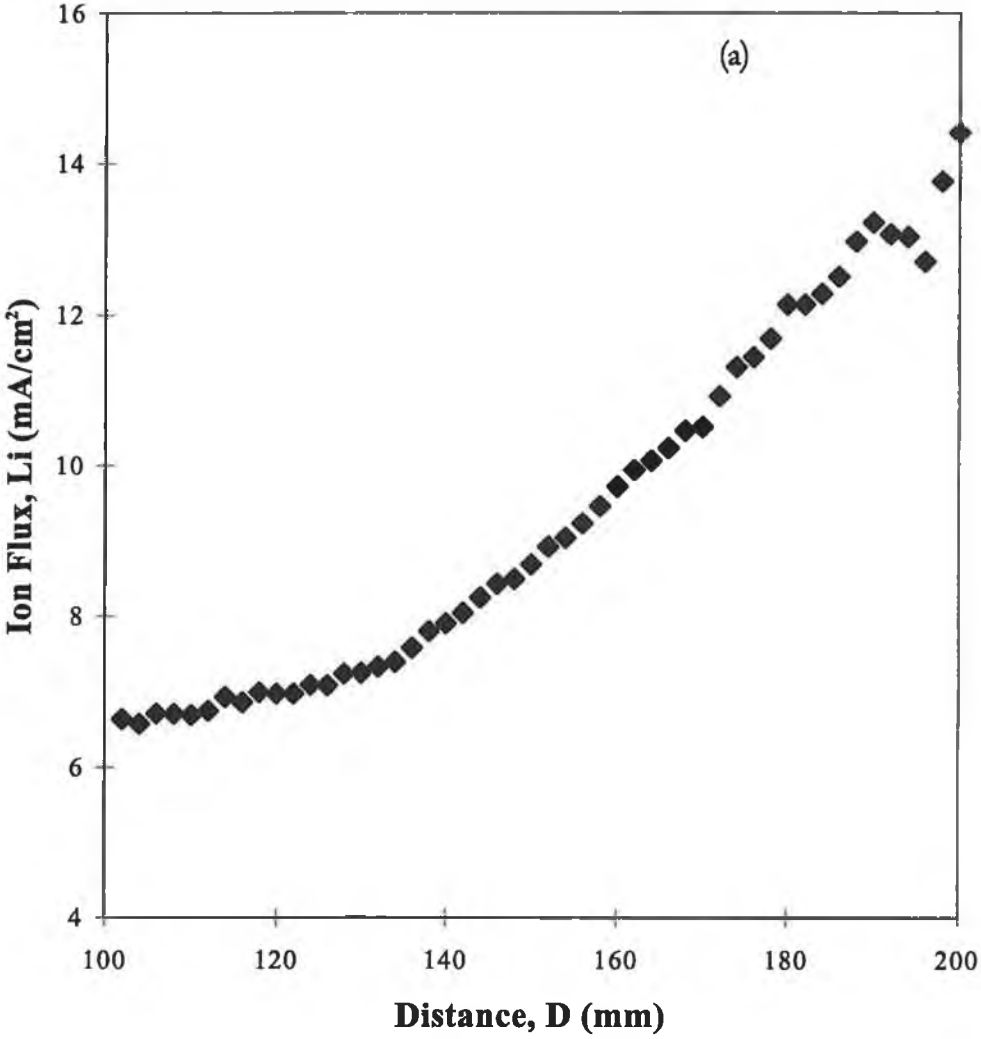

Figure 25: Ion Flux as a function of distance of the probe (a) Bias -50V, 4.5A, 1060V, 6X10^{-4}mbar.

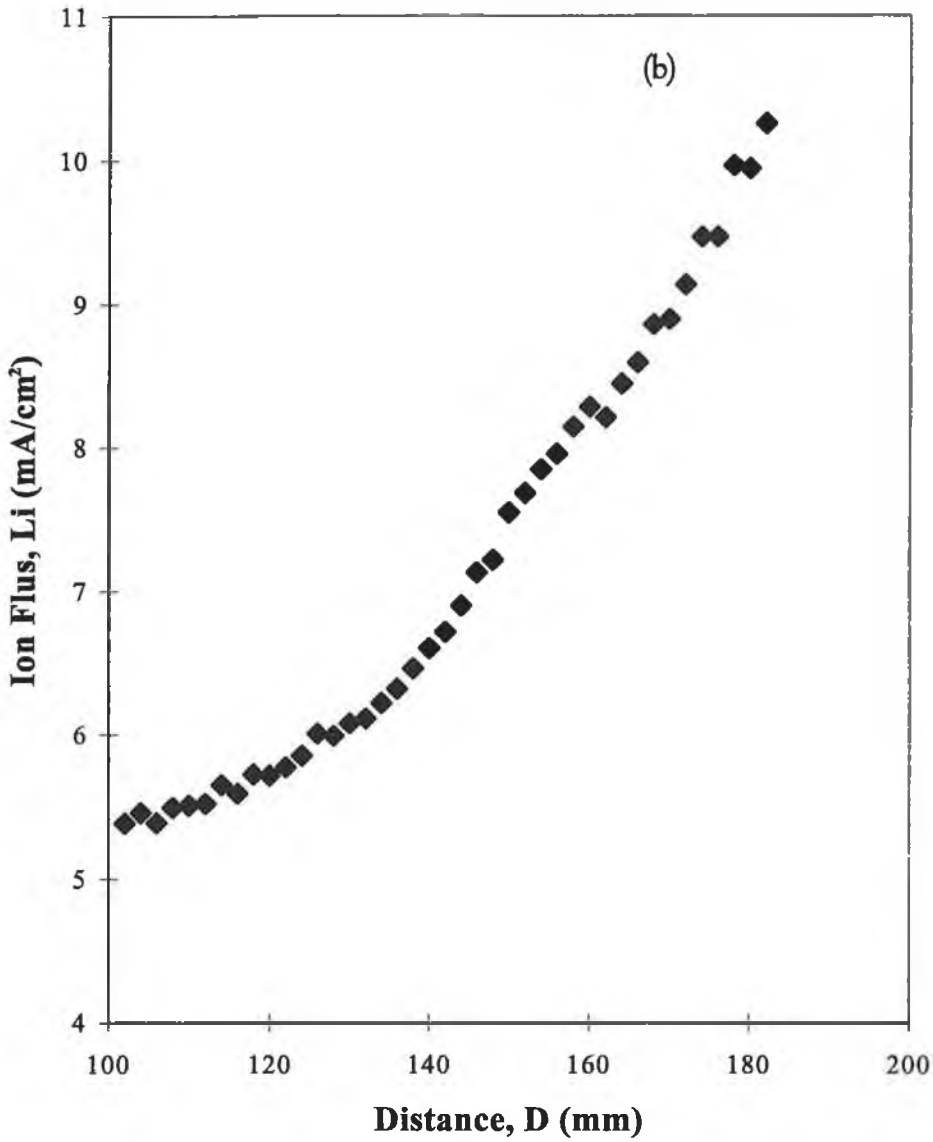

Figure 25: Ion Flux as a function of distance of the probe (b) Bias -50V, 3.0A, 1143V, 1.5X10^{-4}mbar.

Summary

Penning type opposed target magnetron system can be a good source for production of carbon nitride material. Complete entrapment of electrons can be possible by changing the position of the sources. Thus effective ion bombardment can be increased which eventually can increase nitrogen incorporation in the film.

The Langmuir probe measurements show that the source gives rise to magnetic confinement of the hot electrons in the inter-cathode space. They show that there is a high degree of ionisation exceeding 2% in the intense plasma region and that an electric field exists outside the anode and cathode sheaths.

Approximate calculations based on the film composition show that the ion to carbon atom ratio at the substrate is ~ 50 and that the ratio between the ionised and neutral nitrogen molecules at the substrate is ~ 0.25.

Optical emission from the plasma shows that there are CN radicals present in the plasma which come from nitrogen incorporation in the target rather than by chemical sputtering from the substrate.

References

1. C.J. Torng, J.M. Sivertsen, J.H. Judy, C. Chang, J. Mater. Res., 5 (11), 2490 (1990).

2. P.V. Kola, D.C. Cameron, B.J. Meenan, K.A. Pischow, C.A. Anderson, N.M.D Brown and M.S.J. Hashmi, Surface and Coatings Technology, 74-75, (1995), 696.

3. D. Li, X. Chu, S.C. Cheng, X.W. Lin, V.P. Dravid, Y.P. Chung, M.S. Wong, W.D. Sproul, Appl. Phys. Lett., 67 (2), 203 (1995).

4. H. Sjostrom, L. Hultman, J.-E. Sundgren, S.D. Hainsworth, T.F. Page, G.S.A.M. Theunissen, J. Vac. Sci. Technol. A 14 (1), 56 (1996).

5. W. Zheng, T. Ding, I. Ivanov and J.-E. Sundgren, J. Mater. Sci. Technol, 13, 154 (1997).

6. T. Okada, S. Yamada, Y. Takeuchi, T. Wada, J. Appl. Phys., 78 (12), 7416 (1995).

7. M.Y. Chen, X. Lin, V.P. Dradid, Y.W. Chung, M.S. Wong, W.D. Sproul, Tribology Transactions, 36 (3), 491 (1993).

8. T.A. Yeah, C.L. Lin, J.M. Sivertsen, J.H. Judy, IEEE Trans. Magn., Mag. 27 (6), 5163 (1991).

9. N. Nakayama, Y. Tsuchiya, S. Tamada, K. Kosuge, S. Nagata, K. Takahiro, S. Yamaguchi, Jpn. J. Appl. Phys., 32 (10A)(2), L1465 (1993).

10. F.M. Penning, Physica 3, 873 (1936).

11. M.J. Murphy, Ph.D. Thesis, Dublin City University, Ireland, 1996.

12. J.M.E. Harper in Kern and Vossen (Eds.), "Thin Film Processes", Academic Press, 178 (1978).

13. M. Naoe, S. Yamanaka and Y. Hoshi, IEEE Trans. Magn., Mag. 16 (5), 646 (1980.

14. B. Window, F. Sharples, J. Vac. Sci & Tech. A, 3, 10 (1985).

15. S. Kadokura, T. Tomie, M. Naoe, IEEE Trans. Magn., Mag. 17 (6), 3175 (1981).

16. Y. Hoshi, M. Kojima, M. Naoe, S. Yamanaka, IEEE Trans. Magn., Mag. 18 (6), 1433 (1982).

17. M. Matsuoka, Y. Hoshi, M. Naoe, J. Vac. Sci. & Tech. A, 5, 52 (1987).

18. M. Matsuoka, Y. Hoshi and M. Naoe, J. Appl. Phys., 60, 2096 (1986).

19. M. Matsuoka, M. Ono, Appl. Phys. Lett., 53, 2025 (1988).

20. M.J. Murphy, D.C. Cameron, J. Monaghan, A.K.M.S. Chowdhury, M. Tyrrell, R. Walsh, M. Monclus and M.S.J. Hashmi, "Dimag sputtering system and CNx film deposition", presented in the Int. Conf. on Thin Films and Metall. Coatings, San Diego, 22nd-26th April 1996.

21. P.V. Kola, Ph.D. Thesis, Dublin City University, Ireland, 1995.

22. E. Durand, "Electrostatique", Vol. 2, Masson, Paris, pp. 251 (1964).

23. Sheridan, M.J. Goeckner, J. Goree, J. Vac. Sci. & Tech. A, 8, 30 (1990)

24. A.M. Ferendeci, "Physical Foundations of Solid State and Electron Devices", McGraw-Hill, Inc., New York, 1991.

25. G.L. Moore, "Introduction to Inductively Coupled Plasma Atomic Emission Spectroscopy", pp. 6, Elsevier, New York, 1989.

26. M.Z. Karim, Ph.D. Thesis, Dublin City University, Ireland, 1993.

27. G. Herzberg, "Spectra of Diatomic Molecules", Van Nostrand Reinhold, Berlin, 1950.

28. R.W.B. Pearse and A.G. Gaydon, "The identification of Molecular Spectra", Chapman and Hall, London, 1976.

29. N. Hershkowitz in D.A. Glocker and S.I. Shah edn., "Handbook of Thin Film Processing Technology", Institute of Physics Publishing, Bristol, (1995).

30. M.B. Hopkins, J Res. Of the National Institute of Standards and Technology, 100, 415, 1995.

31. Sung. C.M and Sung. M., Materials Chemistry and Physics, 43, 1, 1996.

32. Marton. D, Boyd. K.J., Rabalais. J.W., International journal of Modern Physics B, 9 (27), 3527, 1995.

33. J.F. O'Hanlon, "A user's guide to vacuum technology", John Wiley & Sons, New York, 1989.

Chapter 5

Structural Determination: Techniques

In modern materials analysis one is concerned with the source of radiation, the beam of particles - photons, electrons, neutrons, or ions, the interaction cross section, the emergent radiation, and the detection system. The primary interest of this section is to introduce the techniques for materials characterisation (structural or mechanical). The energy of the emitted particles provides the signature or identification of the atom, the intensity tells the amount of atoms, i.e., sample composition.

In some cases the same incident and emergent radiation is employed. Listed below are examples with commonly used techniques

Electron in, electron out: Auger Electron Spectroscopy (AES)
Ion in, ion out: Rutherford Backscattering Spectroscopy (RBS)
X-ray in, electron out: X-ray Photo electron Spectroscopy (XPS)

A beam of particles incident on a target either scatters elastically or causes an electronic transition in an atom. The scattered particle or the energy of the emergent radiation contains the signature of the atom. The energy levels in the transition are characteristic of a given atom: hence, measurement of the energy spectrum of the emergent radiation allows identification of the atom.

The number of atoms per cm^2 in a target is found from the relation between the number of incident particles and the number of interactions. The term "cross section" is used as a quantitative measure of an interaction between an incident particle and an atom. The information required from analytical techniques is species identification, concentration, depth distribution, and structure. The available analytical techniques have different capabilities to meet these requirements. The

choice of analysis method depends upon the nature of the problem. For example, chemical bonding information can be obtained from techniques that rely upon transitions in the electronic structure around the atoms- the electronic spectroscopies. Structural determination is found from diffraction techniques.

Molecular structure of a material can be determined by vibrational spectroscopy. The spectrum coming from different vibrational frequency due to electromagnetic wave interaction with solid can be very useful for bond structure determination. IR and Raman spectroscopy differ in the means by which photon energy is transferred to the molecule and in the instrumentation used. Thus the information extracted from the spectrum could be different. The molecular vibration frequencies observed by both techniques are nearly the same, but the vibrational band intensities differ because of the different excitation mechanisms and therefore different selection rules. From a quantum mechanical point of view, a vibration is active in the infrared spectrum if the dipole moment of the molecule is changed during the vibration, and is active in the Raman spectrum if the polarizability of the molecules is changed during the vibration.

It is to be mentioned here that although a variety of characterisation techniques are available for elemental or structural analysis, their resolution for these analyses are not same. For examples, XPS and AES are extremely surface sensitive. The techniques can determine elemental analysis of the sample when the surfaces are extremely clean. In this case a technique is required to analyse the bulk of the material. RBS technique has recently became popular for this particular analysis. In case of diffraction techniques, electron diffraction is sometimes required to identify precisely the crystallography of the solid, as XRD sometimes is not sensitive for the atoms of lower atomic number. For mechanical characterisation the simplest ways to measure the mechanical properties of thin films is to deform them on a very small scale. Because indentation testing with a sharp indenter is a convenient means to accomplish this, nanoindentation, or indentation testing at the nanometre scale, has become one of the most widely used techniques for measuring the mechanical

properties of thin films. The chapter discusses briefly these characterisation techniques.

5.1 Rutherford Backscattering Spectroscopy (RBS)

Rutherford Backscattering Spectroscopy (RBS) is an analysis technique of very wide applicability. It is capable of giving depth profiles of major and minor constituents of thin films in the near-surface region. The probing beam of energetic (MeV) ions interact according to the Coulomb law with the target nuclei. If the beam energy is too high, the Coulomb barrier is exceeded and the scattering cross-section is no longer given by the analytical Rutherford expression, and as the beam energy decreases the screening effect of the atomic electrons increases. The screening effect correction is small for typical beams. The energy loss of scattered ions is given by simple kinematic relations together with knowledge of inelastic energy loss of ions in elemental materials. Since the interaction energies are so high no chemical effects are usually seen (these can only be observed for low-Z materials). Therefore in general it is very good approximation to assume that the energy loss in a compound is a linear superposition of the compound's elemental components. The detection probability of the scattered ions is close to 100% [1]. Scattered ions enter a solid state detector usually placed at a large backscattering angle.

The large angle scattering of MeV energy alpha particles by a gold foil, observed by Rutherford, established the atomic model of a positively charged heavy nucleus surrounded by a negatively charged electron cloud. While in those experiments the alpha particles were obtained from the decay of radioactive nuclei, nowadays accelerators are used to obtain a mono energetic beam of light particles, usually H^+ or He^+. In this work we used He^+. The beam is incident on a sample, where the incident particles collide with the nuclei of the sample material, are scattered backwards, and then detected. The processes involved are of classical nature and therefore easily quantifiable: from the energy of the backscattered particles one determines the target's elemental composition; from their intensity, one can determine the target's elemental concentration; and from the energy loss of the

particles while penetrating and coming out of the target, one determines the target's elemental depth distribution. The wide use of the Rutherford backscattering spectroscopy (RBS) technique, based on Rutherford's old experiment, provides the following analyses of materials:

1. The elemental composition of the compound

2. The amount of elements present in the compound

3. The location of the element inside the compound if it is to be analysed as impurity atoms.

5.1.1 Fundamentals

An incident beam of particles with mass m and energy E_o is backscattered at the surface of a sample by atoms with mass M (figure. 1).

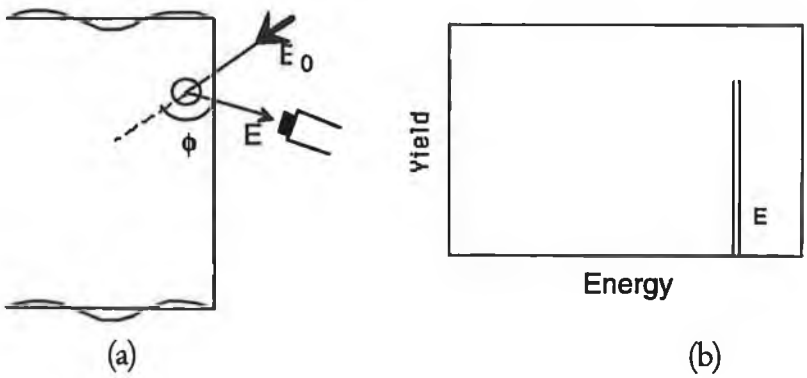

Figure 1: Backscattering phenomena (a) an incident beam of particles is backscattered at the surface of a sample by atoms; (b) the corresponding RBS spectrum.

The energy E of the backscattered particles depends only on the sample atom M and known quantities (E_o, m and the scattering angle Φ), through the kinematic factor [1]

$$k = \frac{E}{E_o} = \left[\frac{\left(M^2 - m^2 \sin^2 \Phi\right)^{1/2} + m\cos\Phi}{M + m} \right]^2 \qquad (1)$$

Hence, measuring E the elemental analysis of the thin film can be done. When more than one species is present in the sample (figure 2), the relative intensity of the respective signals (E_1 corresponding to mass M_1 of the first species and E_2 to M_2 of the second) depends on their concentrations through the known cross-sections (σ) [1]

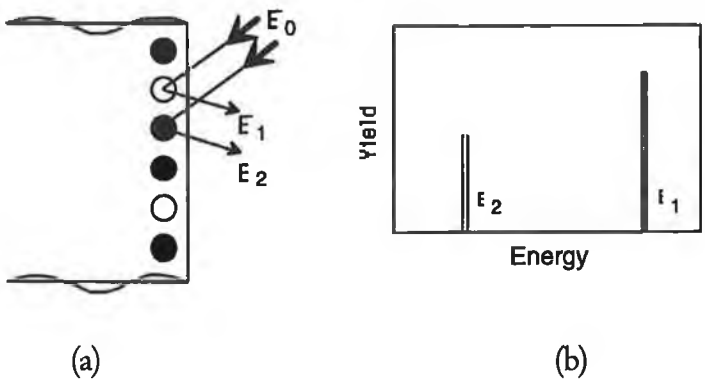

Figure 2: Backscattering phenomena; (a) when the material is composed of two different kind of atoms; (b) the corresponding RBS spectrum.

$$\sigma(\Phi) = \left[\frac{Z_m Z_M e^2}{4E} \right]^2 \frac{4}{\sin^4 \Phi} \frac{\left[\left[1-(m/M)^2 \sin^2 \Phi\right]^{1/2} + \cos\Phi\right]^2}{\left[1-(m/M)^2 \sin^2 \Phi\right]^{1/2}} \qquad (2)$$

Thus, the atomic percentage of an element can be measured by eqn. 2. The identity of target atoms is established by the energy of the scattered particle after an elastic collision. The number N_s of target atoms per unit area is determined by the probability of a collision between the incident particles and target atoms as measured by the total number Q_D of detected particles for a given number Q of particles incident on the target in the geometry shown fig 3. The connection between the number of target atoms N_s and detected particles is given by the scattering cross section. For a thin target of thickness t with N atoms/cm^3, N_s =Nt. For the geometry shown in the figure 3 the number N_s of target atoms/cm^2 is related to the

yield Y or the number Q_D of detected particles (in an ideal, 100% efficient detector that subtends a solid angle Ω) by [1]

$$Y = Q_D = \sigma(\Phi).\Omega.Q.N_S \tag{3}$$

where Q is the total number of incident particles in the beam. The cross-section term, σ(Φ) has the dimensions of an area.

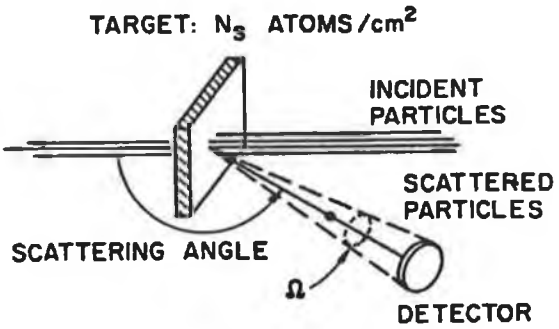

Figure 3: Simplified layout of a scattering experiment to demonstrate the concept of the differential scattering cross section. Only primary particles that are scattered within the solid angle dΩ spanned by the detector are counted [1].

The incident particles lose energy when going through the material, mainly due to electronic scattering (figure 4).

When a particle is scattered by an atom at a certain depth Δt, its energy will be reduced. It further loses energy on the way back through the sample. For small thickness the reduction in detected energy amounts to

$$[S] = \frac{\Delta E}{\Delta t} = K.\frac{dE}{dt}\Big|_{E_o} + \frac{dE}{dt}\Big|_{E_o'} / |\cos\Phi| \tag{4}$$

at normal incidence, where E_o' is the energy of the incident particle immediately after scattering, and [S]=dE/dt is the stopping power of the incident particle in the

given sample. As this quantity is known for most elements, the location of a certain element can be easily found [2].

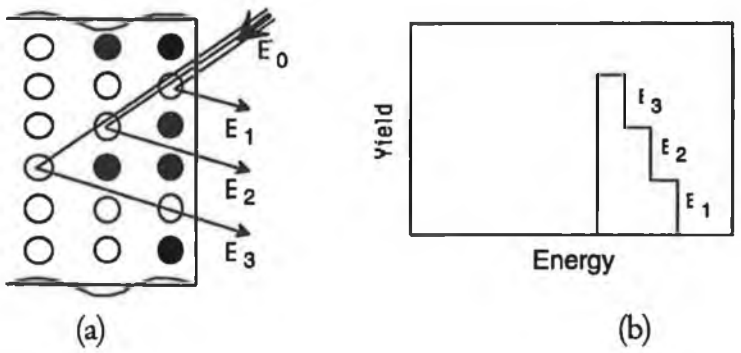

Figure 4: Energy loss during backscattering phenomena; (a) the incident particle lose energy (1)when travelling through the specimen thickness (2) on the way back through the sample; (b) the corresponding RBS spectra.

5.1.2 Experimental details

The line 4-Middle of the University of Surrey 2 MeV Van de Graff accelerator was used for RBS study. The beam was 1.5 MeV He^+ and the scattering angle "Φ" was 160^0 in the IBM geometry, i.e. with the detector located in an horizontal plane with the beam and with an energy spread not exceeding ±0.1%. It is one of the two standard RBS geometries, developed at IBM laboratories. Different angles of incidence were used to separate the carbon and nitrogen signals due to the film from the silicon signal from the substrate. The optimum angle differed from sample to sample due to the different thickness of the films. The atomic percentage ratios were determined with an error of between 5 and 10%. This was possible to achieve because of the absence of background due to heavy elements. Standard calibration procedure was carried out to calibrate the apparatus [3-5].

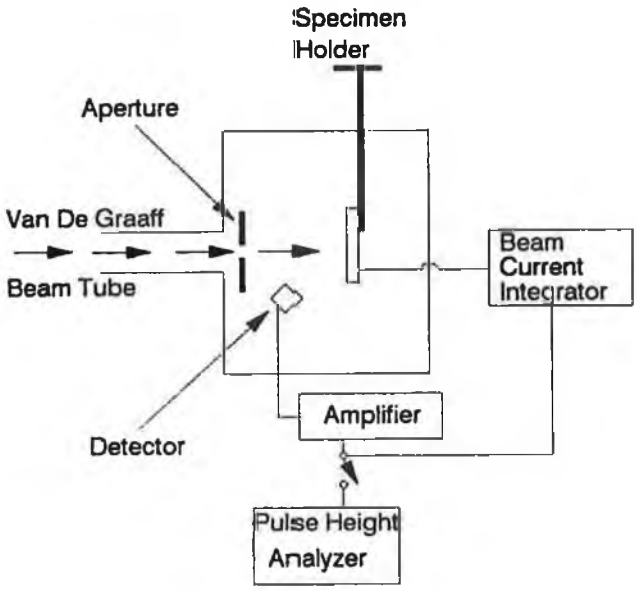

Figure 5: The experimental arrangement for RBS experiments. (Courtesy Surrey Centre for Research in ion beam applications, University of Surrey, UK)

A typical arrangement for RBS experiments is shown in figure 5. The specimen is held on a stage electrically isolated from the chamber so that the incident beam current can be measured. The choice of stage is determined by the requirements of the experiment and may include a multi-specimen capability, X-Y motion or angular movement for crystallographic studies. The elastically scattered ions are detected using a solid state detector capable of angular scanning.

5.1.3 Data Analysis

As seen from eqn.1, the heavier the element, the more energy it will backscatter with, thus light elements will be in the low energy region of the spectrum, superimposed with the signal of heavier elements at large depths. On the other hand, equation 2 means that the scattering cross section is much larger for heavier elements than for light ones, thus if we have film composed of light elements on top of a heavier substrate, as in this work, the relatively weak signal from the film will be superimposed to a larger background signal from the substrate. However, if a careful

analysis is done, high precision can nevertheless be achieved. The first step is to determine the height H of the signals of each elements. Then, since the scattering cross sections σ and the stopping powers [S] are known, the concentrations of C and N in a carbon nitride film can be measured by [3-6]

$$N_N/N_C = H_N/H_C.\sigma_C/\sigma_N.[S]_N/[S]_C \quad (5)$$

A similar formula applies to any other elements that might be present in the sample, such as Fe or O.

5.2 Fourier Transform Infrared (FTIR) and Raman Spectroscopy

Electromagnetic radiation is a good source to understand the bonding structure of compounds when it interacts with the atoms of that compound. Electromagnetic radiation, of which visible light forms an obvious but very small part, may be considered as a simple harmonic wave propagated from a source and travelling in straight lines except when refracted or reflected. The properties which undulate, corresponding to the physical displacement of a stretched string vibrating, or the alternate compression and rarefaction of the atmosphere during the passage of a light wave, are interconnected electric and magnetic fields. This is the basis of molecular spectroscopy. The section discusses the basic principles of FTIR and Raman spectroscopy.

5.2.1 Fundamentals

When electromagnetic radiation interacts with matter, the undulatory electromagnetic fields giving rise to spectrum and can give information of the bonding structure of a molecule. As a first approximation, it is possible to separate the energy of a molecule into three additive components associated with (1) the rotation of the molecule (2) the vibrations of the constituent atoms and (3) the motion of the electrons in the molecule. The basis of this separation lies in the fact that the velocity of electrons is much greater then the vibrational velocity of nuclei, which is again much greater then the velocity of molecular rotation. If a molecule is

placed in an electromagnetic field (e.g. light), a transfer of energy from the field to the molecule will occur only when Bohr's frequency condition is satisfied [7]

$$\Delta E = h\nu \tag{6}$$

where ΔE is the difference in energy between two quantized states, h is Planck's constant, and ν is the frequency of the light. If [7]

$$\Delta E = E'' - E' \tag{7}$$

where E'' is a quantized state of higher energy than E', the molecule absorbs radiation when it is excited from E' to E'' and emits radiation of the same frequency as given by Eq. 6 when it is reverts from E'' to E'.

Because rotational levels are relatively close to each other, transitions between these levels occur at low frequencies (long wavelengths). In fact, pure rotational spectra appear in the range between 1 cm^{-1} and 10^2 cm^{-1} [7]. The separation of vibrational energy levels is greater, and the transitions occur at higher frequencies (shorter wavelengths) than do the rotational transitions. As a result, pure vibrational spectra are observed in the range between 10^2 cm^{-1} and 10^4 cm^{-1} [7]. Finally, electronic energy levels are usually far apart, and electronic spectra are observed in the range between 10^4 cm^{-1} and 10^6 cm^{-1} [7]. Thus pure rotational, vibrational, and electronic spectra are usually observed in the microwave and far-infrared, the infrared, and the visible and ultraviolet regions, respectively. This division into three regions, however, is to some extent arbitrary, for pure rotational spectra may appear in the near-infrared region ($1.5 \sim 0.5 X 10^4$ cm^{-1}) if transitions to higher excited states are involved, and pure electronic transitions may appear in the near-infrared region if the levels are closely spaced [7].

Figure 6 illustrates transitions of the three types mentioned for a diatomic molecule. As the figure shows, rotational intervals tend to increase as the rotational quantum number J increases, whereas vibrational intervals tend to decrease as the vibrational quantum number ν increases. The dotted line below each electronic level indicates

the zero point energy that exists even at a temperature of absolute zero as a result of nuclear vibration. It should be emphasized that not all transitions between these levels are possible. To see whether the transition is allowed or forbidden, the relevant selection rule must be examined. This, in turn, is determined by the symmetry of the molecule. Actually vibrational problems like those mentioned above can be solved for polyatomic molecules in an elegant manner by the use of group theory. The discussion of the group theory is not the scope of this thesis, only relevant points may come when needed.

Since this section is concerned only with vibrational spectra, no description of electronic and rotational spectra is given. Although vibrational spectra are observed experimentally as infrared or Raman spectra, the physical origins of these two types of spectra are different. Infrared spectra originate in transitions between two vibrational levels of the molecule in the electronic ground state and are usually observed as absorption spectra in the infrared region. On the other hand, Raman spectra originate in the electronic polarization caused by ultraviolet or visible light. If a molecule is irradiated by monochromatic light of frequency ν, then, because of electronic polarization induced in the molecule by this incident light, light of frequency ν (Rayleigh scattering) as well as of $\nu \pm \nu_I$ (Raman scattering) is emitted (ν_I represents a vibrational frequency). Thus the vibrational frequencies are observed as Raman shifts from the incident frequency ν in the ultraviolet or visible region.

Although Raman scattering is much weaker than Rayleigh scattering (by a factor of 10^{-3} to 10^{-4}), it is possible to observe the former by using a strong exciting source [7]. There are number of lasers which are used for Raman scattering, but we will use He-Ne (632.8 nm, 15,803 cm^{-1}, red) for Carbon Nitride thin film characterisation. Two types of Raman are currently being used for structural determination; (1) Normal Raman; (2) Resonance Raman. In normal Raman spectroscopy, the exciting frequency lies in the region where the compound has no electronic absorption band. In resonance Raman spectroscopy, the exciting frequency falls within the electronic band and can provide electronic properties of the material. In our current study we will only use normal Raman to analyse the vibrational characters only.

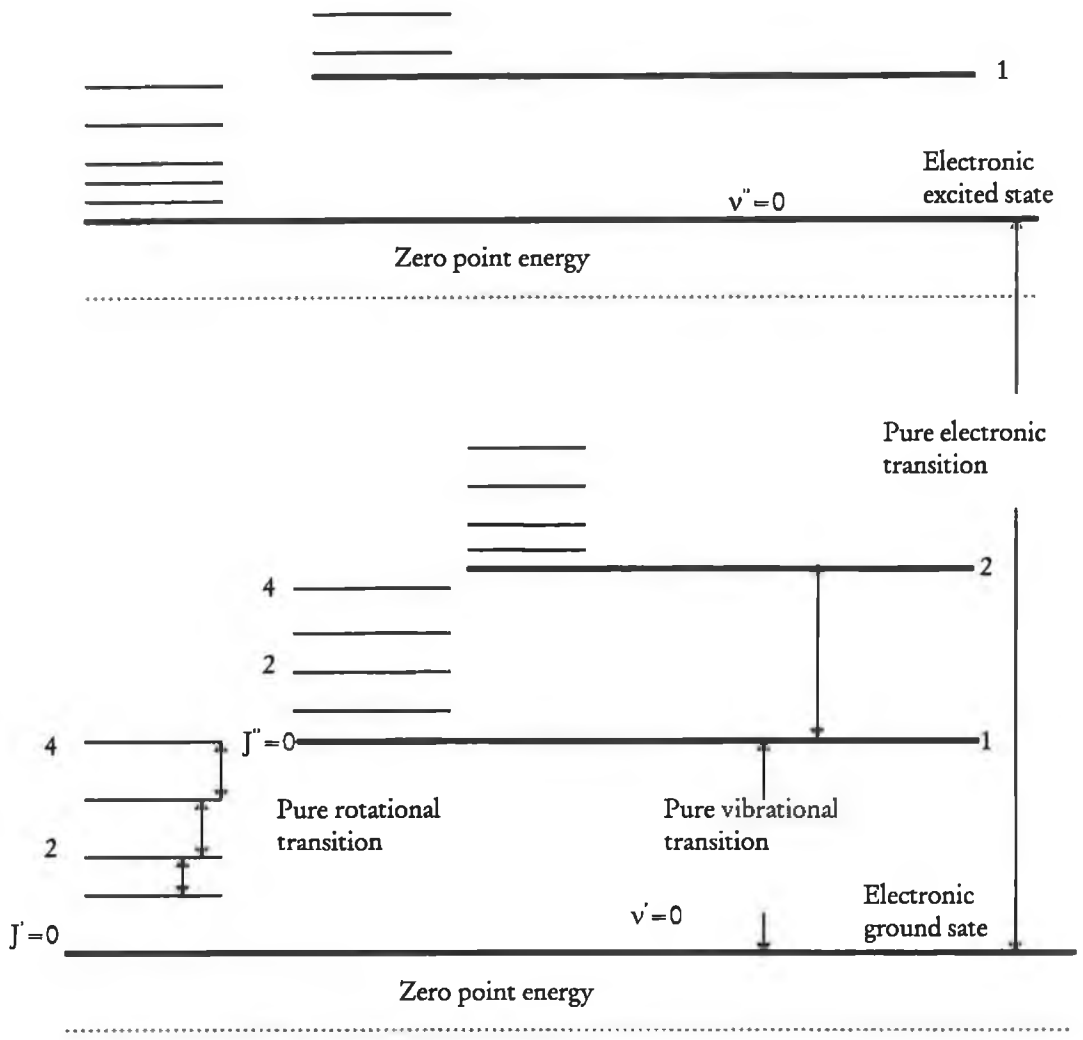

Figure 6: Energy levels of a diatomic molecule [7]. (The actual spacings of electronic levels are much larger, and those of rotational levels much smaller, than those shown in the figure)

The electronic properties of the CN compound will be analysed by X-ray photo electron spectroscopy (XPS) and Auger electron spectroscopy (AES) in later sections.

The origin of Raman spectra can be explained by an elementary classical theory. If we consider a light wave of frequency ν with an electric field strength E, since E fluctuates at frequency ν, we can write [7]

$$E = E_o \cos 2\pi\nu t \tag{8}$$

where E_o is the amplitude and t the time. If a diatomic molecule is irradiated by this light, the dipole moment P given by [7]

$$P = \alpha E = \alpha E_o \cos 2\pi\nu t \tag{9}$$

is induced. Here α is a proportionality constant and is called the polarizability. If the molecule is vibrating with frequency ν_1, the nuclear displacement q is written as [7]

$$q = q_o \cos 2\pi\nu_1 t \tag{10}$$

where q_o is the vibrational amplitude. For small amplitudes of vibration, α is a linear function of q. Thus we can write [7]

$$\alpha = \alpha_o + \left(\frac{\partial\alpha}{\partial q}\right)_o q \tag{11}$$

Here α_o is the polarizability at the equilibrium position, and $\left(\frac{\partial\alpha}{\partial q}\right)_o$ is the rate of change of α with respect to the change in q, evaluated at the equilibrium position. If Eqs. 9 and 11 are combined and expressed in terms of eqns 10 and 11, they become [7]

$$P = \alpha E_o \cos 2\pi\nu t$$

$$= \alpha_o E_o \cos 2\pi\nu t + \left(\frac{\partial\alpha}{\partial q}\right)_o q_o E_o \cos 2\pi\nu t \cos 2\pi\nu_1 t$$

$$= \alpha_0 E_0 \cos 2\pi\nu t + \frac{1}{2}\left(\frac{\partial\alpha}{\partial q}\right)_o q_o E_o \left\{\cos\left[2\pi(\nu+\nu_1)t\right] + \cos\left[2\pi(\nu-\nu_1)t\right]\right\} \qquad (12)$$

According to classical theory, the first term describes an oscillating dipole which radiates light of frequency ν (Rayleigh scattering). The second term gives the Raman scattering of frequencies $\nu+\nu_1$ (anti-Stokes) and ν-ν_1 (Stokes). If $\left(\frac{\partial\alpha}{\partial q}\right)_o$ is zero, the second term vanishes. Thus the vibration is not Raman active unless the polarizability changes during the vibration.

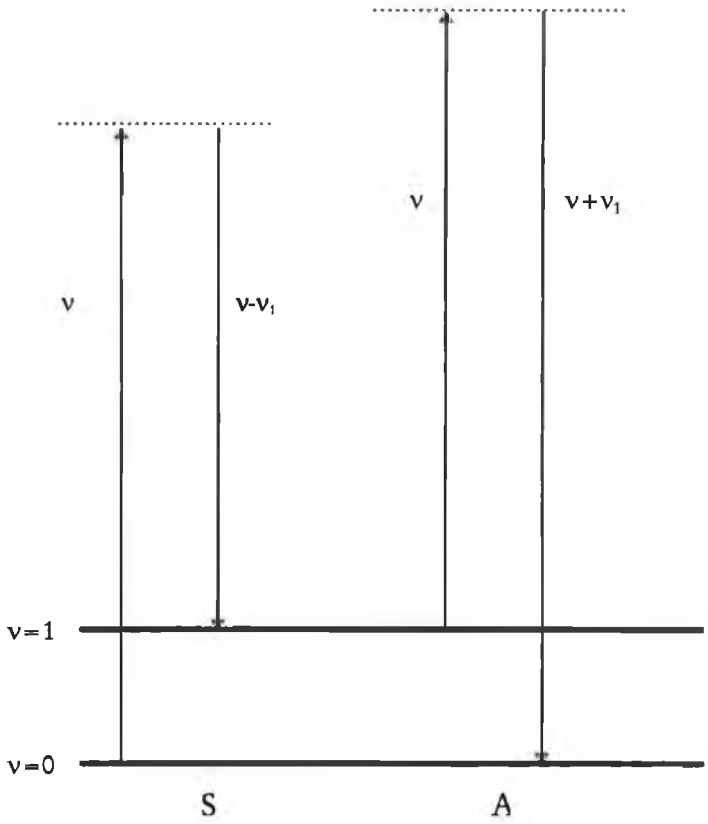

Figure 7: Mechanisms of normal Raman scattering: S, Stokes; A, anti-Stokes. The dashed lines represent the virtual state [7]

Figure 7 illustrates the mechanisms of normal Raman scattering. In this case, the energy of the exciting line falls far below that required to excite the first electronic transition. In the case of Stokes lines, the molecule at $\nu = 0$ is excited to the $\nu = 1$ state by scattering light of frequency ν-ν_1. Anti-stokes lines arise when the molecule initially in the $\nu = 1$ state scatters radiation of frequency $\nu+\nu_1$ and reverts to the $\nu = 0$ state. Since the population of molecules is larger at $\nu = 0$ than at $\nu = 1$ (Maxwell-Boltzmann distribution law), the Stokes lines are always stronger than the anti-Stokes lines. Thus it is customary to measure Stokes lines in Raman spectroscopy.

According to the selection rule for the harmonic oscillator, any transitions corresponding to $\Delta\nu\pm1$ are allowed. Under ordinary conditions, however, only the fundamentals that originate in the transition from $\nu = 0$ to $\nu = 1$ in the electronic ground state can be observed because of the Maxwell-Boltzmann distribution law. In addition to the selection rule for the harmonic oscillator, another restriction results from the symmetry of the molecule. Thus the number of allowed transitions in polyatomic molecules is greatly reduced. The overtones (multiples of some fundamentals) and combination bands (the sum or difference of two or more fundamentals) of these fundamentals are forbidden by the selection rule of the harmonic oscillator. However, they are weakly observed in the spectrum because of the anharmonicity of the vibration. Since they are less important than the fundamentals, we will ignore them or discuss only when necessary.

5.2.2 Absorption Coefficient of thin Film

Infra-red spectroscopy is normally carried out by passing a beam of IR radiation through a sample (film + substrate) and recording which frequencies are absorbed. This technique is often referred to as transmission or absorption spectroscopy. Such a method is not easily applicable to surface studies, because of the difference in refractive indices of the media, substrate (here Si) and the film which causes internal reflection. The film and the substrate absorb the incident IR radiation and the appropriate frequency interacts with vibrations of the species. To be more accurate, the media through which the radiation is passing should be considered. In this case

multiple internal reflection (MIR) of the radiation occurs at the film-substrate, substrate-air, film-air interface [8-11]. To calculate the absorption coefficient of the film, the IR absorbance curve is simulated taking consideration of MIR. Transmission, absorption and reflection of the radiation are shown in the figure 8.

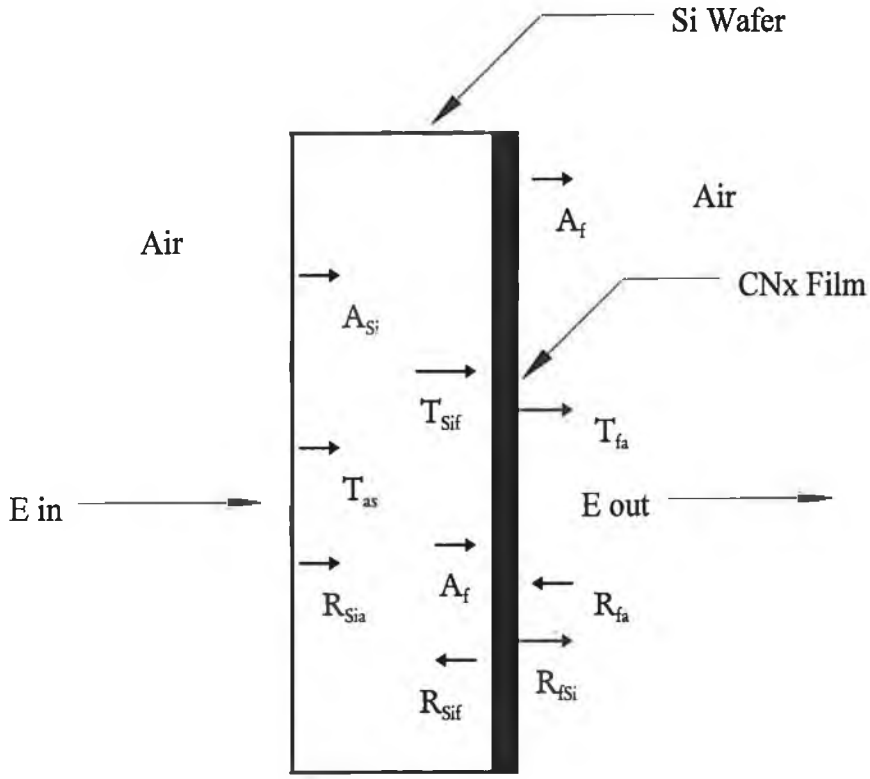

Figure 8: Transmission, multiple internal reflection and absorption of IR radiation through Air-Si-Film-Air interfaces.

For calculation of the absorption coefficient of CN film, IR absorption measured by using a Perkin Elmer FTIR 2000 system, was simulated. The basic equations to calculate the absorbance peaks are

$$\frac{E_{out}}{E_{in}} = \frac{T_{fa}.T_{Sif}.T_{aSi}.A_f.A_{Si}}{(1-A_f^{\,2}).(1-A_{Si}^{\,2}).R_{fa}.R_{Sif}.R_{Sia}.R_{fSi}} \qquad (13)$$

where, E_{in} and E_{out} are radiation before and after interaction respectively, T_{fa}, T_{sif} and T_{aSi} indicate transmission through film-air, Si-film and air-Si respectively, A_f and A_{si} are absorption of radiation by film and Si substrate respectively, R_{fa}, R_{fSi}, R_{sia} and R_{sif}

represents reflection at the film-air, film-Si, Si-air and Si-film interface respectively. Absorption by the Si and film can be calculated by the well known electro-magnetic wave equations [12]

$$\alpha_{Si} = R_e(\alpha_{Si}) + jI_m(\alpha_{Si}) \tag{14}$$

$$\alpha_f = R_e(\alpha_f) + jI_m(\alpha_f) \tag{15}$$

It can be noted that equations 14 and 15 have a real and an imaginary part. For Si, the imaginary part can be ignored considering (1) the surfaces of the Si are not parallel because of the roughened back of the wafers which destroys phase coherence of the transmitted radiation; and (2) the resolution of the instrument is too low to resolve any oscillation in absorbance in the Si which is thick compared to the film. But for the film the imaginary part should be considered. Here R_e and I_m are amplitude and phase related terms, respectively.

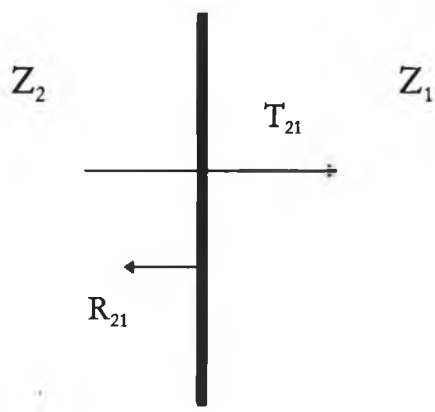

Figure 9: Illustrates the reflection and transmission coefficient between two media 1 and 2.

Transmission between two media can be calculated by

$$T_{21} = \frac{2Z_1}{Z_1 + Z_2} \tag{16}$$

where, T_{21} is the transmission coefficient between media 1 and 2; Z_1 and Z_2 (figure 9)are the impedance of media 2 and 1 respectively. Reflection coefficient between two media can be calculated by

$$R_{21} = \frac{Z_1 - Z_2}{Z_1 + Z_2} \tag{17}$$

where, R_{21} is the reflection coefficient between media 1 and 2.

5.2.3 Instrumentation of FTIR and Raman spectroscopy

The FTIR absorption was measured using a Perkin-Elmer FTIR 2000 system The scanning resolution was 1 cm^{-1}. A deuterated tri-glycine sulphate (DTGS) detector was used for the reflected beam. All the scans were performed at room temperature and normal atmospheric conditions. The specific absorbance of the various peaks due to CN bonding was found from the peak height taking account the background absorption and multiple internal reflections in the films. Strictly, the peak area should be used, however, the peak height gives an adequate demonstration of the trends.

Raman spectra were obtained using a Kaiser system Holoprobe Raman with a He-Ne (633 nm) laser and a Peltier cooled Princeton CCD camera. The scanning resolution was 1 cm^{-1}. A single monochromator and microscope mode with normal incidence were used. Rayleigh scattering was eliminated by the use of two high performance notch filters. The objective lens focal length to diameter ratio was 1.8.

5.3 Electron Spectroscopy

Electrons from various atomic levels ejected during radiation-matter interaction processes may be used to gather analytical data on materials, provided their energy is characteristic of their origin atom. Electron emission may involve any atomic levels, from core levels to external levels, thus resulting in a rather complicated spectrum. Its sensitivity to the chemical state of atoms leads to line shifts which in turn

provides data on chemical bonds. The energy of electrons issued from excitation-relaxation processes are mainly in the low-energy range and are therefore strongly absorbed in the specimen. Those which are able to leave the specimen surface to be measured are therefore issued from a thin surface layer which has a thickness of the order of the electron mean free path. As a result, electron spectrometry is mainly a method of surface analysis. Depending on the primary radiation, the following electron emission may be observed:

1. X-ray excitation generates photoelectrons and Auger electrons.

2. Electron excitation generates secondary electrons and Auger electrons.

5.3.1 Principles of X-ray photo electron spectroscopy (XPS)

For an incident photon beam to be able to excite the X-level of an element A in a specimen, its energy E_o must be higher than the binding energy W_X of the level. The result is then ejection of photo electrons from this level, with a kinetic emission energy (E_o - W_X). Those photoelectrons are able to leave the specimen to be measured if their energy, when arriving at the surface, is greater than the work function $e\Phi$ (Φ is the potential barrier of the solid).

The kinetic energy E of the outgoing photoelectron can therefore be expressed by the following expression [13]

$$E \leq E_p = E_o - W_X - e\Phi \qquad (18)$$

The maximum energy value E_p is related to photoelectrons issuing from a surface layer of thickness equal to their escape depth which can be assimilated in their mean free path "l". Those generated at greater depths loose more or less important fraction of their energy through interactions along their path of the surface. The resulting energy spectrum is therefore dissymmetrical, with a sharp peak at the maximum value E_p, corresponding to the predominance of surface photoelectrons. For a primary monochromatic radiation and for a given value of the work function $e\Phi$,

measuring the energy of these photoelectron peaks leads directly to the energy levels W_X of the atoms in the surface layer of thickness l of the specimen. The mean free path l is of the order of a few nanometres for the commonly observed photoelectron energy range of a few kiloelectronvolts. In addition to identifying the elements, the measurement of the values of E_p, when compared to their corresponding values in standards, provides data on chemical bonds. The photo electron process is shown in figure 10(a).

5.3.1.1 Core Level Spectra and Chemical Shift

The core-level binding energy (BE) is in effect a direct reflection of the electronic structure of an atom. The variation in both position and width of core-level peaks allows the identification of the atoms' electronic environment. The peak width, defined as the full width at half-maximum (FWHM) ΔE, is a convolution of several contributions [14]

$$\Delta E = \left[\Delta E_n^{\ 2} + \Delta E_p^{\ 2} + \Delta E_a^{\ 2}\right]^{1/2} \tag{19}$$

Where ΔE_n is the natural width of the core level, ΔE_p is the width of the photon source (X-ray line) and ΔE_a the analyser resolution.

The binding energies of core-levels reveal much about the central atom. As a rule, the BE will increase as the electronegativity of the attached atoms or groups increases. However, many cases arise in which distinct chemical states give rise to photo-electron peaks whose relative chemical shift is sufficiently small for the peaks to overlap. In principle line-width shifts of 0.2 eV should be measurable, but this is impossible if the contributory peaks have a line-width of typically ~ 2 eV. Deconvolution of these peaks may be and often is attempted [14].

5.3.2 X-ray Photo electron Valence band spectra

The valence band spectra related closely to the occupied density of states structure. This is very useful in the study of the electronic structure of materials. In case of carbon based material, valence bands reveal structural information often unobtainable from core-level studies. Thus it is first very necessary to consider the factors that contribute to the photoemission intensity.

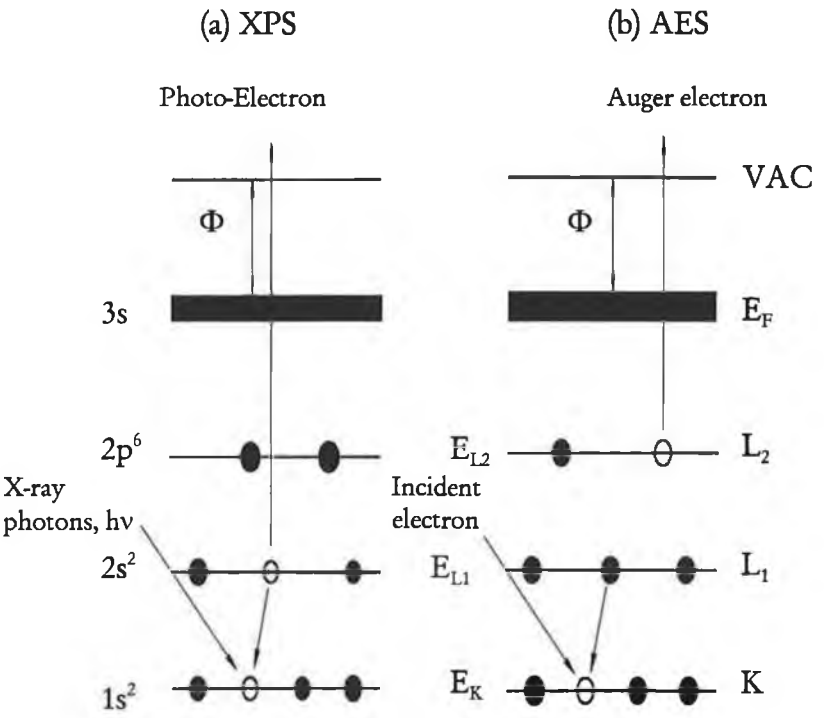

Figure 10: Two Kinds of electron spectroscopy. (a) XPS - here X-ray photons are interacting with electrons at the core level of the atom, as a result the excited electron is coming off the atom leading to the emission of the X-ray line $K\alpha_1$; (b) AES- relaxation process through a non-radiative transition KL_1L_2, laeding to the emission of an Auger electron.

The photoemission intensity at a given energy E may be written given by the expression [15]

$$I(E) \propto p^{i}(E)\sigma(h\omega, E) \tag{20}$$

where $p^{i}(E)$ is the density of initial states in a system and σ is the cross section for the process (assuming one-electron-transition model). In carbon, the cross section term is very important as this term is a function of E in the valence band region. The valence bands arise mostly from the 2s and 2p atomic levels for carbon and the cross-section, σ ratio for photoemissivity by Mg K_α X-rays can be given by the expression [16]

$$\frac{\sigma_p}{\sigma_s} = \frac{I_p}{I_s}\frac{N_s}{N_p} \tag{21}$$

where s and p densities of states N_s and N_p and their contributions to the energy distribution curves (EDC) I_s and I_p [16]. The I_s/I_p of EDC in the valence band spectrum varies due to the change in photoionisation cross sections ratio, σ_s/σ_p, and thus gives structural information when carbon goes into allotropic modification, i.e. diamond, graphite or forms different compound with other atoms.

5.3.3 Principles of Auger Electron Spectroscopy (AES)

When excited at a given level, either by photons or by electrons, an atom undergoes relaxation according to two competitive processes, one of them resulting in emission of a characteristic Auger electron. Whereas X-ray emission is predominant for heavy elements, Auger emission is predominant for light elements and is therefore well designed for their analysis.

The energy E of an Auger electron leaving a solid surface is given by following relation [13]

$$E \leq E_A = W_X - W_Y - W'_{Y'} - e\Phi \tag{22}$$

where X is the primary excitation level, Y the origin level of the electronic transition, Y' the origin level of the Auger electron (given that level X is already

excited, the energy of level Y' is greater than the first isolation energy $W_{Y'}$, hence the notation $W'_{Y'}$) and $e\Phi$ the work function with a few electron volts.

The Auger electron energy E_A corresponds to electrons emitted from a surface layer of thickness equal to the escape depth of Auger electrons which can be assimilated to their mean free path. The emission energy of Auger electrons being of the order of 10-1000 eV, it corresponds to an escape depth of a few angstroms (Å). Like photoelectron spectroscopy, AES is therefore a method for analysing solid surface, i.e. very first few atomic layers. The process is shown in Figure 10 (b).

5.3.4.1 Chemical Shift

Chemical shifts of Auger peaks depend on three levels. Their relationship with chemical surface states is therefore less straightforward than with photo electron spectrometry. The difference between Auger and photo-electron chemical shifts therefore results from the difference in final-state relaxation energies between chemical states. However, chemical shift in the Auger electron spectrum will not be considered in our case. It is important in case of carbon based material to analyse the Auger line shapes, because Auger line shape is very important in bond structure determination, although the technique is not straightforward. It is seen that Auger line shapes are very much sensitive to change in chemical environment.

5.3.4 Instrumentation of XPS and AES

High resolution XPS analyses were carried using a VG spectrometer with a monochromated MgK_α (1253.6 eV) X-ray source with an energy resolution of ~0.5 eV. The binding energy values of the photoelectron peaks were measured with an accuracy of ± 0.05 eV. The spectrometer was calibrated to position the $4f_{5/2,7/2}$ photoelectron line of clean pure Au foil at a binding energy of 87.74 and 84.07 eV. The films were conductive enough to ignore the charging effect.

AES analyses were carried out using a VG spectrometer with a 10kV minimum spot size 200nm scanning electron gun. A CLAM 2 spectrometer analyser was used to

investigate the surface of material through the analysis of electrons emitted from the sample in a constant retard ratio (CRR) mode. The Spectra were recorded using pulse counting in the integral EN(E) mode. Standard first derivative of the recorded spectra were taken and the curves were smoothed using five point Fast Fourier Transform (FFT) filter. The experiment was done *ex situ*.

5.4 Principles of X-ray diffraction (XRD)

X-ray diffraction technique has been used for fundamental research in materials characterisation, specially in finding the crystallographic structure of the material. Although the technique and principle of X-ray crystallography is not unknown, but for the simplicity of the data interpretation in studying carbon nitride material we will go through the basic theory of X-ray crystallography that is relevant in our case.

X-rays are photons with a wavelength of the order of a fraction of a nanometre compared with the hundreds of nanometres of light waves. Thus X-rays are very suitable for crystal planes determination. Usually rows of atoms in a crystalline materials have a spacing of ~ 0.3 nanometres. An X-ray beam incident on a material penetrates many micrometres into the bulk and the direction of the diffracted beam intensity is determined by the periodicity of the atom planes in the crystalline solid. If a beam of characteristic X-rays of wavelength, λ, is incident on a single crystal surface at an angle θ, a beam at an angle θ will be diffracted. Figure 11 shows the X-ray diffraction from atoms in a crystalline material.

The ray from the second row of atoms travels a distance (DA+AC) greater than the ray from the top row. The two rows of atoms are separated by a distance "d". For this to produce a diffraction maximum the path difference must be an integral number of wavelengths. But DA and AC both equal d sin θ and thus the condition for diffraction maxima is [17]

$$2d \sin\theta = n\lambda \qquad (23)$$

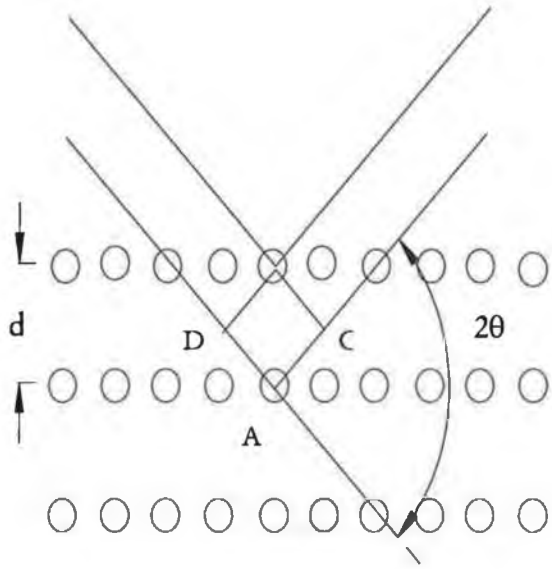

Figure 11: X-ray diffraction from atoms in a crystalline material.

This is the famous Bragg equation for diffraction. By measuring θ, and knowing λ, d may be determined and the crystal spacing indentified. Specific atom species will have an influence on the phase of the diffracted beam and dissimilar atoms in lattice positions can cause certain diffraction peaks to be absent. Thus by observing the diffraction pattern it is possible to indentify the structure of the material. A large library of diffracted pattern from standard atoms and compound are available which helps to identify the unknown phases in a compound.

5.4.1 Intensity of Diffracted X-ray Beams

As we know a compound is composed of a number of unit cells which is in turn are composed of atoms, again atoms are composed of a large nucleus and electrons surrounding the nucleus. All these individual components of a compound take part in the scattering phenomena. The problem of calculating the intensity of a particular diffraction peak is related simply to adding sine waves of different amplitude and phase but of the same wavelength. It is to be noted here that the direction of a diffracted beam is not affected by the type of atom at a particular site and two unit

cells of the same size but with differing arrangements of atoms will diffract X-rays in precisely the same direction. However, the intensities of those diffracted beams may vary and indeed the intensities of certain beams may be zero depending on the constructive or destructive interference of the diffracted beams. The intensity of the diffracted beams depend on the following three steps:

1. Diffraction of X-rays from a single electron

2. Diffraction of X-rays from a single atom using the scattering from a single electron

3. Diffraction of X-rays from a unit cell using the scattering from single atom.

5.4.2 Scattering by an electron

Since an X-ray photon is an electromagnetic wave it will be strongly scattered by an electron. J J Thompson determined that an electron would scatter an X-ray beam of intensity I_o such that the intensity emitted at a distance r from an electron of charge e and mass M is given by [18]

$$I = I_o \frac{e^4}{r^2 M^2 c^4} \sin^2 2\theta \qquad (24)$$

where c is the velocity of light and 2θ is the scattering direction.

5.4.3 Scattering by an atom

An atom consists of a relatively massive positively charged nucleus surrounded by a number of negatively charged electrons. The incident x-ray beam will be scattered by both the nucleus and the electrons. However, according to Thompson's equation it can explained that large mass of nucleus, which is several thousand times that of electron, results in negligible scattering of the incident beam by the nucleus. The total scattering from the atom is therefore essentially the result of the scattering from

all the individual electrons. In the forward direction the scattering will be equal to the sum of the scattering from the individual electrons. However, this is not the case for scattering in other directions because the electrons at different positions around the nucleus will produce scattered waves with different phases which will interfere with another. A quantity, "f" known as the atomic scattering factor is used to describe the efficiency of scattering in a particular direction and is given by [18]

$$f = \frac{A_{atom}}{A_{electron}} \tag{25}$$

where A_{atom} is amplitude of the wave scattered by an atom, $A_{electron}$ is amplitude of the wave scattered by a single electron. "f" is equal to the number of electrons in the atom for $\theta = 0$, that is $f = Z$, the atomic number, but the value decreases as θ increases and λ decreases. There is another point to be made, the scattering just discussed, is coherent in nature, thus unmodified scattering. In some cases when scattering occurs from loosely bound electrons, incoherent, or compton modified scattering results. The intensity of this kind of scattering increases as the proportion of loosely bound electrons increases. The intensity of Compton modified radiation thus increases as the atomic number Z decreases. It is for this reason that it is difficult to obtain good diffraction intensities of light elements, such as carbon, nitrogen, hydrogen, oxygen etc. Thus the scattering intensity from light element will be lower not only due to the lower scattering factor but also for Compton effect. We will need this explanation to interpret the X-ray scattering intensity from Carbon Nitride material.

5.4.4 Scattering by a unit cell

A unit cell can contain number of atoms. The positions of these atoms are described by their position coordinates based on the three principle directions from some origin. Because the scattering effect of each atomic cloud has been considered in the atomic scattering factor f, each atom can be considered as a point atom concentrate at its centre. The problem then reduces to determining the interference effect of the

scattering from atom centres due to their position in space. For forward scattering beams, $\theta = 0$, all the rays are in phase, and their amplitudes are additive. At $\theta \neq 0$, the path lengths of the scattered rays are different, and a phase difference necessarily results in some interference. The measure of this phase difference is contained in an exponential factor that expresses the amplitude shift in terms of the positions of the atoms. The combination of this phase factor and the atomic scattering factor is the structure factor F, [18]

$$F(hkl) = \sum_n f_n e^{2\pi i(hx_n + ky_n + lz_n)} \tag{26}$$

where f_n is the atomic scattering factor for atom n; i is $\sqrt{-1}$; h, k and l are Miller indices of the diffracted direction; and x_n, y_n and z_n are the position coordinate of atom n.

The amplitude of the total beam diffracted from the entire crystal is the sum of the contributions from each unit cell. In the directions of diffraction allowed by the lattice geometry, the resulting rays are always in phase and are additive. In any other direction, they interfere and totally cancel. Several correction factors that enter into the intensity calculations are functions of the experimental technique and the nature of the sample. They correct for such components as atom vibrational motion due to temperature, beam polarisation, varying diffraction time, and beam ansorption in the sample. Considering these elements and the discussion abve, the intensity I of a diffracted beam is [18]

$$I(hkl) = I_o.E_{sc}^{\ 2}.CT.A_s^2 \tag{27}$$

where, E_{sc} is electron scattering coefficient, CT is experimental correction term and A_s is structure amplitude.

5.4.5 Instrumentation

X-ray diffraction analysis on Carbon Nitride samples was performed by a Siemens D-500 diffractometer. The scattering intensities were recorded as a function of diffraction angle. Two scanning time were used: fast scan (scan step 0.05 and scan time 0.5 sec), slow scan (scan step 0.02 and scan time 1.5 sec). The incident beam was Cu kα radiation. The beam was monochromated by Ge crystal.

5.5 Transmission Electron Microscopy (TEM)

In modern materials science, Transmission electron microscopy (TEM) has becomes one of the strongest analytical instruments for structure determination. Specially in the diffraction technique when X-rays do not obtain significant results, electron can play ultimate role for crystal structure determination. Like X-ray diffraction, the geometrical diffraction theory applies to electrons. For interpreting intensities, it must be taken into account that the electron-matter interaction cross-section is some 10^8 times the corresponding value for X-rays. It follows that mean free path is divided by the same factor. It is currently in the range of some 100Å for high-energy electrons (10-1000keV). As the electron beam travels through the thin foil so a fraction of the electrons will be diffracted out of the primary incident beam. Thus the primary beam will lose intensity on passing through successive atom layers of the specimen while the diffracted beams will be increasingly intense. Similarly the diffracted beams will further diffract and lose part of their intensity and indeed a fraction will be diffracted back into the main beam. Electron diffraction in transmission is described essentially by kinematical and dynamic theories. Only the basic principles will be discussed for the clarification of the discussed data. However, in the kinematical theory it is assumed that the incident beam does not lose intensity in passing through the foil and that there is no subsequent interaction between diffracted beams.

5.5.1 Electron diffraction principle

In the case of a thin foil specimen of a crystalline material, most of the electrons will pass through the specimen and exit at the bottom. This is the basis of transmission electron technique. Some of the electrons will not undergo any scattering and will exit the foil with the same velocity and trajectory with which they entered. Other electrons will undergo only inelastic scattering; that is they will suffer a loss in the energy, but their trajectory will be essentially unchanged. The unscattered electrons and the electrons that have undergone only inelastic scattering will form the transmitted electron beam. Other electrons will undergo elastic scattering with essentially no loss in energy but a significant change in trajectory. Some of these electrons will be scattered through very large angles and exit back through the top of the foil as backscattered electron. Many of these electrons will undergo elastic scattering in the foil through smaller angles and exit through the bottom of the foil.

The elastically scattered electrons are directed according to the geometric arrangement of the atomic planes. This system of scattering is called coherent Bragg diffraction, because the electrons will be scatterd in specific directions determined by the crystallography of the specimen. Coherent elastic scattering in the forward direction is responsible for the formation of the diffracted beams in the transmission electron microscope and therefore produces the conventional electron-diffraction patterns in TEM. The angles through which the electrons are scattered are given by Bragg's law which was described in principle of X-ray diffraction technique. According to the Bragg's law, $n\lambda = 2d\sin\theta$, in case of electron diffraction, n is an integer, λ is the wavelength of the electrons (0.0037 nm for 100 keV electrons, in our case), d is the inter-planer spacing for the rows of atoms and θ is the diffracting angle. Diffraction of electrons by crystals is mathematically identical to the diffraction of X-rays by a crystal. The difference between X-ray diffraction and electron diffraction lies primarily in the wavelength of the diffracting radiation. X-rays have a wavelength of the order of tenths of a nanometer; 100 to 200 keV electrons have a wavelength of the order of 10^{-3} nm. Consequently, the diffracting angles for X-rays are typically tens of degrees, but the diffracting angles for electrons are typically

tenths of a degree. Bragg's law can be modified for small angles ($\theta = \sin\theta$) and considering only first-order reflections ($n = 1$). Thus Bragg's law for electron diffraction becomes [19]

$$n\lambda = 2d\theta \tag{28}$$

A further modification of the Bragg's law can be done according to the geometry of TEM. The distance from the transmitted beam to the diffracted beam, R, at the plane of the photographic film is related to the camera constant of the microscope (figure 12a and b). The camera constant is the product of the electron wavelength, λ, and the effective distance from the specimen to the film, L. Thus, modified Bragg's law for TEM is [19]

$$Rd = \lambda L \tag{29}$$

where d is still the atomic inter-planar spacing. The camera constant can be determined for a specific microscope at a specific operating voltage from a diffraction pattern obtained from known standards. Thus from a known d value of a standard, R can be measured and therefore λL can be calculated.

The geometry of the diffraction in the TEM is shown in the figure 12. The angle between the incident electron beam and the diffracted beam is 2θ (analogous with X-rays). Camera length is the effective length between the sample and the photographic plate (given as L), as discussed earlier. R is the distance that the diffracted beam is away from the incident beam when it hits the photographic plate. Thus Bragg's equation becomes [20]

$$d = \frac{0.037}{2.\sin\left(\frac{\tan^{-1}\left(R/L\right)}{2}\right)} \text{ Å} \tag{30}$$

here, the sin term is included to become more accurate.

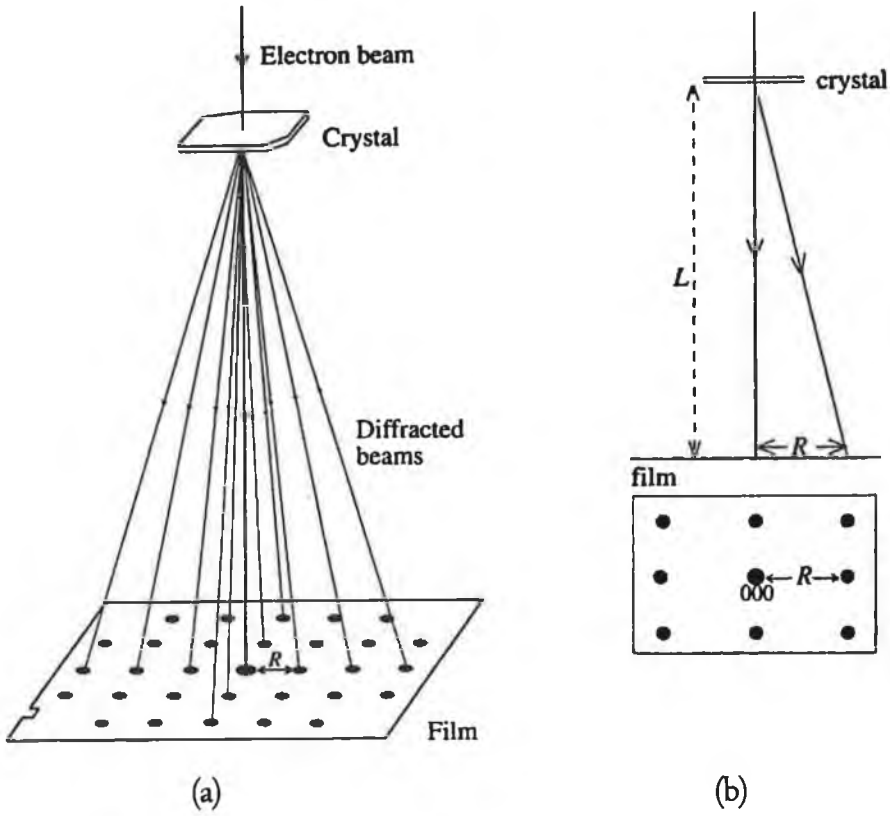

Figure 12: (a) The formation of an electron diffraction pattern from a thin crystal. The diffraction pattern is a projection of the reciprocal lattice section in the plane of the crystal normal to the electron beam. The beam divergences are exaggerated, (b) The geometry of electron diffraction.

5.5.2 Selected-Area Diffraction (SAD)

The standard method for generating diffraction patterns using conventional TEM is by SAD. In SAD, an aperture appropriately termed the selected-area aperture is moved into the microscope column to specify the area of the specimen from which a diffraction pattern is obtained. Proper positioning of the aperture selects the region from which the diffraction pattern will be obtained. Three types of electron diffraction patterns can be generated by SAD: (1) ring patterns from fine grained polycrystalline material (this is the case for Carbon Nitride crystals and will be discussed in the next chapter) in which diffraction occurs simultaneously from many grains with different orientations relative to the incident beam; (2) spot pattern in which diffraction occurs from a single-crystal region of the specimen (this was seen

while calibrating the camera length by taking diffraction pattern from Si (100) single crystal); (3) Kikuchi line patterns in which diffraction occurs from a single crystal region of the specimen, which is sufficiently thick that the diffracting electrons have undergone simultaneous elastic and inelastic scattering, known as Kikuchi scattering. Sometimes Kikuchi diffraction is very important in finding out the zone axis.

Ring patterns arise when many randomly oriented fine grains contribute to the observed diffraction pattern. Ring-pattern analysis, like powder X-ray analysis, can be used to identify unknown or to characterise the crystallography of a new crystalline material (i.e. β-C_3N_4).

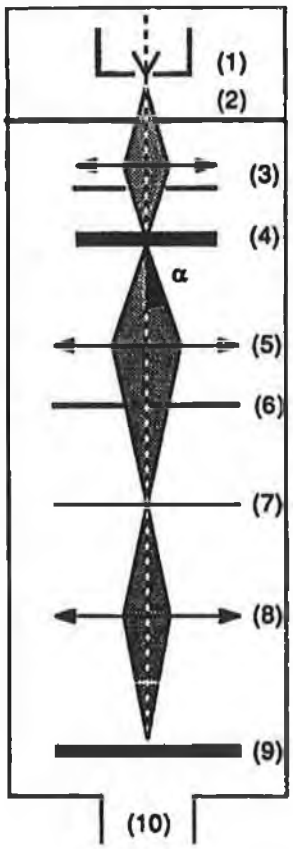

Figure 13: Basic components of a TEM. (1) Electron source at a voltage V_0; (2) grounded anode; (3) condenser system; (4) thin specimen; (5) objective lens; (6) objective back focal plane, with its diaphragm limiting the angular aperture to α; (7) objective image plane (Gaussian plane), conjugate of the object plane with respect to the objective lens; (8) system of projection lenses; (9) fluorescent screen or photographic film; (10) vacuum pumps.

5.5.3 TEM imaging

In the conventional TEM mode, the electron microscope can be operated to produce either a diffraction pattern or any of several types of images on the fluorescent screen or photographic films. The diffracted pattern and the associated images are intimately related in that either the transmitted beam or any of the diffracted beams can be used to form the image. Extraction of quantitative information on the microstructure of the material necessitates combined use of imaging and diffraction-pattern analysis. Before going through the imaging technique, it is necessary to know the components of microscope column. Figure 13 shows the various component of a typical TEM at their relative position.

When the incident electron beam strikes the specimen, some of the electrons pass through the foil without undergoing elastic or inelastic scattering and form the major part of the transmitted beam. Other electrons that have undergone only inelastic scattering, and have therefore not had their trajectory significantly altered, from the remaining portion of the transmitted beam. An image can be produced with the transmitted electrons by inserting an aperture in the plane (known as the back focal plane) at which the diffraction pattern is first formed just below the objective lens and the specimen. This aperture is termed the objective aperture.

5.5.3.1 Bright Field Image

With the aperture centred on the transmitted beam, only the corresponding electrons contribute to the image. Any crystalline parts of the specimen appear dark on a bright background, thus resulting in the bright field image (Figure 14.a). A crystalline particle appears darker the closer its orientation to a prominent zone axis. Any image point appears the brighter the smaller its scattering power.

5.5.3.2 Dark Field Image

With the aperture centred on a given diffracted beam hkl, only the corresponding electrons contribute to the image. Any crystalline parts of the specimen appear

bright on a dark background, thus resulting in the dark field image (figure 14.b). In the image of a polycrystalline specimen, only the crystallites corresponding to the selected reflection hkl appear bright. A crystalline particle appears the brighter the closer its orientation to a prominent zone axis. A dark field image of an amorphous specimen may similarly be observed, but the image intensity is generally low in this case.

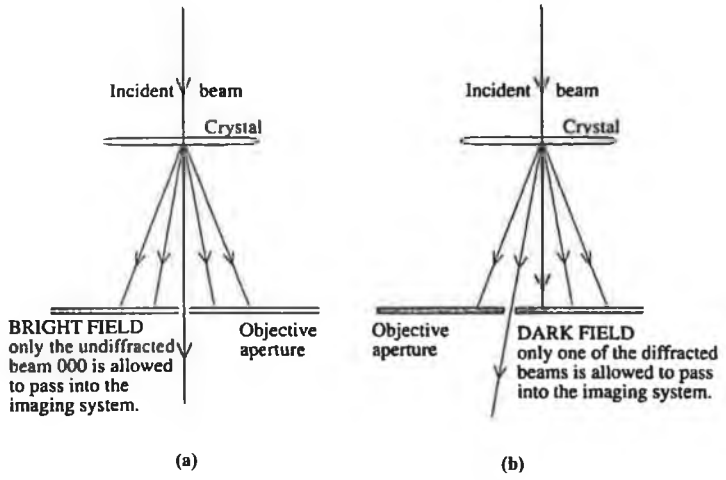

Figure 14: The position and function of the objective aperture for (a) a bright field image (b) a dark field image. In practice the incident beam is tilted to obtain a dark field image, rather than the aperture off-centred, so that the selected diffracted beam is parallel to the microscope column.

5.5.4 Sample Preparation

Sample preparation techniques for TEM analysis is the most complex and time consuming part of the entire experiment. A number of standard techniques are applied for sample preparation depending on the material being analysed [21]. Here, the sample preparation technique for Carbon Nitride thin film will be discussed briefly. Before going to preparation technique it is to be mentioned here that carbon nitride thin films were deposited on Si (100) single crystal. The thickness of Si wafer was 500 μm and the film thickness was 0.3μm. Only one sample was prepared for TEM which contains 33.3 at.% N as measured by RBS.

5.5.4.1 Grinding

Plan view Transmission Electron Microscopy (TEM) specimens were prepared by standard grinding. Specimens were mechanically ground to a thickness of ~200 μm, and 3 mm diameter discs were ultrasonically cut. The silicon side of the specimen was dimple ground to ~15 μm.

5.5.4.2 Ion milling

Ion milling from one side only was performed to perforation. Two high-energy beams (4keV) of Ar^+ ions were used to sputter Si until a perforation results. The specimen was mounted into a holder and placed inside a vacuum chamber. The holder was tilted approximately 15^0 relative to the incident ion beams. During thinning, the specimen holder rotates to ensure uniform thinning.

5.5.5 Instrumentation

An E.A. Fischione dimple grinder 200 apparatus was used for mechanically grinding the sample. 3 mm samples were ultrasonically cut using Gatan Ultrasonic Disk Cutter 601. A Gatan DuoMill 600 ion milling apparatus was used for thinning the sample to a perforation. TEM investigation used a Phillips 400T microscope operating at 100kV.

5.6 Nanoindentation Technique

One of the simplest ways to measure the mechanical properties of thin films is to deform it on a very small scale. Because indentation testing with a sharp indenter is a convenient means to accomplish this, nanoindentation, or indentation testing at the nanometre scale, has become one of the most widely used techniques for measuring the mechanical properties of thin films [22]. Other reasons for the popularity of nanoindentation are: the ease with which a wide variety of mechanical properties can be measured without removing the film from its substrate and the ability to probe a surface at numerous points and spatially map its mechanical properties. The

hardness and modulus of devices can be determined at each point. In addition to microelectronics, nanoindentation has also proved useful in the study of optical coatings [23], hard coatings [24,25] and materials with surfaces modified by ion implantation [26,27] and laser treatment [28].

Nanoindentation systems measure mechanical properties in much the same way as conventional mechanical indentation testing systems; properties are derived from simple measurements of load, displacement and time. Figure 15 illustrates the most common nanoindentation test, in which a sharp diamond indenter is driven into and withdrawn from a film while the loads on and displacements of the indenter are measured.

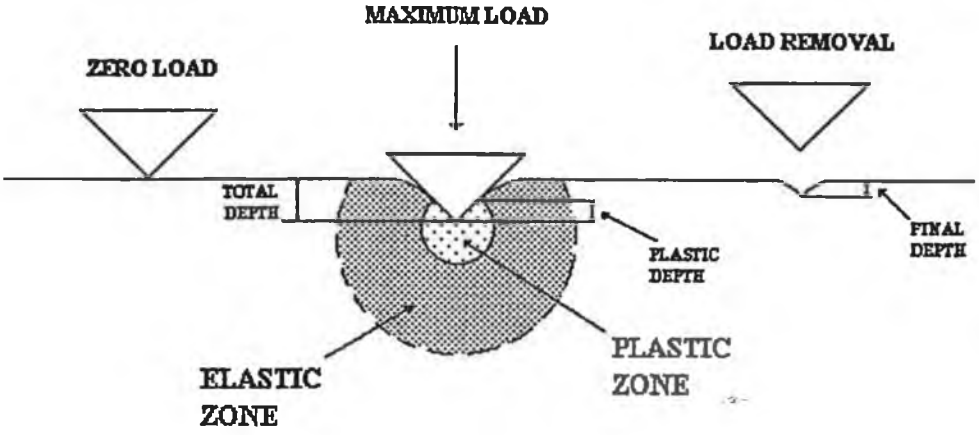

Figure 15: Schematic of the nanoindentation technique showing the surface-indenter interaction.

The nanoindentation test is very straightforward where contact is usually made by sharp indenter, modeled in figure 15, as a cone. Because of this, the contact area is initially small, and there is no distinct elastic region at the beginning of the test, i.e., the deformation has both elastic and plastic displacements from the outset. Furthermore, the contact area continuously changes as the indenter is driven into and withdrawn from the specimen, and these factors complicate the analysis of the data. These problems could be avoided with the use of an indenter with a flat-ended

geometry, but such indenters are rarely used in practice for two reasons. First, as mentioned previously, in order to achieve a high degree of spatial resolution, it is usually desirable to make the contact area as small as possible, and this is best accomplished using sharp indenters. Second, it is difficult to assure that the contact between a flat-ended indenter and the specimen is uniform; i.e., due to surface roughness and misalignment of the indenter, contact does not occur uniformly between the specimen and the indenter. For these reasons, the most frequently used indenter in nanoindentation testing is the Berkovich diamond, a three sided pyramid indenter with the same depth-to area relation as a Vickers indenter [29].

5.6.1 Measurements of Hardness and Elastic Modulus

The thin film properties most frequently measured in nanoindentation experiments are elastic modulus, E, and the hardness, H. Compared to conventional microhardness testing, nanoindentation has much to offer since in conventional microhardness testing, the elastic modulus can not be measured at all, and measurement of the hardness of very thin films is difficult as well. The reason for the difficulty is that in order to assure that the substrate does not influence the measurement, the size of the contact impression must be kept small relative to the film thickness. A conservative rule of thumb is that the depth of the contact should be less than 10% of the film thickness [30], though in some materials substrate independent measurements have been claimed for depths up to 25% [31-33]. In either case, the hardness impressions for films with micron dimensions must be so small that their areas cannot be accurately determined by optical means. These difficulties are overcome in nanoindentation testing by driving the properties from analyses of the indentation load-displacement data, and no imaging required.

5.6.2 The Oliver and Pharr method

In 1992 Oliver and Pharr [34] proposed a commanding method for measuring hardness and modulus using nanoindentation methods involves making a small indentation in the film, usually with a Berkovich indenter, while continuously

recording the indentation load, P, and displacement, h, during one complete cycle of loading and unloading [34-36].

The conical indenter is a natural choice since, like the Berkovich indenter, its cross-sectional area varies as the square of the depth of contact and its geometry is unique at the tip. The load-displacement relationships are nonlinear and the contact area changes continuously during unloading.

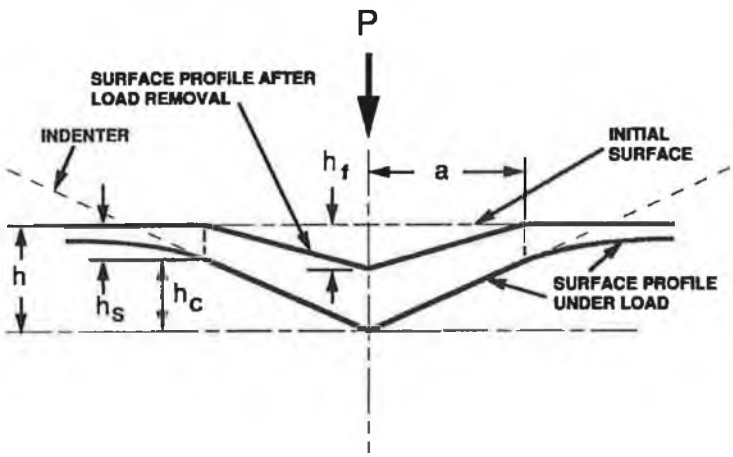

Figure 16: Schematic representation of a section through an indentation showing various quantities used in the analysis [34].

Figure 16 shows a cross section of an indentation and identifies the parameters used in the analysis. As the indenter is first driven into the film, both elastic and plastic deformation occurs. At any time during loading, the total displacement h is written as [34]

$$h = h_c + h_s \tag{31}$$

where h_c is the vertical distance along which contact is made (hereafter called the contact depth) and h_s is the displacement of the surface at the perimeter of the contact. At peak load, the load and displacement are P_{max} and h_{max}, respectively, and the radius of the contact circle is a. Upon unloading, the elastic displacements are

recovered, and when the indenter is fully withdrawn, the final depth of the residual hardness impression is h_f.

The experimental parameters needed to determine hardness and modulus are shown in the schematic load-displacement data shown in figure 17. The three key parameters are the peak load (P_{max}), the depth at peak load (h_{max}), and the initial unloading contact stiffness (S_{max}). It should be noted that the contact stiffness is measured only at the peak load, and no restrictions are placed on the unloading data being linear during any portion of the unloading. The key to the analysis procedure is that as the indenter is withdrawn, the elastic displacements are recovered, and an analysis of the elastic unloading data can then be used to relate experimentally measured quantities to the projected contact area, A, and an

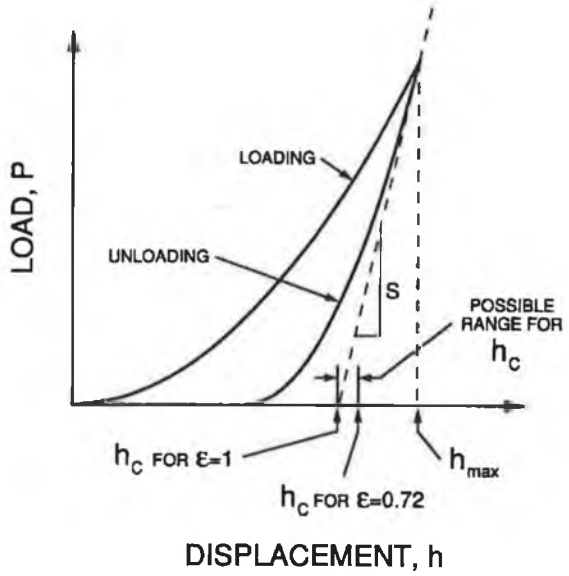

Figure 17: Schematic representation of a typical load-displacement curve showing quantities used in the analysis as well as a graphical interpretation of the contact depth [34]

effective elastic modulus [37-39]. For any axisymmetric indenter the relationship is [34]

$$S = \frac{dP}{dh} = \frac{2}{\sqrt{\pi}} E_r \sqrt{A} \tag{32}$$

where the reduced modulus, E_r, accounts for the fact that measured elastic displacement includes contributions from both the specimen and the indenter. The reduced modulus is given by [34]

$$\frac{1}{E_r} = \frac{\left(1-\nu_f^{\,2}\right)}{E_f} + \frac{\left(1-\nu_i^{\,2}\right)}{E_i} \tag{33}$$

where E_f and ν_f are the elastic modulus and Poisson's ratio for the film, and E_i and ν_i are the same quantities for the indenter (for diamond, E_i = 1,141 GPa and ν_i = 0.07, data given by Simmons et al. [40].

The eqn 32 relates the reduced modulus, E_r, to the contact area, A, and the measured stiffness, S. This relationship holds for any indenter that can be described as a body of revolution of a smooth function and is thus not limited to a specific geometry [34]. Measurement of the initial unloading slope can thus be used to determine the reduced modulus if the contact area at peak load can be measured independently.

The area of contact at peak load is determined by the geometry of the indenter and the depth of contact, h_c. Following Oliver et al [41,42] it is assumed that the indenter geometry can be described by an area function F(h) which relates the cross-sectional area of the indenter to the distance from its tip, h. Given that the indenter does not itself deform significantly, the projected contact area at peak load can then be computed from the relation [34]

$$A = F\left(h_c\right) \tag{34}$$

The functional form of F must be established experimentally prior to analysis.

To determine the contact depth from the experimental data, it is noted that [34]

$$h_c = h_{max} - h_s \tag{35}$$

which follows directly from eqn 31. Since h_{max} can be experimentally measured, the key to the analysis then becomes how the displacement of the surface at the contact perimeter, h_s, can be ascertained from the load-displacement data.

The deflection of the surface at the contact perimeter depends on the indenter geometry. For a conical indenter, Sneddon's expression [37] for the shape of the surface outside the area of contact can be used to give [34]

$$h_s = \frac{(\pi - 2)}{\pi}\left(h - h_f\right) \tag{36}$$

The quantity $(h-h_f)$ appears in this expression rather than h by itself since Sneddons's solution applies only to the elastic component of the displacement. In addition, Sneddon's force-displacement relationship for the conical indenter yields [34]

$$\left(h - h_f\right) = 2\frac{P}{S} \tag{37}$$

where S is the stiffness. Substituting eqn. 36 into eqn. 37 and noting that the contact area of interest is that at peak load, one obtains [34]

$$h_s = \varepsilon \frac{P_{max}}{S} \tag{38}$$

where the geometric constant ε for the conical indenter is given by [34]

$$\varepsilon = \frac{2}{\pi}(\pi - 2) \tag{39}$$

or ε = 0.72. For the flat punch, ε = 1, and for the paraboloid of revolution, ε = 0.75.

The graphical interpretation of eqn. 38 is shown in figure 17. For $\varepsilon = 1$, the value for the flat punch, $h_s = P_{max} / S$, and the contact depth h_c is given by the intercept of the initial unloading slope with the displacement axis. Interestingly, this is precisely the depth used by Doerner and Nix [35] in their analysis based on the flat punch approximation. Thus the current method is consistent with the Doerner and Nix approach when the flat punch geometry is assumed. For the conical and paraboloid indenters, however, the contact depths are greater than those for the flat punch, and this must be accounted for in analyses using these indenter geometries if accurate measurements are to be obtained. The range of h_c for the indenters considered here is shown in figure 17.

In addition to the modulus, the data obtained using the current method can be used to determine the hardness, H. It is defined that the hardness as the mean pressure the material will support under load. With this definition, the hardness is computed from [34]

$$H = \frac{P_{max}}{A} \tag{40}$$

where A is the projected area of contact at peak load evaluated from eqn. 34. It should be noted that hardness measured using this definition may be different from that obtained from the more conventional definition in which the area is determined by direct measurement of the size of the residual hardness impression. The reason for the difference is that, in some materials, a portion of the contact area under load may not be plastically deformed, and as a result, the contact area measured by observation of the residual hardness impression may be less than at peak load.

5.6.2.1 Substrate effects

As mentioned previously, when the depth of the indentation exceeds 10-25% of the film thickness, some consideration must be given to how the properties of the substrate influence the measurement of the hardness and modulus of the film.

The question of how the substrate affects the measurement of hardness is somewhat more difficult to address because of the complex nature of the plastic deformation in vicinity of the indenter. Nevertheless, some progress has been made toward understanding substrate effects on hardness measurement through finite element simulation. A study of the indentation of thin films by conical indenters indicates that two separate equations are needed to describe the variation of the apparent hardness, H, with the total depth of the indentation, h. The applicable equation depends on the relative hardnesses of the film, H_f, to the hardness of the substrate, H_s. For soft films on hard substrates [43]

$$\frac{H}{H_s} = 1 + \left(\frac{H_f}{H_s} - 1\right) \times \exp\left[-\frac{(\sigma_f / \sigma_s)}{(E_f / E_s)}\left\{\frac{h}{t}\right\}^2\right] \tag{41}$$

while for hard films on soft substrates [43]

$$\frac{H}{H_s} = 1 + \left(\frac{H_f}{H_s} - 1\right) \times \exp\left[-\frac{(H_f / H_s)}{(\sigma_f / \sigma_s)\sqrt{E_f / E_s}}\left\{\frac{h}{t}\right\}\right] \tag{42}$$

where σ_f and σ_s are the yield strengths of the film and the substrate, t is the thickness of the film. Detailed discussion of these equations is not the scope of the present work. However, for the present measurements the depth of indentation was taken ~10% of the film thickness in all cases.

5.6.3 Experimental Details

A NanoTest 500 (Micro Materials, UK) is used to measure the hardness amd elastic modulus of carbon nitride thin films. The NanoTest measures the movement of a stylus in contact with a surface. For hardness measurement a programmed load is applied and the stylus is touched at the film surface. Figure 18 shows the schematic of the NanoTest 500 apparatus.

Load is typically applied through a coil and magnet assembly, in which case the load is determined from the current flowing to the coil. The diamond displacement is measured by means of a parallel plate capacitive sensor, where one plate is attached to the diamond holder. When the diamond moves, the capacitance changes and this is measured by a capacitance bridge unit. The limit stop defines the maximum outward movement of the diamond as well as the orientation operation of the pendulum when a load is applied. The balance weight assembly is used to adjust the equilibrium position of the pendulum when there is no current passing through the coil. The typical depth resolution of this apparatus is less than 0.1 nm and the force resolution is less than 100 nN.

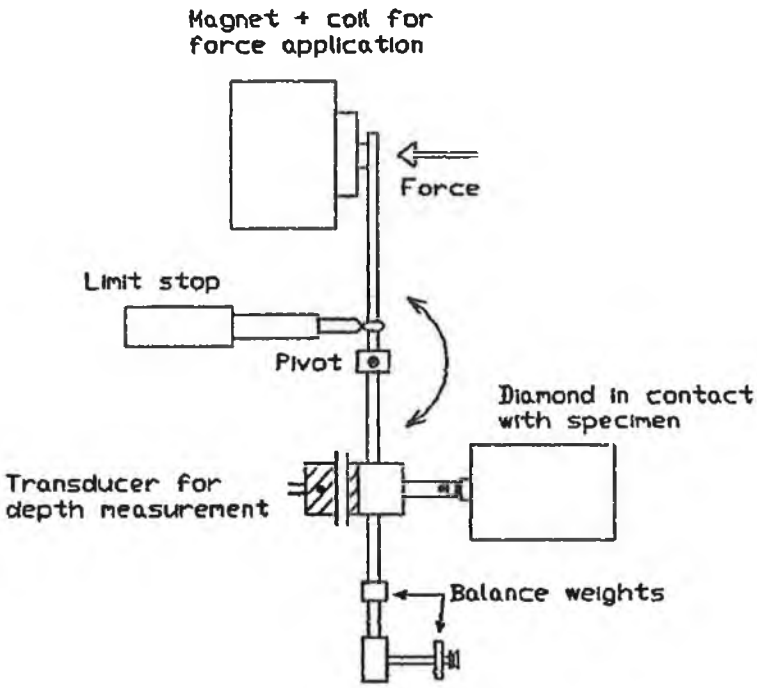

Figure 18: Schematic of NanoTest 500 apparatus showing the mechanism of Nano indentation for the measurement of hardness and elastic modulus of carbon nitride thin films.

A set of carbon nitride thin films with variable composition were loaded into the NanoTest, mounted on a stub by means of rapid setting adhesive. The samples were firmly glued to the aluminium stub holder and then allowed to thermally equilibrate with the nanotester cabinet for few hours to minimise thermal drift. The specimen is

slowly brought into contact with the stylus. The load applied to the stylus at this stage is extremely small, while the stylus is just touching the film surface. For indentation measurement, the depth of penetration is then measured as load is applied. The out put load displacement data thus obtained in volts. The load data was converted to mN and displacement to nm. The data is then transferred to a computer, where a software is used for analysis. A number of tests are usually performed on the same sample to obtain reliable statistical information. In a typical test, usually load, depth of penetration, transverse displacement and time are recorded.

Prior to the experiment the apparatus was calibrated using Oliver and Pharr method and a fused quartz sample is normally employed to check the level of accuracy of the instrument. To rule out the thickness effect the samples, thickness were measured by using a Tencor surface profilometer. The samples thickness were varied from 1 to 1.5μm which were well enough to ignore the substrate effect.

Hardness values are calculated from the expression [44]

$$H = \frac{P_m}{kd_p^{\,2}} \tag{43}$$

where the denominator is the projected area of indentation for a particular diamond geometry. Theoretically for Berkovitch geometry the projected indentation area as a function of plastic indentation can be given by $A = 23.897 \times h_c^{\,2}$. However, the indentation area function is calculated by indenting a known material having constant hardness (quartz). The area function is deduced from the indentation load-displacement data alone by assuming that elastic constants are independent of depth [32]. The area function of the diamond for this experiment was taken as [44]

$$A = k1 \times h_c^{\,2} + k2 \times h_c \tag{44}$$

where k1 = 19.99732 and k2 = 28848.75×10^{-9} [44]; h_c is calculated by applying Oliver and Pharr method as discussed earlier.

In order to obtain reasonable accuracy in the analysis, a maximum indentation (on-load) depth of 100nm was applied for all the measurements, considering a depth/thickness ratio of less than 1/10, which can rule out the substrate effect. The initial load applied was 0.05 mN with the rate of 0.11 $mN.s^{-1}$. For each sample, at least six experiments were done; each experiment consisted of 15 or more indentations, where each indentation was separated by at least 10μm distance.

5.7 Stress Measurements

Chapter 3 discussed about the stress that usually develops in thin films during deposition. The films will possess intrinsic stress, i.e., compressive or tensile stresses, regardless of how they are produced. The interfacial shear stress is responsible for adhesion strength of the film-substrate interface and may lead to cracking and even complete delamination of the films occur depending on the severity of the stress concentration at the interface. Adhesion property of a film is the prime consideration when considered as coating of surfaces. This property will be discussed later in relation to carbon nitride thin film as hard coating.

5.7.1 Intrinsic stress measurement by Bending Beam Method

Physical geometry of a film can be a good parameter to measure the stresses at the cross section of the film. In this case when the film is deposited on a very thin substrate, the substrate will be bent depending on the types of stress. Tensile stress will bend the substrate thus the coated surface becomes concave. Similarly, compressive stress will bend it and the coating surface becomes convex. The deformation of the substrates is measured by observing the deflection of the centre of a beam.

Intrinsic stress of carbon nitride films was measured by bending beam method. When the films were deposited on one side of a very thin substrate, the bent geometry of the film can be observed as shown in figure 19.

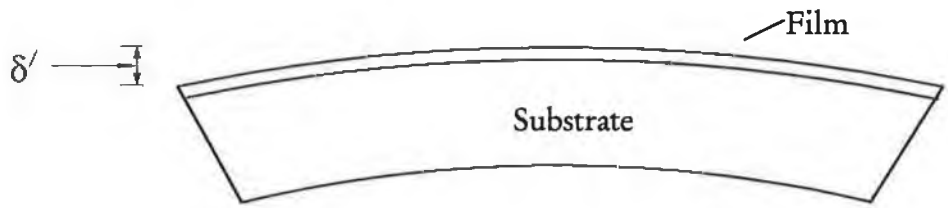

Figure 19: Schematic illustration of the measurement intrinsic stress of carbon nitride thin film using bending beam method.

The film stress is calculated by Stoney's equation [45]

$$\sigma = \frac{E_s d_s}{6\rho d_f} \tag{45}$$

where E_s is the Young's modulus of the substrate and film, ρ is the radius of curvature of the beam, d_s is the substrate thickness, and d_f is the film thickness. A detailed description of this equation and its modifications are given in Appendix C. If the equation 45 is considered for the geometry shown in figure 19 which usually occurs in case of thin films, it becomes (Appendix C),

$$\sigma = \frac{4E_s d_s^2 \delta'}{3(1-\nu_s) l^2 d_f} \tag{46}$$

where,

E_s = Elastic modulus = $1.6X10^{12}$ dynes cm^{-2} (Si substrate)

d_s = Substrate thickness = 508±20 x 10^{-2} cm (Si)

υ_s = Possions ratio = 0.33 (Si)

l = Substrate length

d_f = Film thickness μm

δ = Maximum deflection

Curvatures of the bent films were measured by Tencor™ Sigmascan surface profilometre. The apparatus consisted of a scan and a control unit. The scan unit scans the surface of the film by a mechanical profilometer, while the control unit receives the scanned signal and generates the surface profile as out put. The instrument's resolution is 0.02 μm and as all the measured deflections were at least 1 μm, the data seems to be sufficiently accurate. All scans are carried out over a 10 mm span. All the measurements are carried out from the printed profiles. Film thickness is also measured using the same profilometer, by running a scan from the un-coated to the coated silicon substrate. The resultant step height is the thickness of the deposited film.

5.8 Adhesion and Frictional Properties Measurements

It is of interest to see the frictional and adhesion performances of carbon nitride thin film coating on tool steel. The frictional properties of the film was measured on the basis of a number of cycles a hard pin can rotate on the film surface without failure at a constant load. This test is usually done by a Pin-on-disk tester [46]. An introduction of a typical system is given in this section. To be considered as a good coating, the first criteria of a material would be to have good adhesion to the substrate. A standard Rockwell indenter [47] was used to see the adhesion properties. Adhesion properties evaluation by indentation method is simple and gives a good comparison evaluation. An introduction of Rockwell indentation method is given in this section.

5.8.1 Pin-on-disk tester

A pin-on-disk tester (Implant Sciences Corporation ISC-200 Tribometer) was used to measure frictional properties of carbon nitride thin films on steels. Figure 20 shows

schematic of the apparatus used. A test disk (sample to be evaluated) is mounted in a cup that comes in contact with a pin attached to a precision balance lever arm that is used to apply vertical loads to the pin and read the friction force on the pin. A load of 50 gm is applied on the pin that revolves about the test disk centre against a stationary disk. In any case the wear track on the disk is a circle, involving multiple wear passes on the same track. The pin is a tungsten carbide ball. A load cell on the top platform measures the reaction friction force when hooked up to the lever arm. The analogue friction output is transmitted to the computer and a friction coefficient is displayed on the computer screen. Friction was measured in the normal atmospheric condition. The tester consists of the following parts

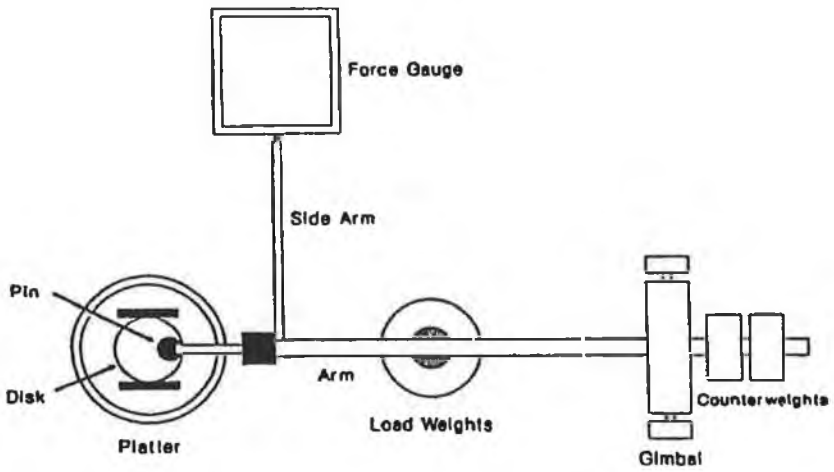

Figure 20: Schematic of the ISC-200 Tribometer pin on disk tester.

(a) Motor Drive: A variable speed motor, capable of maintaining constant speed (±1% of rated full load motor speed) under load is required. The motor is mounted in such a manner that its vibration does not affect the test. Rotating speeds are typically in the range of 0.3 to 3 rad/s (60 to 600 r/min).

(b) Revolution counter: The machine is equipped with revolution counter that records the number of disk revolutions and is capable to be shut off after a pre-selected number of revolutions.

(c) Pin specimen holder and lever arm: The system has stationary specimen holder that is attached to a lever arm consisting a pivot. Adding weights, as option of loading, produces a test force proportional to the mass of the weights applied. Ideally, the pivot of the arm should be located in the plane of the wearing contact to avoid extraneous loading forces due to the sliding friction. The pin holder and the arm are of substantial construction to reduce vibrational motion during the test.

(d) Wear measuring system and data acquisition: The instrument has a sensitivity of higher than 2.0 μm. All the analogue out put data are transferred to a computer for analysis. Thus frictional coefficient and other properties are directly displayed on the screen.

5.8.2 Rockwell indenter

A Rockwell indenter (Indentec 8150BK) was used to measure adhesion properties of carbon nitride thin films on steels. Rockwell indentation testing consists of measuring the additional depth to which an indenter is forced by a heavy major load beyond the depth of a previously applied light minor load. Application of the minor load eliminates backlash in the load train and causes the indenter to break through slight roughness and to crush particles of foreign matters, thus contributing to much greater accuracy in the test.

The minor load is applied first, and a reference or "set" position is established on the dial gage of the Rockwell indentation tester. Then the major load is applied. Without moving the sample being tested, the major load is removed when the film is delaminated from the substrate.

The Rockwell indenter machine consists

(a) Dial gage: This shows the load applied and corresponding hardness or adhesion scale, although the adhesion scale is considered from microscopic evaluation.

(b) Indenter: In case of adhesion properties measurements a diamond brale is used which is discussed earlier.

(c) Anvil: This is the work bench of the apparatus. Usually samples are mounted on the anvil and can be lifted up to the indenter using different anvils.

(d) Crank handle: This acts as a mechanical switch to activate load into the indenter. A load system is connected to one end of a fulcrum, while the other end of the fulcrum is connected to the indenter. The fulcrum is controlled by the crank handle through a shaft by which load is applied to the indenter.

5.8.2.1 Indentation and Adhesion Tests

A 120^0 sphero-conical diamond indenter (Brale) is used for adhesion test. A scale was considered from HF1 to HF6 showing the adhesion properties in a sequential way. Figure 21 shows the scale. When the indenter penetrates the coating, cracks propagate from the indentation point. The technique is a comparative measurement indenting with the same load for all samples. Thus gives the picture of comparative adhesion properties considering the crack network from the indentation spot. HF1 shows excellent adhesion property with a few crack network while HF6 shows the poorest adhesion properties showing complete delaminations of the film. In every indentation a load of 100 Kg was used for all samples. The indentation is monitored by optical microscope and after indentation a photograph of the penetration spot is taken at the magnification of 80x.

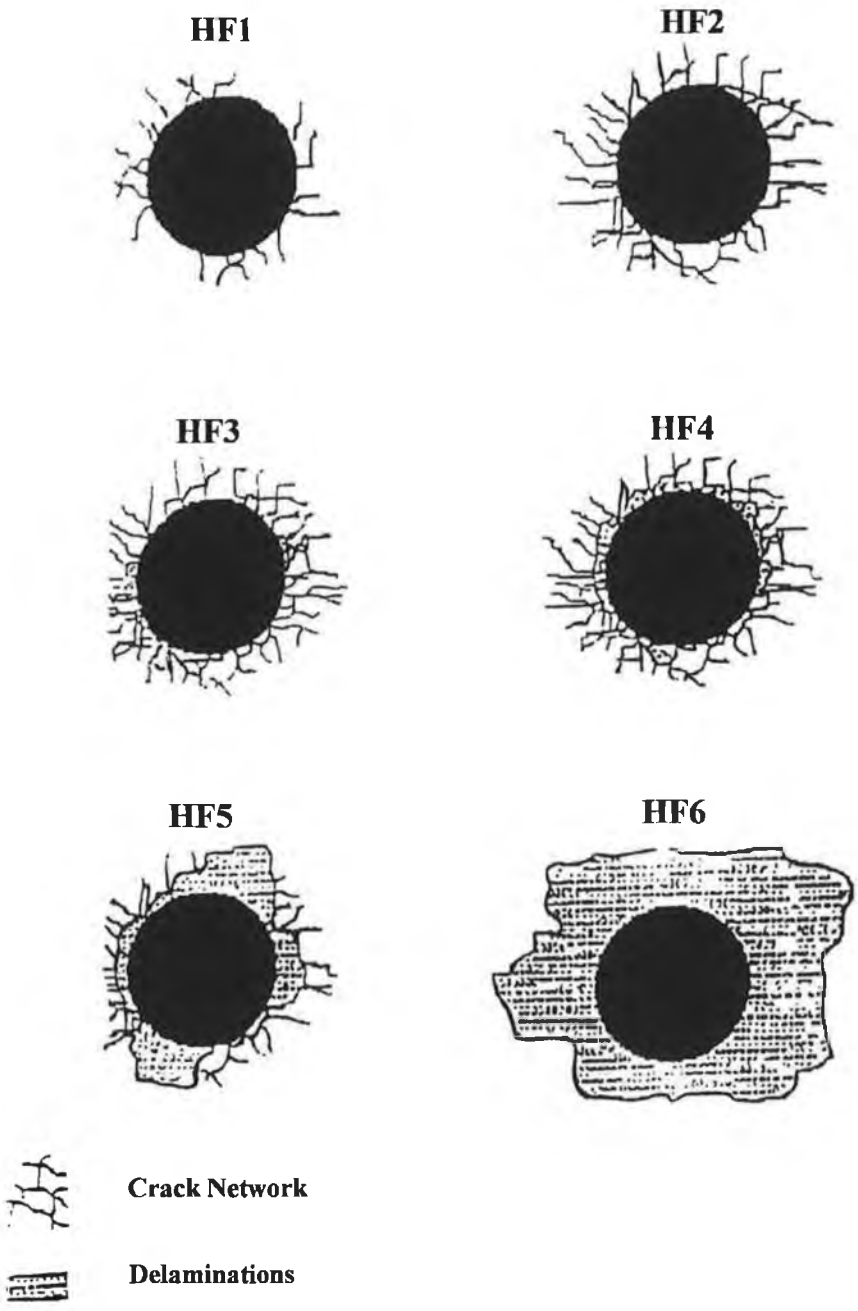

Figure 21: Rockwell indentation scale for adhesion characteristics evaluation.

Summary

A general macroscopic overview of materials characterisation techniques has been given. This has served to introduce the techniques, to highlight the differences among them. This has all been from a very practical viewpoint. Chapter 6 will discuss the results using these techniques.

References

1. L.C. Feldman and J.W. Mayer, Fundamentals of Surface and Thin Film Analysis, North Holland, New York, 1986.

2. J.F. Ziegler, The Stopping and Ranges of Ions In Matter, Vol. 4, Pergamon Press, New York, 1977.

3. C. Jeynes, Z.H. Jafri, R.P. Webb, A.C. Kimber, M.J. Ashwin, Surf. Interface Anal., 25, 254 (1997).

4. N.P. Barradas, J.C. Soares, M.F. da Silva, T.S. Plaskett, P.P. Freitas, Nuclear Instrum. Methods Phys. Res. B, 118, 626 (1996).

5. N.P. Barradas, Nuclear Instrum. Methods Phys. Res. B, (1998), accepted.

6. C. Jeynes, N.P. Barradas, M.J. Blewett, R.P. Webb, Nuclear Instrum. Methods Phys. Res. B, (1998), accepted.

7. K. Nakamoto, Infrared and Raman Spectra of Inorganic and Coordination Compounds, 4th edn, John Wiley & Sons, New York, 1986.

8. N. Maley and I Szafrenek, MRS Proceedings, 192 (1990).

9. A.A. Langford, M.L. Fleet, B.P. Nelson, W.A. Lanford, N.Maley, Phys. Rev. B, 45(23), 13367 (1992).

10. N.Maley, Jap. J. Appl. Phys., 31 (Part I, no. 3), 768 (1992).

11. M. Katiyar and J.R. Abelson, J. Vac. Sci. Technol. A, 13(4), 1995.

12. S. Ramo, J.R. Whinnery, T. van Duzer, Fields and Waves in Communication Electronics, John Wiley & Sons, New York, 1965.

13. J.P. Eberhart, Structural and Chemical Analysis of Materials, John Wiley & Sons, New York, 1991.

14. D. Briggs and M.P. Seah, Practical Surface Analysis, Vol. I: Auger and X-ray Photo Emission Spectroscopy, , 2nd edn, John Wiley & Sons, New York, 1996.

15. F.R. McFeely, S.P. Kowalczyk, L.Ley, R.G. Cavell, R.A. Pollak and D.A. Shirely, Phys. Rev. B, 9 (1974) 5268.

16. L. Ley, M. Cardona, and R.A. Pollak, in L.Ley and M. Cardona (ed.), Topics in Applied Physics: Photoemission in Solids II, Springer-Verlag, Berlin, 1979, p.56.

17. W.L. Bragg, The Crystalline State, Vol. I: A General Survey, George Bell, London, 1933.

18. P.E.J. Flewitt and R.K. Wild, Physical Methods for Materials Characterisation, Institute of Physics Publishing, Bristol, 1994.

19. A.D. Romig, Jr., Analytical Transmission Electron Microscopy, in ASM Handbook, Vol. 10, Materials Characterisations, 1992.

20. A. Putnis, Introduction to Mineral Sciences, Cambridge University Press, Cambridge, 1992.

21. A. Barna, G. Radnoczi, B. Pecz, Preparation Techniques for Transmission Electron Microscopy, in Handbook of Microscopy: Application II, S. Amelinckx, D. van Dyck, J. van Landuyt, G. van Tendeloo edn, VCH Verlags. MbH, D-69451, Weinheim, 1997.

22. W.C. Oliver, MRS Bulletin, 11, 15 (1986).

23. B.D. Fabes and W.C. Oliver, Stresses and Mechanical Properties, in Thin Films, M.F. Doerner, W.C. Oliver, G.M. Pharr, F.R. Brotzen edn, Mater. Res. Soc. Symp. Proc. 188, pp.127, Pittsburgh, 1990.

24. M.E. O'Hern, W.C. Oliver, C.J. McHargue, D.S. Rickerby, S.J. Bull, Stresses and Mechanical Properties, in Thin Films, M.F. Doerner, W.C. Oliver, G.M. Pharr, F.R. Brotzen edn, Mater. Res. Soc. Symp. Proc. 188, pp.139, Pittsburgh, 1990.

25. P.J. Burnett and D.S. Rickerby, Thin Solid Films, 148, 51 (1987).

26. W.C. Oliver and C.J. McHargue, Thin Solid Films, 161, 117 (1988).

27. M. Nastasi, J.-P. Hirvonen, T.R. Jervis, G.M. Pharr, W.C. Oliver, J. Mater. Res., 3, 226 (1988).

28. T.R. Jervis, J.-P. Hirvonen, M. Nastasi, T.G. Zocco, J.R. Martin, G.M. Pharr, W.C. Oliver, New Materials Approaches to Tribology: Theory and Applications, L.E. Pope, L. Fehrenbacher, W.O. Winer edn, Mater. Res. Soc. Symp. Proc. 140, pp.189, Pittsburgh, 1989.

29. M.M. Khruschov and E.S. Berkovich, Industrial Diamond Review, 11, 42 (1951).

30. "Standard Test for Microhardness of Materials", ASTM Standard Test Method E-384, Annual Book of Standards 3.01, American Society for Testing and Materials, Philadelphia, pp. 469, 1989.

31. M.F. Doerner, D.S. Gardner, W.D. Nix, J. Mater. Res., 1, 845 (1987).

32. H.M. Pollock, D. Maugis, M. Barquins, in Microindentation Techniques in Materials Science & Engineering, (ASTM STP 889), P.J. Blau, B.R. Lawn edn., ASTM, Philadelphia, pp.47, 1986.

33. D. Lebouvier, P. Gilormini, E. Felder, J. Phys. D, 18, 199 (1985).

34. W.C. Oliver and G.M. Pharr, J. Mater. Res., 7(6), 1564 (1992).

35. J.L. Loubet, J.M. Georges, O. Marchesini, G. Meille, J. Tribology, 106, 43 (1984).

36. M.F. Doerner and W.D. Nix, J. Mater. Res., 1, 601 (1986).

37. I.N. Sneddon, Int. J. Engng. Sci., 3, 47 (1965).

38. D. Tabor, Proc. R. Soc. A, 192, 247 (1948).

39. N.A. Stillwell and D. Tabor, Proc. Phys. Soc. London, 78, 169 (1961).

40. G. Simmons and H. Wang, Single Crystal Elastic Constants and Calculated Aggregate Properties: A Handbook, 2nd edn., The M.I.T. Press, Cambridge, Masachusetts, 1971.

41. J.B. Pethica, R. Hutchings, W.C. Oliver, Philos. Mag. A, 48, 593 (1983).

42. W.C. Oliver, R. Hutchings, J.B. Pethica, in ASTM STP 889, P.J. Blau and B.R. Lawn edn., ASTM, Philadelphia, pp.90, 1986.

43. A.K. Bhattacharya and W.D. Nix, Int. J. Solids Structures, 24, 881 (1988).

44. Operational Manual (Part I and II), NanoTest 500, Micro Materials Ltd., Wrezham Technology Park, Wrexham, UK, 1994.

45. G.G. Stoney, Proc. Roy. Soc., London, 172 (1909).

46. "Standard Test Method for Wear Testing with Pin-on-Disk Apparatus", G99, ASTM, 1990.

47. "Methods of Nondestructive Inspection", Materials Handbook, vol. 11, 8th edn., ASM, 1976.

Chapter 6

Structural Properties of Carbon Nitride Solid

We have seen in the previous chapters that the production of crystalline β-C_3N_4 has been the goal of much research. We have discussed about various characterisation techniques that can give structural signature of a material, i.e., amorphous or crystalline. Structural and mechanical properties of carbon nitride thin film are discussed in this chapter. The chapter is subdivided into four parts for the ease of presentation of the results and discussion. Part I will discuss the bonding structure in amorphous carbon nitride and part II will discuss the crystalline carbon nitride. Part III will discuss the effect of process parameters which causes the structural modification of the solid, e.g., sp^2 to sp^3 and part IV will highlight the relation between bonding structure and mechanical properties.

Depending on the bonding nature a number of characterisation techniques are necessary to determine the structure of a solid. The first thing will be to determine the composition of the bulk. We have seen that XPS or AES are very surface sensitive. The techniques are commonly used in surface structure or even surface composition determination. In this case, RBS is necessary to determine the bulk composition. XPS is unique in determination of the core level structure of a compound. Sometimes the valence band XPS spectrum fingerprints the over all structure of the solid. Vibrational properties of a solid are also sometimes necessary to understand the symmetric nature of a solid. The correlation of vibrational and electronic properties when gives similar indication, the structural property of a material is then fully understood. When the structure of a material is such that a small amount of nano sized crystals are embedded in the amorphous matrix, structural identification, i.e., bonding nature, becomes tedious with the vibrational

and the electron spectroscopy, because of the limitation of instrumental resolution. Diffraction techniques play an important role in this situation. The microstructure of the solid becomes more important to find out those nanocrystals. In this case TEM plays the unique role.

Part I

6.1 Amorphous Carbon Nitride Films

This part of the chapter discusses the behaviour of the bonding structure of as-deposited carbon nitride films as a function of their nitrogen content and the annealing temperature. The elemental composition of the bulk is measured by RBS. The various components of XPS peaks due to different bond types will be discussed from a comparison of the behaviour of these peaks with the bonding structures identified by FTIR and Raman Spectroscopy. The bonding nature will also be identified by Auger Electron Spectroscopy (AES) from a comparison of the behaviour of the bonds identified by other spectroscopic methods. A complete idea of the bonding nature of Carbon Nitride compound is given.

6.1.1 Elemental Analysis of CN Solid by RBS

A typical RBS spectrum, recorded from a carbon nitride film deposited on Si substrate, is shown in figure 1.

Figures 1 and 2 show the RBS spectra of carbon nitride thin films deposited by using various Ar/N_2 sputtering gas mixture. Table 1 shows the elemental analysis of different samples. The optimum angle differed from sample to sample due to the different thickness of the layers. In some cases for certain angles, the C signal falls on top of the Si signal. Changing the angle allows one to change the position of the buried Si signal and thus C signal can be separated. These angles are also shown in the table 1.

When C or N are components of a heavy material (like in silicon nitride), then normally it is not easy to measure C and N with a 5% error, although possible [1]. In this case however, because the films are mainly CN with no (or very little Fe as seen in the RBS spectra) heavy material, there is no large background (that normally leads to large error) due to heavy elements, and good results can be achieved.

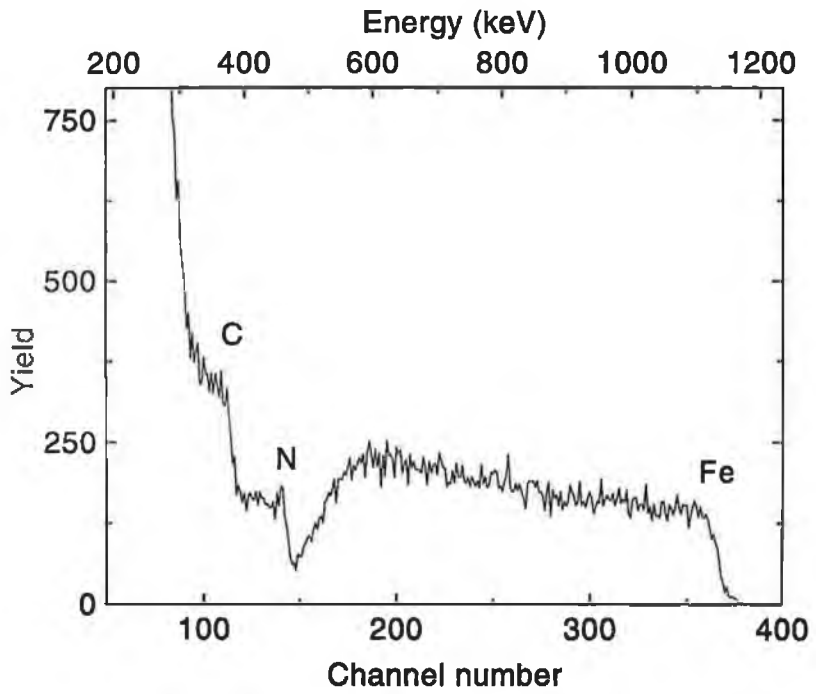

Figure 1: The RBS spectrum of 1.5 MeV He^+ ions incident on Carbon Nitride film containing 42.1 at.% N deposited on Si (100) wafer using no ground shield. Fe signal (2.8 at.% Fe) is observed in the spectrum.

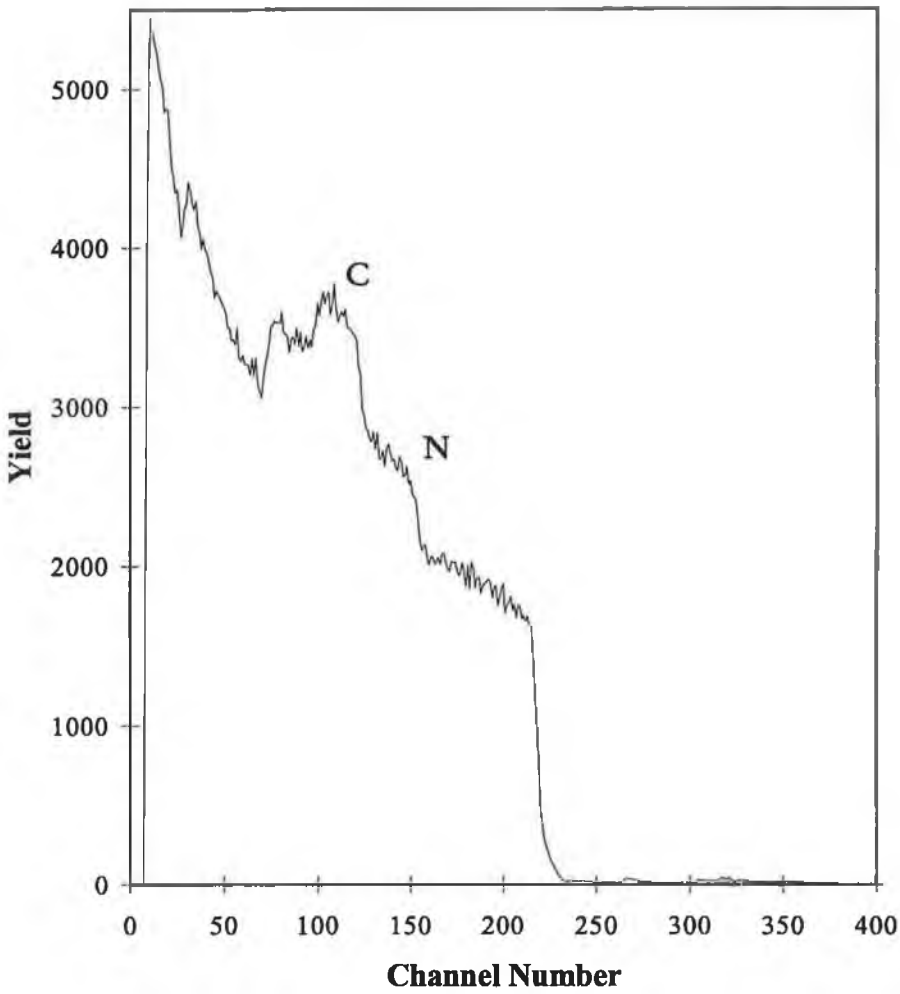

Figure 2: The RBS spectrum of 1.5 MeV He^+ ions incident on Carbon Nitride film containing 37 at.% N deposited on Si (100) wafer using ground shield. No Fe signal (< 0.1 at.%) is observable in the spectrum.

The presence of this small amount of iron in the films are due to sputtering from steel components. This contamination was eventually removed by using a ground shield on the top of the screws which dramatically reduced (< 0.10 at.%) this Fe contamination in the later case. Figure 2 shows a typical RBS spectrum indicating very small amount of (< 0.1 at.%) Fe contamination.

Table 1: Elemental analysis of Carbon Nitride films by RBS

Sample no. (PCN)	Incident Angle (θ)	% N_2 gas used	C	N	O	Ar	Fe
15	0	75	65.1	33.1	0	0	1.8
16	0	50	60.2	36.3	0	0	3.5
17	0	25	64.3	32.2	0	0	3.4
18	0-50	0	82.9	0	0	3.8	13.3
19	0-40	100	65.3	32.5	0	0	2.2
25	0-40	15	70.4	23.8	0	0	5.8
26	0-38	90	55.1	42.1	0	0	2.8

The amount of iron in sample 18 (i.e. PCN18) was more (~13 at.%) than expected, although the other samples showed less than ~2 at.%. This is due to the fact that for sample. 18, 100% Ar was used as the sputtering gas for carbon deposition. Due to its heavy mass, the sputtering yield by 100% argon is higher for iron. It is to be noted here that graphite is not a good material for sputtering. For example, sputtering yield (atoms/ion) of 200 eV Ar ion for Fe is 0.5 and for graphite is < 0.05 [2]. Thus if Ar is reduced and nitrogen (comparatively lower mass) is increased in the sputtering gas mixture, Fe will be less sputtered. Other samples were deposited with reduced amount of argon and contain small amount of iron. Thus iron concentration in the films was increased with increase in Ar (%) in the sputtering gas mixture, as can be seen in the table 1. Due to use of 100% Ar as sputtering gas, a few percentage (~3.8%) of Ar gas was entrapped in the bulk (sample 18). For this particular sample optimum angle was differed from 0 to 50^0 to ensure the presence of

the elements. However, there was no observable oxygen in any of the films. Table 1 shows the complete list of chemical analysis of the films.

6.1.2 Bonding structure and absorption coefficient of CN Thin Film by FTIR

Initially for low concentrations of nitrogen in the N_2/Ar sputtering gas the absorption peaks due to the C≡N bond (2200 cm^{-1}) and C=N bonds (1500 cm^{-1}) increased with nitrogen content in the film as measured by RBS. However, the IR absorption due to carbon-nitrogen bonding was observed to be independent of actual nitrogen content above ~20% N. Figure 3 shows the absorbance per metre for the two main peaks for a series of films grown at 1×10^{-3} mbar and -50 V substrate bias for varying Ar/N_2 gas ratios. It can be seen that over the range 25- 44% N/(C+N) there is no systematic variation of absorption coefficient. This implies that for >25 % N content the excess N is not bonded to C otherwise it would be visible as an increase in absorbance. No other absorption peaks within the instrumental range of 4000 to 600 cm^{-1} develop as the N content increases. The conclusion to be drawn is that the excess nitrogen is present as an IR invisible bond such as a non-polar bond. The most likely candidate would seem to be a N-N bond of some type or possibly inclusions of N_2. This is supported by the fact that the growth rate continues to increase for films with a higher nitrogen content. The structure of the film contains more nitrogen than can be accounted for by carbon-nitrogen bonding. The bonding structure does not change throughout the film thickness.

Zhang et al.[3] discussed the stability of C≡N by post-annealing process in vacuum. He showed that after annealing at 550°C there was a significant loss of C≡N bonds from the film. Veprek et al. [4] showed that sublimation of the paracyanogen could be possible at or above 800°C. The absorption coefficients of carbon nitride films have been investigated in more detail after annealing for 15 minutes under the conditions as described in chapter 4. Figure 4 shows the IR transmission for as-

grown films (the growth temperature was ~100°C) and films annealed at 550 and 600°C.

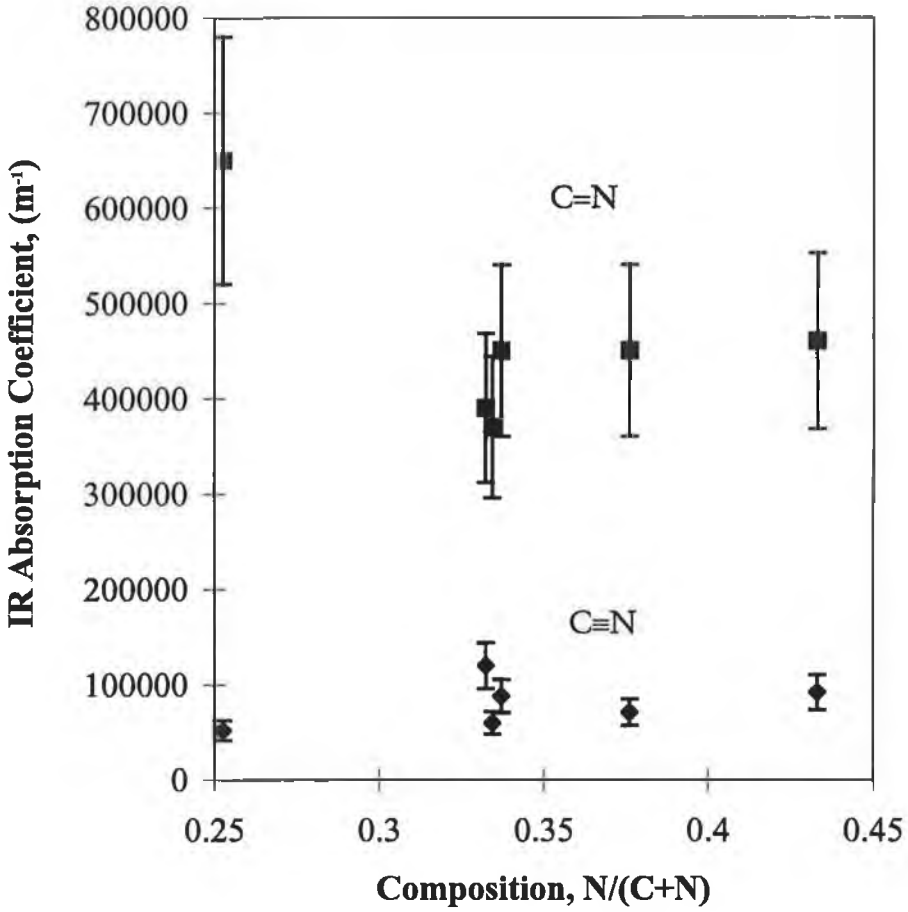

Figure 3: The IR absorption coefficient as a function of at.% Nitrogen for films grown in different Ar/N_2 gas mixture at a pressure of $1X10^{-3}$ mbar.

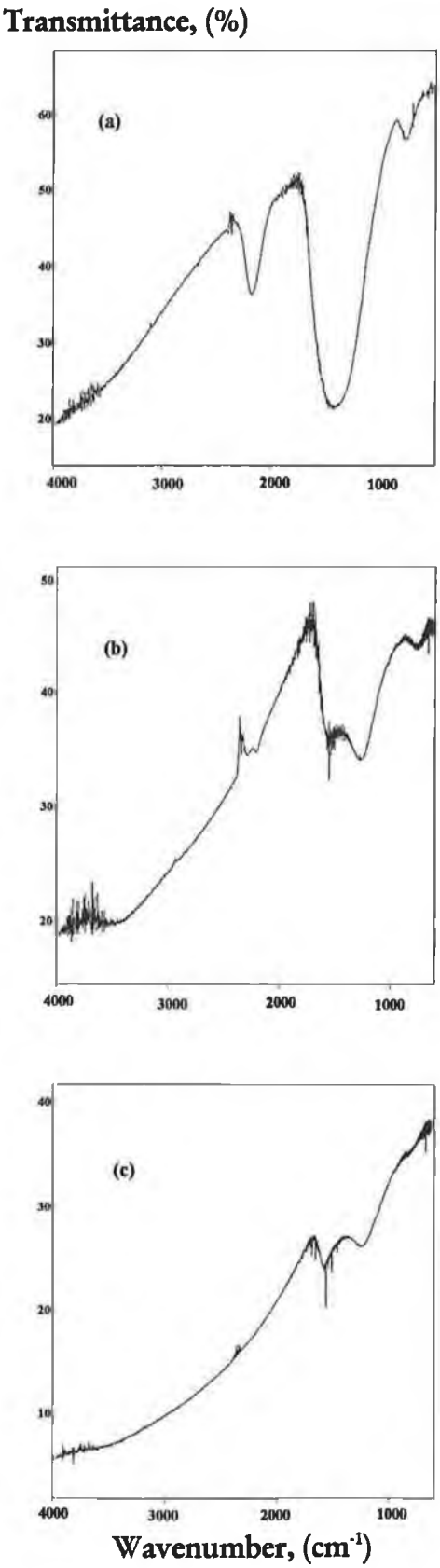
Transmittance, (%)
(a)
60
50
40
30
20
4000
3000
2000
1000
(b)
50
40
30
20
4000
3000
2000
1000
(c)
40
30
20
10
4000
3000
2000
1000
Wavenumber, (cm-1)

Figure 4(a): IR transmittance of the sample containing 39 at.% nitrogen showing the C≡N and C=N/C–N stretching band at 2200 and 1500 cm^{-1} respectively deposited with -50V RF bias at $1.5X10^{-4}$ mbar total working pressure.

Figure 4(b): IR transmittance of the same sample after annealing at 550°C under vacuum at $1X10^{-5}$ mbar. The stretching band at 1500 cm^{-1} has split into two peaks: one at 1565 cm^{-1} which corresponds to the C=N [16] and one at 1250 cm^{-1} which is possibly C-N.

Figure 4(c): IR transmittance of the same sample after annealing at 600°C under vacuum at $1X10^{-5}$ mbar. The diagram shows the complete elimination of C≡N stretching band.

The broad 1500 cm^{-1} peak is due to C=N stretching band which in turn consists of G (~1584 cm^{-1}) and D (~1360 cm^{-1}) bands. The IR-spectrum from the as-grown film does not show any evidence of distinct presence of these bands, but after annealing the bands become visible. For better understanding of this sp^2 region Raman spectroscopy is necessary. We will discuss this band portion in detail in term of symmetry mechanism by Raman spectroscopy. It can be seen that the C≡N peak at 2200 cm^{-1} starts reducing at 550°C as the film is annealed and completely disappears at 600°C while the 1500 cm^{-1} peak is reduced and splits into two peaks at ~1560 cm^{-1} and ~1300 cm^{-1}. The former is the peak due to G band and the latter is possibly due to D band. Very little change was observed below 550°C.

6.1.3 Vibrational properties of CN thin film by Raman Spectroscopy

Figure 5(a) shows the Raman spectra of samples of different nitrogen content. No arbitrary scaling factors were introduced, though successive curves (figure 5.a and 5.b) are translated upwards for clarity. It can be seen here that the spectra resulting from the out-of-plane vibration of C–C at 700 cm^{-1} [5,6] is becoming more intense as the nitrogen incorporation in the film increases. The C=N stretching band appears at the wave number range 1350-1650 cm^{-1}. The Raman active G and D band are very prominent in these spectra. When the film contains 0 at.% nitrogen, these bands can be still resolved. With increasing nitrogen content these bands become stronger.

This means that Raman active G and D bands and others become more active when large amounts of nitrogen are present in the film. The intensity of sp^2 line is sensitive to nitrogen concentration; the 1350-1650 cm^{-1} band feature is mostly due to difference in nitrogen concentration.

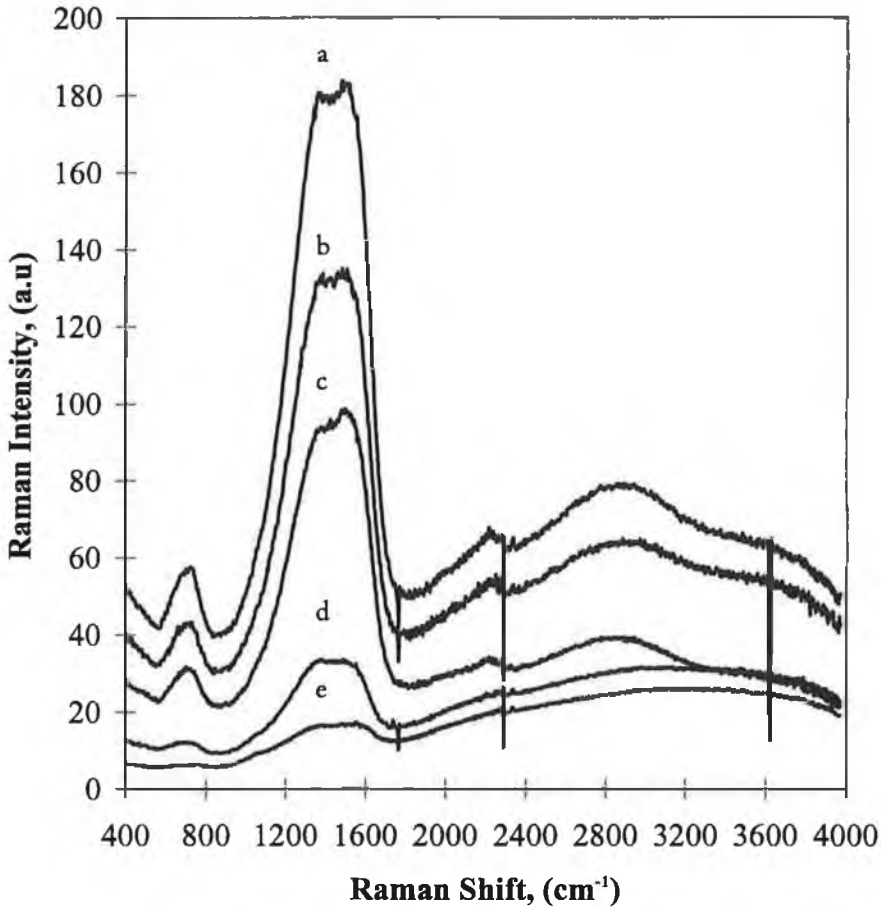

Figure 5: (a) Raman spectra as a function of relative nitrogen concentration. Data were translated but not rescaled (a=43.3 at.%, b=37.6 at.%, c=33.7 at.%, d=25.2 at.%, e=0 at.% nitrogen).

Kaufman et al. [7] concluded that nitrogen substitution is responsible for the symmetry breaking of the E_{2g} mode and the intensity of the G and D bands. The band at ~2200 cm^{-1} is due to stretching vibration of C≡N bonding [7]. In the higher wave number (~2900 cm^{-1}) the C–H stretching band [8] is observed . This band is due to presence of residual water vapour in the chamber during film deposition. There are no other observable bands present in the 600 to 4000 cm^{-1} instrumental

range. Figure 5(b) shows the corresponding IR absorbance spectra of samples of different nitrogen content. The difference between the IR and Raman spectra is that although the E_{2g} symmetry becomes IR active due to incorporation of nitrogen in the film, the G and D bands overlap. The C–C out-of-plane vibrational peak (700 cm^{-1}) is similar to that observed by Raman.

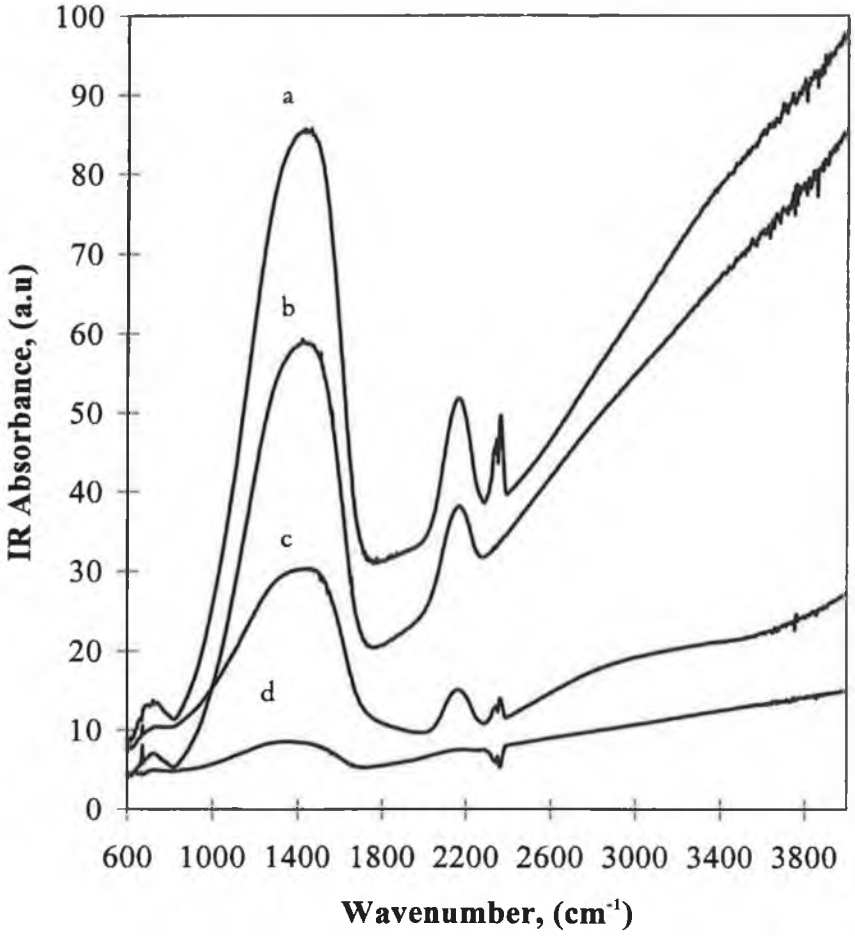

Figure 5(b): IR spectra as a function of relative nitrogen concentration. Data were translated but not rescaled (a=43.3 at.%, b=37.6 at.%, c=33.7 at.%, d=25.2 at.% nitrogen).

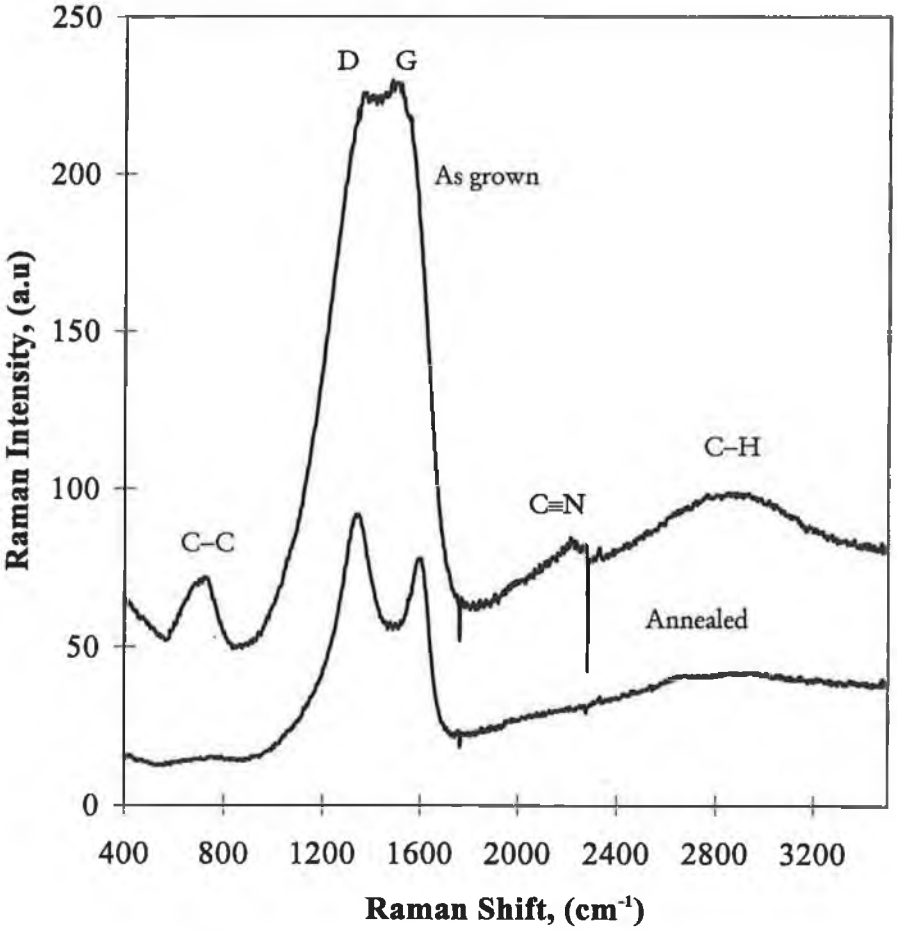

Figure 6: (a) Raman spectra of the as grown sample containing 33.2 at.% N before and after annealing at 600°C (23.2 at.% N).

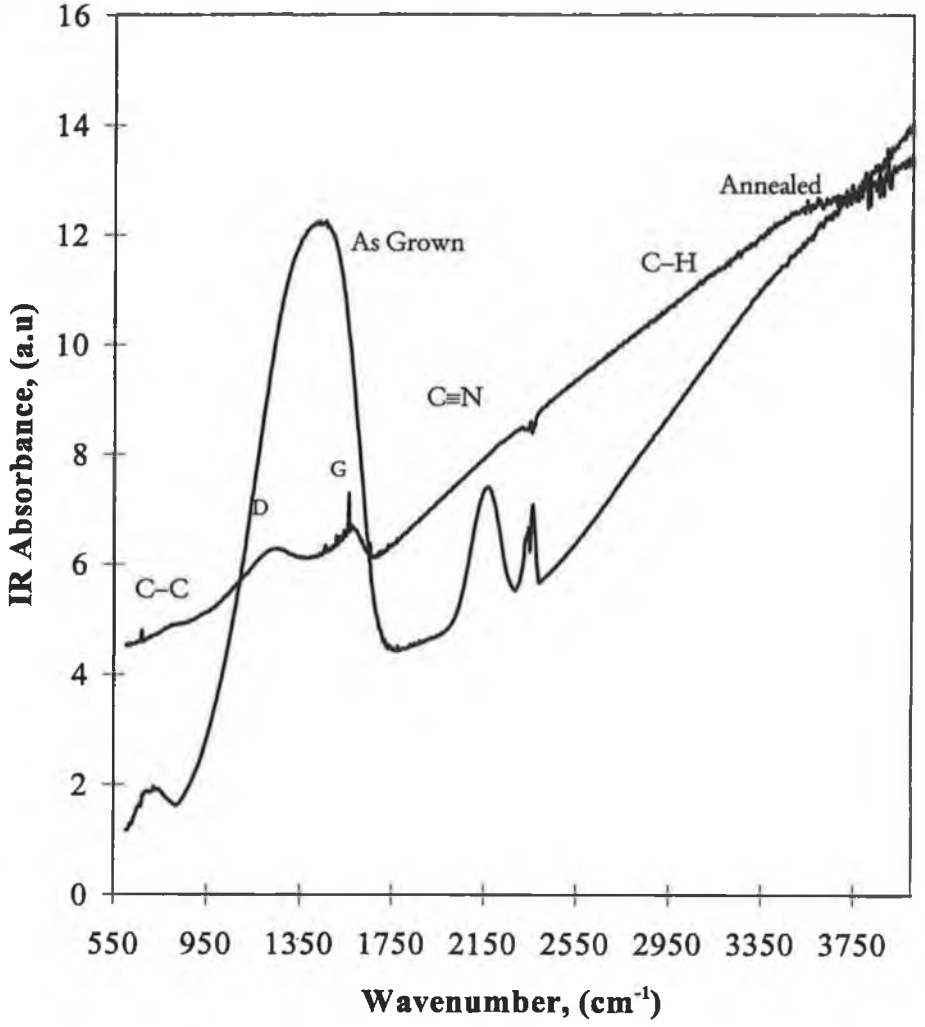

Figure 6: (b) IR spectra of the as grown sample containing 33.2 at.% N before and after annealing at 600°C (23.2 at.% N).

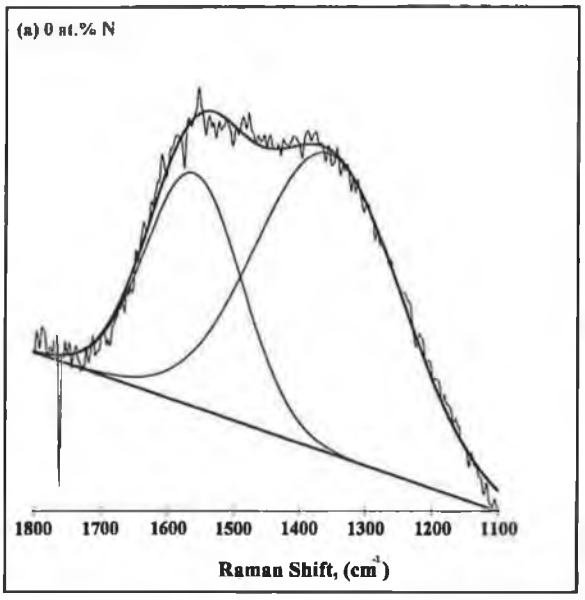

Figure 7(a): Raman spectra from 1100-1800 cm^{-1} region of amorphous carbon nitride film containing 0 at.% N. The deconvoluted peaks have been assigned to D and G. The peak positions are listed in the table 2.

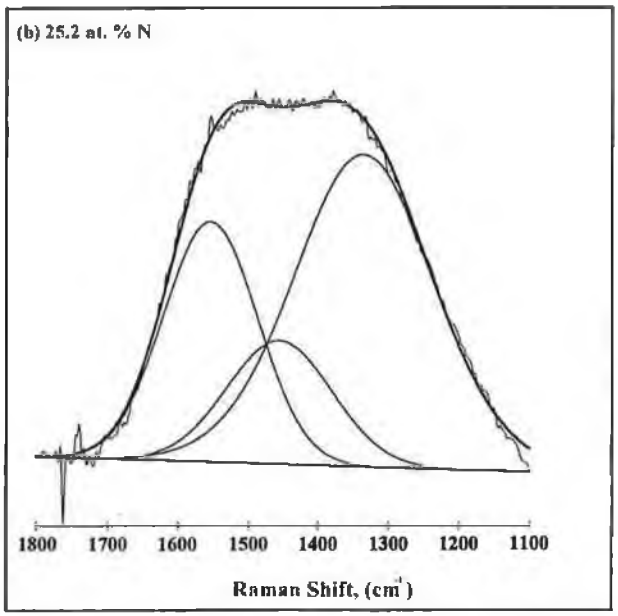

Figure 7(b): Raman spectra from 1100-1800 cm^{-1} region of amorphous carbon nitride film containing 25.2 at.% N. The deconvoluted peaks have been assigned to D, G and N bands. The peak positions are listed in the table 2.

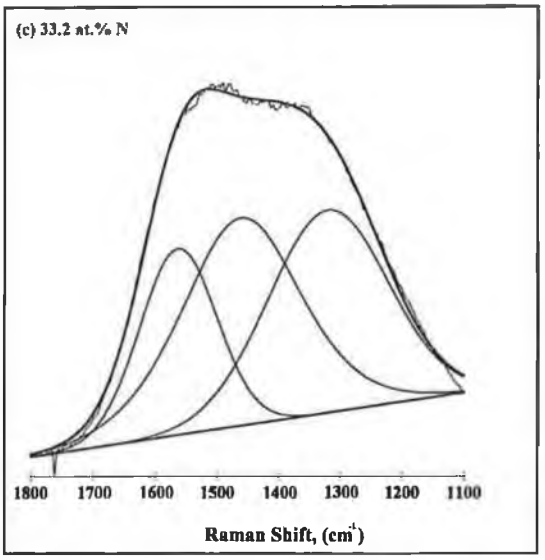

Figure 7(c): Raman spectra from 1100-1800 cm^{-1} region of amorphous carbon nitride film containing 33.2 at.% N. The deconvoluted peaks have been assigned to D, G and N bands. The peak positions are listed in the table 2.

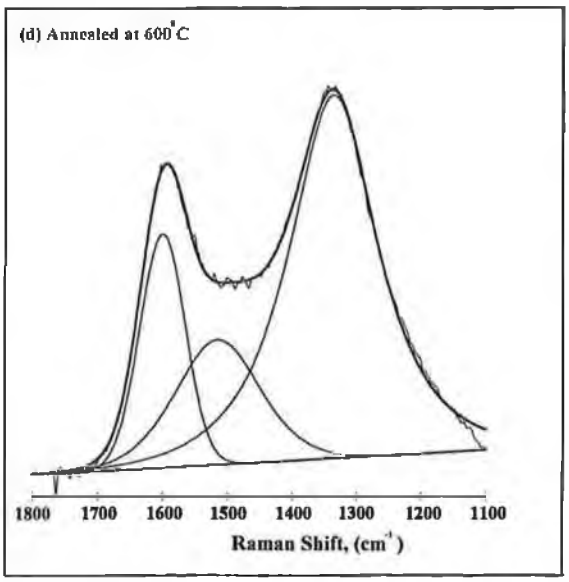

Figure 7(d): Raman spectra from 1100-1800 cm^{-1} region of annealed amorphous carbon nitride film containing 23.2 at.% N after annealing. The film contained 33.2 at.% N (figure 7.c) before annealing. The deconvoluted peaks have been assigned to D, G and N bands. The peak positions are listed in the table 2.

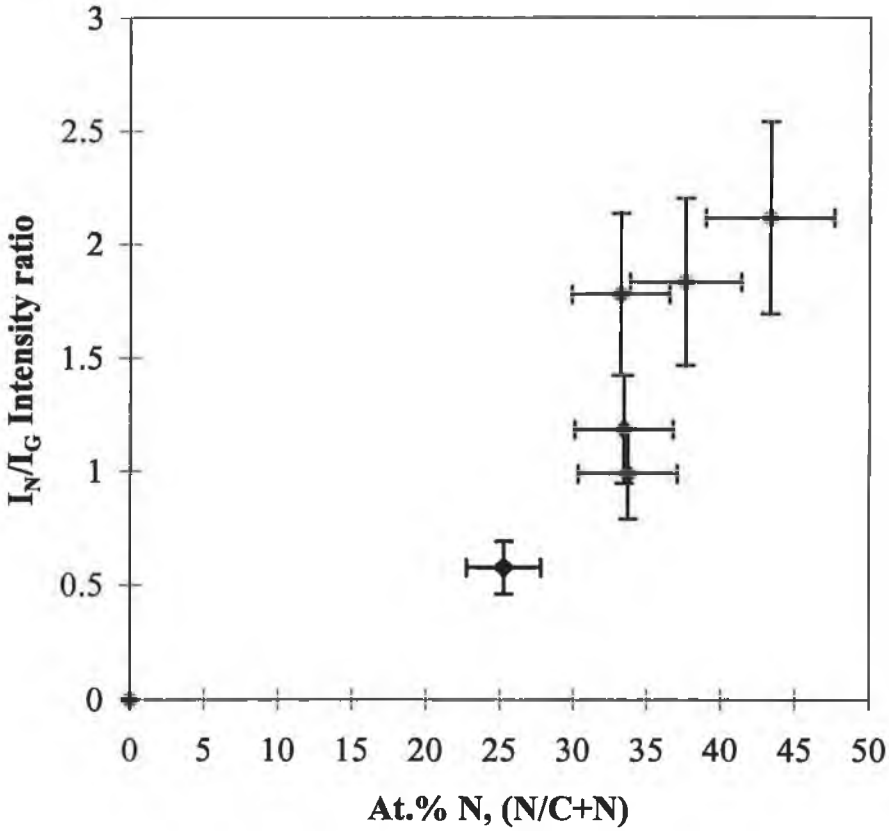

Figure 8: I_N/I_G peak area ratio as a function of nitrogen concentration in the film.

The C≡N stretching band at ~2200 cm^{-1} in the IR spectra are much stronger in comparison to the Raman. It can be seen that this band is becoming more intense as the nitrogen incorporation in the film increases. Thus with higher nitrogen content film the percentage of the C≡N bond will be higher which eventually weakens the structure. The reason for structural weakness due to presence of C≡N bonding will be discussed in part IV of this chapter. Other features are more or less similar. The IR spectrum of the film containing 0% nitrogen shows no IR-active features.

A diatomic molecule that has centre of symmetry is not Raman active. In this respect the N_2 molecule is not IR or Raman active as it has neither net dipole moment nor change in polarizability during the vibration. When nitrogen replaces carbon atoms from the six fold carbon ring, it not only bonds with carbon but also with itself. This bond is stable enough to be retained within the structure. The bonding can be in plane or out of plane depending on the preferred site of the nitrogen incorporation. The formation of an N–N stretching band is unlikely, because there is no evidence of absorption in the 1150-1030 cm^{-1} region [9,10,11]. An N=N stretching mode in vibrational Raman spectra can be observed when nitrogen bonds with the carbon ring, especially with benzene type [12] in the form of C–N=N–C bonding structure. The N=N stretching frequency varies from 1400 to 1500 cm^{-1} [30] depending on the replacement site of carbon atoms and extent of symmetry breaking. This frequency range overlaps the C=N bands [13,14,15] thus it becomes very difficult to identify whether nitrogen is bonded to itself by normal first order Raman scattering. The only possible way to detect this stretching band has been to observe the spectra when nitrogen bonds with benzene or pyridine [9,10,11,12]. It is seen from the figure 5(a) and 5(b) that as nitrogen incorporation increases in CN compound the E_{2g} symmetry becomes more and more IR and Raman active. Thus incorporation of nitrogen in the carbon ring makes this region IR active and increase in intensity of the 1350-1650 cm^{-1} band region explains the Raman active in plane or out of plane N=N stretching band due to excess nitrogen incorporation which overlaps with C=N stretching band. Previously we showed that over the range 25-44 at.% N there is no systematic variation of the FTIR

absorption coefficient. This implies that for >25 % N content the excess N is not bonded to C otherwise it would be visible as an increase in absorbance. This is supported by the fact that the growth rate continues to increase for films with a higher nitrogen content suggesting that it is incorporated somehow into the film. The structure of the film contains more nitrogen than can be accounted for by carbon-nitrogen bonding.

Recently Weich et al [16] derived the possibility of the formation of nitrogen-nitrogen bonding within the CN compound. Our experimental finding regarding nitrogen-nitrogen bonding supports their *ab initio* tight-bonding molecular-dynamics study. They found that this bonding should increase as nitrogen incorporation increases in the film.

Figure 6 shows the annealing behaviour of the sample containing 33 at. % N. The Raman spectra (Figure 6.a) of as grown and annealed sample show that due to annealing the I_D/I_G ratio is increased. This is due to the fact that as annealing progresses the microdomains grow in size or number, making a large contribution to the D band. This feature is also seen by others [17]. Due to annealing, outdiffusion of nitrogen and disruption of bonds occur. This disruption does not affect the N=N bond as much as the other bonding types due its relatively higher bond energy [18]. It can be seen that due to annealing at 600^0 C the C–C out-of plane vibrational band intensity at ~ 700 cm^{-1} becomes very low and also the C≡N band at ~ 2200 cm^{-1} disappears completely. Thus the sp^2 bonding in CN compound is the most stable phase. After annealing, the C–H stretching band intensity became also reduced. Figure 6(b) shows the IR absorbance of the same samples as 6(a) and shows broadly the same results. Interestingly, after annealing the sp^2 band becomes more IR active and shows distinct features of G and D bands which overlapped and were not resolved in the as grown condition. This is due to the fact that the annealing process favours the symmetry breaking mechanism which in turn favours the G and D band to be more IR active in addition to the Raman activity (Figure 6.a).

The above discussions prompt the analysis of the sp^2 Raman region specifically. A range of 1100-1800 cm^{-1} wave number Raman region was deconvoluted using Gaussian-Lorentzian fit [19]. The background from this region is assumed to be linear due to Raman photoluminescence (PL) effect. In general the frequencies in this region reside at the quasi-linear rising portion of this broad Gaussian PL band as described by Shiao et al. [19]. For the analysis a number of samples were taken containing 0 to 44 at.% nitrogen. It proved impossible to accurately match the measured spectra using only the D and G peaks. It was necessary to include a third intermediate peak between them. This peak increased with the nitrogen content of the films and following the arguments regarding nitrogen-nitrogen bonding in the film; it has been assigned to the N=N stretching band. Figure 7 shows the deconvoluted spectra in the sp^2 region for different samples. Figure 7(a) shows the spectra in the sp^2 region deconvoluted in to two peaks, G ($\sim$1561 cm^{-1}) and D (at $\sim$1357 cm^{-1}) band. With nitrogen incorporation into carbon ring, the symmetric features remain more or less same as discussed earlier but the original position of G and D band can be shifted to higher wave number (30-40 cm^{-1}) as the nitrogen content increases [7]. Such a shift could arise from a slight change in sp^2 domain size [20]. Alternatively, each of the D and G peaks consists of a C=C and a C=N contribution at different wave numbers and the observed peak is a summation of the two components. These are unresolvable due to their closeness but with nitrogen incorporation their relative intensity changes giving an apparent shift in the resultant peak. As nitrogen starts to bond with carbon in the six-fold carbon ring structure a third peak at $\sim$1460 cm^{-1}, which we assign to the N=N stretching vibration as the "N" band, appears in the Raman active sp^2 region. This N peak becomes stronger as the nitrogen incorporation in the film increases (figure 7b, and 7c). Table 2 gives a complete list of the peak positions of different samples containing different nitrogen at.%. The I_N/I_G peak ratio as a function of nitrogen concentration is shown in figure 8; it can be seen that there is a monotonic increase. That is, as nitrogen content in the film increases the N=N bonding in the CN compound also increases. Figure 7(c) and 7(d) show the deconvoluted peaks of the same sample before and after annealing. It is interesting to see that after annealing the G and D bands are shifted to $\sim$15 and $\sim$35 cm^{-1} higher wave number region probably due to the change in sp^2 domain

size. The N=N band also shifts by ~50 cm^{-1} because the annealing process allows the bonded nitrogen atoms to be repositioned within the ring giving rise to a wide range of shifting of the N=N stretching band as discussed before. The E_{2g} symmetry remains unaffected, otherwise the Raman sensitive D and G bands would not be observed. After annealing the I_N/I_G ratio of the as grown film changes from 1.78 to 1.03 (figure 7c and 7d). This is due to out diffusion of nitrogen from the film. This point will be discussed further later.

Table 2: Complete list of the peak positions of different samples containing different nitrogen at.%.

Sample	N at.%	D band (cm^{-1})	G band (cm^{-1})	N band (cm^{-1})
1	0	~1357	~1561	-
2	25.2	~1335	~1553	~1455
3	33.2	~1320	~1563	~1461
4	33.4	~1320	~1563	~1461
5	33.7	~1320	~1563	~1460
6	37.6	~1320	~1563	~1459
7	43.3	~1320	~1565	~1459
Annealed	23.2	~1336	~1600	~1515

6.1.4 Core level XPS spectra of Carbon Nitride compound

The measurements reported here were mainly carried out on two samples; sample 1 contained 33 at.% N and sample 2 contained 43 at.% N as measured by RBS.

Figure 9 and 10 show the C(1s) and N(1s) X-ray photoelectron spectra of the films respectively. Figure 9(d) and 10(d) show C(1s) and N(1s) X-ray photoelectron spectra of the films before and after annealing respectively. The N(1s) spectrum can be deconvoluted into three peaks as is normally found. There are a number of points to be made. Firstly, the peak at ~401.2 eV (figure 10) which is typically assigned to N-

N or N-O bonding [21] is found to increase with the nitrogen content of the films. A comparison of the as grown XPS curves for Samples 1 and 2 clearly shows (figure 10) that in sample 2 this peak is relatively much higher than for Sample 1 (Table 3). Since there is no observable oxygen in the films as measured by RBS, the 401.2 eV peak can be assigned to N-N bonds. This behaviour confirms the hypothesis of [1] that the excess nitrogen in the films is in some IR-inactive bonding structure; in fact it is in the form of N-N bonds.

Table 3: Relative N(1s) peak areas as a function of nitrogen content as measured by RBS.

Area ratios	Sample 1: 33 at.% N	Sample 2: 43 at.% N
$Area_{401.2}/Area_{400}$	0.52	0.94

The annealing behaviour is detailed in Table 4. There are two points to be drawn from this. As annealing occurs the ratio of the areas of the 398.8 eV peak to the 400 eV peak reduces with temperature.

Table 4: Relative N(1s) peak areas as a function of annealing temperature.

Area ratios	Before annealing	After 550°C anneal	After 600°C anneal
$Area_{398.8}/Area_{400}$	1.2	1.01	0.4
$Area_{401.2}/Area_{400}$	0.52	0.88	1.36

The FTIR results described previously, show that the intensity of the C≡N bonding (1500 cm^{-1}) reduces compared with the C=N bonding (1500 cm^{-1}). From this correspondence between the FTIR and XPS behaviour, we assign the 398.8 eV peak to C≡N and the 400 eV peak to C=N. It is believed that this conclusion which is based on observed changes in the bonding as seen by other techniques is more reliable than using comparisons with polymeric nitrogen containing carbon compounds.

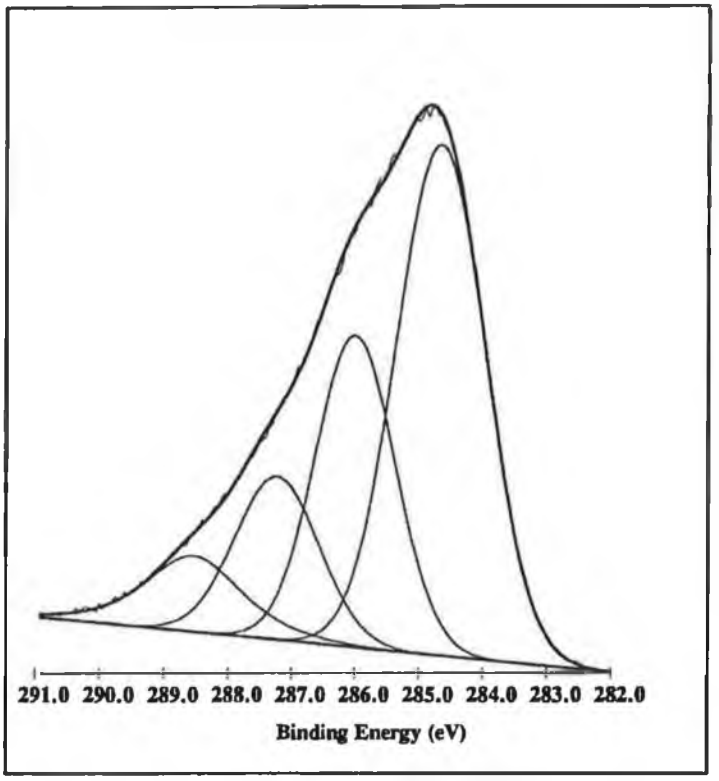

Figure 9(a): X-ray photoelectron spectrum of C(1s) electrons of CN_x film. The spectrum obtained is deconvoluted into four peaks using Gaussian-Lorentzian fit. The C(1s) peaks have been assigned as C-C (sp^3) at ~287.5 eV, C=N (sp^2) at ~286 eV and C≡N (sp) at ~ 288.5 eV for the film containing ~33 at.% N (sample 1, as deposited condition).

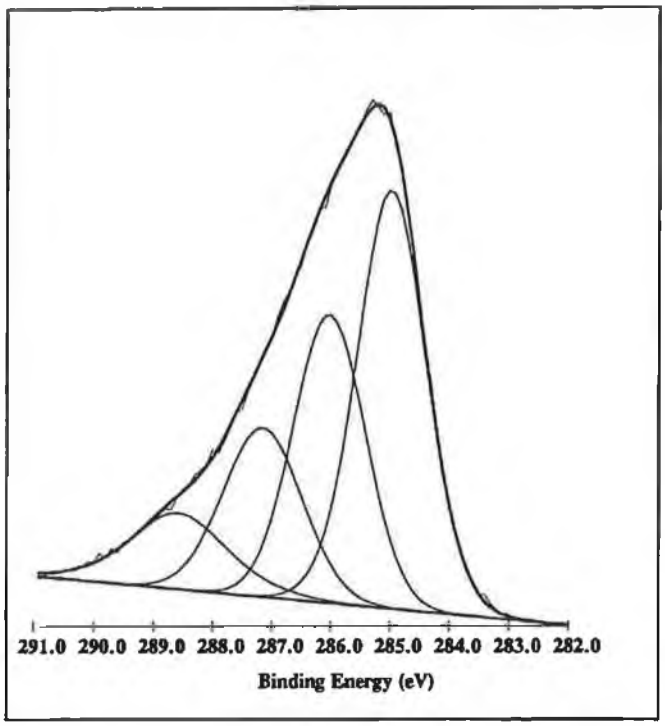

Figure 9(b): X-ray photoelectron spectrum of C(1s) electrons of CN_x film. The spectrum obtained is deconvoluted into four peaks using Gaussian-Lorentzian fit. The C(1s) peaks have been assigned as C-C (sp^3) at ~287.5 eV, C=N (sp^2) at ~286 eV and C≡N (sp) at ~ 288.5 eV for the film containing ~43 at.% N (sample 2, as deposited condition).

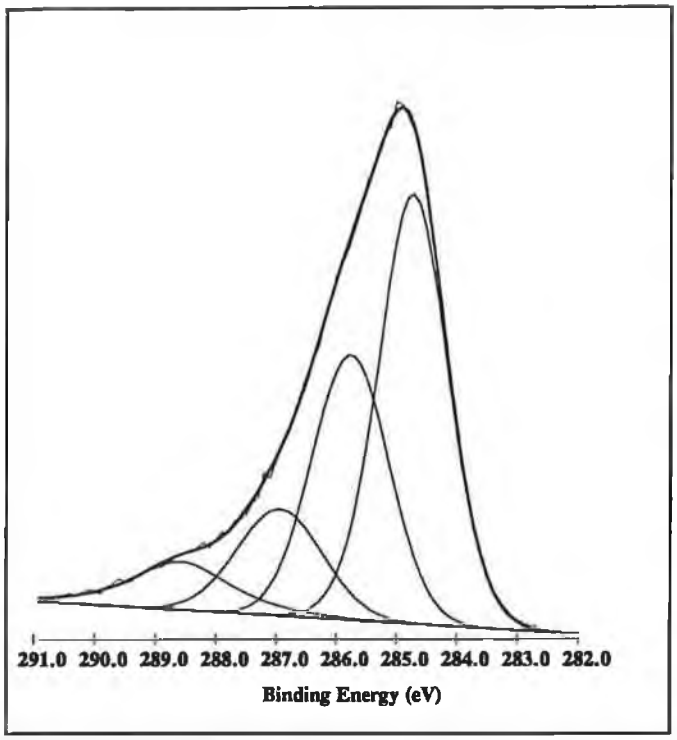

Figure 9(c): X-ray photoelectron spectrum of C(1s) electrons of CN_x film. The spectrum obtained is deconvoluted into four peaks using Gaussian-Lorentzian fit. The C(1s) peaks have been assigned as C-C (sp^3) at ~287.5 eV, C=N (sp^2) at ~286 eV and C≡N (sp) at ~ 288.5 eV for Sample 1 after annealing at 550°C.

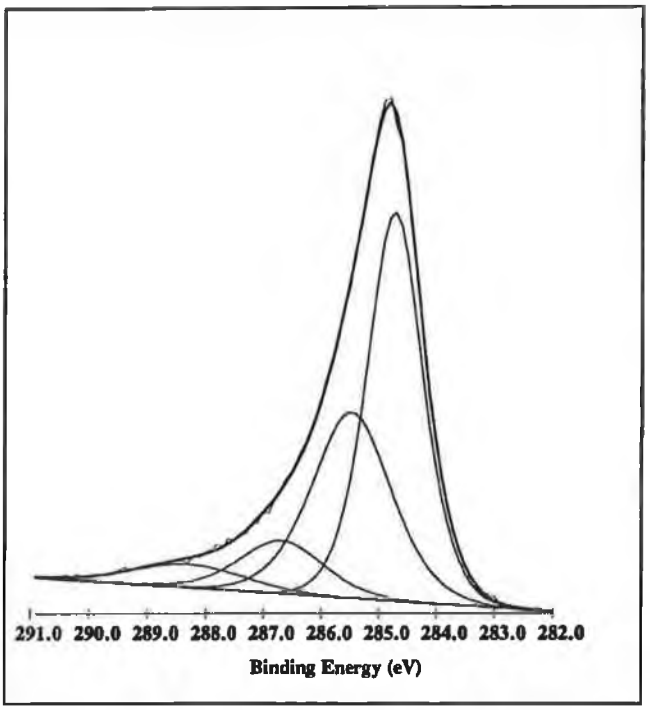

Figure 9(d): X-ray photoelectron spectrum of C(1s) electrons of CN_x film. The spectrum obtained is deconvoluted into four peaks using Gaussian-Lorentzian fit. The C(1s) peaks have been assigned as C-C (sp^3) at ~287.5 eV, C=N (sp^2) at ~286 eV and C≡N (sp) at ~ 288.5 eV for Sample 1 after annealing at 600°C.

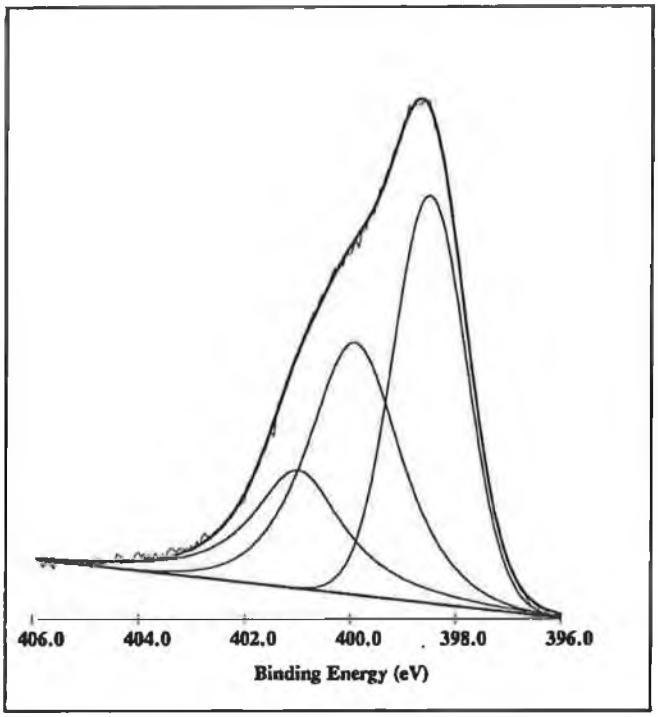

Figure 10(a): X-ray photoelectron spectrum of N(1s) electrons of CN_x film. The spectrum obtained is deconvoluted into three peaks using Gaussian-Lorentzian fit. The N(1s) peaks have been assigned as C≡N (sp) at ~398.8 eV, C=N (sp^2) at ~ 400 eV and N-N (sp^2) at ~401 eV for the film containing ~33 at.% N (sample 1, as deposited condition).

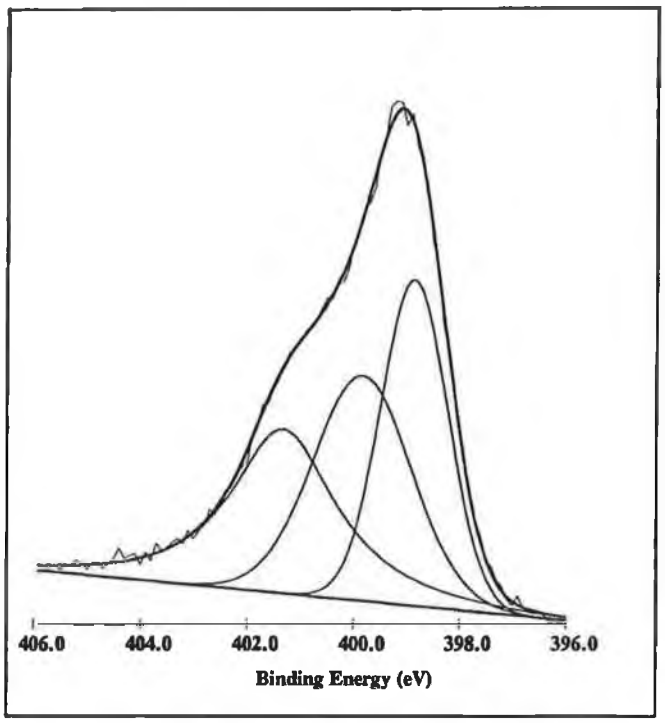

Figure 10(b): X-ray photoelectron spectrum of N(1s) electrons of CN_x film. The spectrum obtained is deconvoluted into three peaks using Gaussian-Lorentzian fit. The N(1s) peaks have been assigned as C≡N (sp) at ~398.8 eV, C=N (sp^2) at ~ 400 eV and N-N (sp^2) at ~401 eV for the film containing ~43 at.% N (sample 2, as deposited condition).

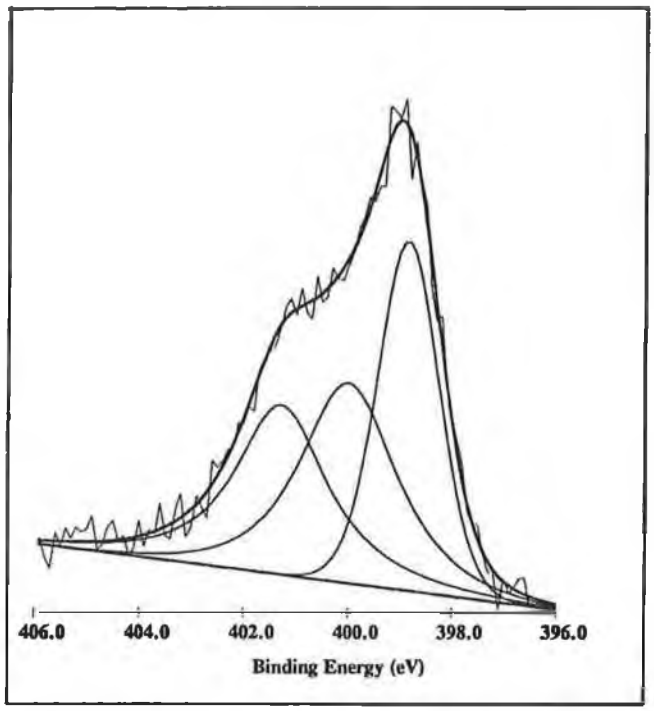

Figure 10(c): X-ray photoelectron spectrum of N(1s) electrons of CN_x film. The spectrum obtained is deconvoluted into three peaks using Gaussian-Lorentzian fit. The N(1s) peaks have been assigned as C≡N (sp) at ~398.8 eV, C=N (sp^2) at ~ 400 eV and N-N (sp^2) at ~401 eV for Sample 1 after annealing at 550°C.

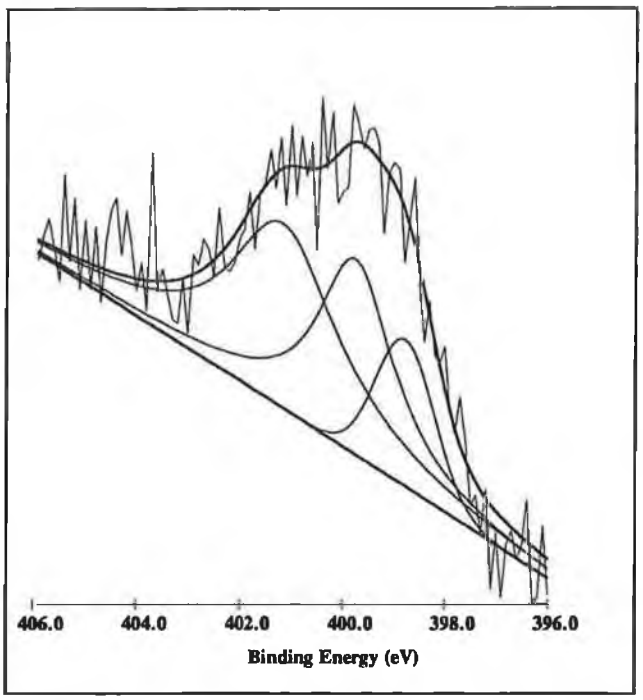

Figure 10(d): X-ray photoelectron spectrum of N(1s) electrons of CN_x film. The spectrum obtained is deconvoluted into three peaks using Gaussian-Lorentzian fit. The N(1s) peaks have been assigned as C≡N (sp) at ~398.8 eV, C=N (sp^2) at ~ 400 eV and N-N (sp^2) at ~401 eV for Sample 1 after annealing at 600°C.

No evidence of sp^3 bonding was seen either from the FTIR or Raman data; it has been reported that the C-N sp^3 bond should be visible at $\sim 1250\ cm^{-1}$ [22]. It is therefore not possible to ascribe any of the N(1s) peaks to a C-N sp^3 structure. In addition, if we compare the changes in the relative areas of the 401.2 eV and 400 eV peaks as annealing progresses, we see an increase in the ratio. This also fits with the assignment of the 401.2 eV peak to a N-N bond since from thermodynamic arguments the N-N bond is stronger than the C-N bonds [23] and would be expected to be more stable under annealing conditions compared with them.

Inferences may also be drawn from the behaviour of the C(1s) peak. Deconvolution shows the existence of four peaks at 285.8 eV (sp^2), 287.1 eV (sp^3) , 288.5 eV (sp) and 284.5 eV. The peak at 284.5 has been generally labeled as due to adventitious carbon (AC) mainly due to atmospheric contamination [24]. Due to their being no evidence of sp^3 C-N bonding in the films, it is ascribed that the 287.1 eV peak purely due to C-C bonds, the others will be due to a combination of carbon-carbon and carbon-nitrogen bonds. As annealing takes place the ratio of the areas of the 285.8 and 287.1 eV peaks increases as shown in Table 5, i.e. the sp^2/sp^3 ratio increases indicating that a greater degree of graphitisation is taking place. This is supported by the shapes of the Raman D and G peaks which become narrower and more characteristic of graphitic material as temperature is increased [24]. The assignment of the 288.5 eV peak as due to C≡N sp bonding is also supported by a comparison of Table 5 and the FTIR data; i.e. the C≡N bonding is reduced compared to the sp^2 bonding as temperature is increased.

Table 5: Relative C(1s) ratios as a function of annealing temperature

Area ratios	As deposited	After 550°C anneal	After 600°C anneal
$Area_{285.8}/Area_{287.1}$	1.8	2.24	3.44
$Area_{288.5}/Area_{285.8}$	0.32	0.25	0.16

Although Torng et al. [26] proposed that incorporation of nitrogen in the film will stabilize the C-C sp^3 type bondings, they did not give any quantitative evidence. The XPS study shows that nitrogen incorporation in the film not only increases the nitrogen-nitrogen bonding but also stabilises the C–C sp^3 type bondings. A comparison of the as grown C(1s) XPS curves for sample 1 and 2 clearly shows that in sample 2 the peak at ~287.5 eV which is assigned to C–C sp^3 bonding increases as the nitrogen incorporation in the film increases (Table 6).

Table 6: Relative C(1s) peak areas as a function of nitrogen content as measured by RBS.

Area ratios	Sample 1: 33 at.% N	Sample 2: 43 at.% N
$Area_{287.1}/Area_{286}$	0.55	0.64

It is not possible at this stage to say that the level of this stabilisation is higher comparable to the sp^3 phase in the a-C:H film stabilised by hydrogen incorporation as proposed by Torng et al [26].

The breaking mechanism of C–C sp^3 type bonding and thus graphitisation of the film proposed by Rossi et al. [27] can be explained by a quantitative XPS study. As annealing progresses, the thermal energy necessary to break the sp^3 bondings helps the graphitisation process. Table 7 shows the C(1s) XPS peak area ratio after annealing up to 600°C.

Table 7: Relative C(1s) ratio as a function of annealing temperature

Area ratios	As deposited (Sample 1)	After 550°C anneal	After 600°C anneal
$Area_{287.1}/Area_{286}$	0.55	0.44	0.29

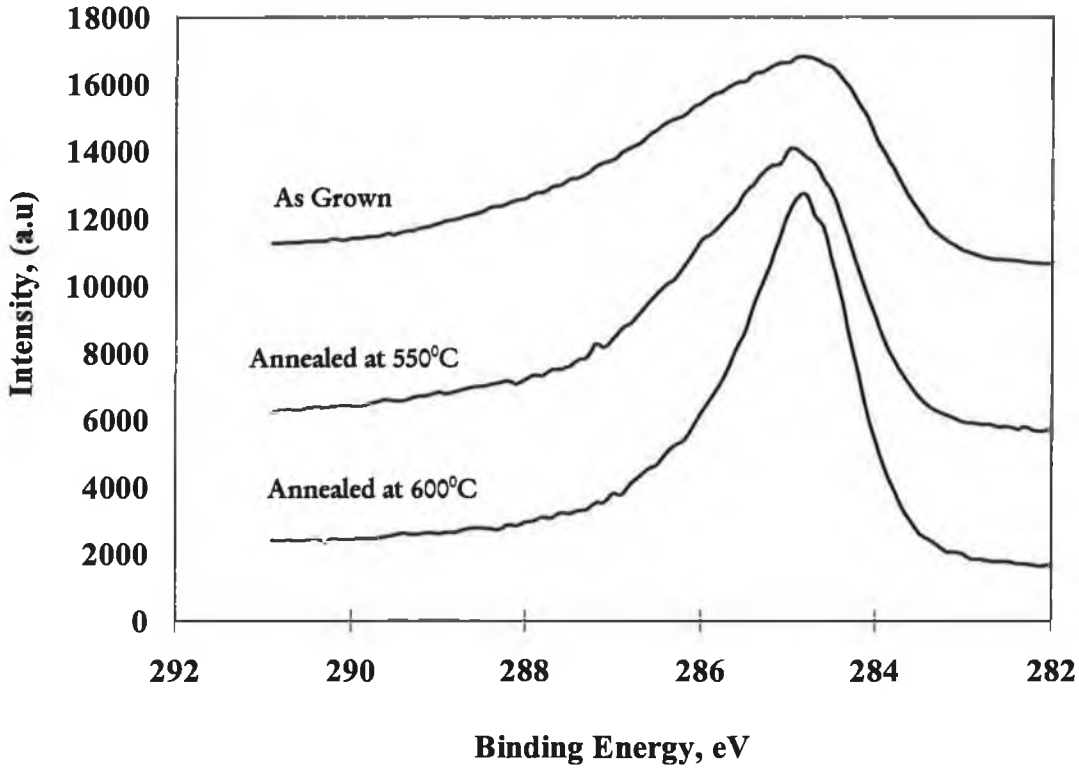

Figure 11: XPS C(1s) core level spectra showing the film behaviour at different annealing temperatures. The film contains 33 at.% N.

Although it is expected that the C-C sp^3 bonding could be stronger than the C=N sp^2 type as its four σ bonds per site are more stable. But due to carbon's atypical nature [28] in having its p orbital more compact and tightly bound compared to s states, carbon's sp^2 σ bonds are stronger than its sp^3 bonds and favour the sp^2 structure. Thus for CN_x film, the C=N sp^2 phase is more stable than C-C sp^3 phase. This argument is supported by the annealing behaviour of the film. Figure 11 shows the behaviour of XPS C(1s) peak envelopes in different annealing conditions. It is apparent from this figure and Table 7 that due to loss of C–C sp^3 component of C(1s) spectrum, the peak envelope becomes more sharp at 600°C. However, the sp^2 phase was not affected at all.

The behaviour of the XPS N(1s) peak in different annealing conditions is shown in figure 12. The deconvolution data of these envelopes, discussed before (table 3), confirm the hypothesis regarding nitrogen-nitrogen peak. Previously it was shown that >25 at.% nitrogen incorporation in the film, the excess nitrogen bonds to itself rather than bonding with carbon. It was also shown that as annealing progresses the nitrogen-nitrogen peak was less affected by the annealing temperature as compared to the carbon-nitrogen bondings. This occurs because the dissociation energy of nitrogen-nitrogen bonding is much higher than the carbon-nitrogen bondings [29]. This argument also suggests that a multiple bonding structure could be present in the nitrogen-nitrogen bonding.

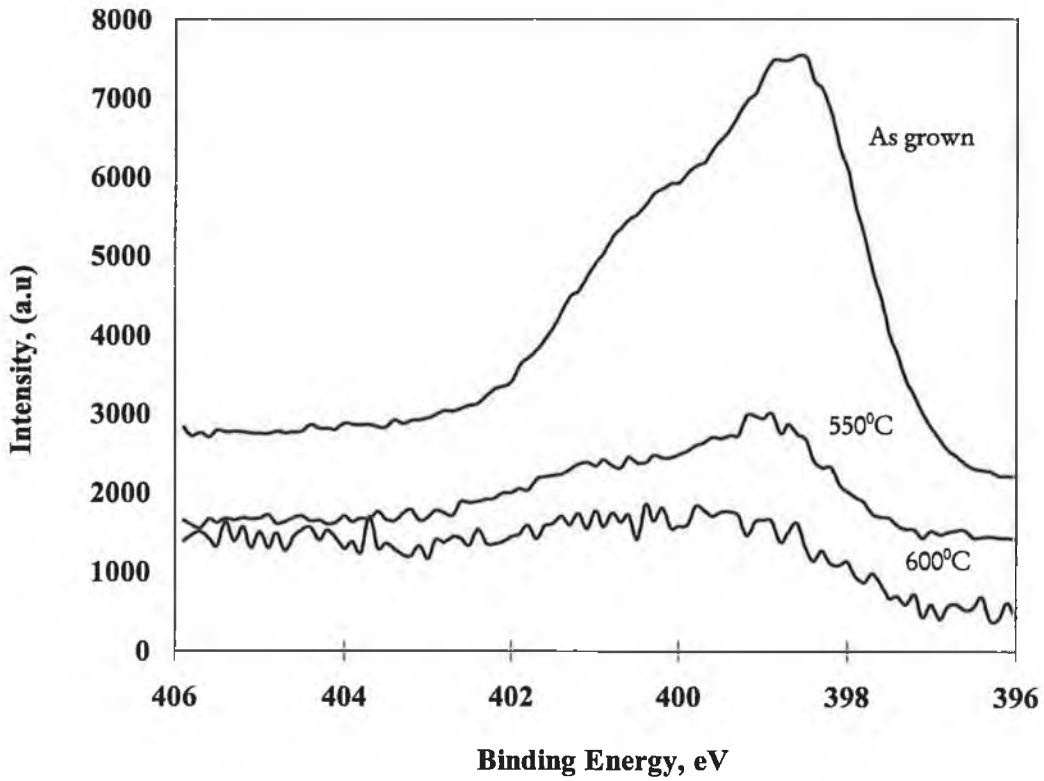

Figure 12: XPS N(1s) core level spectra showing the film behaviour at different annealing temperature. The film contains 33 at.% N.

6.1.5 Valence Band XPS spectra of Carbon Nitride Solid

The fingerprinting capacity of valence band spectra due to s and p characters in the bonds in carbon based materials for structural information can be very valuable since this information is sometimes unobtainable from core-level photoelectron spectrum [30]. Although the valence band density of states itself a complex and important research area specially for carbon nitride material, only its ability to predict structural information will be discussed. It is of interest to compare the valence bands of different forms of carbon because of the different coordination e.g. trigonal in graphite and tetrahedral in diamond. Figure 13 shows the valence band spectra of a CN compound containing 33 at.% nitrogen in both as grown and annealed condition. There are three regions: I at ~5-14 eV, II at ~17.5-22.5 eV, III at ~22.5-27.5 eV. For diamond (figure 14), peak I (~5-10 eV) is stipulated to be pure 2p states, peak II (~10-14 eV) composed of s-p hybridised states while peak III (~16-20 eV) is proposed to be due to predominantly 2s states [31,32]. It can be seen from figure 13 that the features at II and III are shifted to the higher binding energy when compared with diamond valence band structure (figure 14).

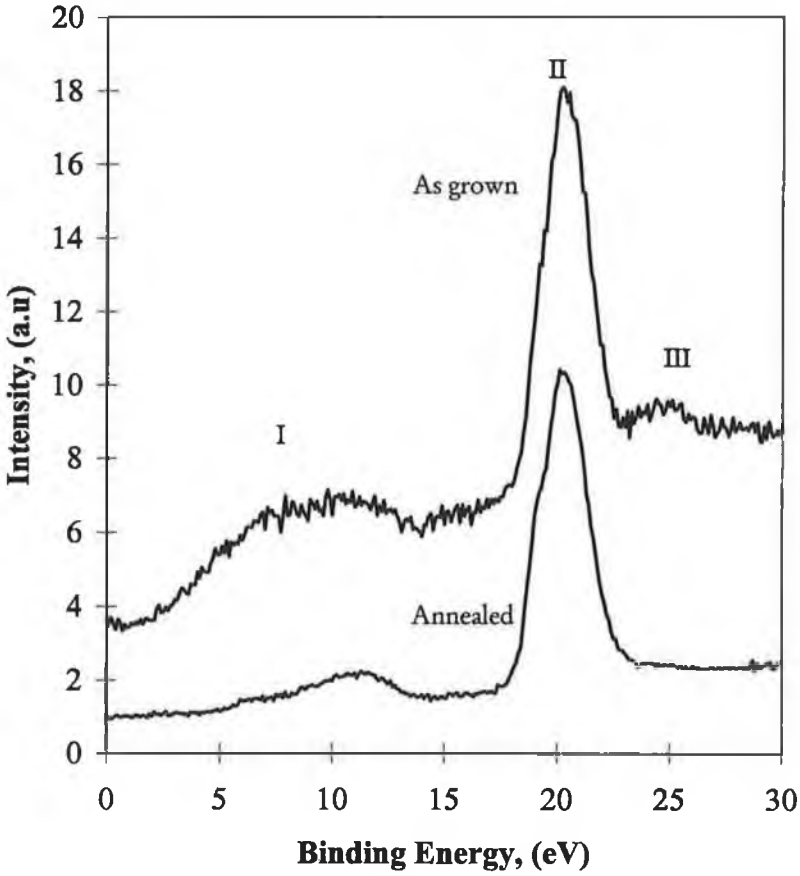

Figure 13: Valence Band XPS spectra of a carbon nitride thin film revealing its s, p and s-p characteristics: as grown (33.2 at.% N) and annealed (23.2 at.% N).

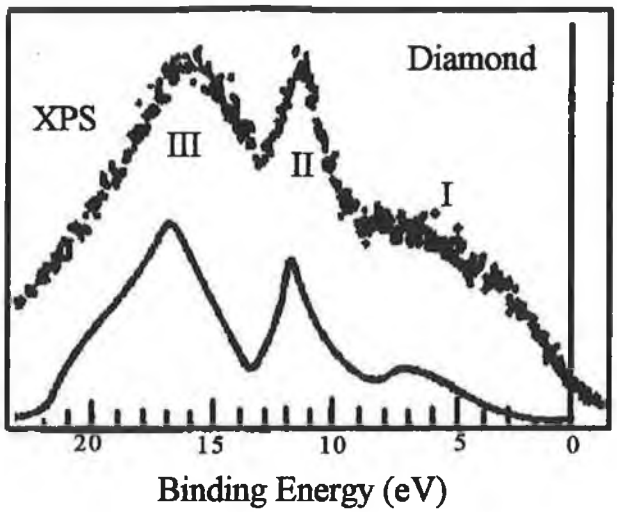

Figure 14: XPS spectrum of the valence bands of diamond (dots) compared with the results of theoretical tight-binding valence bands calculation (solid line) [31,32].

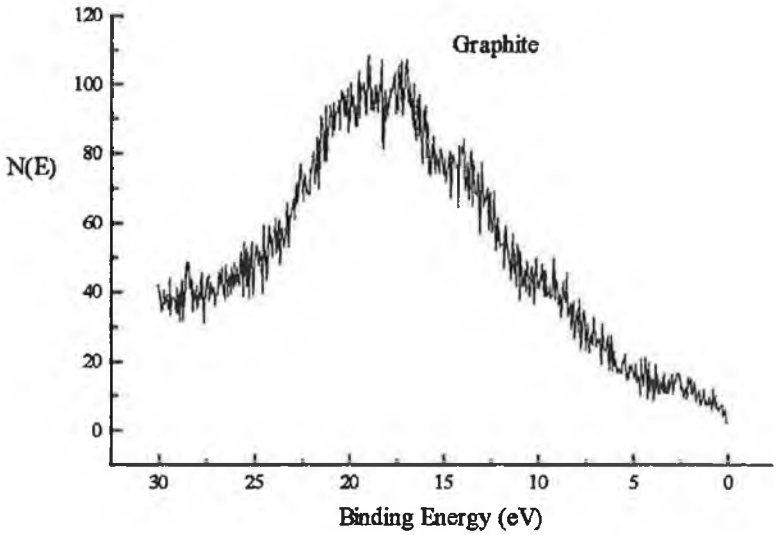

Figure 15: Valence band spectra of graphite revealing its s, p and s-p characteristics [33].

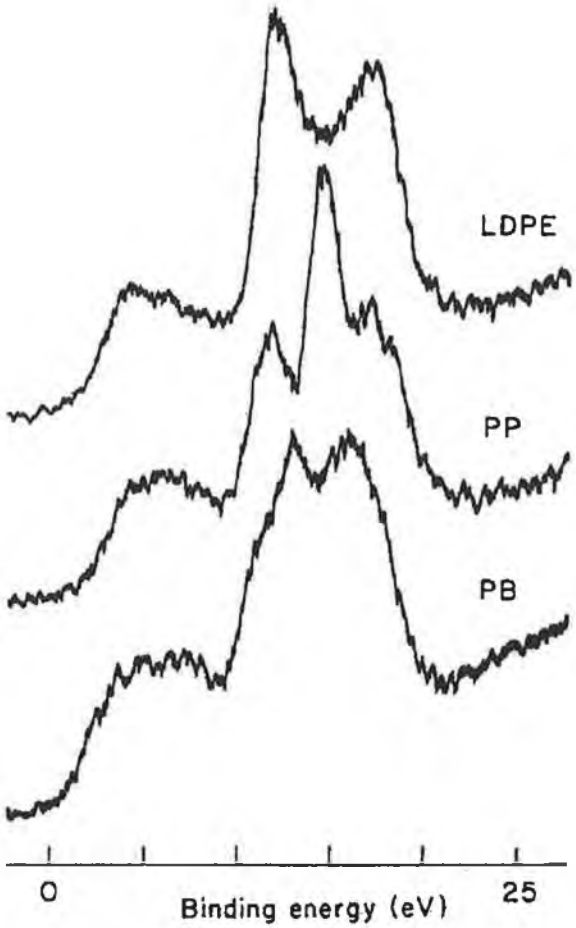

Figure 16: Valence band spectra from the hydrocarbon polymers: low-density polyethylene (LDPE), polypropylene (PP) and poly(but-1-ene) (PB). It is to be noted that all these polymers give identical C 1s XPS spectra, but their valence band XPS spectra changes due to change in carbon network [30].

A different spectrum is observed for graphite material (Figure 15). Two peaks (4 eV and 8 eV) are observed at region I, region II is observed at 10-15 eV and region III is observed at ~17.2 eV [33]. When carbon forms a polymer with hydrogen, i.e. polyethylene, polypropylene etc. an intense peak at region II (~11-22 eV) and a wide peak at I (~5-10 eV) are observed [30] and the III peak is absent. Now if the valence band spectra (figure 13) of carbon nitride is compared with diamond, graphite and polymers (Figures 14-16), it is easily seen that nature of the sp hybridised region (II peak) of carbon nitride is very similar to that of polymers. However, region I of graphite and diamond could be comparable to CN region I.

The reason for the variation of the intensity ratio I_{III}/I_I from allotropic C to CN compound is solely the change in atomic photoionisation cross sections due to the change in population of 2s and 2p atomic levels, thus giving the idea of density of states. To see the stability of the features discussed above the sample was annealed at 600°C. It is interesting to note that the feature at III is gone and region I is more refined (Figure 13) but region II did not change at all. It can be concluded that sp^2 hybridised bonding is the most stable and dominating structure of amorphous carbon nitride material and the overall structure of the compound has to some extent the interlinked carbon backbone nature.

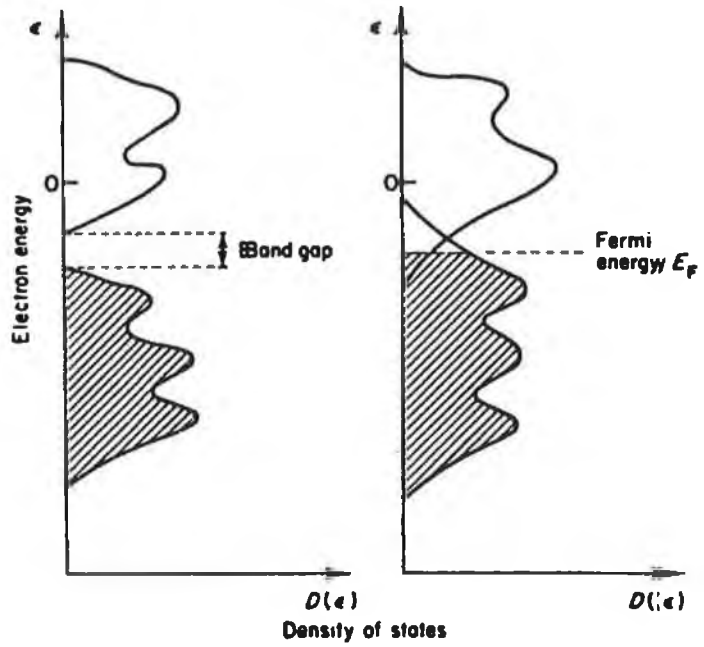

Figure 17: Schematic density of states for (a) an insulator, left (b) a conductor (metals), right. The shading indicates the extent to which the energy levels are occupied [30]

As mentioned earlier valence band spectra relate closely to the occupied density of states structure. This is very useful in the study of the electronic structure of the material. Electronic properties, i.e., band structure, are very sensitive to structural changes of the material. The valence band spectral interpretation sometimes gives direct information about conductivity of the material. Although this part of study is

not the scope of this thesis, the spectral interpretation can be a good source for detailed study in future. Before going to the spectral interpretation it is worthwhile to talk about the density of states of insulator and metals. Two situations can be distinguished as in figure 17, i.e., insulators and conductors (metals). Figure 17 illustrates the density of electron states (per unit energy in unit volume) in these two cases.

In the case of an insulator the occupied valence band is separated from the empty conduction band, whilst in the case of a metal these bands overlap and the uppermost occupied state is termed the Fermi level (E_F). It is to be noted here that E_F is not the true zero point of the electron energy scale, although binding energy (BEs) are often referenced to this point. The true zero is the vacuum level (E_V) and, to a very first approximation, $E_F - E_V = \Phi$, where Φ is the work function of the material as discussed earlier. Briggs [30] mentioned that the observed density of states in case of XPS, closely reflects the initial filled density of states. In Figure 13 the peak labelled I actually indicates the 2p states for carbon nitride. This state is in fact the transition of valence band and conduction band, thus is dominated by 2p states. Any change in electron density at this state can be detected by XPS spectra. A wide peak is observed in the 5-10 eV range (region I) in fugure 13. After annealing a distinct peak is observed at $\sim$10 eV. The effect of annealing on conductivity of carbon nitride material can be explained by a detailed study of the spectra at this region.

6.1.6 AES spectra of Carbon Nitride Solid

Auger Electron Spectroscopy (AES) was also used to determine the structural changes of CN films. The nature of the Auger peak is highly sensitive to the bonding structure of the film. Lurie et al. [34] studied extensively the AES carbon spectra of diamond, graphite and amorphous carbon (figure 18).

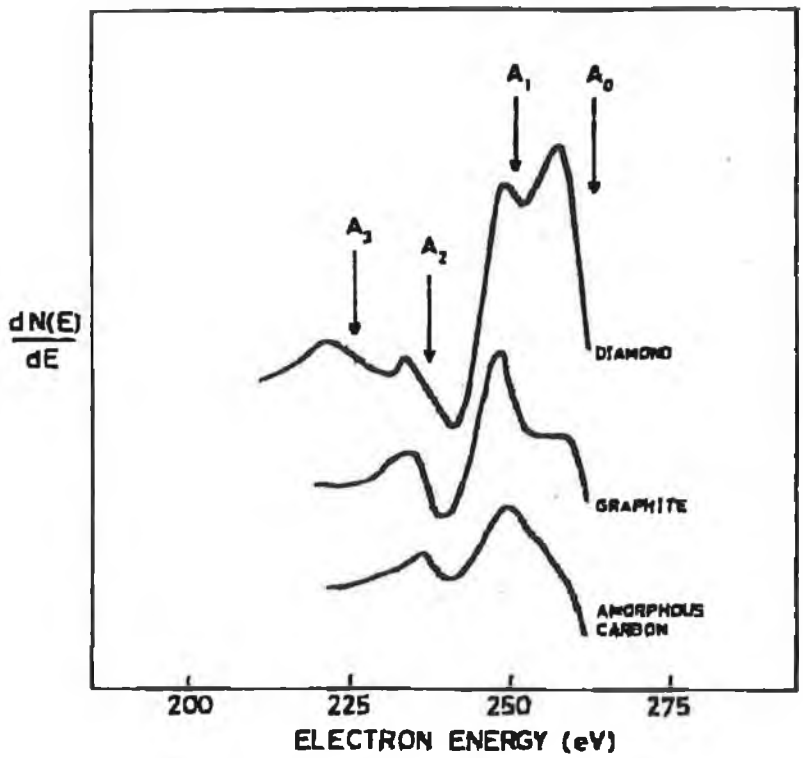

Figure 18: Comparison of the fine structure of the carbon KLL Auger spectra from diamond, graphite and amorphous carbon. The peaks have been labeled A_0 to A_3 where A is used to denote an Auger peak. In the figure the main peaks have been aligned to the diamond A_0 position. Depending on the structure (diamond to amorphous carbon), the shoulders appear in the spectra [34].

The detail discussion of figure 18 is not the scope of this thesis. This study will be extended for the CN film containing 33 at.% nitrogen. The fine peaks obtained at the lower band region are not yet possible to explain but fine peaks near the *KLL* carbon peaks can be compared with standard carbon Auger peaks. The Auger signal for carbon is very sensitively dependent on the exact bonding nature and atomic arrangement of the structure. The C-C sp^3 phase is a metastable structure in CN film [35]. This phase can be degraded [36] into graphite like (sp^2) or even amorphous carbon by argon ion bombardment. To retain the as grown structure we did not perform any pretreatment on the film surface such as sputter cleaning or heat treatment. There is a basic difference between the carbon Auger peak of carbon

nitride solid and diamond or graphitic structures at the upper-wing of the C *KLL* peak labeled C_0 (Figure 19.a).

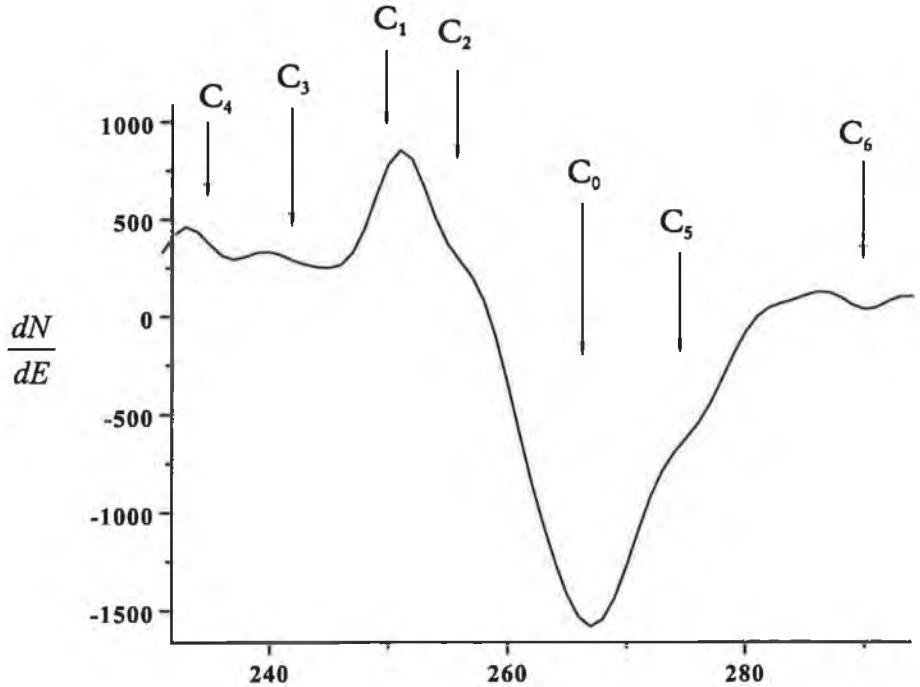

Electron Energy, (eV)

Figure 19(a): Carbon *KLL* Auger spectrum of CN_x film containing 33 at.% N (as deposited condition). The components were labeled by C.

A feature C_1 occurs at the lower energy side of the upper-wing of the *KLL* C_0 peak in the case of diamond structure while in graphite a feature occurs on the other side of this wing at C_2 position. For amorphous carbon no feature will be observed but C_0. It can be mentioned here that the sp^2 phase due to the C=N bondings is heterocyclic in nature which is structurally different from graphite. This comparison of data shows that both graphitelike C_2 and diamondlike C_1 nature exits in our film. It can be seen from the AES carbon spectrum of our CN film that the C_2 feature is more prominent than the C_1 feature. Thus our film is more graphitic in nature. Although the intensity of C_1 feature in our film is very low, the presence of a satellite peak, labeled C_6, at ~292 eV confirms the presence of C–C sp^3 structure in our film [34]. This satellite peak is a characteristic Auger emission spectrum of

diamondlike C–C sp^3 phase. As no shift in electron energy for this satellite peak was observed, the sp^3 phase is essentially C–C not C–N. This argument is supported by Raman, FTIR and XPS results.

The shape of the fine structure features observed at C_3 and C_4 electron energy level was similar to other AES modeling data on CN films [37]. The feature C_3 can be assigned to excited π electrons of the valence band of C=N sp^2 bonding. The feature C_4 can be assigned to excited σ electrons of the same band due to C–C sp^3 bonding structures. A distinct feature labeled at C_5 is sometimes assigned to a defect-related π state [37] which has not been explained before, although the origin of this feature came from damaged-graphite [38]. The feature observed in the CN film is more prominent than is found in the damaged-graphite. Thus the reason for this feature in damaged-graphite may not be the same as is found in carbon nitride films. Previously it was mentioned that the formation of C≡N bonding will terminate the carbon backbone leading to less tightly bound carbon atoms, thus forming a defect in the structure. It is suspected this defect-related feature is due to the formation of sp type C≡N bondings which undoubtedly result from π state electrons.

Figure 19(b) shows the N *KLL* AES spectra. Three components were identified in the N *KLL* spectra. The feature labeled at N_0 is the main *KLL* Auger transition. Features labeled at N_1 and N_2 are due to the excited π and σ electrons respectively which are assigned to different C–N bondings. It can be noted here that the feature labeled at N_0 is actually due to overlapping peaks which could be a good indication of nitrogen-nitrogen multi bonding *KLL* Auger transitions.

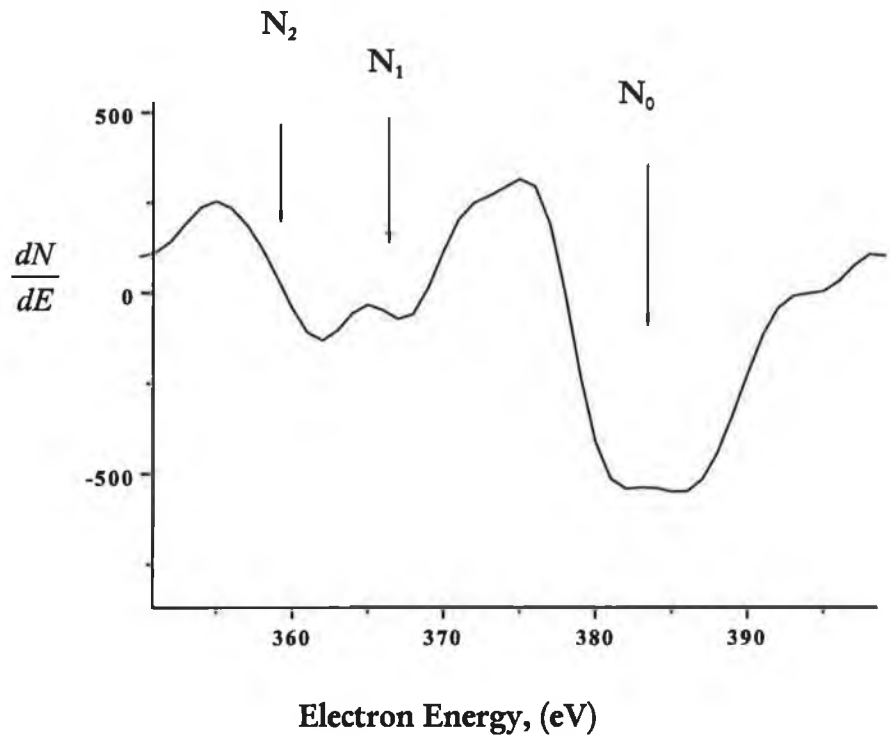

Figure 19(b): Nitrogen *KLL* Auger spectrum of CN_x film containing 33 at.% N (as deposited condition). The components were labeled by N.

Summary

The measurements of film composition and IR absorbance show that for films with >20% nitrogen content the nitrogen is mostly bonded to carbon. With increasing nitrogen content above 20%, excess nitrogen is not bonded to carbon but probably exists as N-N bonds of some description.

Annealing has been shown to lead to a loss of nitrogen from the films at temperature above approx. 550°C. As annealing progresses the C≡N is totally removed at 600°C and the appearence of G and D band which is usually Raman active, becomes IR active.

The evolution of the C–C, C=N, C≡N bond intensities in amorphous carbon nitride film deposited by reactive magnetron sputtering process has been described. It has also been shown that between the Raman D and G peaks their exists a third peak at ~1455 cm^{-1}, designated the "N" peak, which has been assigned to the N=N stretching vibration. As the nitrogen incorporation in the film increases, the N=N, C≡N and C–C bonding intensities increase. These experimental results are also in good agreement with the theoretical predictions and thus identify bands in vibrational spectra in the amorphous carbon nitride solid.

It has been shown by comparing FTIR, Raman, XPS and RBS data that the nature of the nitrogen incorporation in sputtered carbon nitride films changes with the amount of nitrogen incorporated. In particular, above ~25 at.% N content, an increasing amount of the nitrogen occurs in the form of N-N bonds. As annealing progresses, the C≡N sp bonds are eliminated preferentially and the relative amount of nitrogen-nitrogen bonds increases due their relative stability.

The XPS peaks have been assigned to different types of bond by correlating their behaviour as annealing takes place at different temperatures with changes in the bond structure as detected by vibrational spectroscopy, rather than the typical process which involves comparison with nitrogenated polymers. The various components of the N(1s) XPS peaks forms are ascribed as follows: C≡N (sp) at ~ 398.8 eV, C=N (sp^2) at ~ 400 eV and N-N (sp^2) at ~401.2 eV. The C(1s) peaks have been assigned as C-C (sp^3) at ~287.5 eV, C=N (sp^2) at ~286 eV and C≡N (sp) at ~ 288.5 eV.

The valence band spectra shows the interlinked carbon backbone nature of the carbon nitride solid and thus identifies the structural nature of this solid which is significantly different from diamond-like and graphitic features.

It can be seen from AES spectra that both graphitelike C_2 and diamondlike C_1 nature exits in our film. It can be seen from the AES carbon spectrum of our CN film that the C_2 feature is more prominent than the C_1 feature. Thus our film is

more graphitic in nature. The presence of a satellite peak, labeled C_6, at ~292 eV confirms the presence of C–C sp^3 structure in our film. Formation of sp type C≡N bonding resulting from π state electrons terminates the carbon backbone leading to less tightly bound carbon atoms, thus forming a defect in the structure as shown in the AES C *KLL* spectra.

As nitrogen incorporation in the film increased, the C-C sp^3 phase was also found to increase, thus nitrogen acts as a stabilising medium of the sp^3 phase. The presence of this bonding structure rather than the C–N sp^3 type, is confirmed by AES, XPS and Raman spectroscopy studies.

The breaking of C–C sp^3 bonds results from the input thermal energy as annealing progresses and leads to graphitisation of the film. Due to carbon's atypical nature in having its p orbital more compact and tightly bound compared to s states, the C=N sp^2 phase is more stable than C-C sp^3 phase. This argument is supported by the annealing behaviour of the film. As C=N sp^2 phase dominates the structure, we propose the film at this stage is mainly graphitelike with some proportion of C–C, C≡N and N=N bonds. Determination of crystalline phases in the film, if present, requires diffraction techniques and Transmission Electron Microscopy.

Part II

6.2 Continuous crystalline β-C_3N_4 films

There have been many reports of amorphous carbon nitride films of uncertain composition but there have only been a few observations of crystalline β-C_3N_4 produced by diode sputtering, laser ablation and hot filament CVD [39-42]. The films reported have been discontinuous with isolated crystals [42] or showing only a few isolated grains in an amorphous matrix [39,41] and in most cases high substrate temperatures (600-950°C) were required. In this research it is reported for the first time that the deposition of carbon nitride thin films that contain large continuous nanocrystalline areas (>10 μm^2) of crystallography consistent with the β-C_3N_4 structure. In addition the creation of these β-C_3N_4 regions has been achieved with low substrate temperatures (<270°C) and high deposition rates (2 - 3 $\mu m.hr^{-1}$), as mentioned in chapter 4. The Penning type opposed target sputtering technique is a novel approach for the production of large amount of crystalline carbon nitride phases in the film. The films were studied by X-ray diffraction technique to identify the crystalline phases, although it was found that electron diffraction was necessary for crystalline carbon nitride phase determination. The film microstructure containing a large amount of nanocrystals are studied by transmission electron microscopy. This part of the chapter discusses these features in detail.

6.2.1 Structural analysis of Carbon Nitride material by X-ray diffraction technique

The observation of reflections due to the *d* spacings characteristic of β-C_3N_4 is confirmed by XRD measurements on the films containing 33.4 at.% N (PCN17), 33.2 at.% N (PCN19) and 43.3 at.% N (PCN26). As the films were deposited on Si (100) wafer, diffraction pattern was also recorded from the substrate to identify the diffracted peaks which are actually coming from the film. The incident X-ray beam is reflected by both from the amorphous and the crystalline material. There was some evidence of crystalline diffraction, however peak intensities were low. This

was attributed to the low atomic scattering factor associated with X-ray diffraction from both carbon and nitrogen. The *d* spacing corresponding to the sharp reflection peaks are tabulated from sample PCN19, deposited using 100% nitrogen sputtering gas (Table 8-10). The diffracted pattern (Figures 20-23) showed a prominent diffuse amorphous peak at $2\theta \sim 14^{\circ}$. Thus further crystallographic investigation required electron diffraction.

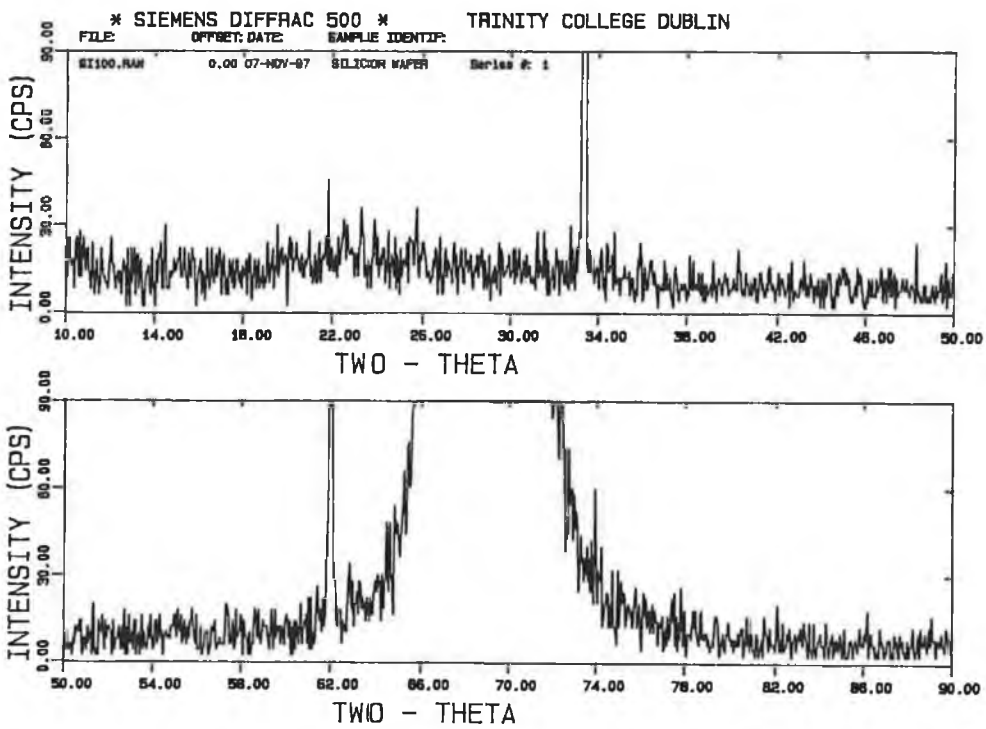

Figure 20: X-ray diffraction pattern of n-type Si (100) crystal. The highest intense peak is coming from <400> direction at $\sim 2\theta = 68.92^{0}$.

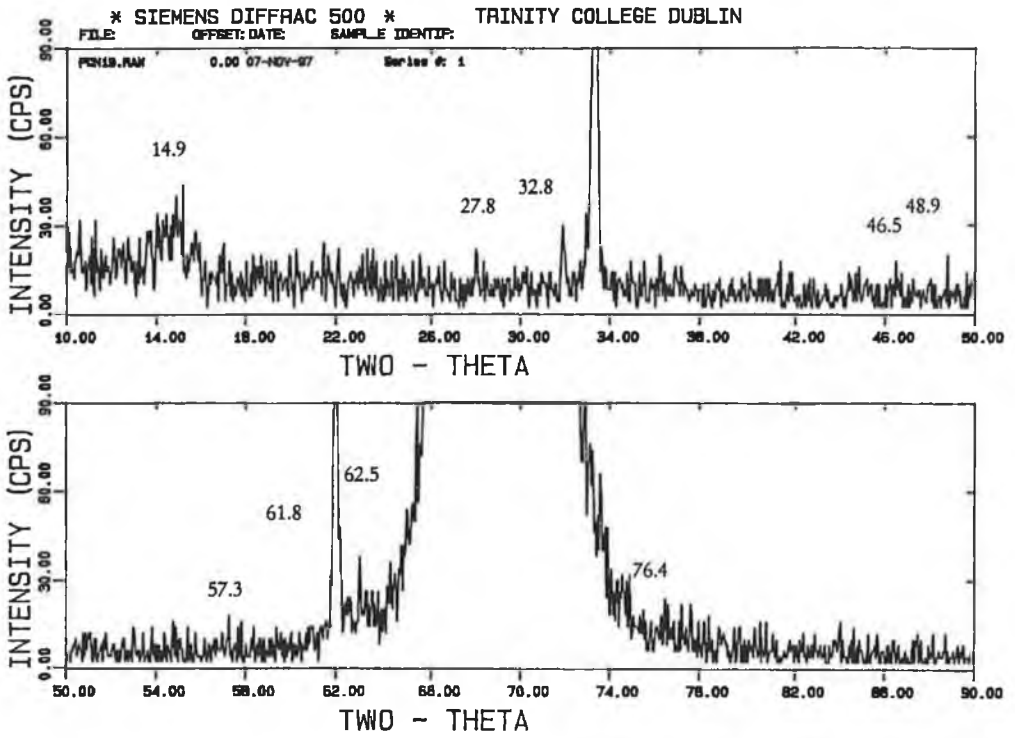

Figure 21(a): X-ray diffraction pattern of the crystalline β-C_3N_4 phases deposited on the n type Si (100) substrate (sample PCN19). Although relative intensity of the peaks are low (see text), indexing of the crystalline phases are given in the table 8. The prominent diffuse amorphous peak at 2θ ~ 14° can be identified.

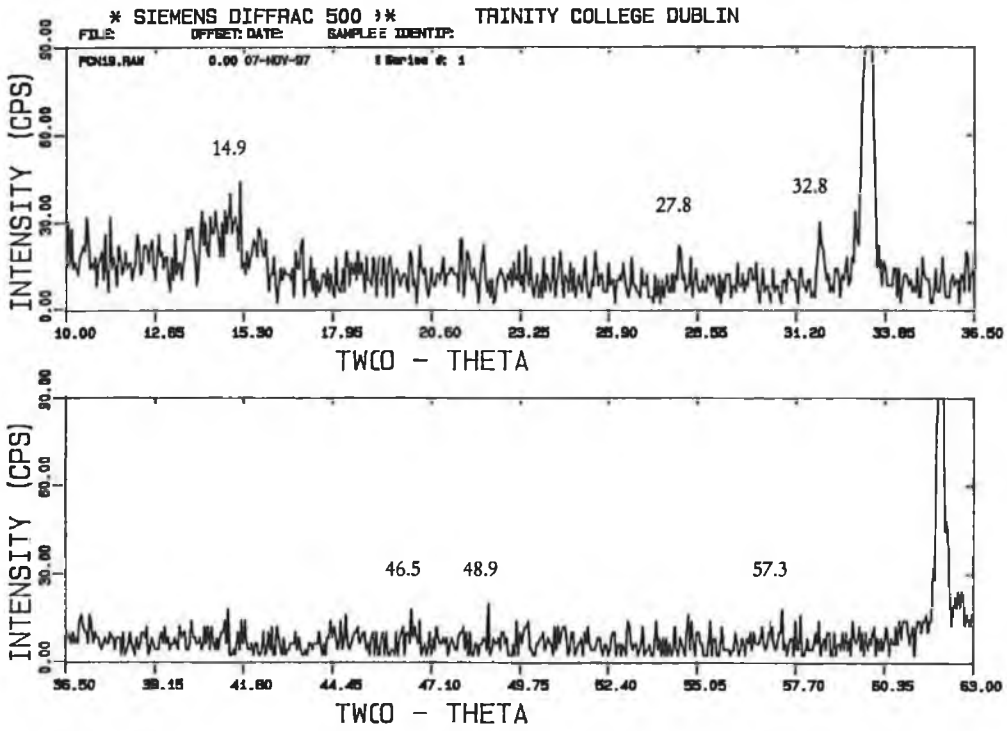

Figure 21(b): X-ray diffraction pattern of the crystalline β-C_3N_4 phases deposited on the n type Si (100) substrate (sample PCN19). Enlarged scale (from 2θ = 10 to 63°) is shown for clarity. Indexing of the crystalline phases are given in the table 8.

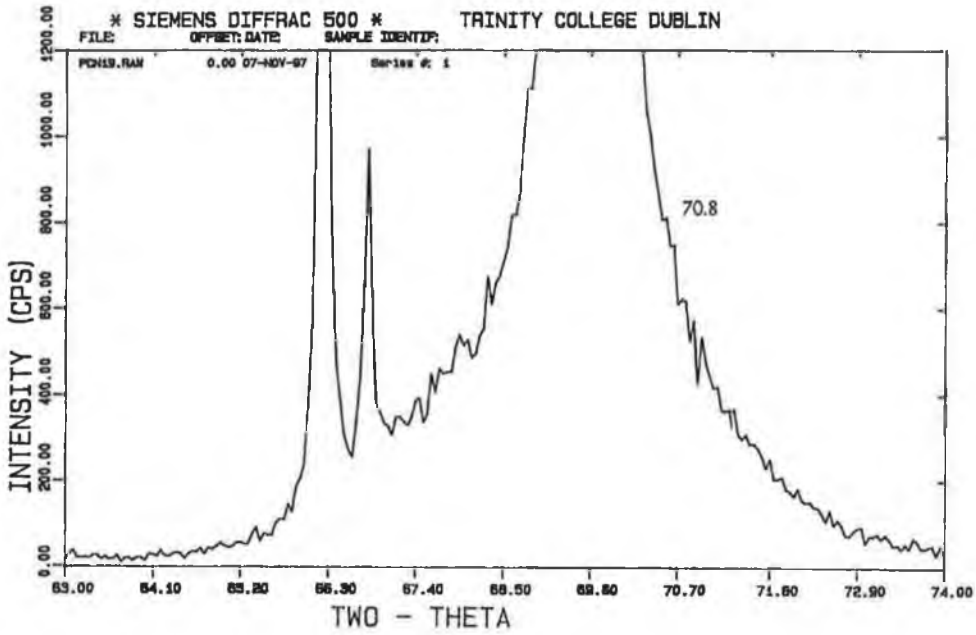

Figure 21(c): X-ray diffraction pattern of the crystalline β-C_3N_4 phases deposited on the n type Si (100) substrate (sample PCN19). Enlarged scale (from 2θ = 63 to 74°) is shown for clarity. Indexing of the crystalline phases are given in the table 8.

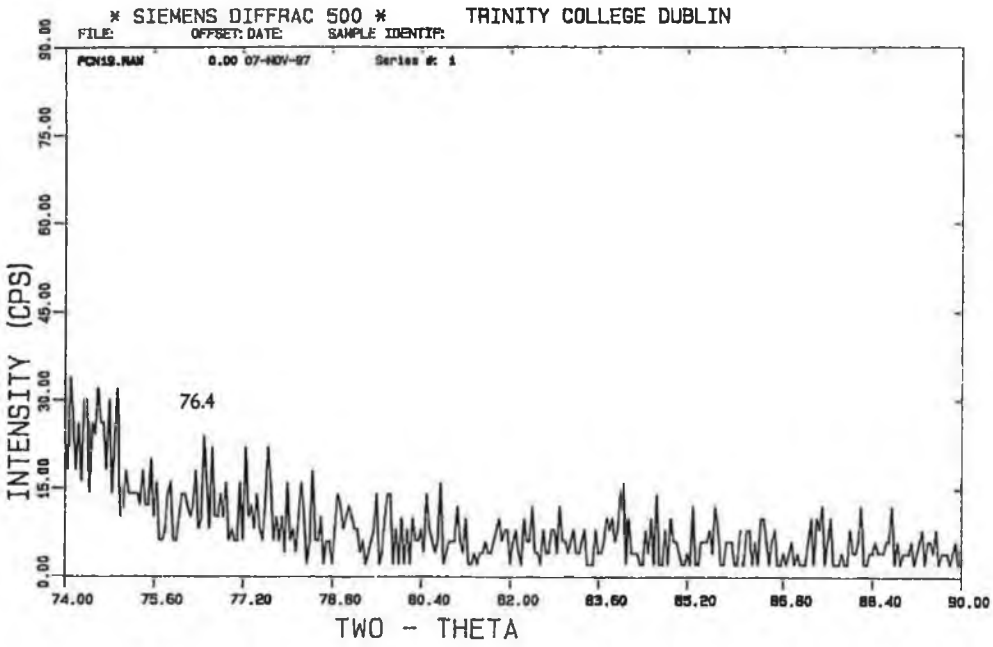

Figure 21(d): X-ray diffraction pattern of the crystalline β-C_3N_4 phases deposited on the n type Si (100) substrate (sample PCN19). Enlarged scale (from 2θ = 74 to 90°) is shown for clarity. Indexing of the crystalline phases are given in the table 8.

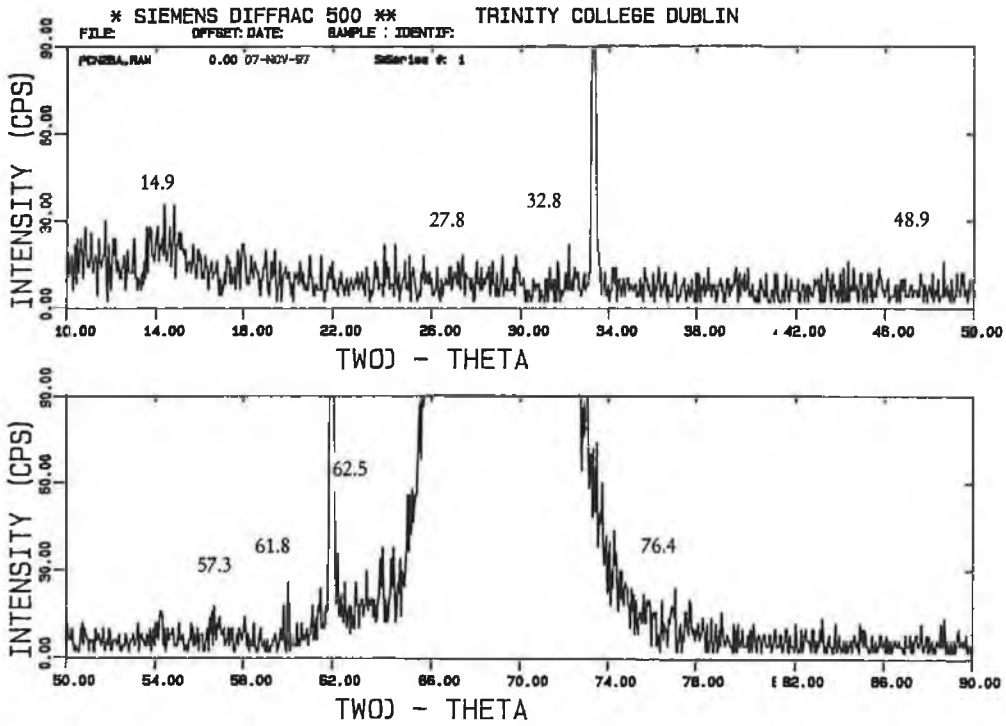

Figure 22: X-ray diffraction pattern of the crystalline β-C_3N_4 phases deposited on the n type Si (100) substrate (sample PCN26). Although relative intensity of the peaks are low (see text), indexing of the crystalline phases are given in the table 9. The prominent diffuse amorphous peak at 2θ ~ 14° can be identified.

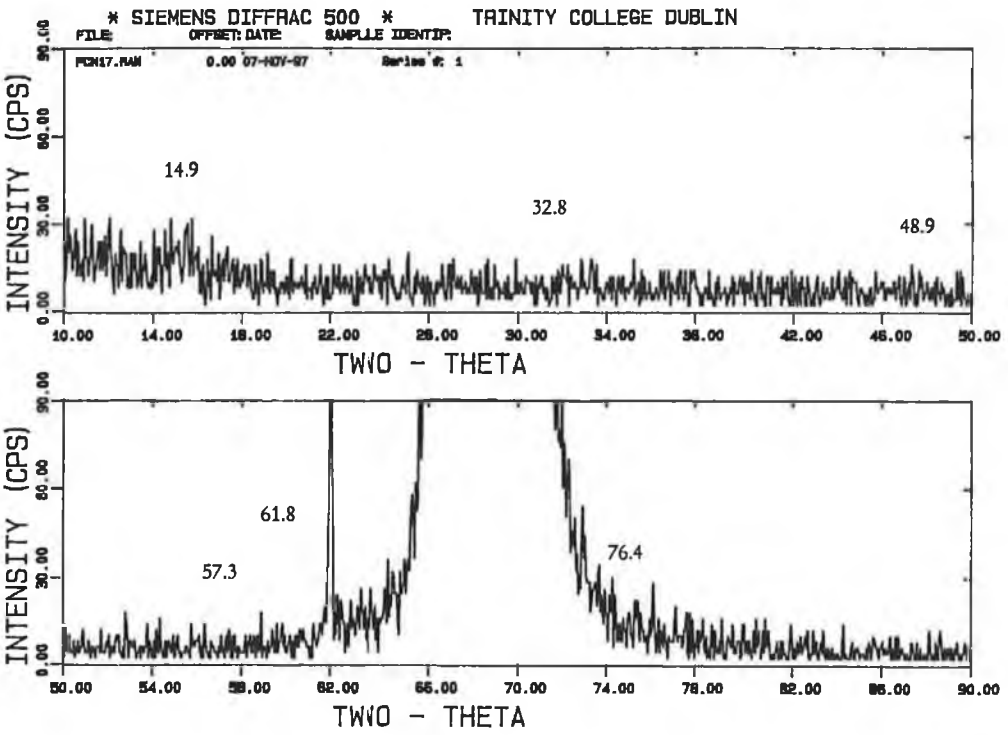

Figure 23: X-ray diffraction pattern of the crystalline β-C_3N_4 phases deposited on the n type Si (100) substrate (sample PCN17). Although relative intensity of the peaks are low (see text), indexing of the crystalline phases are given in the table 10. The prominent diffuse amorphous peak at 2θ ~ 14° can be identified.

It was interesting to see that the some of the diffracted peaks from β-C_3N_4 of the film (33.2 at.% N) deposited by using 100% N_2 sputtering gas, were missing in the case of films deposited by 10% Ar/90% N_2 gas mixture even though a higher N content is found (43.3 at.% N). A possible explanation is that since the momentum of the Ar^+ ions is higher than that of either N_2^+ or N^+ ions then the increased momentum transfer into the growing film causes disruption of the β-C_3N_4 crystals producing amorphous material. This question may be clarified by deposition studies using He as sputtering gas. From these weak peak intensities due to the lower atomic scattering factor, it is not possible to conclude the effect of Ar gas in the sputtering during the film growth. However, a detailed study using different sputtering gas is required for the clarification of this point.

Table 8: XRD data of crystalline phase of carbon nitride film (PCN19) on Si(100) with the calculated β-C_3N_4 powder-diffraction pattern. S, m, w, vw represent strong, medium, weak and very weak diffraction intensities. The unit of inter-planer spacing "d" is in Å.

PCN19

Observed from X-ray diffraction				Calculated values		
2 Theta	d		Intensity	Calc. d	(hkl)	Intensity
14.9	5.95	(+/-0.01)	s			
				5.54	100	m
27.8	3.21	(+/-0.01)	m	3.2	110	m
32.8	2.73	(+/-0.03)	m	2.77	200	s
				2.24	101	s
				2.095	210	m
46.5	1.95	(+/-0.01)	m	1.945	111	m
48.9	1.86	(+/-0.01)	m	1.85	300	m
57.3	1.6	(+/-0.01)	m	1.59	211	w
61.8	1.51	(+/-0.04)	m	1.54	310	w
62.5	1.48	(+/-0.01)	m	1.48	301	w
70.8	1.33	(+/-0.02)	w	1.35	221	w
76.4	1.25	(+/-0.03)	m	1.28	320	w
				1.23	2	m
				1.13	321	w
				1.125	202	w

Table 9: XRD data of crystalline phase of carbon nitride film (PCN26) on Si(100) with the calculated β-C_3N_4 powder-diffraction pattern. S, m, w, vw represent strong, medium, weak and very weak diffraction intensities. The unit of inter-planer spacing "d" is in Å.

PCN26

Observed from X-ray diffraction				Calculated values		
2 theta	d		Intensity	Calc. d	(hkl)	Intensity
14.9	5.95	(+/-0.01)	s			
				5.54	100	m
27.8	3.21	(+/-0.01)	m	3.2	110	m
32.8	2.73	(+/-0.03)	m	2.77	200	s
				2.24	101	s
				2.095	210	m
				1.945	111	m
48.9	1.86	(+/-0.01)	m	1.85	300	m
57.3	1.6	(+/-0.01)	m	1.59	211	w
61.8	1.51	(+/-0.04)	m	1.54	310	w
62.5	1.48	(+/-0.01)	m	1.48	301	w
70.8	1.33	(+/-0.02)	w	1.35	221	w
76.4	1.25	(+/-0.03)	m	1.28	320	w
				1.23	2	m
				1.13	321	w
				1.125	202	w

Table 10: XRD data of crystalline phase of carbon nitride film (PCN17) on Si(100) with the calculated β-C_3N_4 powder-diffraction pattern. S, m, w, vw represent strong, medium, weak and very weak diffraction intensities. The unit of inter-planer spacing "d" is in Å.

PCN17

Observed from X-ray diffraction				Calculated values		
2 theta	d		Intensity	Calc. d	(hkl)	Intensity
14.9	5.95	(+/-0.01)	s			
				5.54	100	m
				3.2	110	m
32.8	2.73	(+/-0.03)	m	2.77	200	s
				2.24	101	s
				2.095	210	m
				1.945	111	m
48.9	1.86	(+/-0.01)	m	1.85	300	m
57.3	1.6	(+/-0.01)	m	1.59	211	w
61.8	1.51	(+/-0.04)	w	1.54	310	w
62.5	1.48	(+/-0.01)	w	1.48	301	w
70.8	1.33	(+/-0.02)	w	1.35	221	w
76.4	1.25	(+/-0.03)	m	1.28	320	w
				1.23	2	m
				1.13	321	w
				1.125	202	w

6.2.2 TEM analysis of Carbon Nitride Solid

A Carbon Nitride thin film sample was prepared for TEM analysis using 100% N_2 as the sputtering gas. The film was deposited for this purpose for 5 minutes which gave the desired thickness (0.3μm) for plan view TEM analysis. The temperature varied from 120°C after sputter cleaning to 270°C after deposition. A detail description of deposition is given in chapter 4.

Bright field images and associated diffraction patterns from the carbon nitride films are shown in Figure 24. It can be seen that variations in structure across the film occur. Figure 24a shows an area that is largely amorphous. This is confirmed by characteristic diffuse diffraction shown in Figure 24b. Figure 24(c).I and 24(c).II show bright field image from a strongly crystalline region of the film. Electron diffraction patterns from this area (Figure 24d) show only the sharp rings associated with diffraction from a crystalline medium. The spatial transition from amorphous to crystalline is observed (figure 24e) to be relatively continuous with a mixed transition region several microns in width.

Table 11 shows the calculated interplanar spacings obtained from electron diffraction patterns taken from the nanocrystalline regions of the carbon nitride films. Diffraction measurements were calibrated to the silicon substrate <100> zone axis diffraction pattern. Table 11 also shows the theoretical interplanar spacing values for β-C_3N_4 [39]. It can be seen that there is reasonably close correspondence between the measured and theoretical values. Measured values are systematically lower than those theoretically predicted, however this observation is consistent with previous research [39,43,44]. Further, Table 11 shows that the ratios of the interplanar spacings agree well between observation and theory. There are several reflections predicted by theory that are not observed in the measured diffraction patterns. Such absences are not unusual in thin film analysis and may be attributed to a degree of preferential orientation.

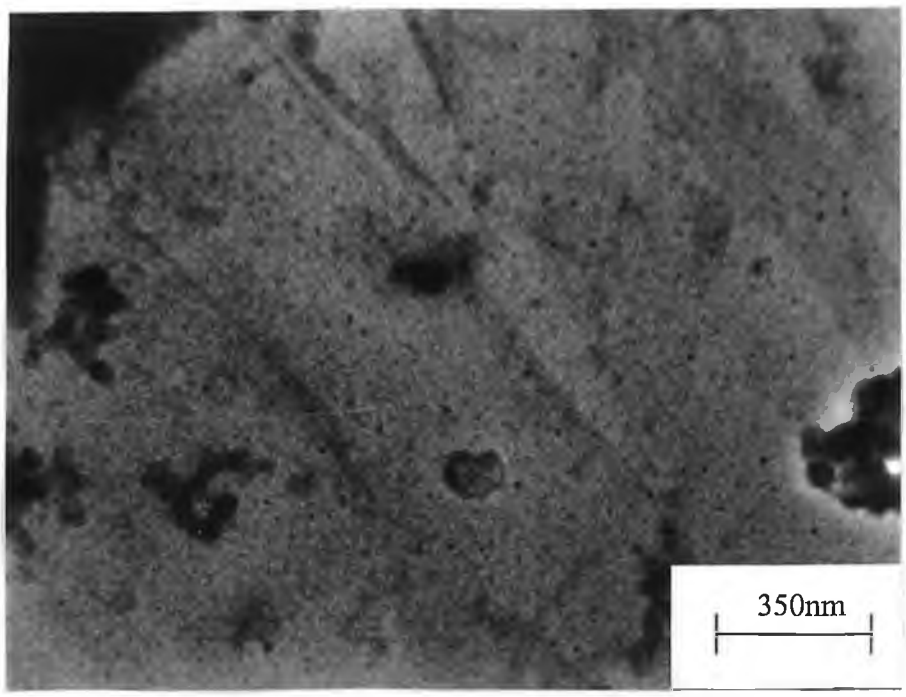

Figure 24: (a) Bright field TEM image of an amorphous region of the carbon nitride film

Figure 24: (b) Selected area diffracted from the amorphous region

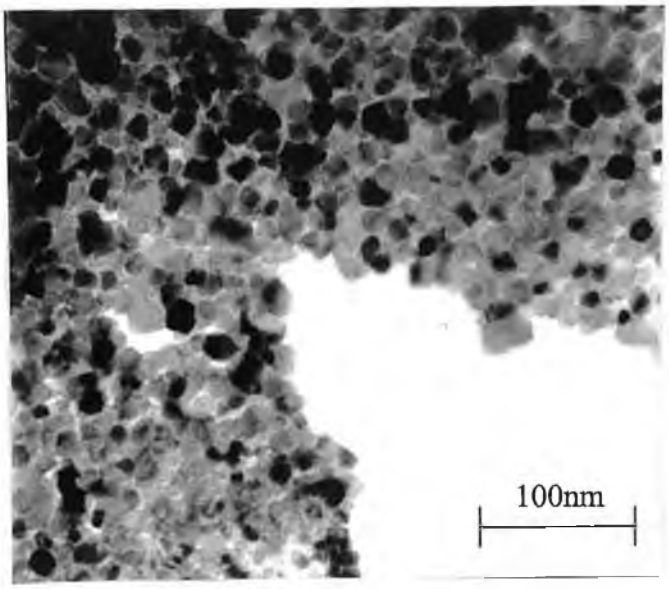

Figure 24: (c) I. Bright Field TEM image of a crystalline region of the film.

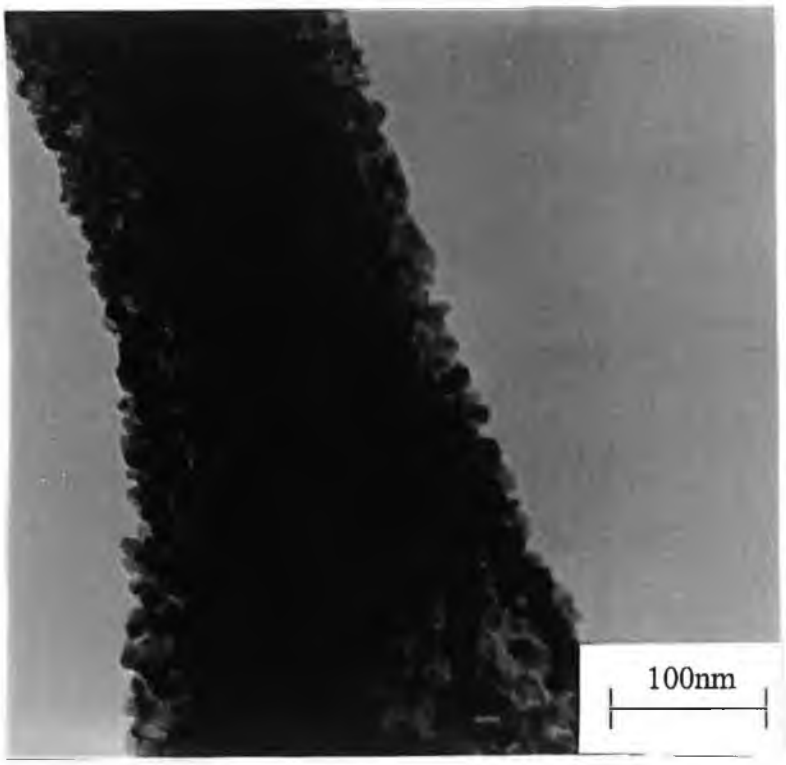

Figure 24: (c) II. Bright field TEM image of a crystalline region of the film.

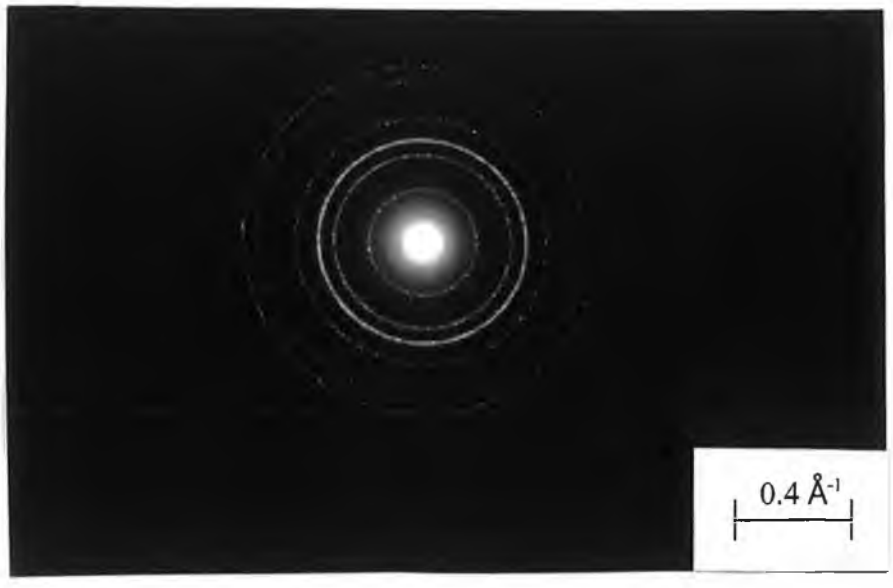

Figure 24: (d) Selected area diffraction from a crystalline region. These sharp rings index well to β-C_3N_4.

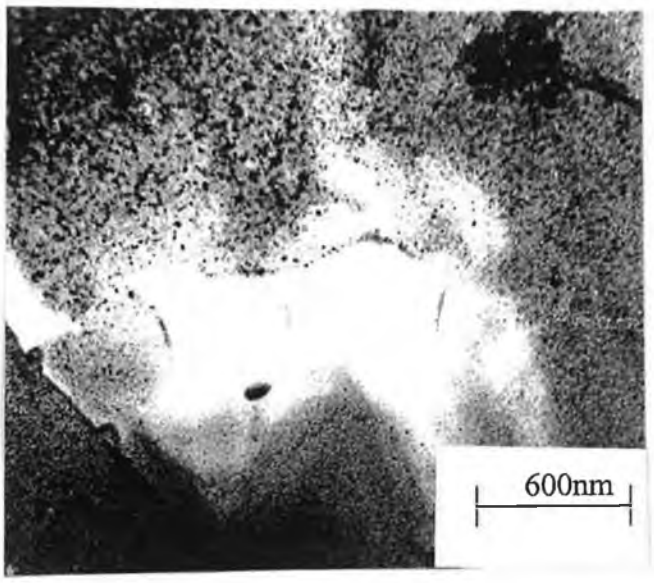

Figure 24: (e) Bright field TEM image of the spatial transition from amorphous to crystalline phases in carbon nitride films.

However, it is important to note that every observed reflection can be successfully attributed to one expected from theory. There are therefore no observed diffraction periodicities that are inconsistent with the β-C_3N_4 structure. If such reflections were present they would require explanations in terms of impurity phases. There is no evidence for impurity phases here.

It therefore seems likely that the crystalline regions produced in these carbon nitride films are indeed β-C_3N_4. However, for greater certainty Table 12 explores how the experimentally observed diffraction information compares with the diffraction expected from all the other likely phases mentioned in previous work [39,44]. Powder Diffraction File (PDF) numbers are quoted and interplanar spacings have been calculated from the values of 2θ given on these file cards.

As can be seen, the diamond structure gives an extremely poor fit with the observed data. Chaoite, on the other hand, can account for many of the experimental diffraction maxima, however observed d_{hkl}'s of 5.2 Å and 1.7 Å cannot be attributed to this crystal form. Also if the observed material were chaoite there would be an uncomfortable number of diffraction absences in the experimental data.

Lonsdaleite gives a poor fit with the observed data, and for the graphite structures periodicities of 5.2 Å and 2.6 Å cannot be accounted for. Graphitic structures also have problems accounting for all of the observed reflections in the 1.2-1.4 Å range.

α-C_3N_4 can account for all of the observed reflections. However, the differences between observed data and that predicted from theory is greater than for β-C_3N_4, and there would be 11 reflections absent due to orientation rather than 2. This seems somewhat unlikely.

The above discussion therefore shows that the crystallography of the observed regions is not only consistent with β-C_3N_4, but is also inconsistent with other likely crystal phases. Over the measured sample, the relative amount of crystalline to amorphous material in the films observed so far is estimated to be $>20\%$. Moreover

within the crystalline regions, the films are totally crystalline and no amorphous material can be observed. Such large proportions indicate that the deposition technique used may offer the best possibility to date of obtaining 100% β-C_3N_4 thin films.

The characteristics of the deposition system which give rise to the formation of crystalline films must be considered. Two important parameters are:

(i) the ion flux/neutral flux ratio (mainly N_2^+/N_2) and

(ii) the carbon atom flux/ion flux ratio (mainly C/N_2^+).

In chapter 4 it has been shown from the Langmuir probe measurements that the ion flux /neutral flux ratio is ~ 0.15, where the neutral flux is calculated from the impingement flux of neutral gas molecules at the deposition pressure. The carbon atom flux is calculated from the rate at which the carbon atoms are incorporated into the β-C_3N_4 structure in order to give the measured deposition rate, assuming a sticking coefficient of 1. The carbon atom flux /ion flux ratio is ~ 0.02. The large overabundance of ionised nitrogen compared with carbon may be significant in the formation of the crystalline material. It is also found that the degree of ionisation in the inter-target region is $>4\%$ giving a very high concentration of excited and reactive species.

Tables 11: Comparison between the interplanar spacing information obtained experimentally and that obtained by calculation from β-C_3N_4.

Chapter Two Observed from TEM Diffraction			Calculated for β-C_3N_4			
d(Å)	Intensity	Ratio d/d_{max}	d(Å)	(hkl)	Intensity	Ratio d/d_{max}
5.2± 0.15	*m*	1.0	5.54	100	*m*	1.0
3.1± 0.15	*m*	0.60	3.20	110	*m*	0.58
2.6± 0.15	*s*	0.50	2.77	200	*s*	0.50
2.2± 0.1	*m*	0.42	2.24	101	*s*	0.40
			2.095	210	*m*	0.38
1.8± 0.1	*vw*	0.34	1.945	111	*m*	0.35
1.7± 0.1	*w*	0.32	1.85	300	*m*	0.33
1.5± 0.1	*m*	0.29	1.59	211	*w*	0.29
			1.54	310	*w*	0.28
1.4± 0.1	*vw*	0.27	1.48	301	*w*	0.27
1.3± 0.05	*w*	0.25	1.35	221	*w*	0.24
1.25± 0.05	*vw*	0.24	1.28	320	*w*	0.23
1.21± 0.05	*vw*	0.23	1.23	002	*m*	0.22
1.15± 0.05	*vw*	0.22	1.13	321	*w*	0.20
1.12± 0.05	*w*	0.22	1.125	202	*w*	0.20

Table 12: Comparison between the interplanar spacings found experimentally and those expected from a variety of possible C-N phases.

Observed d_{hkl}	Diamond PDF ref [9] 6-675		Chaoite PDF ref [9] 22-1069		Lonsdaleite PDF ref [9] 19-268		Graphite PDF 26-1079		Graphite PDF 25-284		Graphite PDF ref [9] 23-64		α-C_3N_4 ref [2] calculated		β-C_3N_4 ref [2] calculated	
	d	(hkl)	*d*	(hkl)	*d*	(hkl)	*d*	(hkl)	*d*	(hkl)	*d*	(hkl)	*d*	(hkl)	*d*	(hkl)
5.2 ± 0.15													5.66	100	5.54	100
			4.47	110												
			4.26	111												
			4.12													
			3.71	201									3.64	101		
3.1 ± 0.15			3.22	104			3.35	003	3.35	002	3.36	002	3.27	110	3.20	110
			3.03	203												
			2.94	210									2.83	200	2.77	200
2.6 ± 0.15			2.55	301												
			2.46	213									2.43	201		
													2.37	002		
			2.28	205												
2.2 ± 0.1			2.24	220	2.19	100							2.19	102	2.24	101
	2.06	111	2.10	304	2.06	002	2.08	101	2.13	100	2.13	100	2.14	210	2.10	210
			1.98				1.96	012	2.03	101	2.03	101	1.95	211	1.95	111
			1.91	305	1.92	101							1.92	112		
													1.89	300	1.85	300
1.8 ± 0.1									1.80	102	1.80	102	1.75	301		
1.7 ± 0.1							1.68	006	1.68	004	1.68	004				
							1.62	104					1.59	212	1.59	211
													1.57	310		
1.5 ± 0.1			1.50	227	1.50	102	1.46	015	1.54	103	1.55	103	1.52	103	1.54	310
													1.49	311	1.48	301
1.4 ± 0.1			1.37	416									1.35	222	1.35	221
1.3 ± 0.05			1.29	600					1.32	104			1.31	312		
1.25 ± 0.05	1.26	220	1.26	336	1.26	110	1.23	110	1.23	110	1.23	110	1.27	213	1.28	320
													1.25	321	1.23	002
1.21 ± 0.05													1.21	303		
			1.20	516			1.19	107					1.20	411		
1.15 ± 0.05			1.18	427	1.17		1.15	113	1.15	112	1.16	112	1.18	004		
1.12 ± 0.05							1.12	009	1.13	105	1.14	105	1.14	322	1.13	321
									1.12	006	1.12	006			1.12	202
	1.07	311	1.08	339	1.08	112	1.08	018	1.05	201	1.05	201				

Summary

In summary it can be seen that large areas of continuous nanocrystalline carbon nitride film can be produced at low temperature by DC reactive magnetron sputtering. Crystallographic analysis shows lattice spacings characteristic of β-C_3N_4 with some degree of preferential orientation. No spurious periodicities that cannot be assigned to β-C_3N_4 are observed. It is hoped that the volume fraction of the crystalline regions can be increased by depositing on a substrate that has a better lattice match with β-C_3N_4 than {100} Si. The exact roles of other deposition parameters such as temperature, pressure etc. are still to be determined.

Part III

6.3 Effect of Process Parameters

The previous parts of this chapter discussed the bonding structure of the carbon nitride solid. It is of interest to see the effect of process parameters, e.g. nitrogen pressure, substrate bias, etc. on bonding structure. A clear understanding of the process parameters are required to have control on deposition of carbon nitride thin film. It is of interest to find a way to increase the sp^3 bonding in the film and thus make the film more crystalline. The part discusses the effect of process parameters on the film characteristics: (1) the growth rate; (2) nitrogen incorporation; (3) the sp^3/sp^2 ratio since it is of interest to increase the ratio as far as possible. The part also discusses Robertson's model [45] to increase sp^3 bonded structure from sp^2 phases and its implementation in case of carbon nitride thin film.

6.3.1 Effect of experimental parameters on Carbon Nitride thin film

During growth of carbon nitride thin films the total amount of N incorporated in the films depends on the effective N-sticking coefficient on the growth surface which in turn depends on parameters such as the N_2 dissociation rates and the desorption rates of volatile N_2 and CN molecules. Although the effect of temperature on these above mentioned processes is not known in the present case, W. Zheng et al. [46] described the physical dependence of these processes on temperature. Usually plasma assisted growth processes are not straight forward due its complex nature of processes occurring on the growth surface, thus a detail analysis behind N incorporation and structure formation is required.

During these days much attention was given on the process parameters, i.e., nitrogen partial pressure, bias voltage and temperature on carbon nitride growth. Here the effect

of these process parameters in case of present deposition condition will bediscussed, although the physical reasons of growth process by sputtering technique should be more or less similar.

An experiment was carried out to see the effect of substrate negative bias on nitrogen incorporation in the film. Table 13 shows the elemental analysis by RBS of three samples deposited in three different conditions.

Table 13: Elemental analysis of the samples deposited by the Penning type magnetron sputtering system. 100% N_2 gas was used in all depositions.

Sample no.	Working pressure (mbar)	Substrate bias	C at.%	N at.%	O at.%	Fe at.%
PCN2	$1x10^{-3}$	0	68	26	0.4	1.7
PCN3	$1.5x10^{-4}$	-50	57	39	0	3.7
PCN5	$1x10^{-3}$	-50	58	38	0	3.9

It can be observed from the table 13 that nitrogen incorporation in the film does not vary much with increasing total working pressure, but a strong variation can be observed when substrate negative bias was increased. An increase in nitrogen incorporation in the film is seen with increase in substrate negative bias. This is due to the fact that with increase in substrate negative bias nitrogen ions become more energetic and can penetrate the subsurface layer resulting more nitrogen content in the bulk.

Zheng et al. [46] found that as nitrogen partial pressure increases, the growth rate increases, while nitrogen incorporation in the film remains almost constant. Based on an increased gas scattering growth rate would, however, be expected to decrease as nitrogen partial pressure increases. At lower pressure about 80% of the sputtered C atoms will not collide before they reach the substrate, while at higher pressure more than 80%

experience collisions with the N_2 molecules before reaching the substrate. Thus, at high pressure the C atoms will have lower energy and the flux will be more diffuse. It should be pointed out that the experimentally observed increase in growth rate with nitrogen partial pressure is in sharp contrast to the behaviour during reactive sputtering of transition metal nitrides. For example, during growth of TiN by reactive sputtering the target nitride formation results in a decrease (by a factor of $3 \sim 4$) in growth rate as nitrogen partial pressure increased. This decrease is due to the lower physical sputtering yield of TiN compared to that of pure Ti [46].

They also mentioned that the experimental observed increase in growth rate with nitrogen partial pressure probably be due (1) to an increased sputtering rate of C species from the target as the steady state N concentration increases on the target surface, or (2) to a decreased film density owing to the lower energy of the C and N species impinging on the growing film surface. An increased sputtering rate of C containing species from the target surface is reasonable and can be explained by an increased ion induced desorption rate of C-N species (chemical sputtering) as the steady N-concentration on the target surface increases with nitrogen partial pressure. A pronounced ion induced desorption rate during carbon nitride film growth has also been demonstrated by Sjotrom et al [47] and Todorov et al [48]. Zheng et al [46] mentioned that if nitrogen incorporation in the film remains constant with increase in nitrogen partial pressure, then situation (2) is more likely as an explanation. They observed experimentally that nitrogen concentration remains almost constant at a value of 30% over the investigated pressure range. The fact that nitrogen incorporation remains constant supports the interpretation that the observed increase in growth rate is not caused by an increase N sticking at the growth surface but rather by an increased impingement rate of both N and C containing precursors.

Although Zheng et al [46] mentioned about the relationship between nitrogen partial pressure and deposition rate and also nitrogen incorporation in the film, it would be quite interesting to see the effect of Ar/N_2 gas mixture on deposition rate and nitrogen

incorporation in the film at a constant pressure. Figure 25 shows the relationship between the deposition rate and nitrogen gas (%).

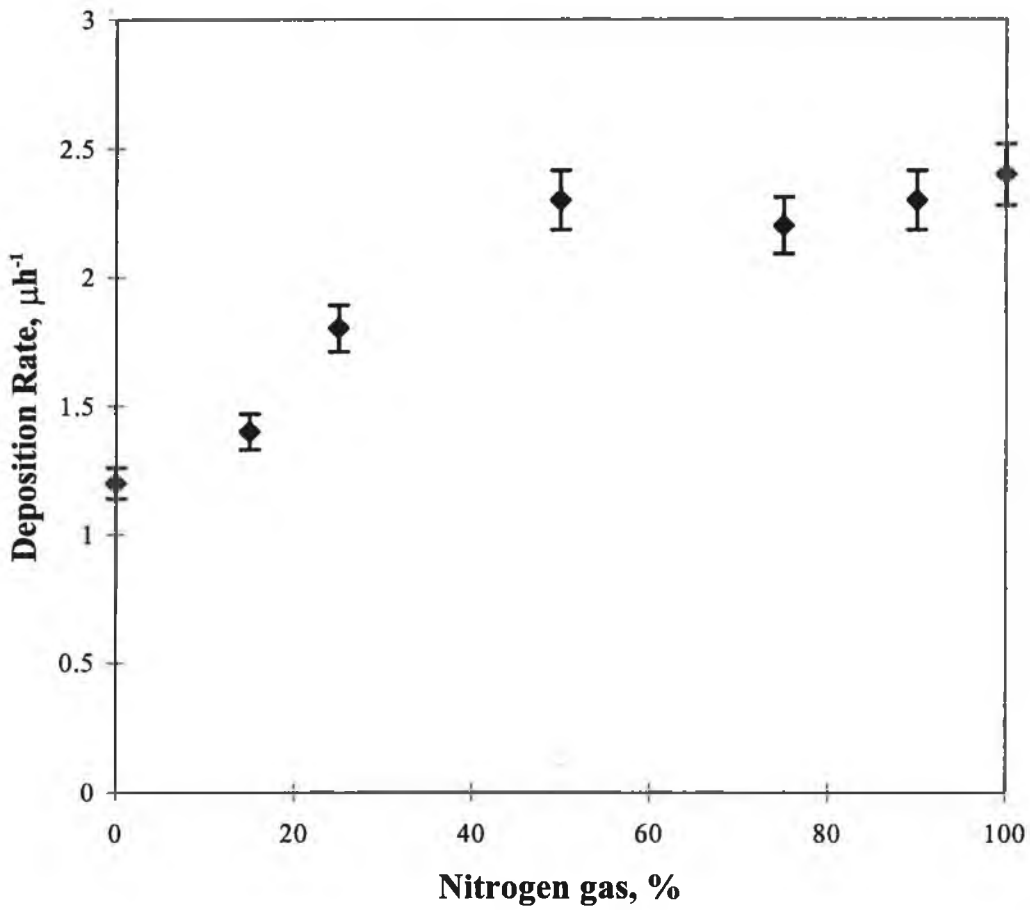

Figure 25: Deposition rate as a function of Nitrogen gas (%), keeping substrate negative bias constant at 50 V. The gas mixture was Ar/N_2 and the working pressure was maintained at $1x10^{-3}$ mbar in all cases.

Addition of argon in the sputtering gas mixture should enhance the sputtering rate of graphite from the target, as the sputtering yield of graphite by Ar gas is expected to be higher due to higher mass. In this case, it is expected that the deposition rate would decrease with increase in nitrogen gas in the Ar/N_2 gas mixture. It can be seen (figure 25) that deposition rate monotonically increases with increase in nitrogen gas (%). This is probably due to substrate effect rather than sputtering effect at the target by Ar. Both

energetic and neutral Ar species probably enhance the mobility of nitrogen species to the growing surface of the film. If the Ar percentage increases in the mixture, there will not be enough nitrogen species available at the growth surface and deposition rate falls. The feature is also related to nitrogen incorporation in the film.

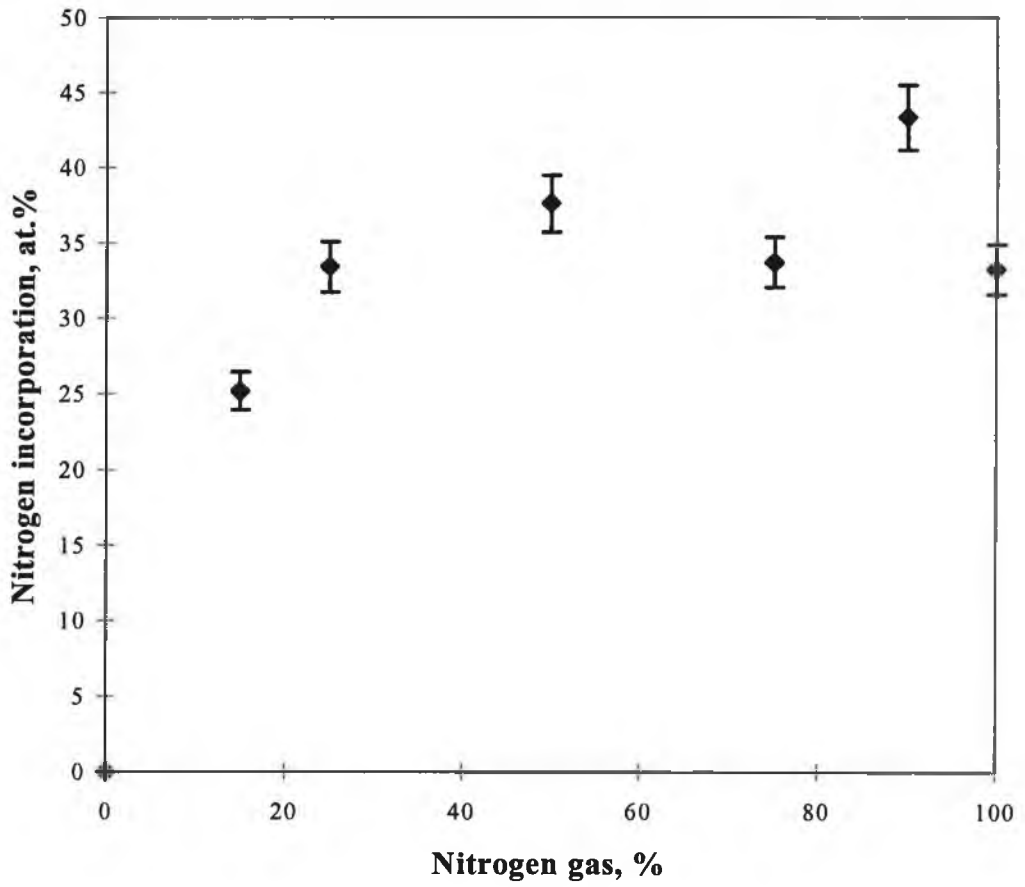

Figure 26: Nitrogen incorporation (at.%) as a function of nitrogen gas (%), keeping substrate negative bias constant at 50 V. The gas mixture was Ar/N_2 and the working pressure was maintained at $1x10^{-3}$ mbar in all cases.

It can be seen from figure 26 that increase in nitrogen gas increases the nitrogen incorporation in the film. This is probably due to increased sputtering rate of C species from the target as the steady state N concentration increases on the target surface.

Energetic or neutral Ar species probably enhance the nitrogen species' mobility and increase N sticking at the growth surface. This also supports the previous explanation that Ar acts as nitrogen carrier which in turn enhances the deposition rate. It can be noted from the figure 26 that maximum amount of nitrogen incorporation (~43 at.%) in the film, can be observed as measured by RBS at 10% Ar gas mixture. There is indeed an effect of Ar mixture on the nitrogen incorporation in the film. The fact that with ≤10% Ar, sputtering rate of carbon and N sticking effect at the growth surface is maximum. If Ar increases further in the sputtering gas mixture, two things can happen, (1) the sputtering rate of carbon increases with respect to ionised nitrogen species, thus the film contains less nitrogen; (2) chemically enhanced preferential sputtering of nitrogen from the film surface can occur by the energetic Ar species. Increase in Ar gas in the sputter gas mixture may also disrupt the film structure, as discussed before. The fact that the momentum of the Ar^+ ions is higher than that of either N_2^+ or N^+ ions then the increased momentum transfer into the growing film causes disruption of the bonding structure of the film producing amorphous material. This question may be clarified by deposition studies using different sputtering gas mixtures e.g. He/N_2. It can be seen that with 100% N_2 sputtered film, nitrogen incorporation is lower than the 10% Ar/90%N_2 gas sputtered film. Thus a few percentage (≤ 10 %) of Ar can increase the nitrogen incorporation in the film.

Zheng et al. [46] observed that deposition rate of carbon nitride thin film increases with substrate RF negative bias from 0 to 50 V, and decreases with the negative bias from 60 to 100 V. They explained the phenomena that at lower value of negative bias the nitrogen ions with lower kinetic energies can increase atomic mobility and chemical reactivity. While at high value of negative bias, chemically enhanced preferencial sputtering and backscattering by nitrogen start to become significant [49].

The effect of negative RF substrate bias shows rather a different situation in case of deposition by a Penning source. Figure 27 shows the relationship of substrate RF negative bias with deposition rate.

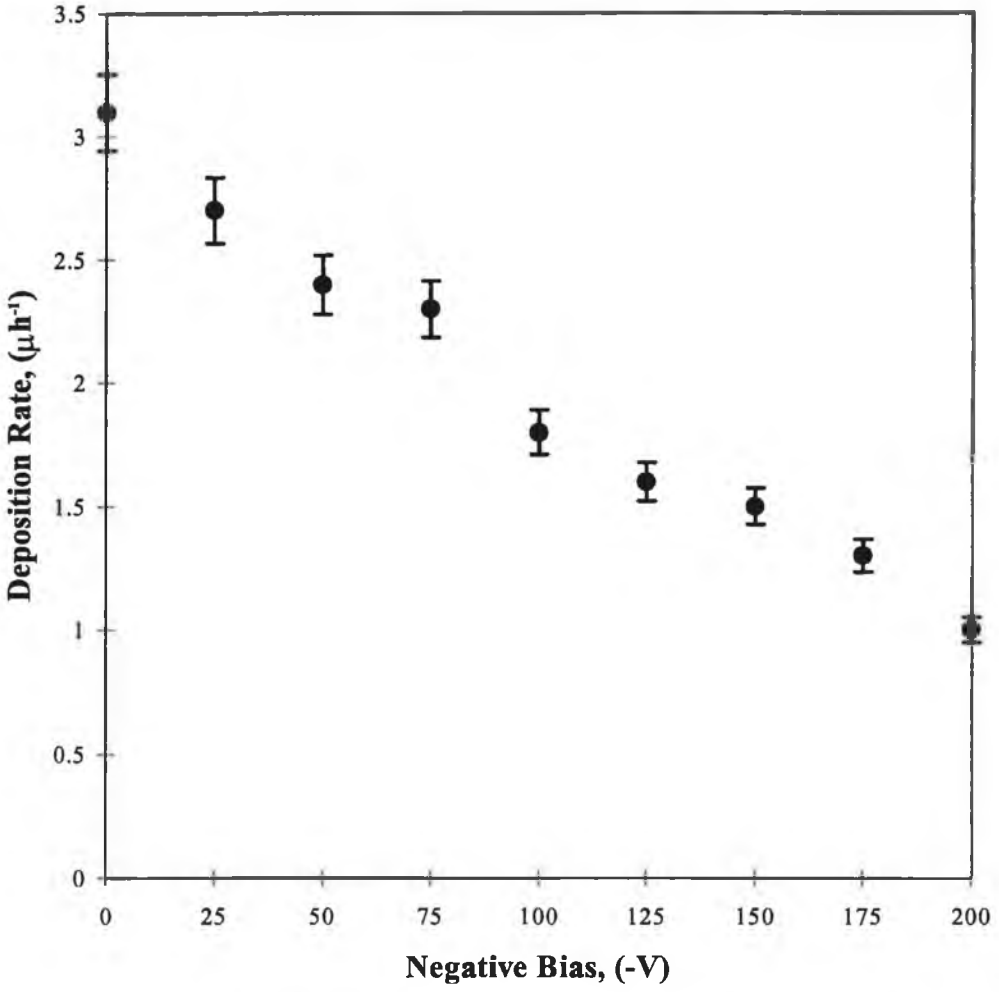

Figure 27: Deposition rate as a function of substrate negative bias, using 100% N_2 as sputtering gas in all cases. The working pressure was maintained at $1x10^{-3}$ mbar in all cases.

It can be seen that with negative RF substrate bias the deposition rate decreases. No intentional substrate heating was applied, although substrates were experiencing ~325°C from the plasma. In all cases, 100% pure nitrogen gas was used as the sputtering media. In Penning type sputtered deposition there was not any evidence of a threshold

where the deposition rate increases and then decreases which was observed by Zheng et al. [46]. The decrease in deposition rate can be explained in a different way, although chemically enhanced preferential sputtering can not be ruled out for the lower deposition rate. This point can be clarified if the nitrogen incorporation in the film decreases with increase in substrate negative bias. (The elemental analyses of the films, deposited using different substrate negative bias, can be done by RBS which is currently not available).

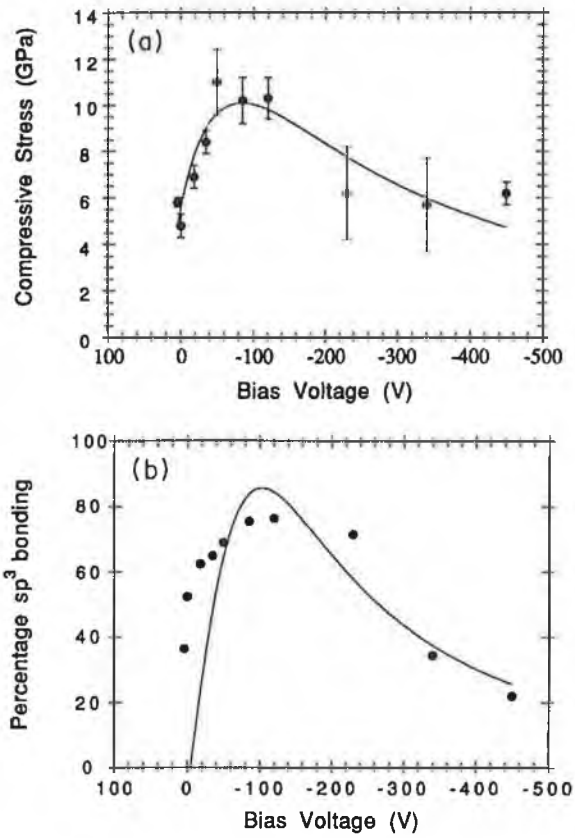

Figure 28: (a) Theoretical description (solid line) for the (a) compressive stress, described by Davis [60]; (b) sp^3 fraction, described by Robertson [45]; fitted to the experimental data [61].

Once the energetic species penetrate the subsurface layer, it is more likely for the ion to accommodate at some suitable bonding configuration resulting in metastable phase,

transformation of the existing phase, or to become a trapped atom dissipating its excess energy as thermal spikes as mentioned by Robertson [45]. The decrease in deposition rate with increase in negative bias can be explained by the structural modification of carbon nitride thin film. It was discussed in the previous Parts of this chapter that carbon atoms bond with nitrogen and form sp, sp^2 and even sp^3 bonded structure. These structures are different in atomic arrangements giving tight bonding system and result in different density, although all of these structures are carbon nitride compound. Spencer et al [50] proposed that sp^3 sites arise from the preferential sputtering of sp^2 sites, but this is unlikely due to the low sputtering yield of carbon [51]. Weissmantel [52] suggested that sp^3 bonding arose from the thermal spike shock-wave of the ion cascade. Lifshitz et al [51] proposed a subimplantation (low energy implantation) mechanism in which ions enter subsurface sites. They also proposed that a preferential displacement of sp^2 sites causes an accumulation of sp^3 sites. The idea of preferential displacement arose from early estimates of different displacement thresholds of graphite and diamond, 25 eV and 80 eV respectively [52,53]. However, recent direct measurements of the threshold find similar values for graphite (35 eV) and diamond (37-47 eV), as measured by Steffen et al. [54] and Koike et al. [55] and thus invalidate this mechanism. McKenzie et al [56] proposed that sp^3 bonding was stabilised by compressive stress which moves a-C into the stability domain of diamond. The compressive stress arises from ion bombardment, following the ion-peening ideas of Windischmann [57]. Molecular dynamics simulations of the deposition mechanism have generally supported a subplantation process in which ions enter subsurface sites [58,59]. The subplantation model was given a microscopic basis by Robertson [45] and Davis [60]. They proposed that the sp^3 bonding occurs by ion flux causing a metastable increase in density. In the highly energetic conditions of ion bombardment, atomic hybridizations are expected to adjust readily to the local density, becoming more sp^2 if the density is low and more sp^3 if the density is high. The density will increase if an incident ion penetrates the first atomic layer of the film and enters an interstitial, subsurface position, where it rebounds to its neighbours and acquires bulk bonding of the appropriate hybridization. Lower energy ions do not

penetrate but stick to the surface, forming sp^2 bonded a-C. Higher energy ions penetrate further and increase the density in deeper layers. However, the ion uses only part of its energy in penetrating the surface. The excess energy dissipates quite rapidly in about 10^{-12} s in a "thermal spike", during which the excess density can relax. Hence, a maximum density occurs at an optimum ion energy which maximizes the penetrative yield but minimizes the relaxation of the density increment. This is the basis of Robertson's model [45].

Fallon et al [61] first showed experimentally the effect of negative bias to produce higher energetic ion. Figure 28 shows the calculated sp^3 fraction with the values measured by Fallon et al.. The proportionality between density and sp^3 fraction has been confirmed experimentally for sputtered a-C [60,61]. Davis [62] showed the relation of sp^3 fraction with compressive stress generation (figure 29).

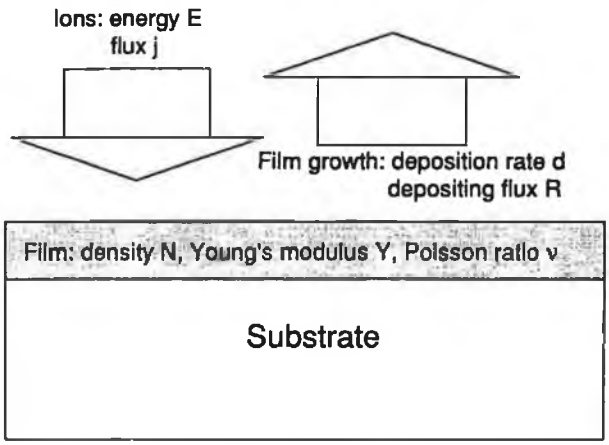

Figure 29: Schematic diagram of a film growing at a rate d, with simultaneous bombardment by a flux j of ions with energy E [62].

He mentioned that compressive stress arises when a growing film is bombarded by atoms or ions with energies of tens or hundreds of electron volts by a process of "atomic

peening". The energetic ions cause atoms to be incorporated into spaces in the growing film which are smaller than the usual atomic volume and this leads to an expansion of the film outwards from the substrate. In the plane of the film, however, the film is not free to expand and the entrapped atoms cause macroscopic compressive stress. The conditions of energetic bombardment which lead to the production of compressive stress also favour the formation of dense thin films with properties approaching those of the bulk material. Fallon et al [61] theoritically and experimentally showed the relationship of compressive stress and sp^3 fraction. They showed that film density and compressive stress increase with increase in sp^3 fraction.

Based on Fallon et al's findings and Robertson's model effect of substrate negative bias is examined in case of carbon nitride thin film deposited by Penning type DC sputtering. Decrease in deposition rate with increase in negative bias (figure 27) is in good agreement with Robertson's model. It is an interest to see the effect of structural changes on the deposition rate with increase in negative substrate bias. Valence band XPS spectra fingerprint the structural changes as discussed in Part I of this chapter. The valence band electrons are responsible for bonding and thus a significant change in the density of states (DOS) occurs during structural modification. Although analysis of core level spectra can give detail bonding configuration, valence band spectra gives an overall structural nature of the solid. In bond formation core level electrons are not affected that much as valence band electrons are. Figure 30 shows the valence band XPS spectra of carbon nitride thin film deposited with different negative bias. It can be seen that sp hybridised peak ($\sim$19 eV) becomes sharper with increase in bias voltage (0 to -50 V). This is due to the fact that nitrogen incorporation in the film increases with increase in negative bias voltage (0 to 50V) as can be seen from table 13. After that the peak at $\sim$19 eV becomes weak due to structural modification. When the film is deposited with higher negative bias (>-50V) a denser, structurally different film is obtained as discussed by Fallon et al. [61]. At this substrate bias atomic rearrangement occurs at the very subsurface region due to higher energetic ion subplantation mechanism as proposed by Robertson [45]. The film becomes more diamond like, i.e., sp^3 fraction increases, above

-75V substrate bias. A dramatic change in peak shape at ~24 eV and ~19 eV is observed for -100 to -150 V bias. After that the peak at ~19 eV becomes sharper again. The peak shape at ~24 eV (s region) and 19 eV (sp region) become more distinct at these negative bias regions and finally become diamondlike. A comparison of valence band XPS spectra of diamond, graphite, a-C and polymers are given in part I of this chapter. Thus a threshold negative bias voltage of -100 V can be observed for sp^2 to sp^3 transformation. The fact that the sp^3 fraction in the film increases with increase in bias voltage (-100 to -150). At about -175 bias voltage the excessive energy dissipates as thermal spike which is reasonably enough to break the sp^3 fraction to sp^2. Thus the mechanism of sp^2 to sp^3 transformation of carbon nitride solid is similar to that are observed in DLC film, deposited by sputtering technique using negative bias substrate bias [61]. This strong experimental evidence is in good agreement with Robertson's model and can be a good indication to increase the amount of crystalline β-C_3N_4 structure in the film which is theoretically predicted as tetrahedrally bonded C-N structure. The quantitative measurements of sp^3/sp^2 ratios in these samples can be done by Electron Energy Loss Spectroscopy (EELS) which is not currently available. However, this could be a future study to see the increase in sp^3 fraction in carbon nitride solid with increase in substrate negative bias.

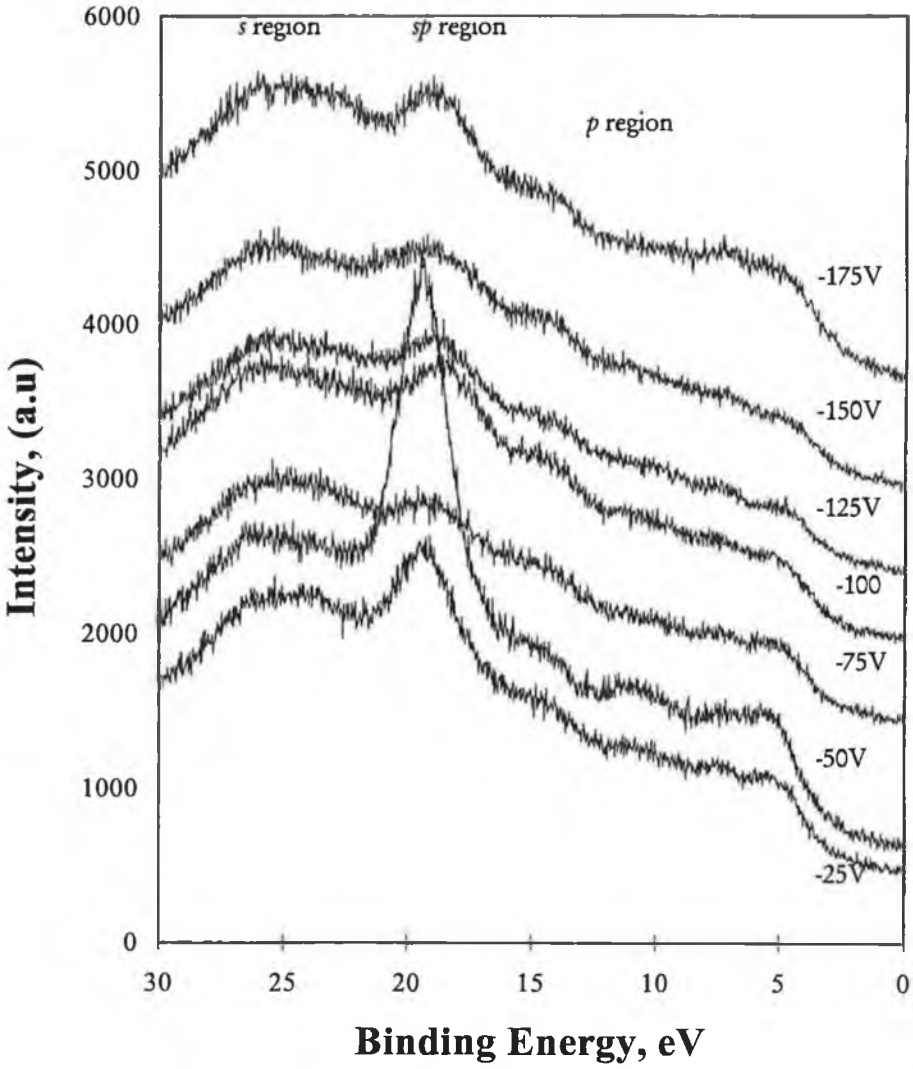

Figure 30: Valence band XPS spectra of carbon nitride films showing the structural changes with increase in substrate negative bias.

6.3.2 Effect of Hydrogen on CN film

It was interesting to see that when carbon nitride thin film deposited at high pressure ($1x10^{-2}$ mbar) does not stick to the substrate (Si). The film becomes disrupted with time.

Generation of intrinsic stresses in sputtered deposited films were discussed in chapter 3. A few points will be discussed further. In a general view, this kind of stress arises from the microstructure of the coating. If we do not go to the atomic state of stress generation, especially in the case of non metallic films, it looks as if the stresses are due to the energy and flux bombarding particles or atomic peening during the growth process, although this is obviously true for most of cases. This stress pattern can be tensile or compressive. The transition of tensile to compressive stress arises when the film density increases gradually. It is often greater than the yield strength of the coating. However, it may relax depending on the deposition temperature. Two cases are mostly seen: (1) the relaxation effect can be seen at low temperature (T/T_m in the range 0.1 to 0.3 where T_m is the melting point of the coating as discussed in the chapter 3) which is known as recovery, and (2) the relaxation of stresses occur due to recrystallisation of the strained grains into new strain free grains [63]. Microstructurally this explanation and stress evidence are well established for oxides and metallic films.

In case of amorphous hydrogenated carbon coating grown by PECVD in a methane plasma, typical sinusoidal stress patterns are seen. This type of stress pattern is defined as buckling failure due to compressive intrinsic stress. The buckles propagate in the directions normal to the sinusoidal paths thus forming a regular network. It is also seen that atmospheric humidity accelerates the effect.

A similar type of stress pattern was seen in carbon nitride thin film when deposited at high pressure (10^{-2} mbar). At this pressure the diffusion pump does not efficiently pump down the chamber. The residual moisture inside the chamber environment (although very small amount) takes part in the sputtering process. This is the only source of

Hydrogen contamination in the film. Holloway et al. [64] tried to see the effect of hydrogen in the growing carbon nitride film by using hydrogen gas intentionally. They mentioned that addition of as little as 1.5 at.% molecular hydrogen in the growth chamber caused a total disruption (poisoning) of film growth. In this section we will describe the role of hydrogen during carbon nitride film growth.

A film, grown at the pressure mentioned above, was analysed by RBS. The RBS spectrum of a film (PCN24) is shown in the figure 31. The elemental analysis is given in table 14. It is seen that sample PCN24 contains 3.6 at.% O, i.e, ≈7.2 at. % Hydrogen, assuming the atomic O is present as H_2O. The amount of hydrogen was high enough to cause disruption of the film in our case if compared with film deposited by Holloway et al. In fact, hydrogen causes excessive stress in the film that is high enough to break the adhesion between the substrate and the film. Figure 32(a) shows the initial state of disruption of the film due to excessive stress. As the film is not sticking with the substrate, it can not support its excessive stress thus resulting in buckling and it could not propagate in the directions normal to their sinusoidal paths thus forming a closed loop. After a few days the film was completely disrupted and the broken fragments are seen on the substrate. Figure 32(b) shows the final state of the film after 5 days of deposition.

Table 14: Elemental analysis of the samples deposited at different N_2 gas pressure.

Sample no.	N_2 gas (%)	Deposition pressure (mbar)	C at.%	N at.%	O at.%	Fe at.%
PCN19	100	$1x10^{-3}$	65.3	32.5	0	2.2
PCN24	100	$1x10^{-2}$	55.2	40.8	3.6	0.4

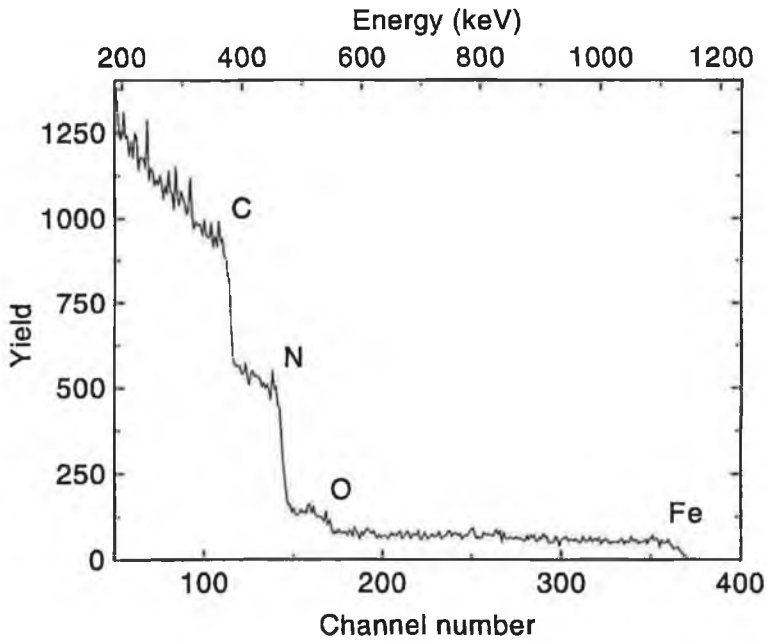

Figure 31: The RBS spectrum of 1.5 MeV He^+ ions incident on Carbon Nitride film containing 41 at.% N deposited on Si (100) wafer.

The intrinsic stress as seen in the figure 32(a) and (b) can be explained in terms of atomic level stress generation. Before going to this discussion, let us recall the vibrational properties of CN compound. Figure 33(b) shows the IR absorbance spectra of the sample discussed above. In usual condition (figure 33a) carbon nitride shows C–C (~700 cm^{-1}), a broad C=N (~1550 cm^{-1}), and C≡N ~2200 cm^{-1}) stretching vibrational modes in the infrared region. There are also three vibrational modes, i.e. G (usually 1588 cm^{-1}) D (usually 1360 cm^{-1}) and N=N bands observed by Raman spectroscopy. In the case of high pressure (10^{-2} mbar) deposition the intense C–H, N–H and O–H bands at ~2900, ~3300 and ~3500 cm^{-1} are also observed in the infra red region (fig. 33).

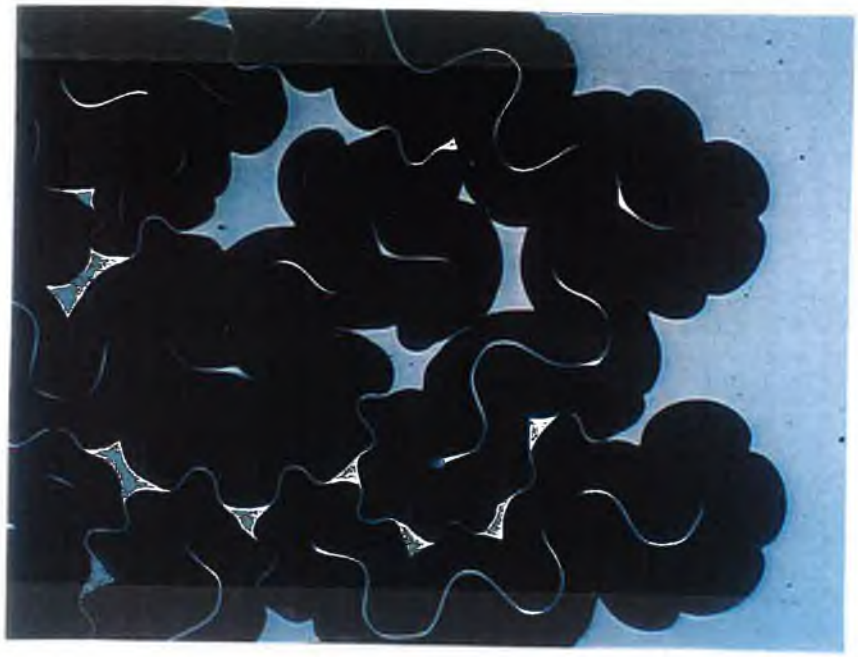

(a)

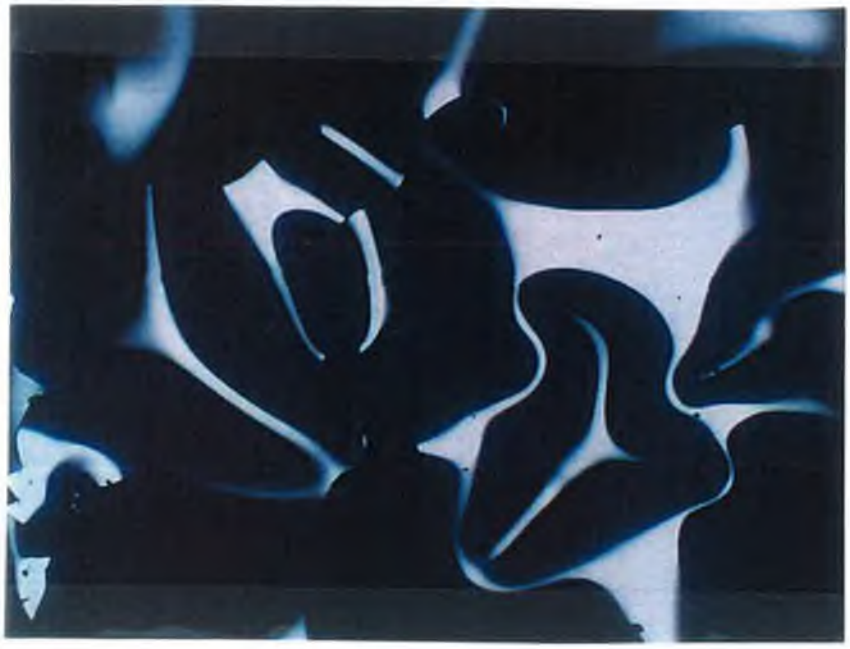

(b)

Figure 32: Hydrogen attack; (a) the initial state of disruption of the film containing hydrogen showing excessive stress. This condition is just after deposition when the film is taken out of the deposition chamber; (b) the final state of the stressed film showing the fragments of the film on Si substrate. (Magnification 80x)

The presence of O–H bonding in the film (figure 33) confirms that hydrogen contamination is due to the residual moisture in the chamber. If hydrogen is present in the sputtering gas, the formation of C–H and N–H bonds becomes more prominent. The comparison between the figure 33(a) and (b) shows the presence of these hydrogen containing bands in the film. Seth et al. [65] mentioned that hydrogen incorporation in the CN films results in absorption at 3200 and 3365 cm^{-1} owing to the $-NH_2$ symmetric and asymmetric bending modes.

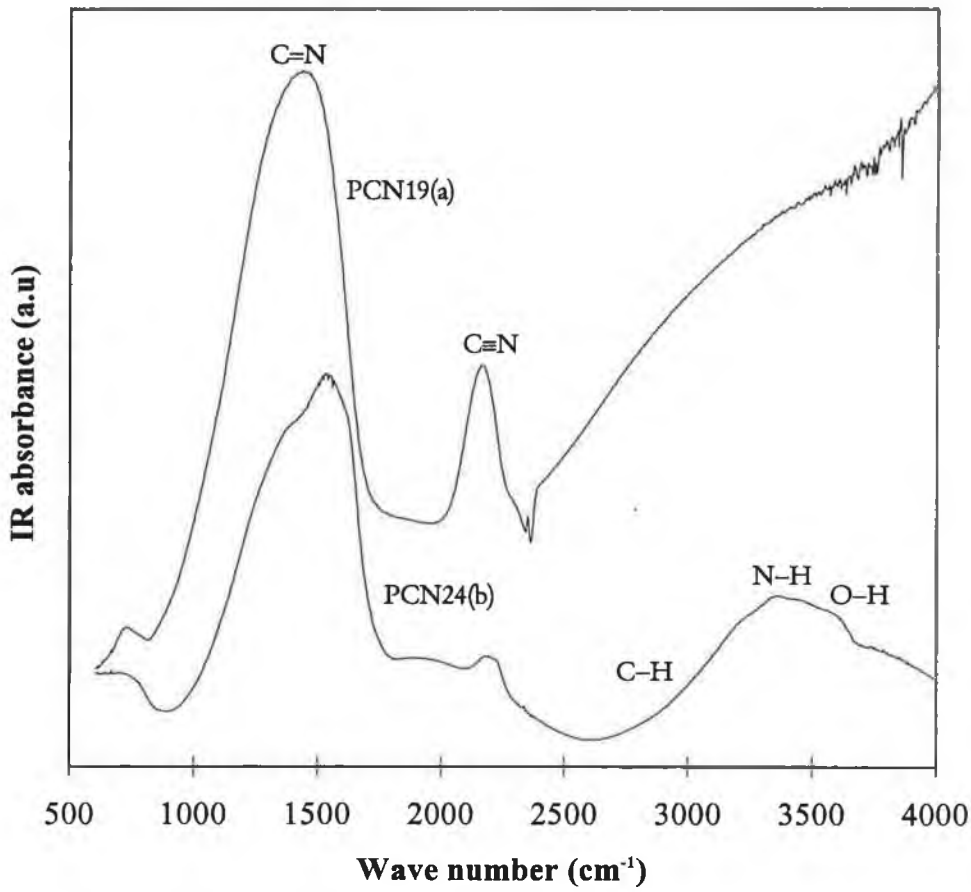

Figure 33: IR absorbance spectrum of the films (a) low pressure deposition where not hydrogen were traced, (b) high pressure deposition where intense N–H and O–H stretching bands can be observed.

Sato et al. [66] first investigated the hydrogen contamination in CN film using different chamber pressure. They found that even though no H_2 was introduced into the deposition chamber, absorption bands arising from the CH and NH modes at 2920 and 3365 cm^{-1} appear in the spectra at nitrogen pressures of 1.5 and 3 mbar. Seth et al [65] mentioned that incorporation of hydrogen in the films is due to (1) the absorbed water on the graphite target, or (2) contamination from moderate vacuum ($\sim 10^{-2}$ mbar) conditions in deposition chambers pumped by oil diffusion pumps.

Schotzau et al. [67] mentioned the mechanism of hydrogen poisoning, i.e., "Wall Process" in the cyanogen film, although they explained the role of hydrogen in the C–H bond formation and considered the mechanism as a surface reaction. Our infrared evidence of the presence of N–H bonding suggests that hydrogen attacking occurs not only at the surface but also in the bulk. The comparison of figure 33(a) and (b) also suggests that the IR absorbance intensity at 2200 cm^{-1} stretching vibrational band (C≡N) region becomes much lower in the film containing hydrogen and the C=N bonding peak was not affected that much although the Raman active G and D band in the C=N region becomes IR active due to the E_{2g} symmetry breaking. It is seen that as nitrogen incorporation helps in the E_{2g} symmetry breaking, thus G and D bands become more IR and Raman active. The difference between the figure 33(a) and (b) at ~ 1500 cm^{-1} region is that although the E_{2g} mode becomes IR active due to incorporation of nitrogen in both cases, but the G and D bands overlap in case of the film deposited at lower pressure. In case of high pressure deposited film (figure 33b) the G and D band can be easily resolved. This suggests that incorporation of hydrogen in the film helps in E_{2g} symmetry breaking that makes G and D band more IR active. The lower intensity of C≡N bonding (figure 33b) suggests that if hydrogen is present, the C≡N bonding breaks up and the released nitrogen and carbon forms C–H and N–H bonding. The C–H bonding starts to form at the surface due to presence of excess carbon. In the case of paracyanogen (C=N), carbon atom can accommodate two hydrogen atoms to become stabilised as described by Schotzau et al. [67]. In case of sputtered deposited CN films,

the N–H bonding starts to form in the bulk due to sputtering of hydrogen. The formation of these newly bonding causes excessive stress as shown in the figure 34.

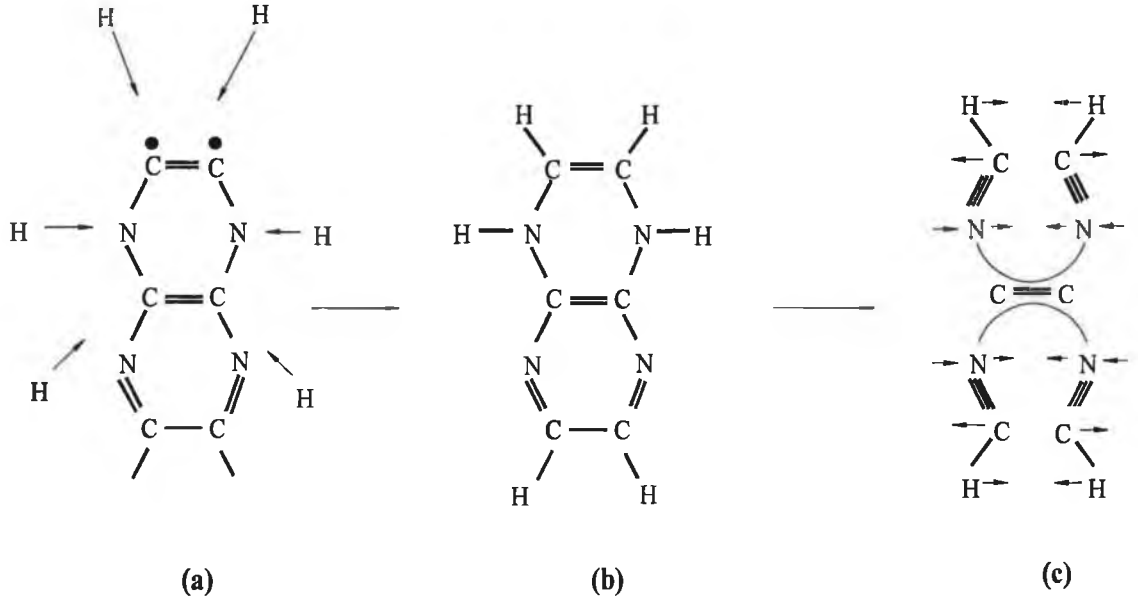

Figure 34: Formation of stretch due to incorporation of hydrogen in CN compound. (a) initial stage of hydrogen attack, (2) hydrogen bonds with surface and interface carbon, thus the film loses the adhesion with the substrate; hydrogen also bonds with nitrogen in the bulk thus gives extra push to buckle, (C) this stage shows the stress effect due to hydrogen bonding with carbon and nitrogen; here hydrogen bonds with open carbon. Due to its unsaturated bonding it tries to bond with itself resulting compressive stress in the film; due to bonding with hydrogen, carbon loses its bonding with its neighbouring carbon atom thus tensile stress develops between them as there is no force to keep them stable (arrows show the stress direction). To stabilise the tensile forces between the carbon atoms, nitrogen atoms move toward each other resulting buckling of the film. Same situation is applicable for the bottom layer of the film. Two situation may arise: (1) C≡N bonding may form; (2) C=N bonding may form which accommodates extra hydrogen atoms resulting C–H and N–H bonding. The second situation is more likely, as it can be seen in the IR absorbance spectra that N–H and C–H bondings are more intense than the C≡N bonding.

The compressive stretching of hydrogen atoms and tensile stretching of carbon atoms are due to the reaction of hydrogen and CN compound and can be shown by the following chemical reaction,

$$(CN)_X + xH \rightarrow (CH)_X + (NH)_X \qquad (1)$$

When carbon atoms are in tensile stretching condition, the next layers of nitrogen atoms in the ring are in compressive stretching to make the chain stable, this compression becomes highly supportive when hydrogen is present in the neighbouring state, i.e., in the bulk. This additional compressive stretching is higher than the bonding strength of the CN compound with the substrate, and thus comes off the substrate. This process continues during the film growth. The mechanism is shown in the figure 34.

There is another point to be mentioned here. When the film is taken out in the atmospheric condition, the stress becomes severe. The initial compressive stress becomes more supportive due to the presence of moisture in the atmosphere. Thus after a few days a complete disruption of the film occurs (figure 32b).

Summary

Effect of process parameters, i.e., nitrogen gas pressure, substrate negative bias on film characteristics are discussed. Deposition rate and nitrogen incorporation in the film increase with increase in nitrogen gas (%). A threshold negative bias voltage of -100 V can be observed for sp^2 to sp^3 transformation. The fact that the sp^3 fraction in the film increases with increase in bias voltage (-100 to -150). At about -175 bias voltage the excessive energy dissipates as thermal spike which is reasonably enough to break the sp^3 fraction to sp^2. The mechanism of sp^2 to sp^3 transformation of carbon nitride solid is similar to that are observed in DLC films, deposited by sputtering technique using negative bias substrate bias. This strong experimental evidence is in good agreement with Robertson's model and can be a good indication to increase the amount of

crystalline β-C_3N_4 structure in the film. However, the increase in sp^3 fraction can be checked by EELS technique which is not currently available.

When films are grown at high chamber pressure ($\sim 10^{-2}$ mbar), the diffusion pump does not efficiently pump down the chamber. The residual moister inside the chamber environment (although very small amount) takes part in the sputtering process. This is the only source of hydrogen contamination in the film. This hydrogen bonds with carbon and nitrogen in the films producing compressive stress. The compressive stresses due to hydrogen at each atomic layer of the film becomes highly supportive. This additional compressive stretching is higher than the bonding strength of the CN compound with the substrate, and thus comes off the substrate.

Part IV

6.4 Mechanical Properties of CN Solid

Although theoretically the material shows extremely high hardness value, it is of interest to see its mechanical properties, e.g., hardness, intrinsic stress and to correlate these properties with bonding structure. This part will highlight these properties. The part will also discuss the change in hardness of the solid when annealed at elevated temperature.

6.4.1 Mechanical Characterisation by Nanoindentation Technique

The hardness values are shown in Table. 15. The films were deposited using different N_2/Ar sputtered gas mixture to obtain films with different nitrogen concentration. A wide range of this gas mixtures were used to see the effect on bonding structure and their corresponding mechanical properties. A detailed deposition technique was discussed in chapter 4. Prior to nanoindentation analysis all the samples were analysed by RBS for elemental analysis.

Table 15: Hardness and elastic modulus of carbon nitride films containing different N at.%.

Sample no.	N at.%	Mean Hardness (GPa)	Elastic Modulus, E_r (GPa)
PCN18	0	11.45	153.3
PCN25	25.2	10.4	132
PCN19	33.2	7.09	83.6
PCN17	33.4	9.34	107.2
PCN15	33.7	8.23	85.4
PCN16	37.6	8.7	93.6

Figure 35 shows a typical load displacement curve of a sample containing 33.7 at.% nitrogen (PCN15). From the figure % of elastic recovery (%R) can be calculated by the following expression [68]

$$\%R = \frac{h_{max} - h_{res}}{h_{max}} \times 100 \qquad (2)$$

where h_{res} represents the residual depth, i.e., the final residual displacement point. An 0% R value indicates the material fully plastic. For the film shown in the figure shows ~78% elastic recovery.

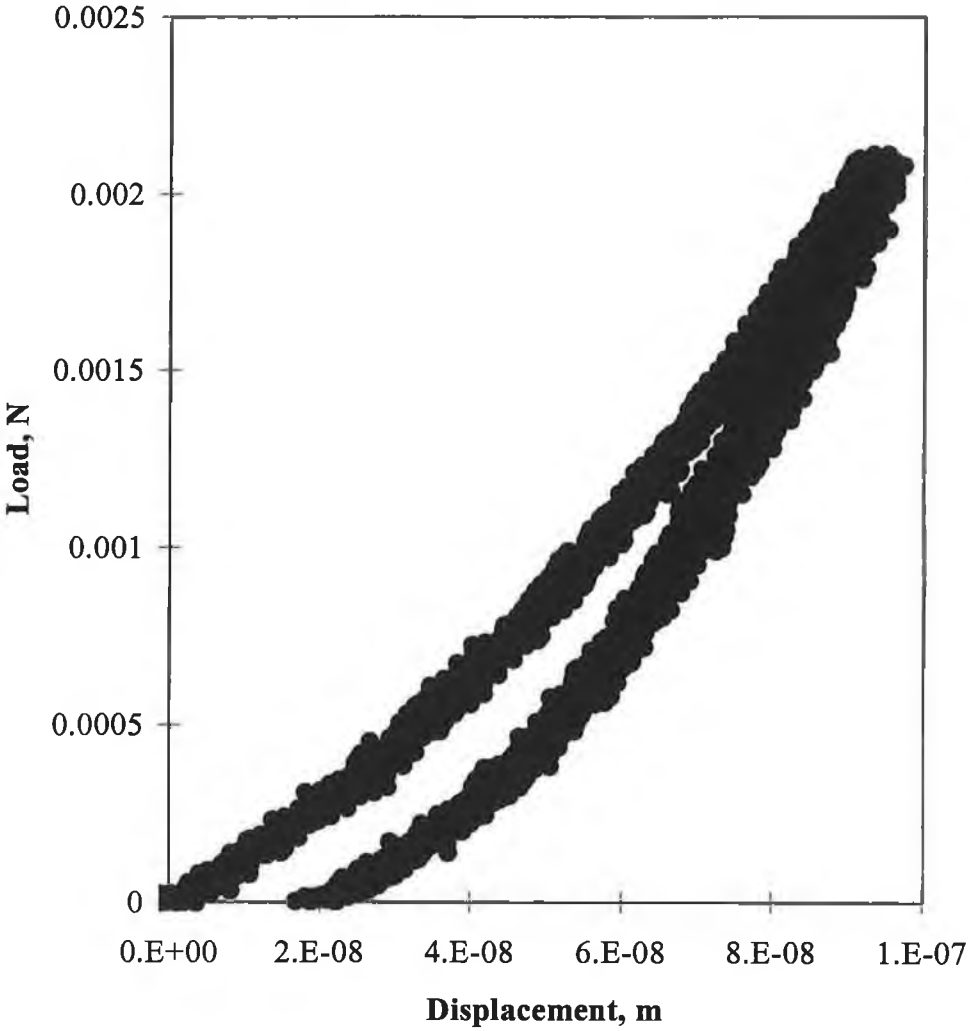

Figure 35: A typical Load-displacement curve of carbon nitride thin film containing 33.7 at.% nitroge.

6.4.1.1 Hardness and bonding structure

In Part I of this chapter bonding structure of the film was discussed. It can be seen that carbon bonds with nitrogen in sp, sp^2 and even in sp^3 configuration.

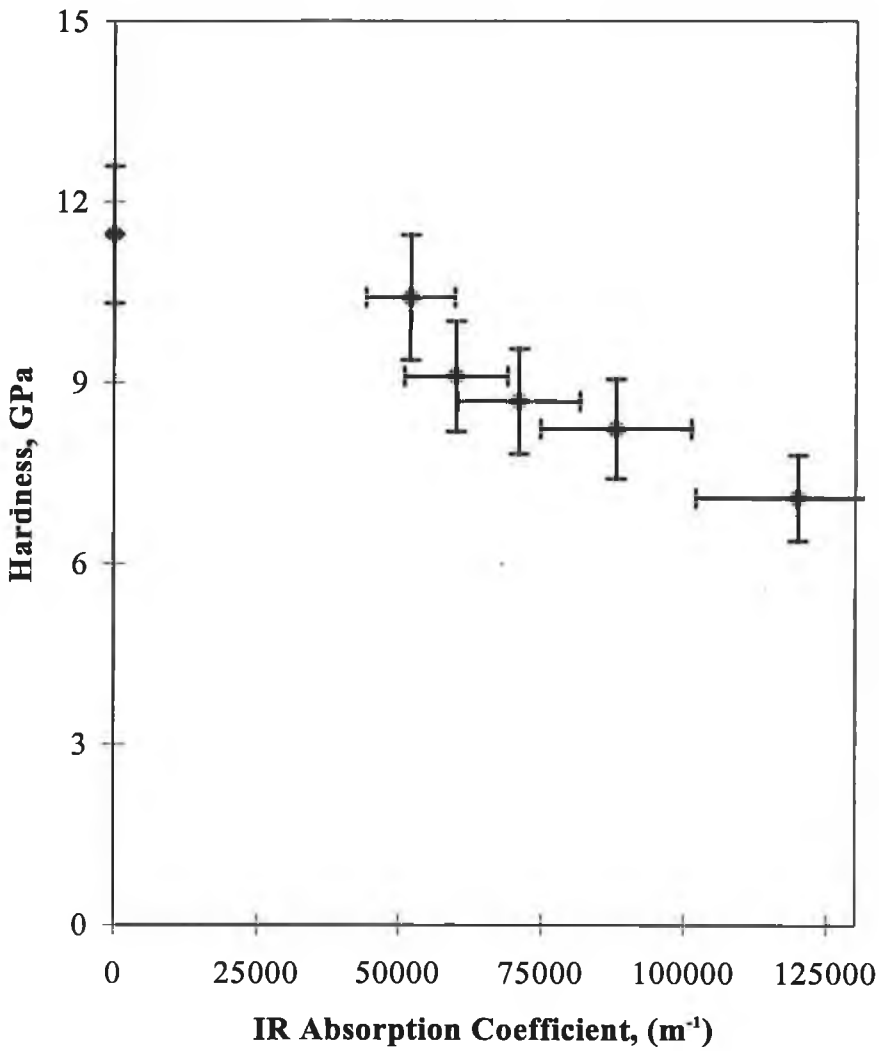

Figure 36: Hardness as a function of C≡N absorption coefficient peak for different samples deposited under different Ar/N_2 gas mixtures at $1x10^{-3}$ mbar total working pressure.

IR absorption coefficient of sp (C≡N) and sp^2 (C=N) were measured to see the effect of nitrogen incorporation on bonding structure. However, there was no sign of sp^3 bonded CN phase for the samples deposited up to -50 substrate bias. The hardness of the films was measured as a function of the nitrogen content and the IR peak absorption coefficients. It was found that correlation was best seen between hardness and the absorbance at 2200 cm^{-1} (figure 36) rather than the N/(C+N) ratio (figure 37) or the absorbance at 1500 cm^{-1}.

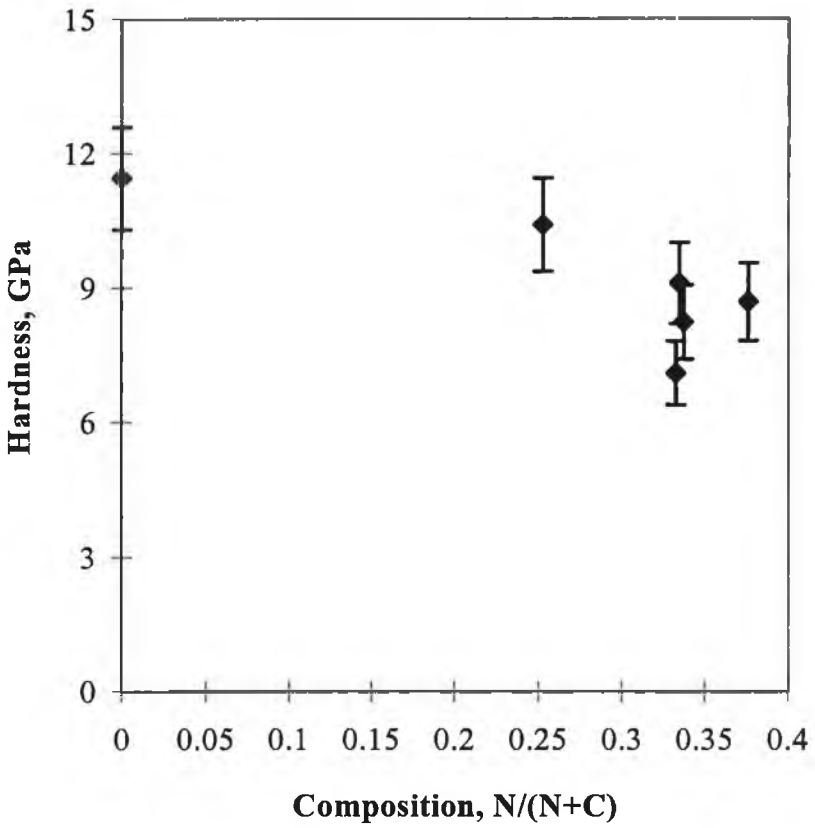

Figure 37: Hardness as a function of composition for different samples deposited under different Ar/N_2 gas mixtures at $1x10^{-3}$ mbar total working pressure.

This indicates that it is the C≡N bond concentration which controls the hardness. It is known that the strength of this bond is less than that of the C-C, C=C, C-N and C=N (or even N-N) bonds, due to presence of number of π bonds. The hardness is also likely

to be affected by the fact that the C≡N bond will terminate the carbon backbone leading to less tightly bound C atoms.

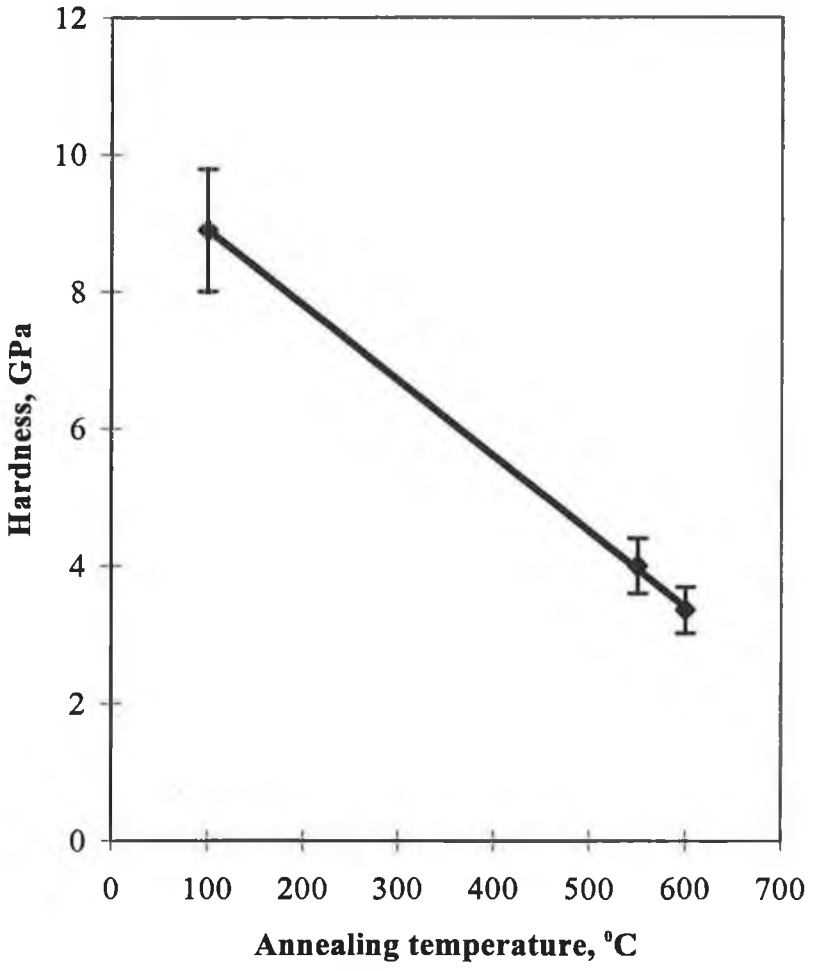

Figure 38: Hardness as a function of temperature (°C) for the samples annealed at different temperatures for 15 min under vacuum.

It was discussed in Part I of this chapter that when CN solids are annealed upto 600°C, the C≡N bonding is completely gone and C=N bonding is slightly affected. Their cohesive energies are also discussed. Hardness values of the annealed samples are measured to show if structural changes have a significant effect on the mechanical properties. Figure 38 shows the film hardness measured after annealing. The film

became softer even though the nitrogen content was reduced. This may be due to the breaking of carbon-nitrogen bonds which leaves vacant lattice sites. The nitrogen atoms so produced are likely to combine as N_2 molecules in the film and may disrupt the structure as they desorb. This interpretation is supported by the appearance of the films which become less specular after annealing.

6.4.2 Stress measurements

Chapter 3 discussed about the stress that usually develops in thin films during deposition. The films will possess intrinsic stress, i.e., compressive or tensile stresses, regardless of how they are produced. The interfacial shear stresses is responsible for adhesion strength of the film-substrate interface and may lead to cracking and even complete delamination of the films occur depending on the severity of the stress concentration at the interface. Adhesion property of a film is the prime consideration when considered as coating of surfaces. This property will be discussed later in relation to carbon nitride thin film as hard coating.

6.4.2.1 Intrinsic stress in carbon nitride film

Film stress was found to be lower for the nitrogenated films than for pure carbon films. Unlike the film hardness it was found to be independent of the nitrogen content for films with >20 % N. It was also found to be independent of film thickness indicating that the stress was introduced at the film-substrate interface during the initial growth process rather than in the bulk of the film. Indeed, if the stress per unit thickness is plotted as a function of the reciprocal of film thickness (figure 39), the graph extends to zero or even slightly tensile values of stress as thickness increases (i.e. as thickness^{-1} tends to zero). Thus the addition of nitrogen bonding in the films significantly relieves the high levels of stress normally found in hard carbon films.

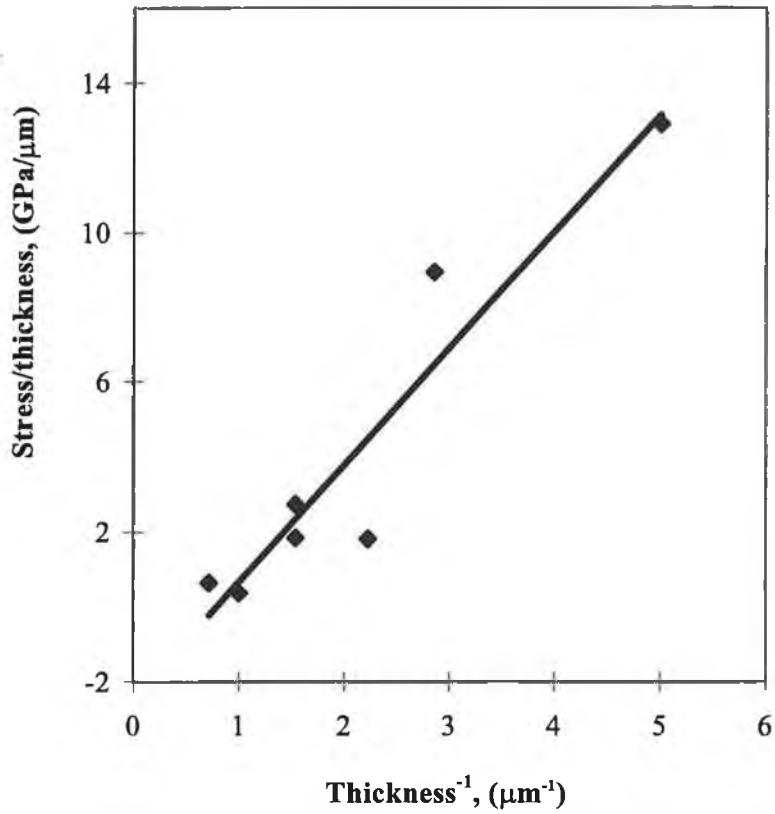

Figure 39: Stress as a function of thickness^{-1} of different samples deposited under different Ar/N_2 gas mixture at $1x10^{-3}$ mbar total working pressure.

Summary

The film hardness appears to be controlled by the amount of C≡N bonding, rather than nitrogen content, i.e. the C≡N bond appears to be significantly weaker than the others. The hardness is also likely to be affected by the fact that the C≡N bond will terminate the carbon backbone leading to less tightly bound C atoms. This behaviour is mirrored by the stress measurements. The stress is shown to be concentrated at the film-substrate interface whereas the bulk of the film is stress-free.

Annealing has been shown to lead to a loss of nitrogen from the films at temperature above approx. 550°C. The loss appears to come preferentially from the less saturated carbon-nitrogen bonds and leads to a softer, weakened film structure.

References

1. N.P. Barradas, Nuclear Instrum. Methods Phys. Res. B, (1998), accepted.

2. L. Maissel, in Handbook of Thin Film Technology, L. Maissel and R. Glang edn., McGraw Hill, New York, pp.4-1, 1970.

3. Z.J. Zhang, S. Fan, J. Huang and C.M. Lieber, J Electron. Mats., 25, 57 (1996).

4. S. Veprek, J. Weidmann and F. Glatz, J. Vac. Sci. Technol. A, 13(6), 2914 (1995).

5. S. Kumar and T.L. Tansley, Thin Solid Films, 256 (1995) 44.

6. G. Socrates, Infrared Characteristic Group Frequencies, John Wiley & Sons, New Yoirk, 1980.

7. J.H Kaufman, S. Metin and D.D. Saperstein, Physical Review B, 39 (18), 13053 (1989).

8. J. Seth, R. Padiyath and S.V. Babu, Diamond and Related Materials, 3210 (1994).

9. R.N. Hazeldine and B.J.H. Mattinson, J. Chem. Soc., London, 4172 (1955).

10. P. Tarte, J. Chem. Phys., 23, 979 (1955).

11. R.L. Williams, R.J. Pace and G.J. Jeacoke, Spectrochim. Acta, 20225 (1964).

12. N.B. Colthup, L.H. Daly and S.E. Wiberly, Introduction to Infrared and Raman Spectroscopy, 3rd Ed., Academic Press, New York, 1990.

13. D. Hadzi, J. Chem. Soc., 2143 (1956).

14. P.J. Trotter, Appl. Spectrosc., 31, 30 (1977).

15. P.M. Drozdzewski, Spectrochim. Acta, 41A, 1035 (1985).

16. F. Weich, J. Widany and Th. Frauenheim, Phys. Rev. Lett., 78(17), 3326 (1997).

17. R.O.Dillon, J.A. Woollam and V. Kathanant, Phys. Rev. B, 29 3482 (1984).

18. B.E. Douglas, D.H. McDaniel and J.J. Alexander, Concepts and Models of Inorganic Chemistry, 3rd Ed., John Wiley and Sons, Inc., New York, p.70, 1994.

19. J. Shiao and R.W. Hoffman, Thin Solid Films, 283 (1996) 145.

20. H. Seki, International Conference on Metallurgical Coatings, San Diego, 1988.

21. D. Marton, K.J. Boyd, A.H. Al-Bayati, S.S. Todorov and J.W. Rabalais, Phys. Rev. Lett., 73(1), 118 (1994).

22. M.R. Wixtom, J. Am. Ceram. Soc., 73 (1990) 1973.

23. N.N. Greenwood and A. Earnshaw, Chemistry of the elements, Pergamon press, New York, 1st edn., 1984.

24. T.L. Bar and M.P. Yin, J. Vac. Sci. Technol. A, 10, 2788 (1992).

25. F.L. Freire, Jr., C.A. Achete, G. Mariotto, R. Canteri, J.Vac. Sci. Technol. A, 12(6), 3048 (1994).

26. C.J. Torng, J.M. Sivertsen, J.H. Judy, C.Chang, J. Mater. Res., 5(11), 2490 (1990).

27. F. Rossi, B. Andre, A. van Veen, P.E. Mijnarends, H. Schut, F. Labohm, M.P. Delplancke, H. Dunlop and E. Anger, Thin Solid Films, 253, 85 (1994).

28. J. Robertson, Advances in Phys., 35(4), 317 (1986).

29. B.E Douglas, D.H. McDaniel and J.J. Alexander, Concepts and Models of Inorganic Chemistry, 3rd ed., John Wiley & Sons, New York, pp.70, 1994.

30. D. Briggs and M.P. Seah, Practical Surface Analysis, Vol 1: Auger and X-ray Photoelectron Spectroscopy, 2nd edn., John Wiley & Sons, New York, 1996.

31. V.G. Aleshin and Yu.N. Kucherenko, J. Electrons Spectros., 8, 411 (1976).

32. V.V. Nemoshkalenko, V.G. Aleshin, Yu. N. Kucherenko, Solid State Commun., 20, 1155 (1976).

33. S.C. Sharma, M.Green, R.C. Hyer, C.A. Dark, T.D. Black, A.R. Chourasia, D.R. Chopra and K.K. Mishra, J. Mater. Res., 5, 2424 (1990).

34. P.G. Lurie and J.M. Wilson, Surface Science, 65, 476 (1977).

35. C.J. Trong, T.Yeh, J.M. Sivertsen, J.H. Judy, in Diamond, Boron Nitride, Silicon Carbide and Related Wide Bandgap Semiconductor, J.T. Glass, R.F. Messier and N. Fijimori edn, Mater. Res. Soc. Symp. Proc. 162, Pittsburgh, PA, 1990.

36. F.R. McFeely, S.P. Kowalczyk, L.Ley, R.G. Cavell, R.A. Pollak and D.A. Shirely, Phys. Rev. B, 9, 5268 (1974).

37. K.J. Boyd, D. Marton, S.S. Todorov, A.H. Al-Bayati, J. Kulik, R.A.Zuhr and J.W. Rabalais, J Vac. Sci. Technol. A, 13(4), 2110 (1995).

38. D. Marton, K.J. Boyd, T.E, Lytle, and J.W. Rabalais, Phys. Rev. B, 48, 6757 (1993).

39. K. M. Yu, M. L. Cohen, E. E. Haller, W. L Hansen, A. Y. Liu and I. C. Wu, Phys. Rev. B, 49, 5034 (1994).

40. Z. Ze-Bo, L. Yin-An, X. Sie-Shen and Y Guo-Zhen, J. Mater. Sci. Letts., 14, 1742 (1995).

41. C. Niu, Y. Z. Lu and C. M. Lieber, Science, 261, 334 (1993).

42. E. G. Wang, Y. Chen and L. Guo, Physica Scripta, T69, 108 (1997).

43. HE Xiaoming, LI Wenzhi and LI Hengde, Chinese Science Bulletin, 40 (20),1752-1757, (1995).

44. J. Szmidt, A. Werbowy, K. Zdunek, A. Sokowska, J. Konwerska-Hrabowska, S. Mitura, Diamond and Related Materials, 5, 564-569, (1996).

45. J. Robertson, Diamond and Related Materials, 2, 984 (1993).

46. W. Zheng, T. Ding, I. Ivanov, J.-E. Sundgren, J. Mater. Sci. Technol., 13, 154 (1997).

47. H. Sjotrom, I. Ivanov, M. Johansson, L. Hultman, J-E. Sundgren, S.V. Hainsworth, T.F. Page, L.R. Wallenberg, Thin Solid Films, 246, 103 (1994).

48. S.S. Todorov, D. Marton, K.J. Boyad, A.H.Al-Bayati, J.W. Rabalais, J. Vac. Sci. Technol., A12, 3192 (1994).

49. D. Li, S lopez, Y.W. Chung, M.S. Wong, D. Sproul, J. Vac. Sci. Technol., A13, 1063 (1995).

50. E.G. Spencer, P.H. Schidt, D.C. Joy, F.J. Salasone, Appl. Phys. Lett., 29, 118 (1976).

51. Y. Lifshitz, S.R. Kasi, J.W. Rabalais, Phys. Rev., Lett., 68, 620 (1989).

52. C. Weissmantel, Thin Solid Films, 92, 55 (1982).

53. B.T. Kelly, Physics of Graphite, Applied Science, London, 1981.

54. H.J. Steffen, D. Marton, J.W. Rabalais, Phys. Rev. Lett., 68, 1726 (1992).

55. J. Koike, D.M. Parkin, T.E. Mitchell, Appl. Phys. Lett., 60, 1450 (1992).

56. D.R. McKenzie, D. Muller, B.A. Pailthrope, Phys. Rev. Lett., 67, 773 (1991).

57. H. Windischmann, J. Appl. Phys., 62, 1800 (1987).

58. B.A. Pailthrope, J. Appl. Phys., 70, 543 (1991).

59. H.P. Kaukonen and R.M. Nieminen, Phys. Rev. Lett., 68, 620 (1992).

60. C.A. Davis, Thin Solid Films, 226, 30 (1993).

61. P.J. Fallon, V.S. Veerasamy, C.A. Davis, J. Robertson, J. Koskinen, Phys. Rev. B, 48(7), 4777 (1993).

62. J.J. Cuomo, J.P. Doyle, J. Bruley, J.C. Lui, Appl. Phys. Lett., 58, 466 (1991).

63. J.A. Thornton and D.W. Hoffman, Thin Solid Films, 171, 5-31 (1989).

64. B.C. Holloway, D.K. Shuh, M.A. Kelly, W. Tong, J.A. Carlisle, I. Jimenez, D.G.J. Sutherland, L.J. Terminello, P. Pianetta, S. Hangstrom, Thin Solid Films, 94-98, 290 (1996).

65. J. Seth, R. Padiyath, S.V. Babu, Diamond and Related Materials, 3, 210 (1994).

66. T. Sato, S. Furuno, S. Iguchi, M. Hanabusa, Appl. Phys. A, 45, 355 (1988).

67. H.J. Schotzau and S. Veprek, Appl. Phys., 7, 271 (1975).

68. S.V. Hainsworth, H.W. Chandler, T.F. Page, J. Mater. Res., 11(8), 1987 (1996).

Chapter 7

Carbon Nitride Thin Film as Hard Coating on Tool Steel

Carbon nitride in thin film form is a good candidate for hard coating but it has poor adhesion on tool steel due to diffusion of nitrogen or carbon atoms into the substrate at the deposition temperature (typically $\sim 325^{0}$C). This is the first time an attempt is taken to use this material as a hard coating directly on tool steel. The adhesion property can be improved when a diffusion barrier is created at the steel surface. TiN or TiCN can be deposited on tool steel prior to carbon nitride deposition, due to their good adhesion to bulk and to the coating itself. Application of these interlayer is not only expensive but also complex. A process is required to obtain good adhesion of carbon nitride films on tool steel without any thin film interlayer. In this study AISI H13 and AISI/SAE8620 tool steels are used as the substrates. RBS and XPS are used to observe the diffusion of nitrogen into the steel surface. The relevant adhesion characteristics along with mechanical properties of the deposited film are discussed in this chapter. The chapter also discusses the reasons of poor adhesion of carbon nitride materials on steel surfaces.

As a good candidate for overcoat a material should show (1) good adhesion on the substrates; (2) low wear resistance; (3) low frictional coefficient. With all these three qualities, a material with hardness values similar to diamond, can be applied as thin film hard coating on tool steel. During deposition at $\sim 400^{0}$C on steels, diffusion of carbon from the film breaks up the bonding at the interface, thus shows poor adhesion. In case of carbon nitride, the usual deposition temperature is $\sim 350^{0}$C from

the plasma in Penning type opposed target DC sputtering technique. The deposition temperature is expected to be higher when used laser ablation, or any other ion beam techniques. According to the Fe-N binary phase diagram, a substantial amount of nitrogen is diffused into steel from the film during deposition, leaving a poor adhere film on the substrate. Similarly carbon diffusion occurs into the bulk at this temperature according to the Fe-Fe_3C binary phase diagram.

It is shown for the first time, the successful direct deposition of carbon nitride thin film as hard coating of tool steel. Films with a thickness of ~1.1μm were deposited on tool steels. The adhesion and wear properties of the films are discussed.

7.1 Sample preparation prior to deposition

The experiment is carried out considering the following points

1. During carbon nitride deposition the substrate was experiencing 325°C from the plasma. At this temperature nitrogen and a small amount of carbon will diffuse into the steel surface leaving a weak bonded film at the interface. These films do not have enough strength to show good adhesion at the interface.

2. The first step will be to create a diffusion barrier at the interface. This barrier should be such that steel does not have any interstitial or substitutional lattice sites to be accommodated by nitrogen or carbon atoms from films at the deposition temperature.

3. Only if the steel surface can be saturated with carbon or nitrogen prior to deposition, a possible diffusion barrier can be obtained.

Conventionally multilayer coating is needed for good adhesion of carbon based thin films. In this case TiN or TiCN are commonly used as an interlayer prior to carbon

based thin film deposition. This interlayer deposition not only causes process complexity but also is expensive. Conventional nitriding or carburising can be a good alternative to these interlayer deposition. The nitrided or curburised surface acts as the diffusion barrier which shows better adhesion of carbon nitride thin film on the steel surface. A number of tool steel samples i.e., AISI H13 and AISI/SAE8620 type are nitrided and carburised respectively. Typical analysis of the substrates are given in table 1 and 2.

Table 1: Typical analysis (%) of AISI H13 tool steels (courtesy Orvar® Supreme, Uddeholm Ireland)

C	Si	Mn	Cr	Mo	V
0.38	1.0	0.4	5.3	1.3	0.9

Table 2: Typical analysis (%) of AISI/SAE8620 tool steel (courtesy Impact Ireland Metals)

	C	Mn	Si	S	P	Cr	Mo	Ni
% Min	0.18	0.70	0.15	-	-	0.40	0.15	0.40
% Max	0.23	0.90	0.35	0.040	0.035	0.60	0.25	0.70

7.1.1 Heat Treatment Furnace

A fluidised bed type furnace was used for both nitriding and carburising processes [1]. The dimension of the furnace is 300 mm diameter and 600 mm height. Aluminium Oxide (Mesh size 100μm) was used as fluidising medium.

7.1.2 Nitriding

Nitriding is a surface-hardening heat treatment process that introduces nitrogen into the steel surface at a temperature range of 500 to 550°C. At this temperature steel is in ferritic condition and thus does not get any change for grain growth. Figure 1 shows the Iron-Nitrogen binary phase diagram indicating the phases present during nitriding. Nitriding is a case hardening process with a minimum distortion and with excellent dimensional control compared to other surface hardening techniques. Nitriding process can be understood from the Fe-N binary phase diagram [2]. Nitrogen has partial solubility in iron. It can form a solid solution with ferrite at nitrogen contents up to about 6%. At about 6% N, a compound called γ' (gamma prime) with a composition of Fe_4N is formed. At nitrogen contents greater than 8%, the equilibrium reaction product is ε compound, Fe_3N. The γ' layer is undesirable and can be overcome by using special nitriding technique, e.g., fluidised bed. The ε layer is desirable and can be achieved if a prolonged diffusion time is given during the process in a neutral atmosphere.

The Nitriding process of AISI H13 is as follows:

The specimens were placed in the fluidised bed furnace at a temperature of 525°C for a period of 150 minutes in an atmosphere of N_2 and NH_3. After that, the atmosphere was maintained using only N_2 for a period of 30 minutes to develop a diffusion zone to obtain ε layer at the surface. The above processes are repeated for several times as necessary. The specimens were then quenched in a fluidised bed. Hardness values of 58 to 62 Rockwell C are achieved at the nitrided surfaces. Thus a case depth of 0.15mm is achieved as a diffusion barrier for the carbon nitride films.

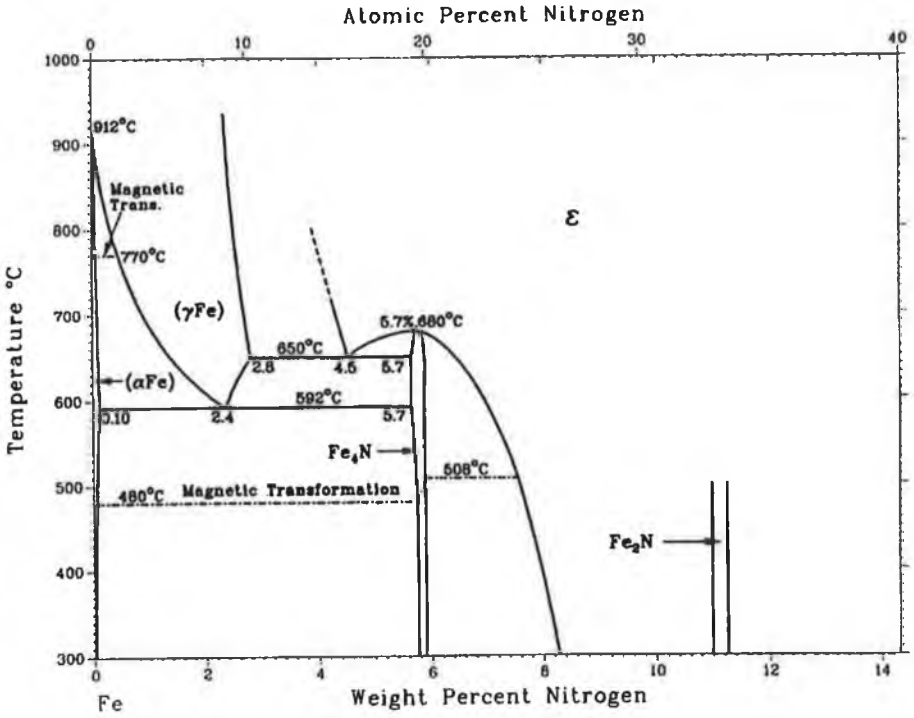

Figure 1: Iron-Nitrogen binary phase diagram showing the phases at nitriding temperatures [2].

7.1.3 Carburising

Carburising is the addition of carbon to the steel surface of low-carbon steels at temperatures 850 to 950°C. At this temperature the steel is in the austenitic phase and can dissolve maximum of 2% carbon. Figure 2 shows the Iron-Iron Carbon binary phase diagram showing the composition and temperature range where carburising is usually carried out. Specifically the figure represents a partial binary system which is of interest, because higher carbon content region does not have any technological importance.

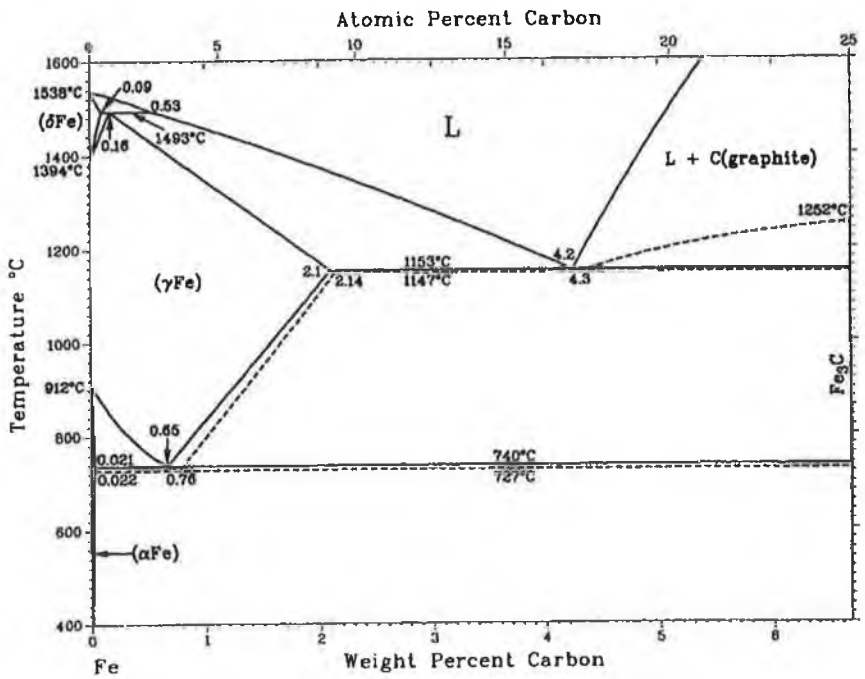

Figure 2: Iron-Iron carbide binary phase diagram showing the phases at carburising temperature [2].

When this solid solution is quenched, martensitic structure (a super-saturated solid solution of carbon trapped in a body-centred tetragonal structure, containing max. of 1.08% carbon) is formed at the surface that causes the hardened layer while the core remains fine grained steel. Conventionally the steel contains ~0.2% carbon before carburising and this concentration is maintained at 0.8 to 1.0% level at the carburised layer. When the carbon content becomes more than 1.0% the layer contains retained austenite and brittle martensite which is not at all desirable. With higher carbon content the martensitic structure becomes brittle as because proeutectoid carbides (Fe_3C) may form at the grain boundary causing brittle structure. This problem can be overcome using fluidise bed carburising technique where a diffusion time is

maintained to give enough time for redistribution of excess carbon into the core prior to quenching. The process is good to maintain the core grain size as well. After carburising it is common practice to temper the sample for stress relief due to formation of martensite.

The Carburising Process of AISI/SAE8620 is as follows:

Specimens were placed in the fluidised bed furnace at a temperature of 925°C for a period of 90 minutes in an atmosphere of N_2 and CH_4. The temperature was lowered to 870°C over a period of 30 minunes in an atmosphere of N_2 only to develop a diffusion zone. The specimens were then quenched in oil. They were tempered at 150°C for 60 minutes to reduce the stress concentration at the case and bulk which was developed during quenching from ausenitic zone to room temperature. Hardness values of 58 to 60 Rockwell C were achieved at the carburised surface. Thus a case depth 0.8 to 1.0 mm was obtained as a diffusion barrier for the carbon nitride thin films.

Nitriding is similar to carburising in that surface composition is altered. In case of nitriding, nitrogen is added when iron is in ferritic phase and for carbusing, carbon is added when iron is in austenitic phase. Because nitriding does not involve heating into the austenitic phase regime and a subsequent quench to form martensite, nitriding can be accomplished with minimum distortion and with excellent dimensional control.

7.1.4 Surface Polishing

The treated specimens were mechanically polished using a polishing grinder. As the average case depth was ~0.15 mm for both cases, care was taken during the polishing process. The specimen surfaces were polished down to 1 and 3 μm roughness for carbon nitride thin film deposition.

7.2 Carbon nitride thin film coating on case hardened steel

Carbon nitride thin film was deposited on five steel substrates using different substrate surface conditions. In all cases 100% nitrogen gas and -50 V substrate bias were used. Deposition rate was kept more or less constant for all cases. Substrate roughness was varied prior to film deposition to see the difference in adhesion and frictional properties. Table 3 shows the summary of deposition conditions for all these five samples.

Table 3: Deposition conditions for the samples coated.

Sample no.	Substrate condition (treated/untreated)	Surface roughness (μ) (before deposition)	Film thickness (μm)
PCN30	Untreated	1	1.1
PCN31	Nitrided	1	1.1
PCN32	Carburised	1	1.1
PCN33	Nitrided	3	1.1
PCN34	Carburised	3	1.1

The reason of taking just only one parameter i.e., two different surface roughnesses was to see this effect on film adhesion. Mattox [3] showed the surface effects on growth, adhesion and properties of reactively deposited hard coatings. Figure 3 illustrates his model. PVD and CVD processes are commonly known as atomistic deposition processes. The growth, properties and functionality of PVD hard coatings depend strongly on the physical, mechanical and chemical properties of the substrate surface. Initially the substrate surface strongly influence the adatom nucleation mode, nucleation density and interface formation. Surface roughness causes the film to grow in a less than fully dense manner due to geometrical effects. The surface chemistry affects nucleation, diffusion and reaction at the substrate surface.

7.2.1 Mattox's comments on "Surface effects on the growth, adhesion and properties of reactively deposited hard coatings"

Mattox [3] discussed three possible surfaces that can affect the film's growth, adhesion and mechanical properties, deposited by PVD/CVD technique. Substrate surface roughness and the angular distribution of the depositing vapour atoms (adatoms) in PVD processing have significant influence on the generation of a macro-columnar morphology due to geometrical shadowing effects (see chapter 3). This macro-columnar morphology will be superimposed on the normal columnar morphology of atomistically deposited films giving a less than fully dense deposit and an increasing surface roughness with thickness. Figure 3 shows the effects of surface roughness on the distribution of the deposited film material and the resulting film morphology. Surface coverage can be improved by simultaneous ion bombardment to sputter and redeposit materials deposited on the rough surface [4,5]. This bombardment during deposition also densifies the depositing film material and enhances the chemical reactivity in reactive deposition processes [5].

If the film material is less than fully dense then it will compact under load resulting in a lowered hardness values as well as increased friction, wear and galling. The density of a deposited coating depends primarily on the morphology of the surface and the growth morphology of the depositing film material. If the surface has a texture, such as from directional grinding, the macro-columnar morphology will be anisotropic with direction. Typically, PVD hard coatings range in thickness from less than a micrometer to 15-25 μm; this is often in the range of substrate surface features such as grinding and machining marks and the roughness of hot pressed and sintered materials.

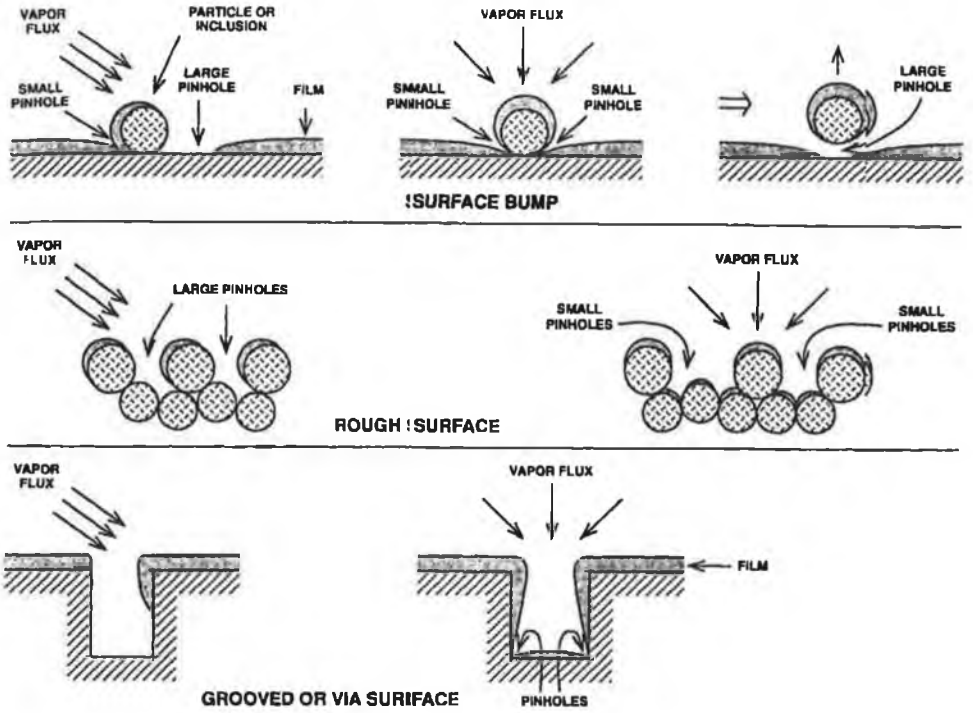

Figure 3: Effect of surface features and angular distribution of depositing flux on the film deposition: top, inclusion or particulate contamination; middle, rough surface; bottom, single surface feature [3].

The surface mobility and nucleation of the adatoms is primarily controlled by chemical interaction with the surface. It is desirable to have a strong chemical interaction in order to obtain a high nucleation density on the surface. In order to form an adherent coating a diffusion or compound type of interface should be formed [6]. Removal of contaminants and barrier layers to diffusion and reaction is important in obtaining good contact to the substrate surface.

7.3 Structural properties of the films deposited on steel surfaces

It is now necessary to find out the reason of poor adhesion of carbon nitride thin film and if there is any structural changes due to deposition on steel. Surface composition will be studied by XPS and RBS and structural properties of the films will be analysed by Raman Spectroscopy.

7.3.1 Surface analysis by XPS and RBS

To get a measure of diffused nitrogen or carbon atom during deposition, an untreated steel substrate surface was analysed by XPS and RBS. To do this experiment, the untreated steel substrate (1μ surface roughness) was coated with carbon nitride thin film. This sample was coated at the same time with other nitrided and carburised samples. Thus gives the same deposition condition. Extreme care was taken to mechanically polish the substrate on an 1μ paper to remove the coating from the subsurface level ensuring that no coating was left on the steel surface. To ensure the total film removal from the substrate surface, additional material from the substrate was removed. The surface was sputter cleaned for 5 min in the XPS preparation chamber to get rid of any surface contamination.

The XPS spectrum (figure 4) shows a sharp carbon peak at ~284 eV, a weak nitrogen peak at ~399 eV. There was a very weak oxygen peak at ~532 eV which probably due to residual surface contamination. Carbon peak (~284 eV) was coming from the bulk as the substrate contains ~0.4 at.% carbon as discussed before. Nitrogen peak (399 eV) in the XPS spectra confirms diffusion at the interface level which is essentially a good reason for breaking up the film bonding. To get a quantitative analysis at the interface RBS analysis was done on the same sample. Due to a huge difference in scattering cross section of iron and nitrogen/carbon atoms, no peak from nitrogen/carbon was observed. It is to be noted here that as a very little amount of

nitrogen was diffused at angstrom level subsurface, the level of backscattered He^+ ions from nitrogen will be very low.

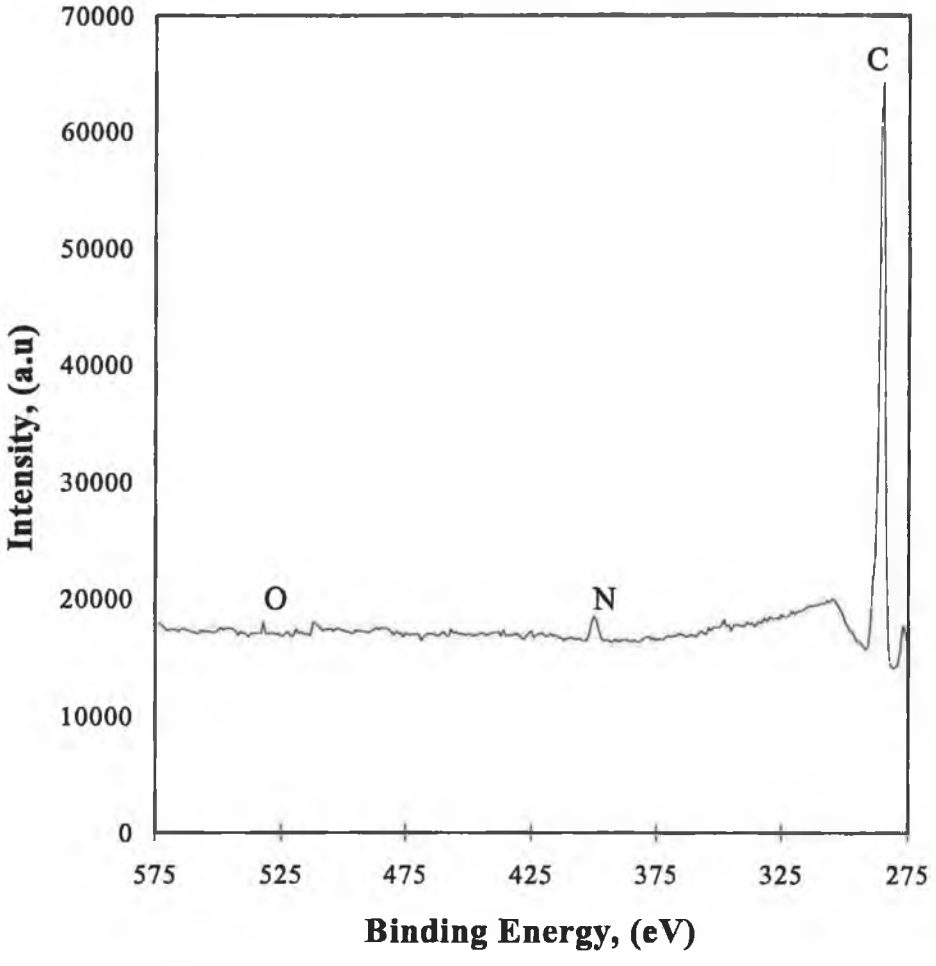

Figure 4: X-ray Photoelectron Spectrum of the untreated steel surface to detect nitrogen diffusion during carbon nitride thin film deposition at the interface. The film was removed completely before the analysis.

7.3.2 Vibrational properties by Raman spectroscopy

Raman analysis was carried out on carbon nitride films deposited on untreated, nitrided, carburised steel substrates to see if there is any bonding-structural change in the film due to substrate effect. A detailed description of vibrational properties of the film is given in the previous chapter. The C–C (~700 cm^{-1}), D(~1357 cm^{-1}), G (~1561 cm^{-1}), C≡N (~2200 cm^{-1}) and C–H (~2900 cm^{-1}) stretching vibrations can be observed in figure 5. No shift in these peak positions are observed. There was no other (i.e., FeN or FeC) bonding observed in the instrumental range ensuring no Fe diffusion in the film due to energetic ion bombardment on the substrate. The Raman scattering takes place from the whole thickness of the film. Thus it can be presumed that structure remained reasonably unaffected throughout the bulk and diffusion is occurring at the interface which is breaking up the adhesion of the film with the substrate.

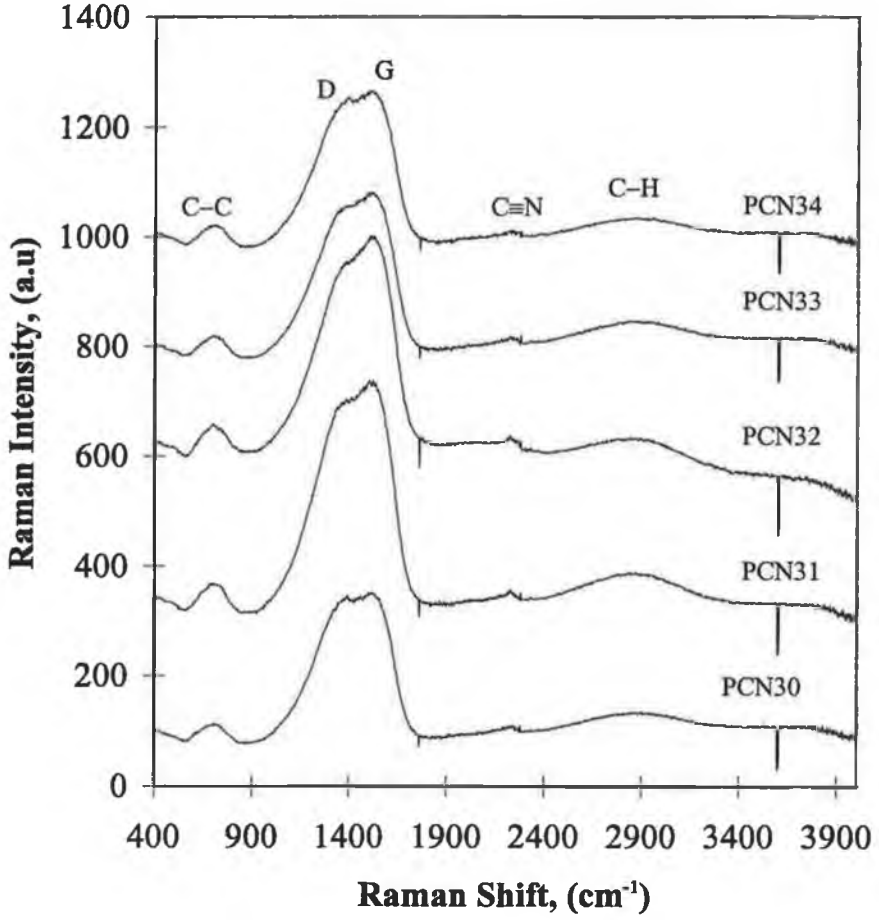

Figure 5: Raman spectra of carbon nitride thin film deposited on different (treated/untreated) steel samples.

7.4 Adhesion and frictional properties of the films

Five samples were evaluated for adhesion and frictional coefficient measurements. Adhesion evaluation is usually done by Rockwell indentation method by comparing the indentation pattern (chapter 5) which is scaled from HF1 to HF6 as discussed before. From the preliminary evaluations, three samples (PCN30, PCN32 and PCN34) were eliminated due to poor adhesion (table 4). The other two samples (PCN31and PCN33) had good adhesion (Rockwell HF3-4). Figure 6(a) to (e) shows the Rockwell indentation photographs with the magnification of 80x in all cases.

Table 4: Rockwell indentation evaluation

Sample no.	Substrate condition (treated/untreated)	Surface roughness (μ) (before deposition)	Rockwell evaluation
PCN30	Untreated	1	HF6
PCN31	Nitrided	1	HF3
PCN32	Carburised	1	HF5
PCN33	Nitrided	3	HF4
PCN34	Carburised	3	HF6

The frictional properties of the samples PCN31 and PCN33 were measured with a pin-on-disk wear tester. The wear tracks were made with the tester. The measurements gave a measure of the friction of a tungsten carbide ball (pin) on the rotating sample (disk). The friction was monitored and plotted as a function of the number of revolutions of the pin on the disk. By monitoring the friction it is possible to determine the number of revolutions of the pin on the disk required for the coating to be worn through. The experimental conditions and results are summarized in the table 5.

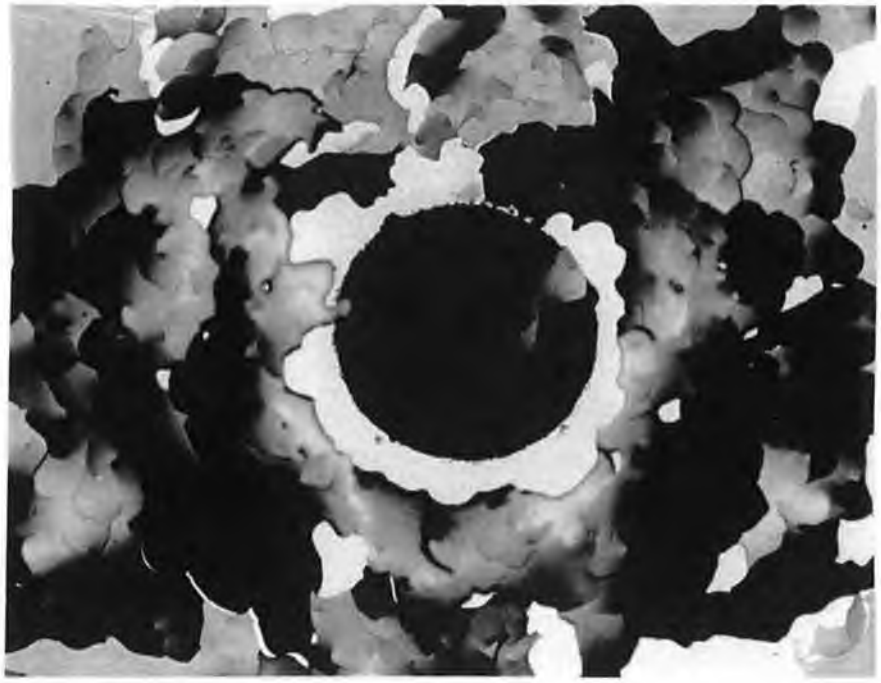

(a)

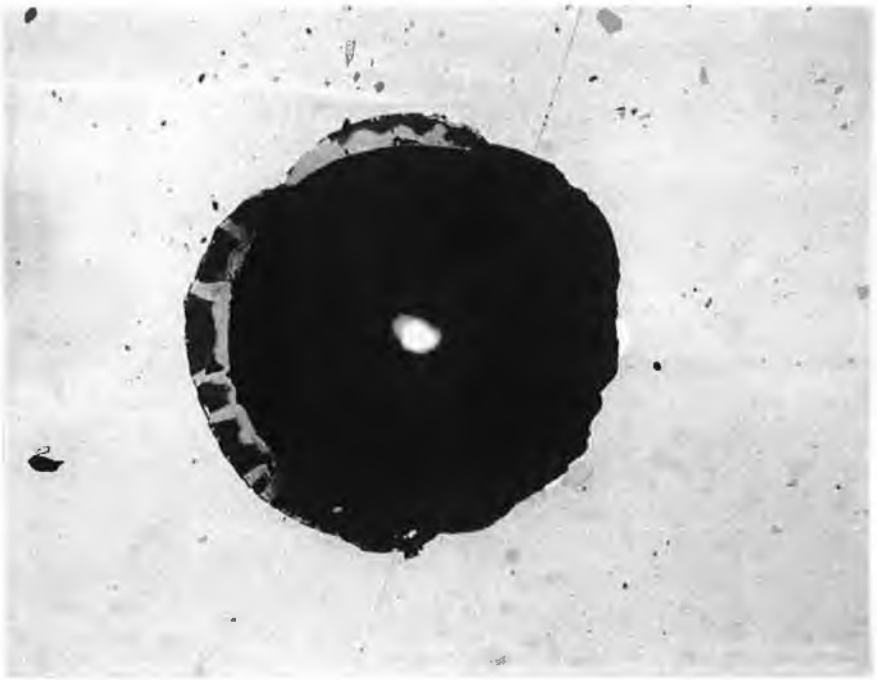

(b)

Figure 6: Rockwell indentation for adhesion evaluation (a) untreated sample (PCN30), complete delamination of the film is observed, this feature represents adhesion in HF6 Rockwell indentation scale; (b) nitrided sample (PCN31), the sample surface was 1μm smooth; the feature represents adhesion in HF3 Rockwell indentation scale and shows slight delamination of the film at the edge of the indentation spot. The fragments of the film are due to indentation (small spots). (Magnification 80x)

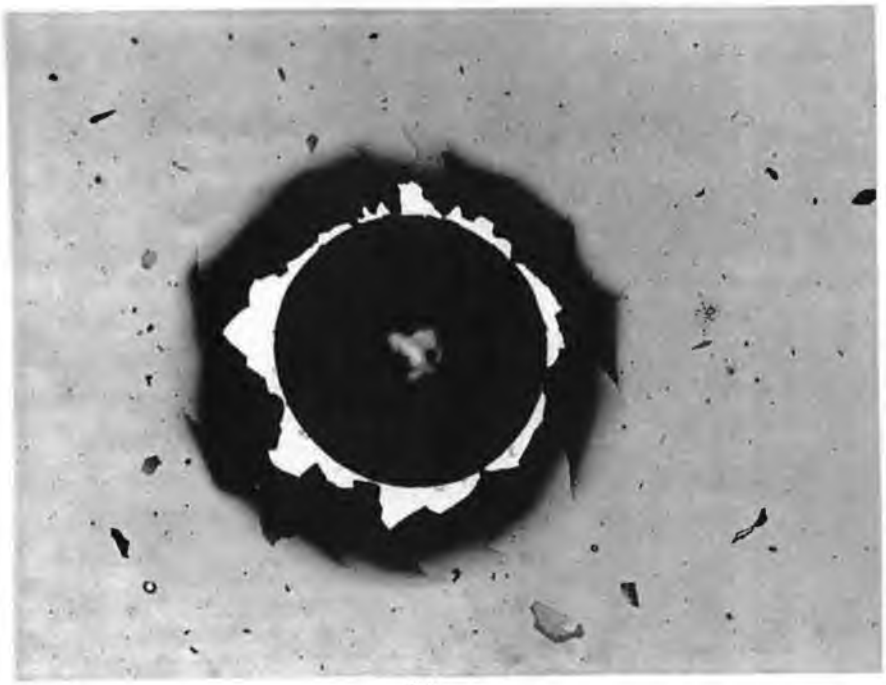

(c)

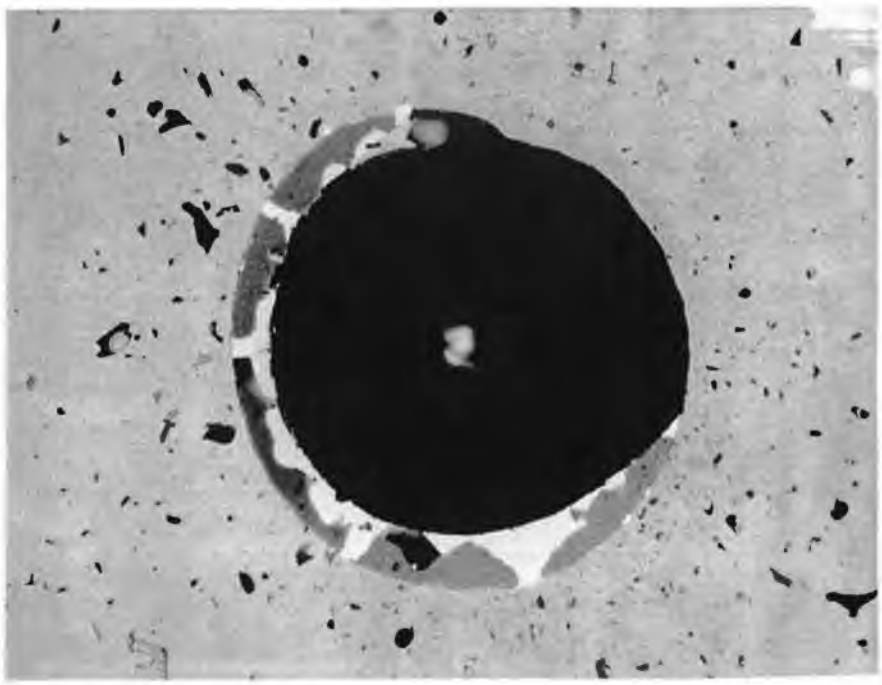

(d)

Figure 6: Rockwell indentation for adhesion evaluation (c) carburised sample (PCN32), the sample surface was 1μm smooth, delamination of the film at the edge of the indentation is observed, this feature represents adhesion in HF5 Rockwell indentation scale; (d) nitrided sample (PCN33), the surface was 3μm smooth; the feature represents adhesion in HF4 Rockwell indentation scale, at the edge of the indentation spot a little delamination of the film is observed. The fragments of the film are due to indententaion (small spots). (Magnification 80x)

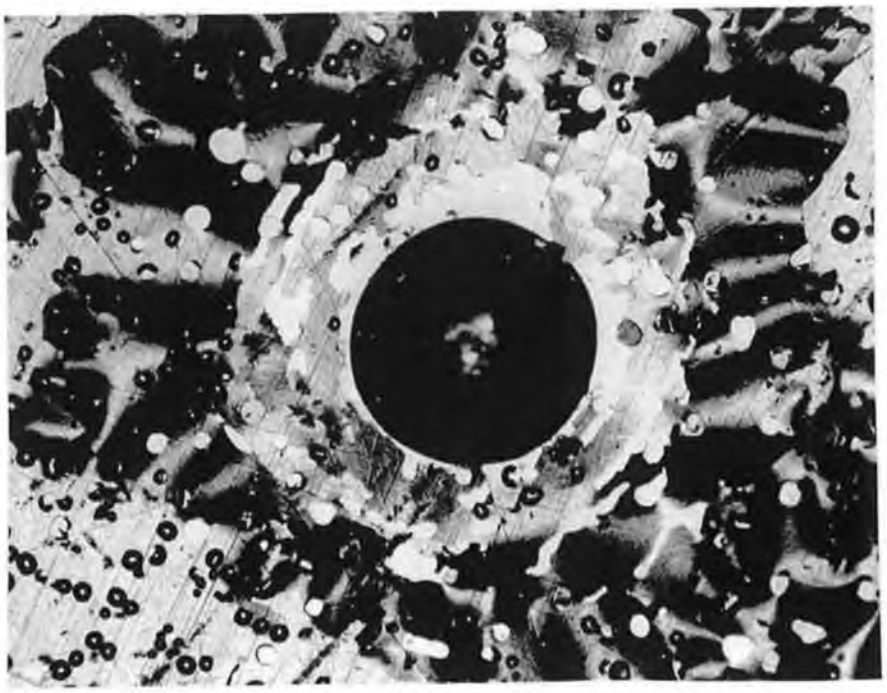

(e)

Figure 6: Rockwell indentation for adhesion evaluation (e) carburised sample (PCN34), the sample surface was 3μm smooth, complete delamination of the film at the edge of the indentation is observed, this feature represents adhesion in HF6 Rockwell indentation scale. The fragments of the film are due to indententaion (small spots). (Magnification 80x)

The results from the pin on disk tests show that the friction of carbon nitride films on steel substrates is not particularly low. The frictional tests were done on the same samples 5 days after the Rockwell indentation tests were carried out. After this friction measurement, the coating on PCN33 visibly delaminated from the surface. Figures 7 and 8 show the wear characteristics of carbon nitride coatings on steel surfaces.

Table 5: Wear test results

Sample no.	Load (g)	Track radius (mm)	Linear speed (m/sec)	Relative humidity (%)	Total no. of revs	No. of revs to $\mu > 0.6$
PCN31	50	7	10	31	10000	6900
PCN33	50	7	10	32	10000	3300

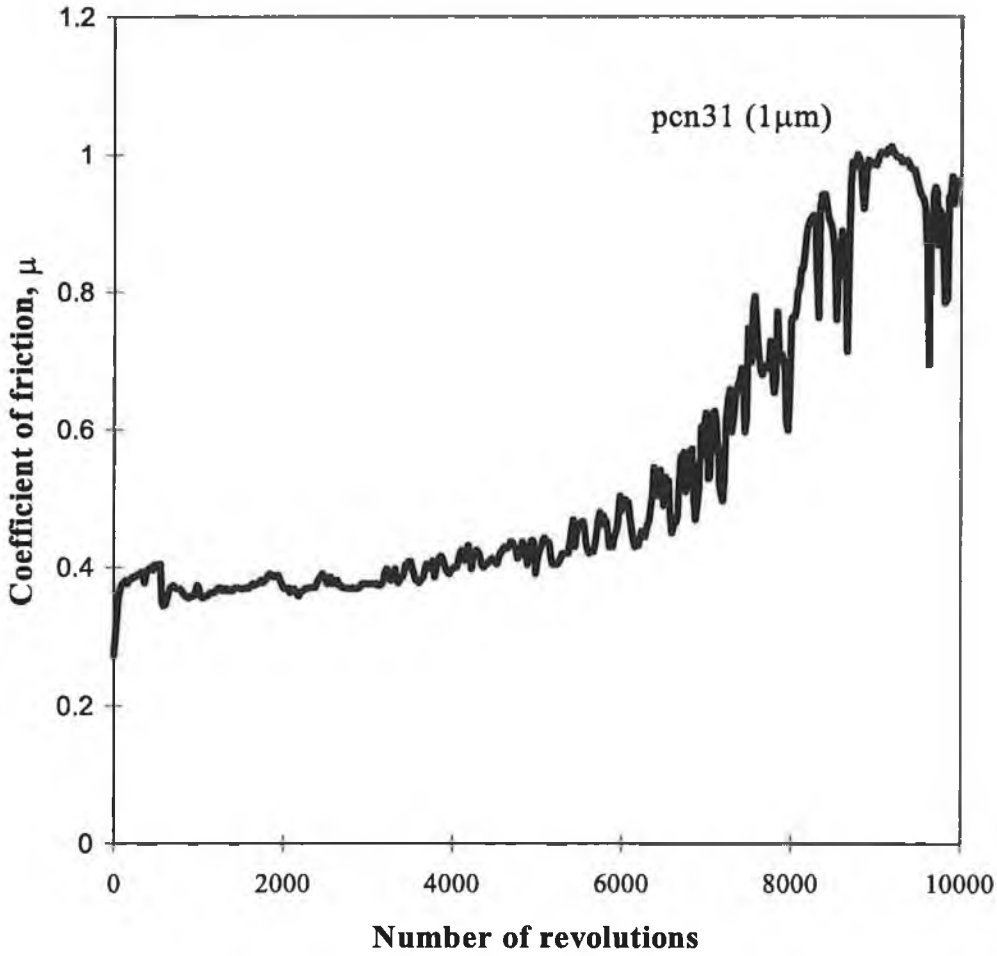

Figure 7: Wear characteristics of sample PCN31 (substrate surface roughness 1μm). The plot also shows the frictional coefficient of the film (<0.4).

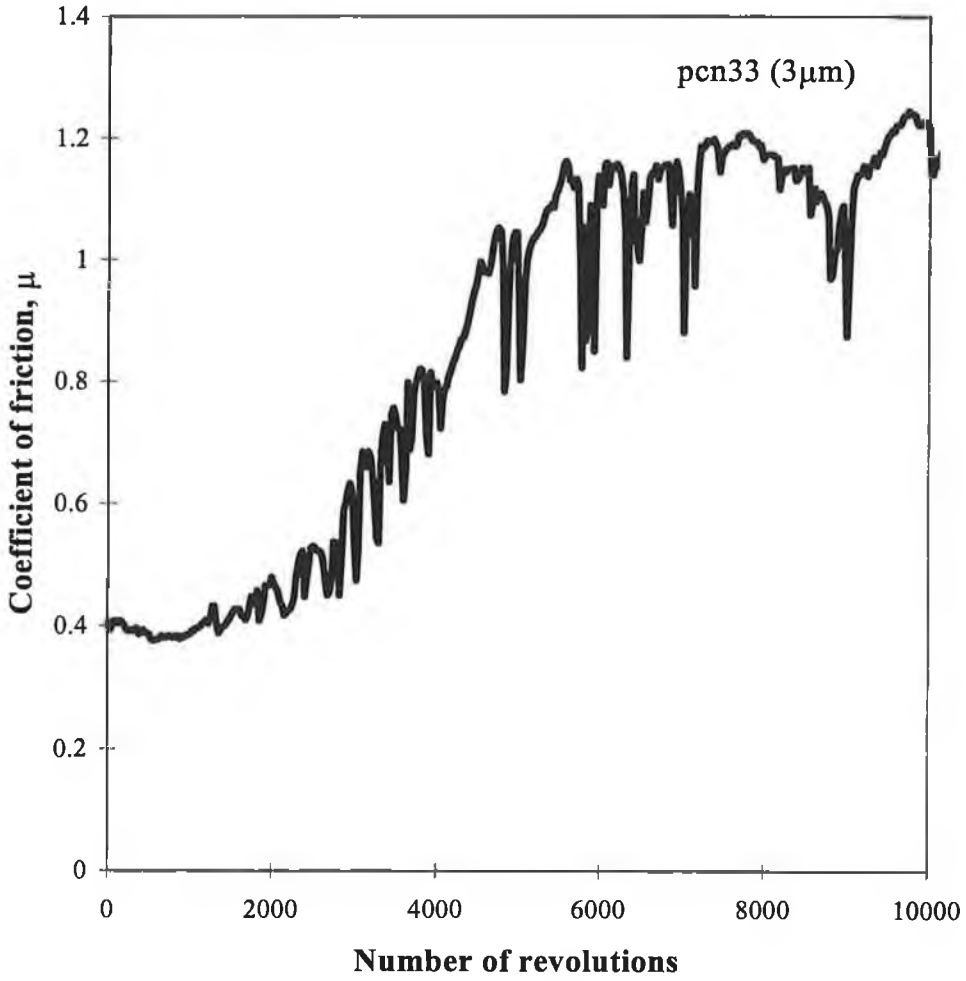

Figure 8: Wear characteristics of sample PCN33 (substrate surface roughness 3μm). The plot also shows the frictional coefficient of the film (≥0.4).

Summary

Above discussion on coating evaluation shows that the adhesion properties of carbon nitride film on steel surface improves when the steel surfaces are saturated by nitriding technique. To make any conclusive comment we need to point several facts:

(1) Carburising technique does saturate the steel surface to act as a diffusion barrier, but the process itself does not have that good dimensional control and has high distortion when compared with nitriding process. Thus it is expected to get good results when nitriding is done for diffusion barrier.

(2) In case of PVD processes, the smoothness and adhesion of the deposited layer is controlled by the surface roughness. The surface roughness used prior to deposition merely gives a trend of adhesion properties. The adhesion could be better if the surfaces were polished further.

The frictional properties are also influenced by the substrate surface roughness. It can be easily seen that the sample PCN31 shows better frictional properties ($\mu < 0.4$) than the sample PCN33 ($\mu \geq 0.4$). The only difference between these two samples are the surface roughness. Thus the substrate surface roughness also affect the wear properties of the coating.

However, nitrogen or carbon diffusion from the film at the interface to the subsurface of the steel is evidently a good reason of poor adhesion of carbon nitride film on steel surface. The adhesion properties can be improved by providing a diffusion barrier layer. To prevent nitrogen diffusion from the film, the steel substrate can be saturated by nitrogen forming a Fe_3N layer. This layer is stable and can be deposited by conventional nitriding technique. In case of carbon diffusion, a protective layer can be formed at the interface by saturating the steel surface with carbon. To achieve this, conventional carburising was carried out on the steel samples. The desirable structure

at the surface after carburising is martensite, but sometimes due to high carbon content an proeutectoid Fe_3C structure may form at the grain boundaries, leaving the overall surface brittle and may cause defects. As this technique is a high temperature process, a good control is required. However, carbon nitride thin film on carburised surface did not show satisfactory results. Although it is hard to come to any conclusion in case of carbirised surface, because 100% marensite at the surface is very hard to achieve to make a good protective layer, but at this stage it can be inferred that carbon does not diffuse at the steel subsurface. It is nitrogen that diffuses into the steel subsurface and causes the poor adhesion at the interface. Thus a protective layer that is saturated with nitrogen can provide good adhesion of carbon nitride film on steel surfaces.

References

1. ASM Handbook for Heat Treatment, ASM, Materials Park, OH, pp. 484-491, 1991.

2. ASM Handbook, Alloy Phase Diagram, vol. 3, ASM, Materials Park, OH, 1992.

3. D.M. Mattox, Surf. Coat. Technol., 81, 8 (1996).

4. D.W. Skelly and L.A. Grunke, J. Vac. Sci. Technol. A, 4(3), 457 (1986).

5. D.M. Mattox, Appl. Surf. Sci., 48-49, 540 (1991).

6. D.M. Mattox, in ASM Handbook, vol. 5, Surface Engineering, ASM, Materials Park, OH, pp.136, 1994.

Chapter 8

Conclusions and Recommendations

8.1 Deposition Technique

Carbon Nitride thin films were deposited using a Penning-type opposed-target DC reactive sputtering source. This differs from the conventional magnetron system in that the two targets are parallel to each other and the magnetic flux lines are oriented along the axis between them. The use of Nd-Fe-B magnets ensures a very high flux density in the inter-target region. The electrons therefore experience strong magnetic confinement between the two cylindrical targets leading to very intense ionisation in the plasma and a high ion flux at the substrate. Complete entrapment of electrons can be possible by changing the position of the sources. Thus effective ion bombardment can be increased which eventually can increase nitrogen incorporation in the film. It was shown that the reactor can be a good source for the production of crystalline carbon nitride material.

The Langmuir probe measurements show that the source gives rise to magnetic confinement of the hot electrons in the inter-cathode space. They show that there is a high degree of ionisation exceeding 2% in the intense plasma region and that an electric field exists outside the anode and cathode sheaths.

Approximate calculations based on the film composition show that the ion to carbon atom ratio at the substrate is ~ 50. It was observed from the Langmuir probe measurements that the ion flux /neutral flux ratio is ~ 0.15, where the neutral flux is calculated from the impingement flux of neutral gas molecules at the deposition pressure. The carbon atom flux is calculated from the rate at which the carbon atoms

are incorporated into the carbon nitride structure in order to give the measured deposition rate, assuming a sticking coefficient of 1. The large overabundance of ionised nitrogen compared with carbon may be significant in the formation of the crystalline material. It is also found that the degree of ionisation in the inter-target region is $>4\%$ giving a very high concentration of excited and reactive species.

Optical emission from the plasma shows that there are CN radicals present in the plasma which come from nitrogen incorporation in the target rather than by chemical sputtering from the substrate.

8.2 Characterisation Techniques

A general macroscopic overview of materials characterisation techniques i.e., physical and mechanical, has been given. This has served to introduce the techniques and to highlight the differences among them. It was seen that due to resolution problem the spectroscopic characterisations i.e., FTIR, Raman, XPS, AES, of the film did not show any sp^3 bonded CN which is the theoretical crystalline phase in the film. The nanocrystals were identified by diffraction techniques. There was some evidence of crystalline diffraction by XRD, however peak intensities were low. This was attributed to the low atomic scattering factor associated with X-ray diffraction from both carbon and nitrogen. Thus further crystallographic investigation required electron diffraction.

8.3 Film Structure: Amorphous

The IR absorption due to carbon-nitrogen bonding was observed to be independent of actual nitrogen content above ~ 25 at.% N. It can be seen that over the range of 25-44% N/(N+C) there is no systematic variation of absorption coefficient. It was predicted and shown that films with >25 at.% nitrogen content, the nitrogen is

mostly bonded to carbon either as C=N or C≡N bonds and a significant amounts of nitrogen were bonded with itself in IR-invisible structures.

Annealing has been shown to lead to a loss of nitrogen from the films at temperature above approx. 550°C. The loss appears to come preferentially from the less saturated carbon-nitrogen bonds and leads to a softer, weakened film structure. The results indicate that as annealing progresses the C≡N is totally removed at 600°C and the appearence of G and D band which is usually Raman active, becomes IR active.

The evolution of the intensities of the C–C, C=N, C≡N bond intensities in amorphous carbon nitride film has been described. The signature of nitrogen-nitrogen bond formation was further investigated by Raman spectroscopy as the IR forbidden E_{2g} symmetry is Raman active. It has been shown that between the Raman D and G peaks their exists a third peak at ~ 1455 cm^{-1}, designated the "N" peak, which has been assigned to the N=N stretching vibration. As the nitrogen incorporation in the film increases, the N=N, C≡N and C–C bonding intensities increase. These experimental results are also in good agreement with the theoretical predictions and thus identify bands in vibrational spectra in the amorphous carbon nitride solid.

It was seen that the E_{2g} symmetry is broken due to the replacement of carbon atoms by nitrogen in the six fold carbon ring structure and the ring was not disrupted, otherwise significant change in the G(graphitic) and D(disorder) band in the Raman spectrum would be observed. This replacement and finally E_{2g} symmetry breaking makes the Raman G and D band more IR active. The post annealing process of the same film confirms the presence of the third peak at ~ 1500 cm^{-1} band region which is due to nitrogen-nitrogen sp^2 bond. After annealing, the G and D bands become sharper and the FWHM of the peaks become narrower due to graphitisation.

It has been shown by comparing FTIR, Raman, XPS and RBS data that the nature of the nitrogen incorporation in sputtered carbon nitride films changes with the amount

of nitrogen incorporated. In particular, above ~25 at.% N content, an increasing amount of the nitrogen occurs in the form of N-N bonds. As annealing progresses, the C≡N sp bonds are eliminated preferentially and the relative amount of nitrogen-nitrogen bonds increases due their relative stability.

The XPS peaks have been assigned to different types of bond by correlating their behaviour as annealing takes place at different temperatures with changes in the bond structure as detected by vibrational spectroscopy, rather than the typical process which involves comparison with nitrogenated polymers. The various components of the N(1s) XPS peaks forms are ascribed as follows: C≡N (sp) at ~ 398.8 eV, C=N (sp^2) at ~ 400 eV and N-N (sp^2) at ~401.2 eV. The C(1s) peaks have been assigned as C-C (sp^3) at ~287.5 eV, C=N (sp^2) at ~286 eV and C≡N (sp) at ~ 288.5 eV.

The valence band spectra shows the interlinked carbon backbone nature of the carbon nitride solid and thus identifies the structural nature of this solid which is significantly different from diamond-like and graphitic features.

It can be seen from AES spectra that both graphitelike (C_2) and diamondlike (C_1) nature exits in our film. It can be seen from the AES carbon spectrum of our carbon nitride film that the C_2 feature is more prominent than the C_1 feature. Thus our film is more graphitic in nature. The presence of a satellite peak, labeled C_6, at ~292 eV confirms the presence of C–C sp^3 structure in our film. This satellite peak is a characteristic Auger emission spectrum of diamondlike C–C sp^3 phase. As no shift in electron energy for this satellite peak was observed, the sp^3 phase is essentially C–C not C–N.

The physical explanation of the weakness of the polymeric CN network is probably due to the formation of this C≡N bonding which terminates the carbon backbone leading to less tightly bound C atoms. This feature was indicated by AES in the C *KLL* Auger spectrum and defined as a defect related π state in the structure. It was also

seen that nitrogen incorporation in the film not only increases the nitrogen-nitrogen bonding but also stabilizes the C-C sp^3 type bonding. The presence of C–C sp^3 bonding structure rather than the C–N sp^3 type, is confirmed by AES, XPS and Raman spectroscopy studies.

The breaking of C–C sp^3 bonds results from the input thermal energy as annealing progresses and leads to graphitisation of the film. Due to carbon's atypical nature in having its p orbital more compact and tightly bound compared to s states, the C=N sp^2 phase is more stable than C-C sp^3 phase. This argument is supported by the annealing behaviour of the film. As C=N sp^2 phase dominates the structure, we propose the film at this stage is mainly graphitelike with some proportion of C–C, C≡N and N=N bonds. Determination of crystalline phases in the film, if present, requires diffraction techniques and Transmission Electron Microscopy.

8.4 Film Structure: Crystalline

It was shown that large areas of continuous nanocrystalline carbon nitride film can be produced at low temperature by DC reactive magnetron sputtering. Crystallographic analysis shows lattice spacings characteristic of β-C_3N_4 with some degree of preferential orientation. No spurious periodicities that cannot be assigned to β-C_3N_4 are observed. It is hoped that the volume fraction of the crystalline regions can be increased by depositing on a substrate that has a better lattice match with β-C_3N_4 than {100} Si. The exact roles of other deposition parameters such as temperature, pressure etc. are still to be determined.

The characteristics of the deposition system which give rise to the formation of crystalline films must be considered. Two important parameters are:

(i) the ion flux/neutral flux ratio (mainly N_2^+/N_2) and

(ii) the carbon atom flux/ion flux ratio (mainly C/N_2^+).

8.5 Effect of Process Parameters

Effect of process parameters, i.e., nitrogen gas pressure, substrate negative bias on film characteristics are discussed. Deposition rate and nitrogen incorporation in the film increase with increase in nitrogen gas (%). A threshold negative bias voltage of -100 V can be observed for sp^2 to sp^3 transformation. The fact that the sp^3 fraction in the film increases with increase in bias voltage (-100 to -150). At about -175 bias voltage the excessive energy dissipates as thermal spike which is reasonably enough to break the sp^3 fraction to sp^2. The mechanism of sp^2 to sp^3 transformation of carbon nitride solid is similar to that are observed in DLC films, deposited by sputtering technique using negative bias substrate bias. This strong experimental evidence is in good agreement with Robertson's model and can be a good indication to increase the amount of crystalline β-C_3N_4 structure in the film. The film becomes denser with increase in substrate negative bias indicating the increase in sp^3 fraction in the film. However, the increase in sp^3 fraction can be checked by EELS technique which is not currently available.

When films are grown at high chamber pressure ($\sim 10^{-2}$ mbar), the diffusion pump does not efficiently pump down the chamber. The residual moisture inside the chamber environment (although very small amount) takes part in the sputtering process. This is the only source of hydrogen contamination in the film. This hydrogen bonds with carbon and nitrogen in the films producing compressive stress. The compressive stresses due to hydrogen at each atomic layer of the film becomes highly supportive. This additional compressive stretching is higher than the bonding strength of the CN compound with the substrate, and thus comes off the substrate.

8.6 Mechanical Properties of the film

The film hardness appears to be controlled by the amount of C≡N bonding, rather than nitrogen content, i.e. the C≡N bond appears to be significantly weaker than the others. The hardness is also likely to be affected by the fact that the C≡N bond will terminate the carbon backbone leading to less tightly bound C atoms. This behaviour is mirrored by the stress measurements. The stress is shown to be concentrated at the film-substrate interface whereas the bulk of the film is stress-free.

Annealing has been shown to lead to a loss of nitrogen from the films at temperature above approx. 550°C. The loss appears to come preferentially from the less saturated carbon-nitrogen bonds and leads to a softer, weakened film structure.

8.7 Carbon Nitride Thin Film as Hard Coating

Adhesion properties of carbon nitride film on steel surface improves when the steel surfaces are saturated by nitriding technique. To make any conclusive comment we need to point several facts:

(1) Carburising technique does saturate the steel surface to act as a diffusion barrier, but the process itself does not have that good dimensional control and has high distortion when compared with nitriding process. Thus it is expected to get good results when nitriding is done for diffusion barrier.

(2) In case of PVD processes, the smoothness and adhesion of the deposited layer is controlled by surface roughness. The surface roughness we used prior to deposition merely gives a trend of adhesion properties. The adhesion could be better if the surfaces were polished further.

The frictional properties are also influenced by the substrate surface roughness. It can be easily seen that the sample PCN31 shows better frictional properties ($\mu < 0.4$) than the sample PCN33 ($\mu \geq 0.4$). The only difference between these two sample are the surface roughness. It is interesting to see that substrate surface roughness also affect the wear properties of the coating.

However, nitrogen or carbon diffusion from the film at the interface to the subsurface of the steel is a good reason of poor adhesion of carbon nitride film on steel surface. The adhesion properties can be improved by providing a diffusion barrier layer. To prevent nitrogen diffusion from the film, the steel substrate can be saturated by nitrogen forming a Fe_3N layer. This layer is stable and can be deposited by conventional nitriding technique. In case of carbon diffusion, a protective layer can be formed at the interface by saturating the steel surface with carbon. To achieve this, conventional carburising was carried out on the steel samples. The desirable structure at the surface after carburising is martensite, but sometimes due to high carbon content an proeutectoid Fe_3C structure may form at the grain boundaries, leaving the overall surface brittle and may cause defects. As this technique is a high temperature process, a good control is required. However, carbon nitride thin film on carburised surface did not show satisfactory results. Although it is hard to come to any conclusion in case of carbirised surface, because 100% marensite at the surface is very hard to achieve to make a good protective layer, but at this stage it can be inferred that carbon does not diffuse at the steel subsurface. It is nitrogen that diffuses into the steel subsurface and causes the poor adhesion at the interface. Thus a protective layer that is saturated with nitrogen can provide good adhesion of carbon nitride film on steel surfaces.

8.8 Strategy for Carbon Nitride thin film deposition

It was shown that continuous crystalline β-C_3N_4 thin film can be obtained by magnetron sputtering technique. We have also seen that due to complex nature of the

plasma, it is not easy to picture a complete idea of ions-neutrals-electrons interactions for the film formation, although a reasonable calculation can be obtained. On the basis of our observed data, a strategy can be formulated as a precondition for the synthesis of β-C_3N_4 solid by sputtering technique

1. An intense low pressure nitrogen plasma is required which provides a high concentration of atomic nitrogen in order to drive the β-C_3N_4 phase. The film becomes more paracyanogen $(CN)_n$ when the nitrogen incorporation in the film is low (<20 at.%).

2. As carbon is three-fold (sp^2) coordinated in $(CN)_n$ but four-fold (the metastable sp^3 hybridization) in C_3N_4 the substrate should be biased during the deposition to provide bombarding with ions at energies of 100-150 eV which stimulates the formation of sp^3 and decreases that of sp^2 hybrids [1].

3. The processes just discussed cannot fully avoid the simultaneous formation of three-fold (sp^2) coordinated CN structure, a temperature $\geq 650^0$C should be used to facilitate the evaporation of paracyanogen nuclei whenever formed. Although very high substrate temperature, i.e., 1000-1200^{0}C may be thermodynamically necessary to obtain crystalline β-C_3N_4 phase, at this high temperature one can expect (if Si is used as substrates) (1) Si diffusion during growth; (2) evaporation and re-deposition of Si; (3) catalytic action of Si in crystal growth. Although effect (1) and (2) can be ruled out but incorporation of Si together with high substrate temperature has catalytic action for C-N-Si crystal formation [2]. Thus a low temperature (<400^{0}C) process is required.

4. Considering the well established crystal chemistry of the iso-structural Si_3N_4 one can expect the formation of amorphous C_3N_4 under the conditions discussed above, because the formation of crystalline β-Si_3N_4 requires temperatures in excess of 1350^{0}C as mentioned by Wells [3]. Thus amorphous Si_3N_4 can be

expected when deposited below 1000°C. This point can be ignored if the following route is considered for sputtering technique: the use of strong magnets (e.g., Nd-Fe-B type) ensures a very high flux density in the inter-target region of a Penning type opposed target DC sputtering source. The electrons therefore experience strong magnetic confinement between the two cylindrical targets leading to very intense ionisation in the plasma and a high ion flux at the substrate. The characteristics of the deposition system which give rise to the formation of crystalline films must be considered. Two important parameters are:

(i) the ion flux/neutral flux ratio (mainly N_2^+/N_2) and

(ii) the carbon atom flux/ion flux ratio (mainly C/N_2^+).

The strategies discussed above should be taken as a precondition for the formation of crystalline β-C_3N_4 film at low temperature (~320°C) where no Si can diffuse to form C-N-Si ternary phase if Silicon single crystal is used as the substrate. Considering these four points strategy a good amount of work can be done on crystalline carbon nitride thin film deposition as future work.

8.9 Future work

Sufficient interesting events have been discovered during the course of this investigation to suggest that further experimental work may bring Carbon Nitride solid to the position occupied today by diamond or other hard compounds where it can contribute its share to the range of hard coating for magnetic storage devices or even in tool steels.

It was seen that floating potential of the substrates becomes positive when the inter target spacing of the Penning source is kept at 7.5 to 5 cm. These inter-target spacing may significantly change the ionisation process within the plasma, because there will be no electron bombardment at the substrate surface. Thus carbon nitride will be

produced at a different plasma mode. This experimental set up may itself can be an interesting direction to proceed.

It was interesting to see that β-C_3N_4 was produced in the case of 100% N_2 sputtering gas even though a higher N content is found for 10% Ar/90% N_2. A possible explanation is that since the momentum of the Ar^+ ions is higher than that of either N_2^+ or N^+ ions then the increased momentum transfer into the growing film causes disruption of the β-C_3N_4 crystals producing amorphous material. This question may be clarified by deposition studies using different sputtering gas mixtures e.g. He/N_2. The role of temperature in growth process can be a good possible direction for future work. In situ Langmuir Probe characterisation of plasma using different gas mixture and discharge current can be done to understand their effects. TEM/TED analyses can be done to identify the crystal structure using different gas mixture and temperature during deposition. Nano probe EELS technique can be used to measure C/N ratio in the crystals.

It is hoped that the volume fraction of the crystalline regions can be increased by depositing on a substrate, e.g., {111} Si, that has a better lattice match with β-C_3N_4 than {100} Si. The exact roles of other deposition parameters such as temperature, pressure, substrate negative bias, etc. can be studied further.

The adhesion properties of carbon nitride thin film were affected by the degree of surface smoothness. A similar investigation can be carried out using smoother (< 1μm) nitrided or curburised steel surfaces. Plasma nitriding or carburising can be done in situ in order to have better surface tolerances to create a diffusion barrier of nitrogen/carbon.

References

1. J. Robertson, Surf. Coat. Technol., 50, 185 (1992).

2. L.C. Chen, D.M. Bhusari, C.Y. Yang, K.H. Chen, T.J. Chuang, M.C. Lin, C.K. Chen, Y.F. Huang, Thin Solid Films, 303, 66 (1997).

3. A.P. Wells, Structural Inorganic Chemistry, 5th ed., Clarendon, Oxford, 1984.

Publications

The following publications/manuscripts resulted from this work presented in this thesis

Journals

1. A K M S Chowdhury, D.C. Cameron, M.S.J. Hashmi and M.J. Gregg, "Deposition of continuous crystalline β-C_3N_4 films" submitted in Physical Review Letters.

2. A K M S Chowdhury, D C Cameron, M Monclus, M J Murphy, N.P. Barradas, J.Gilvarry and M.S.J. Hashmi, "The composition and bonding structure of CNx films and their influence on the mechanical properties", Thin Solid Films, 308-309 (1997), 130-134.

3. J Gilvarry, A K M S Chowdhury, M Monclus, D C Cameron, P J McNally and T Toumi, "Stress behaviour of reactively sputtered nitrogenated carbon films", Surface and Coatings Technology 98 (1998) 979-984.

4. A K M S Chowdhury, D.C. Cameron and M.S.J. Hashmi, "Vibrational properties of carbon nitride film by Raman Spectroscopy", Thin Solid Films, in press.

5. A K M S Chowdhury, D C Cameron and M.S.J. Hashmi, "Bonding structure in CNx films: Variation with nitrogen content and annealing temperature", Surface and Coatings Technology, in press.

6. M A Monclus, A K M S Chowdhury and D C Cameron, "Electrical Properties of reactively sputtered nitrogenated carbon", Thin Solid Films, in press.

7. M J Murphy, J Monaghan, M Tyrrell, R Walsh , D C Cameron, A K M S Chowdhury, M Monclus and M S J Hashmi, "A Penning type magnetron sputtering source and its use in the production of Carbon Nitride coatings", Journal of Vacuum Science & Technology, (accepted).

8. A K M S Chowdhury, D C Cameron and M S J Hashmi, "Adhesion of carbon nitride thin films on tool steel", Presented in the sixth international conference on Plasma Surface Engineering (PSE) '98, Garmisch-Partenkirchen, Germany, Sept. 14-18, 1998, (Key note paper), to be published in Surface and Coatings Technology.

9. A K M S Chowdhury, D C Cameron and M S J Hashmi, "Effect of substrate negative bias on sp^2 to sp^3 phase transformation in carbon nitride thin film", submitted to ICMCTF'99 conference, San Diego, California, USA.

Refereed international conference proceedings

1. A K M S Chowdhury, D.C. Cameron and M.S.J. Hashmi, "Bonding structure in CNx films" in Hard coatings based on borides, carbides and nitrides: synthesis, characterisation and application, proceedings of the international symposium sponsored by the Surface modification & Coatings technology committee of the materials design and manufacturing division of the Minerals, Metals and Materials Society (TMS) edited by Kumar, Chung and Chia, p 61-72, San Antonio, Texas, Feb 16-19, 1998.

2. A K M S Chowdhury, D.C. Cameron, and M.J. Gregg, "Structural characterisation of sputtered deposited CNx films by Transmission Electron Microscopy" Presented in the 21st Annual Symposium of The Microscopical Society of Ireland, Queens University, Belfast, UK, 9th-11th September, 1997, Supplement to Proceedings of The Royal Microscopical Society 33, (1), 1998.

3. A K M S Chowdhury, D C Cameron and M S J Hashmi, "Carbon nitride (CN_X) thin film: Its structural characterisation", in Proceedings of the International Conference on Structure, Processing and Properties of Materials, SPPM'97, edited by E. Haque and A S M A Haseeb, paper No., Str 7, p. B44-B52, Dhaka 1000, Bangladesh, November 15-17, 1997.

Poster presentation at international conference

A K M S Chowdhury, D C Cameron, M B Hopkins, C O'Morain and M S J Hashmi, "Plasma characterisation of a Penning-type sputtering source during CNx thin film deposition" presented at Final Workshop, COST 515 programme, Nancy, France, 11-12th Sept 1997.

Presentation at international conference

M J Murphy, D C Cameron, J Monaghan, A K M S Chowdhury, M Tyrrell, R Walsh, M Monclus and M S J Hashmi, "Dimag sputtering system and CNx film deposition", presented in the Int. Conf. on Thin Films and Metall. Coatings, San Diego, 22nd-26th April 1996.

Appendix A

Nomenclature in Emission Spectroscopy

Theory and notation used for electronic transition are out of the scope of this study, but a brief note will be given here to identify the emission of N_2 plasma. A detailed discussion is given in the reference [1].

The quantum number Λ corresponding to the component of the electronic orbital angular momentum along the internuclear axis can take the values

$\Lambda = 0,1,2.....$

According as $\Lambda = 0, 1, 2, ...$, the corresponding molecular state is designated a Σ, Π, Δ, Φ, ..., state. The multiplet structure of atoms due to electron spin is added as a left superscript. Thus the singlet, doublet, and triplet states of Π state are written as $^1\Pi$, $^2\Pi$, $^3\Pi$ respectively. In a diatomic molecule, any plane through the internuclear axis is a plane of symmetry. Therefore the electronic eigenfunction [1] of a Σ state either remains unchanged or changes sign when reflected at any plane passing through both nuclei. In the first case, the state is called a Σ^+ state, and in the second case, it is called a Σ^- state. Even electronic states are designated by g and odd states by u in right subscript of a state (i.e., Σ_g or Σ_u).

If several electronic states of a molecule are known, they are distinguished by a letter X, A, B,...., a, b,..., in front of the term symbol. X is frequently used for the ground state of the molecule. The upper state is always written first and then the lower in designating a given electronic transition, e.g., $A^1\Pi$-$X^1\Sigma$.

References

1. G. Herzberg, Spectra of Diatomic Molecules, Van Nostrand Reinhold, Berlin, 1950.

Appendix B

XPS Peak Fitting Program

PSPEAK Version 2.0 for WIN95

The program can convert the peak parameters to a list of peak intensities. A few features are added into the program, e.g., a better way to locate a point at a noise baseline for the Shirley background calculations, combine the two peaks of $2p_{3/2}$ and $2p_{1/2}$, fitting different XPS regions at the same time.

Version 2.0 of the program has been extensively tested and debugged. A file conversion program is also included to convert the older file format to this one. In addition, Tougaard background subtraction was added. Because this subtraction requires a large scan range, the maximum number of points in each spectrum has been increased to 2000. Many checking codes are added so that the program will not end so easily.

The program was written in Visual Basic 4.0 and uses 32 bit processes by Dr. Raymund W.M. Kwok, Department of Chemistry, The Chinese University of Hong Kong, Shatin, Hong Kong.

Features of the program

(1) Background

Shirley, Linear and Tougaard background. For Tougaard background, the program can optimize the B1 parameter by minimizing the "square of the difference" of the

intensities of ten data points in the high binding energy side of the range with the intensities of the calculated background.

One can choose None (1 point), 3, 5, 7, and 9 point average. This will average the intensities around the binding energy one selected. Hence, we do not need to locate a point with intensity at the middle of a noisy baseline.

(2) Peak types: p, d and f.

Each of these peaks combines the two splitting peaks. The FWHM is the same for both the splitting peaks, e.g. a p-type peak with FWHM=0.7eV is the combination of a $p_{3/2}$ with FWHM at 0.7eV and a $p_{1/2}$ with FWHM at 0.7eV, and with an area ratio of 2 to 1. If the theoretical area ratio is not true for the splitted peaks, the old way of setting two s-type peaks and adding the constraints should be used. The "s.o.s." stands for spin orbital splitting.

(3) Peak constraints

This program uses four parameters for each peak, i.e., peak position, area, FWHM, and the %Gaussian-Lorentzian. Since peak area depends on peak height, FWHM and %GL, useing peak height as a peak parameter cannot directly reflect concentration. Thus, peak area is used as a better way of correlating the concentration ratios. The optimisation of the %GL value is allowed in this program. A suggestion to use this feature is to find a nice peak for a certain setting of the instrument and optimise the %GL for this peak. Then we can fix the %GL in the later peak fitting process when the same instrument settings were used.

For setting constraints, each parameter can only be the following three types: "referenced by others", "reference to another parameter", and "not involved in

referencing". The parameter cannot be both "referenced by another parameter" and "reference to another parameter". One can set the constraints in the follow way,

Position: Peak 2 = Peak 1 + 1.6

Position: Peak 3 = Peak 1 + 15

but one cannot

Position: Peak 2 = Peak 1 + 1.6

Position: Peak 3 = Peak 2 + 13.4.

(4) Optimisation

One can optimise a single peak parameter, the peak (the peak position, area, FWHM, and the %GL if the "fix" box is not ticked), a single region (all the parameters of all the peaks in that region if the "fix" box is not ticked), or all the regions. During optimisation, one can press the "Cancel" button and the program will stop the process in the next cycle.

(5) Option

The %tolerence allows the optimisation routine to stop if the change in the "difference" after one loop is less that the %tolerence. The optimisation routine will also stop if the maximum number of loop is reached. We may also confirm the search range by selecting "medium" or "small". The "difference" means the sum of the square of the difference between each point in the calculated and the experimental curve. This is a little bit faster that using Chi^2 since Chi^2 requires an additional division calculation for each point.

(6) Import

The program can read the Kratos's *.DES files. The peak fitting parameters in the file will also be read. It can also import ASCII file in the following format:

Binding Energy Value 1	Intensity Value 1
Binding Energy Value 2	Intensity Value 2
..	..

The B.E. list must be in ascending or descending order. However, the file cannot have other lines before and after the data, and sometimes, TAB may cause reading error.

Limitations

This program limits the maximum number of points for each spectrum to 2000 and the maximum of peaks for all the regions to 21.

Appendix C

Bending beam method

The formula used for calculating stress in terms of the end deflection of the beam has been derived by various workers. The earliest analysis by G.G Stoney [1] assumed that Young's moduli of the film and the substrate were identical and that the stress was isotropic. Under these circumstances he obtained

$$\sigma = \frac{E_s d_s}{6\rho d_f} \tag{1}$$

where E_s is the Young's modulus of the substrate and film, ρ is the radius of curvature of the beam, d_s is the substrate thickness, and d_f is the film thickness (figure 1a).

This can be easily turned into an equation relating stress to end deflection by substituting

$$\rho = \frac{l^2}{2\delta} \tag{2}$$

where l is the length of the substrate and δ is the deflection of the free end, thus,

$$\sigma = \frac{E_s d_s \delta}{3l^2 d_f} \tag{3}$$

The theory used to derive eqn. 3 is limited in its applicability. There are number of points to be considered: (1) substrate length must be at least twice the width, (2) deflection must not be greater than the substrate thickness.

Three factors may be noted with regard to the use of this equation. Firstly, if the film is not in the form of a flat continuous slab but is an island structure as during the initial stages of growth, either the stress must be defined from eqn. 1 using an average value for the thickness derived from the known rate of deposition, or the cross-sectional area of the average island must be found.

Secondly, the stress in a film does not necessarily become zero as the film thickness goes to zero because the film thickness d_f appears in the denominator of eqn. 3. However, the end deflection of the beam does tend to zero so that it is often more convenient to plot the force per unit width σd_f, as this is proportional to the deflection, i.e.,

$$\sigma d_f = \frac{E_s d_s}{3l^2}\delta \qquad (4)$$

Thirdly, the equation 4 has neglected the effect of stress in plane of the substrate and at right angles to the beam length on the beam curvature. Eqn 4 therefore needs to be modified by the introduction of Poission's ratio of the substrate ν,

$$\sigma d_f = \frac{E_s d_s}{3l^2(1-\upsilon)}\delta \qquad (5)$$

If the equation 5 is considered for the geometry shown in figure 1(b) which usually occurs in case of thin films, a few modifications are still needed.

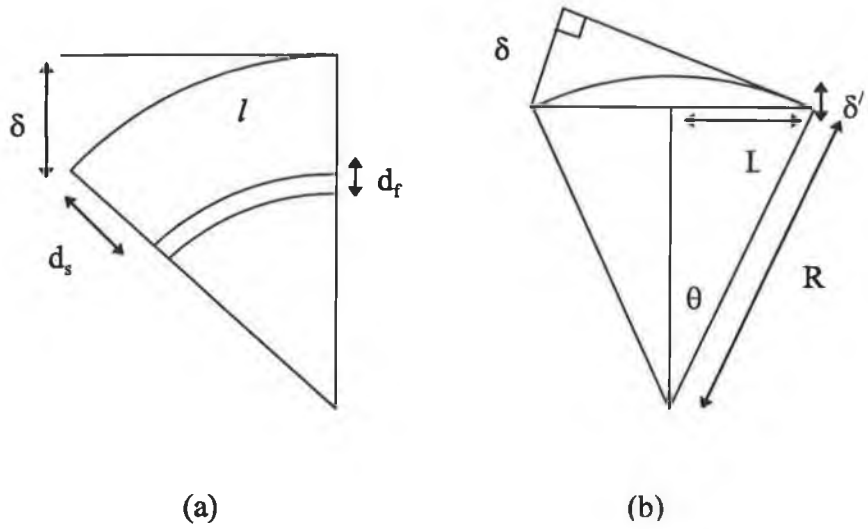

Figure 1: (a) Schematic of bending beam, clamped at one end, (2) schematic geometry of a bent thin film due to intrinsic stress.

According to the figure 1(b), when the film bends due to stress, δ' is taken as the deflection instead of δ. In this case the geometry becomes

$$\sin\theta = \frac{L}{R} \text{ and } \cos\theta = \frac{R-\delta'}{R} = 1-\frac{\delta'}{R} \tag{6}$$

The $\sin\theta$ term becomes

$$\sin\theta = \sqrt{1-\cos^2\theta} = \sqrt{1-\left(1-\frac{\delta'}{R}\right)^2} \approx \sqrt{1-\left(1-\frac{2\delta'}{R}\right)} = \sqrt{\frac{2\delta'}{R}} \tag{7}$$

$$\delta = 2L\sin\theta = 2L\sqrt{\frac{2\delta'}{R}} \tag{8}$$

$$L = R\sin\theta = R\sqrt{\frac{2\delta'}{R}} \tag{9}$$

$$\delta = 2R\sqrt{\frac{2\delta'}{R}}\sqrt{\frac{2\delta'}{R}} = 4\delta' \tag{10}$$

Thus the eqn. 5 becomes

$$\sigma d_f = \frac{4E_s d_s}{3l^2(1-\upsilon)}\delta' \tag{11}$$

References

1. G.G. Stoney, Proc. Roy. Soc., London, 172 (1909).